U.PORTO
FACULDADE DE CIÊNCIAS
UNIVERSIDADE DO PORTO

universidade de aveiro

Universidade do Minho

PhD

3rd CYCLE

FCUP
UA
UM
2025

U.PORTO

The role of 4*f* - 3*d* electron interactions on the physical properties of perovskites: the case of $NdNiO_3$ and $NdFeO_3$

Mariana Melo Nogueira Rosa Gomes

FC

U.PORTO
FACULDADE DE CIÊNCIAS
UNIVERSIDADE DO PORTO

universidade de aveiro

Universidade do Minho

The role of *4f* – 3*d* electron interactions on the physical properties of perovskites: the case of $NdNiO_3$ and $NdFeO_3$

Mariana Melo Nogueira Rosa Gomes
Physics Doctoral Program MAP-Fis
Faculty of Sciences of the University of Porto, University of Aveiro and University of Minho
2025

PhD

The role of 4*f* – 3*d* electron interactions on the physical properties of perovskites: the case of $NdNiO_3$ and $NdFeO_3$

Mariana Melo Nogueira Rosa Gomes
Thesis carried out as part of the Physics Doctoral Program MAP-Fis
Department of Physics and Astronomy, Faculty of Sciences of the University of Porto
2025

Supervisor
Joaquim Agostinho Moreira, Associate Professor, FCUP

Co-supervisor
Hélder Crespo, Associate Professor, FCUP

Co-supervisor
Leonard Deepak Francis, Researcher Group Leader, INL





All the corrections determined by the jury, and only those, were made.

The Supervisor,

Porto, _____/_____/_____

Note: This page should only be included **in the final version after defence and only if the jury approves the thesis with a recommendation for the student to correct errors, inaccuracies or formal inaccuracies** identified and expressly mentioned during the tests. **This page must be deleted from the version to be submitted as part of the thesis submission prior to the defence.**

Assinado por: **Joaquim Agostinho Gomes Moreira**
Num. de Identificação: 12964526
Data: 2025.07.10 14:28:48+02'00'

“ Só se nos detivermos a pensar nas pequenas coisas chegaremos a compreender as grandes. ”

José Saramago

Acknowledgements

The work presented in this thesis would not been possible without the scientific and technical support from all who collaborated with me.

I was extremely lucky to collaborate with researchers outside my home institution. A considerable part of experimental work was indeed done with the help and guidance of external collaborators. I am deeply grateful:

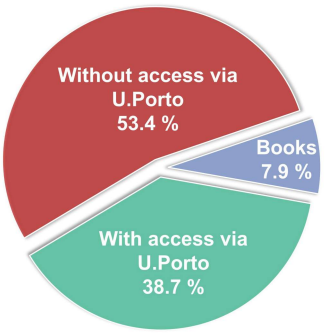
- to Dr. Marian Mihalik and Dr. Matus Mihalik (Slovak Academy of Sciences) for providing the crystals of $NdFeO_3$, whose high-quality was crucial for the reliability of experimental data;
- to Prof. Jens Kreisel (University of Luxembourg) for providing a $NdNiO_3$ film of such good quality;
- to Abderrazzak Bassou and Prof. Pedro Tavares (Universidade de Trás-os-Montes e Alto Douro) for the XRD measurements and discussions;
- to Dr. Ihsan Çaha and my co-supervisor Dr. Leonard Francis (INL) for the STEM measurements and analysis;
- to Prof. Bernardo Almeida (Universidade do Minho) for the electric resistivity measurements;
- to Dr. Jorge Íñiguez-González (University of Luxembourg) and Dr. Hong Jian Zhao (Jilin University) for the DFT calculations;
- to Dr. Christelle Kadlec, Dr. Filip Kadlec and Dr. Stanislav Kamba (Czech Academy of Sciences) for guiding me with FTIR and THz spectroscopic experiments and analysis, and for the fruitful discussions, the stays abroad at your institute had a significant impact on my PhD journey;
- to Prof. Michael Carpenter (University of Cambridge) for all the inputs, fundamental for the interpretation of RUS data;
- to both Prof. Rui Vilão and Prof. José Paixão (Universidade de Coimbra) for all the availability in helping me navigate the muon analysis and for the magnetizations measurements, respectively;

- to all scientists from the large-scale facilities who provided me support during and after beamtimes;

Also, my gratitude goes to all the colleagues, members and staff of IFIMUP that have accompanied my journey in this institution. I want to empathize how important was the support provided by the staff from DFA workshop and from the secretary of IFIMUP and DFA.

To all my supervisors, Dr. Leonard Francis, Prof. Hélder Crespo and Prof. Joaquim Agostinho Moreira, thank you for supporting this PhD project.

I must point out that more than 50% of the citations in this thesis were not available via U.Porto, and therefore I am deeply grateful to SciHub and all the colleagues from other institutions who provided me access to those papers.



To my research team, I want to express my deepest gratitude. Specially to Prof. Joaquim Agostinho Moreira, my main supervisor, I am deeply grateful for his guidance and support, for pushing me forward to become a better scientist and for always be willing to send me abroad. Also to my colleague and friend Rui Vilarinho, thank you for showing me the positive side to every situation and for the long scientific (and non-scientific) discussions.

Obrigado à minha mãe, que apesar de não entender bem o que é que eu estudo, apoia-me incondicionalmente.

Oscar Wilde once wrote: "*We are all in the gutter, but some of us are looking at the stars*". Lastly, I want to thank my boyfriend André, for always pointing me the way to "*the stars*".

Muito obrigado a todos!

This PhD was funded by Quantum Portugal Initiative, an INL and FCT partnership, through the grant number SFRH/BD/151051/2021.

Resumo

Nesta tese, investigamos as interações ferróicas de óxidos perovskites de neodímio: $NdNiO_3$ e $NdFeO_3$. O principal objectivo é compreender como o catião do site-B (B = Ni ou Fe) influencia as propriedades físicas destes compostos, e como a interação entre eletrões $3d$ dos metais de transição e as $4f$ das terras raras, governam o comportamento estrutural, electrónico e magnético.

Para $NdNiO_3$, os estudos focam-se no forte acoplamento eletrão-rede, típico dos niquelatos. Investiga-se a percolação de fases estruturais durante a transição metal-isolador. Espectroscopia Raman é a técnica usada não só na identificação das fases estruturais, mas também para a sua quantificação. Estes resulatdos demonstram a natureza percolativa das transições de fase nos niquelatos.

Para $NdFeO_3$, é dado ênfase à interação spin-rede. Teoria de grupos combinada com diversas técnicas de espectroscopia, permitem a classificação das simetrias e a análsie das regras de selecção de fonões e magnões, que suportam as interpretações ao longo da tese. Com o uso de mapeamento de imagem magneto-ótico, espectroscopia de ultrasons e susceptibilidade magntéctia AC, investiga-se a dinâmica de domínios magnéticos e estruturais. Evidências de pequenas distorções estruturais, que acompanham a reorientação de spins, levou-nos a usar uma técnica de sondas locais para detectar a mudança de simetria prevista na fase Γ_{24}. O abaixamento de simetria para a fase monoclínica $P2'_1/n'$ é revelada através de espectroscopia de muões. Esta é a primeira confirmação experimental da fase monoclínica durante a reorientação de spins em ortoferrites. Devido à natureza magnetoestructural da $NdFeO_3$, também se explorou o controlo das configurações magnéticas através da aplicação de campo magnético. Duas transições distintas induzidas por campo são identificadas: reorientação de spins e spin-flop para altos campos, ambas dependentes da direção de campo aplicado. Os diagramas de fases resultantes evidenciam o forte acoplamento entre as duas sub-redes magnéticas e o papel fundamental da anisotropia das orbitais $4f$ do Nd.

A combinação de estudos eletrónicos, estruturais e magnéticos revelam o papel crítico das interações entre os eletrões $3d$ (Ni/Fe) e $4f$ (Nd) na determinação das propriedades físicas únicas destas perovskites. Este trabalho tem implicações abrangentes na compreensão das interações ferróicas em perovskites de terras raras e sistemas de redes magnéticas não-equivalentes.

Palavras-chave: perovskites, niquelatos de terras raras, ortoferrites de terras raras, acoplamento eletrão-rede, acoplamente spin-rede, distorções estruturais, anisotropia magnética

Abstract

In this thesis, we investigate the ferroic interactions in neodymium-based perovskite oxides: $NdNiO_3$ and $NdFeO_3$. The main objective is to understand how B-site cation (B = Ni or Fe) influences the physical properties of these compounds, and how the interplay between $3d$ transition metals and $4f$ rare-earth electrons governs their structural, electronic, and magnetic behaviour.

In $NdNiO_3$, the studies are centred on strong electron-lattice coupling typical of nickelates. We investigate structural phase percolation across the metal-to-insulator transition. Raman scattering spectroscopy is a technique employed not only to identify structural phases, but also to quantify them. These findings shed light on the percolative nature of the transitions in nickelates.

In $NdFeO_3$, particular emphasis is placed on the spin-lattice interaction. Group theory combined with several spectroscopic techniques, enables the symmetry assignment and selection rule analysis for phonons and magnons that support the interpretations throughout the thesis. Using magneto-optical imaging, resonant ultrasound spectroscopy, and AC magnetic susceptibility, we investigated the dynamics of magnetic and structural domains. The indication of subtle structural distortions accompanying the spin reorientation transition led us to employ a local probe technique to detect the predicted symmetry breaking of the Γ_{24} phase. Symmetry lowering to the monoclinic $P2_1'/n'$ space group is revealed by muon spin spectroscopy, where the separation of spectral components is interpreted as Fe-site Wyckoff position splitting, consistent with monoclinic symmetry. This represents the first experimental confirmation of monoclinic symmetry during SRT in orthoferrites. Taking advantage of the magnetostructural nature of $NdFeO_3$, we also explore the control of magnetic configurations under external magnetic fields. Two distinct field-induced transitions are identified: a spin reorientation and a novel high-field spin-flop transition, both dependent on the direction of the applied magnetic field. The resulting phase diagram highlights the strong coupling between magnetic subsystems and the critical role of Nd-$4f$ anisotropy.

The combined studies of electronic, structural and magnetic investigations revealed the role of $3d$(Ni/Fe) - $4f$(Nd) electron interactions in determining the unique physical properties of these perovskites. Overall, this thesis contributes to a broader understanding of ferroic interactions in rare-earth perovskites and related materials with inequivalent magnetic sublattices.

Keywords: perovskites; rare-earth nickelates; rare-earth orthoferrites; electron-lattice coupling; spin-lattice coupling; structural distortions; magnetic anisotropy

Table of Contents

Acknowledgements iii
Resumo v
Abstract vii

Table of Contents ix
List of Tables xiii
List of Figures xv
List of Abbreviations xxiii

1. Introduction 1
   1.1. Perovskite structure: ABO_3 3
      1.1.1. P*nma* or P*bnm* setting 6
      1.1.2. Magnetic ordering in perovskites 8
   1.2. Rare-earth nickelates 11
      1.2.1. Phase diagram of RNiO$_3$ 12
         1.2.1.1. Electronic transition 13
         1.2.1.2. Structural transition 14
         1.2.1.3. Magnetic transition 16
      1.2.2. The case of NdNiO$_3$ 17
         1.2.2.1. Percolations effects: electronic and magnetic 18
   1.3. Rare-earth orthoferrites 21
      1.3.1. Phase diagram of RFeO$_3$ 22
         1.3.1.1. Spin reorientation transition model 23
         1.3.1.2. Magnetic ressonances: magnons 25
      1.3.2. The case of NdFeO$_3$ 29
         1.3.2.1. Magnetic ordering of Fe^{3+} ions 29
         1.3.2.2. Magnetic ordering of Nd^{3+} ions 32
         1.3.2.3. Structural and magnetic symmetries considerations across SRT 33
   1.4. Aim of the thesis 37
2. Experimental Techniques 39
   2.1. Sample processing techniques 39
      2.1.1. NdNiO$_3$ thin film 39

2.1.2. $NdFeO_3$ crystals 39
2.2. Characterization techniques 40
2.2.1. X-ray diffraction 40
2.2.2. X-ray photoelectron spectroscopy (XPS) 40
2.2.3. Scanning Transmission Electron Microscopy (STEM) 41
2.2.4. Raman scattering spectroscopy 42
2.2.5. Fourier Transform Infrared spectroscopy (FTIR) 44
2.2.6. Time-domain THz spectroscopy 45
2.2.7. Electric and magnetic properties 46
2.2.8. X-ray magnetic circular dichroism 47
2.2.9. Resonant ultrasound spectroscopy (RUS) 48
2.2.10. Muon-spin rotation spectroscopy (μSR) 49
2.2.11. Magneto-optical microscopy 51
3. Structural percolation across MIT in $NdNiO_3$ 53
3.1. Morphological, chemical, and structural characterization 54
3.1.1. STEM 56
3.2. Metal-to-insulator phase transition 58
3.3. Magnetic phase transition 59
3.4. Structural phase transition 60
3.5. Discussion 63
3.6. Summary 66
4. Optically active lattice and magnetic excitations of $NdFeO_3$ 67
4.1. Lattice excitations 68
4.1.1. Group theory analysis of the phonons 68
4.1.2. Raman active modes 69
4.1.3. Infrared active modes 72
4.2. Magnetic excitations 76
4.2.1. Magnon selection rules 76
4.2.2. Temperature evolution of magnons by TDS-THz spectroscopy 80
4.2.3. Room temperature magnons signature by Raman spectroscopy 81
4.2.4. Crystal-field excitations 82
4.3. Summary 82
5. Magnetic and structural domain walls dynamics in $NdFeO_3$ 85
5.1. Magneto-optic imaging of domain walls 86
5.2. Magnetoelastic properties 87
5.3. AC magnetic susceptibility 89
5.4. Discussion 90
5.4.1. Correlation between elastic and magnetic domain walls 90

5.4.2. Elastic softening and stiffening across SRT 91
5.4.3. Acoustic loss and domain wall mobility 97
5.4.4. Magnetic susceptibility vs elastic compliance 99
5.5. Summary 100
6. Monoclinic phase across SRT in $NdFeO_3$ 101
6.1. Muon-spin:local magnetic probes 102
6.1.1. Symmetry considerations 102
6.1.2. μSR analysis 102
6.2. Hypothesis: splitting or coexistence? 108
6.3. Summary 109
7. Spin structure control in $NdFeO_3$: the role of $4f$ magnetic anisotropy 111
7.1. Coupling of the two magnetic sublattices 112
7.2. Magnon behaviour under magnetic field 114
7.3. Other excitations under magnetic field 122
7.3.1. Nd^{3+} phonons 122
7.3.2. Crystal-field excitation of Nd^{3+} 123
7.4. Discussion 125
7.5. Summary 129
8. Conclusions 133
Bibliography 138
A. Appendix 163
A.1. Conversion from standard to non-standard setting 163
A.2. Classification of magnetic point and space groups 164
A.3. Structural analysis of $NdNiO_3$ film on cooling 166
A.4. IR reflectivity analysis in $NdFeO_3$ 167
A.5. RUS data on cooling for $NdFeO_3$ 168
A.6. Landau-type theory for SRT in $NdFeO_3$ 169
A.7. Phenomenological description of elastic relaxation process in SRT 170
A.8. $NdFeO_3$ magnon and phonon spectra under magnetic field 172

List of Tables

1.1. Wyckoff positions in the setting groups P$m\bar{3}m$ and P*bnm* of a ABO_3 perovskite. Adapted from WYCKPOS tool from Bilbao Crystallographic Server. 7
1.2. Transformation properties of the base vector of B-cation [19]. 10
1.3. Transformation properties of the base vector of A-cation [19]. 11
1.4. Magnetic irreducible representations (irrep) and the corresponding magnetic space groups derived from P*bnm* [19]. 11
1.5. Wyckoff positions splitting in the transformation P*bnm* $\longrightarrow$ P$2_1/n$. Adapted from WYCKPOS tool from Bilbao Crystallographic Server. 37

3.1. Results from the XPS analysis, namely the percentage of Ni^{2+} and Ni^{3+} of the sample is calculated based on the peak areas, from which the oxygen vacancy is estimated. 56

4.1. Experimental and theoretical band positions, the corresponding symmetry assignment and main atomic motions (identified from DFT calculations) of the observed Raman-active modes in $NdFeO_3$. The values at 10 K were taken from [81]. 70
4.2. Experimental and theoretical (only for transversal phonons) band positions, the corresponding symmetry assignment of the observed transversal and longitudinal IR-active modes in $NFeO_3$ 74
4.3. Theoretical and experimental values of some crystal-field (CF) excitations of $NFeO_3$. Note that each CF excitation has two calculated values representing the up and down spin energies (due to Zeeman effect). 82

A.1. Parameters obtained from the IR reflectivity spectra fitting and corresponding symmetry assignment. 167

List of Figures

1.1. Schematic representation of the dominant interactions in ABO_3 materials with A-site occupied by Nd^{3+} cation and B-site by either Ni^{3+} or Fe^{3+} cations. The respective electronic configurations of each cation is also presented. 2
1.2. Ideal perovskite structure with P$m\bar{3}m$ symmetry, with primitive unit cell Z=1. 3
1.3. Scheme presenting the space group relationships associated with tilt system. Solid lines indicate second order phase transitions while dashed lines first order phase transitions. Adapted from [13]. 6
1.4. Symmetry-adapted distortion modes of the orthorhombic P*bnm* space group with respect to the P$m\bar{3}m$ structure. Adapted from [16]. 8
1.5. Types of magnetic orders emerging from the interactions between the four magnetic B-sites atoms of P*bnm* unit cell: collinear orders from (a)-(e) and non-collinear orders from (f)-(h). Adapted from [5]. 9
1.6. Phase diagram of RNiO$_3$ along the rare-earth substitution. Squares and circles correspond to MIT and magnetic transition, respectively. Adapted from [6]. 12
1.7. Illustration of the MIT characteristic of RNiO$_3$, where the insulator phase has two inequivalent nickel sites. Adapted from [24]. 13
1.8. (a) Main atomic distortions that promote the P*bnm* and then P$2_1/n$ phases, having as a starting point P$m\bar{3}m$. R_{xy}: $[110]_{pc}$ anti-phase rotation of octahedra cages around x- and y-axis, M_z: $[001]_{pc}$ in-phase rotation of octahedra cages around z-axis, B_{OC}: breathing of the oxygen octahedra. Energy wells associated to the freezing of individual distortion of increasing amplitude in the cubic cell are shown for different R cations and either a ferromagnetic (full line) or E′-type antiferromagnetic (dashed line, only for R = Y) spin arrangement: $SmNiO_3$ (green), $GdNiO_3$ (orange) and $YNiO_3$ (blue). (b) Energy wells as a function of breathing distortion's amplitude for fixed amplitudes of oxygen rotations (R_{xy} and M_z) for the case of $YNiO_3$ with ferromagnetic spin arrangement. Adapted from [28]. 15
1.9. (a) Temperature evolution of Ni magnetic moment for R =Pr, Nd, Sm and Eu. Lines represent the Brillouin fitting function. Adapted from [29]. (b) Antiferromagnetic arrangement of the nickelates magnetic structure. The red arrow highlights the Bragg vector $(½\ 0\ ½)_{orth}$ in orthorhombic notation, which corresponds to $q_0 = (¼, ¼, ¼)_{pc}$ in pseudocubic notation. Adapted from [6]. 16
1.10. (a) Resistivity versus temperature of 30 u.c. NNO film deposited on $NdGaO_3$ substrate, where T_{IM} (red dot) and T_{MI} (blue dot) are extracted from peaks of (b). (b) Plot $-\frac{dln(R)}{dT}(T)$ during heating and cooling cycles. Adapted from [45]. 18
1.11. Volume fraction of insulating phase (left axis) and derivative of logarithm of resistivity (right axis) as a function of temperature for (a) NNO ceramic and (b) NNO thin film on $NdGaO_3$ substrate. Peak maximum (T_{MI}) coincides with percolation threshold $V_{ins} = \frac{2}{3}$. Adapted from [36]. 19

1.12 (a) Magnetic texture evolution with temperature, where black dashed lines are the contour of AFM domains at 130 K. Measurements using RMXS nano-probes. (b) Macroscopic resistivity curve. (c) RMXS measurements where (¼, ¼, ¼)$_{pc}$ diffraction peak intensity is measure with nano-probes (symbols) and macroscopic X-ray beam (lines). (d) XPEEM mapping at 100 K. Adapted from [50]. 20
1.13 (a) Phase diagram of *R*FeO_3 along the rare-earth substitution. Filled circles mark the Néel transition temperature, establishing $G_xA_yF_z$ magnetic state. Open circles and squares correspond to the spin reorientation transitions $G_xA_yF_z \rightarrow F_xC_yG_z$ and $G_xA_yF_z \rightarrow A_xG_yC_z$, respectively. Adapted from [5]. (b) Magnetic ordering of Fe^{3+}, with the canting induced out of the ab-plane, giving rise to a small ferromagnetic component along c-axis. Adapted from [59]. 22
1.14 Spin configurations for different magnetic phases, with rotational SRT $\Gamma_4 \longrightarrow \Gamma_2$, with respect to the S_1, S_2, S_3, S_4 spins of Fe^{3+} (blue arrows). The R^{3+} are also represent in the scheme by S_5, S_6, S_7, S_8 (orange arrows). The weak-ferromagnetic component ***F*** is represented by green arrow. 24
1.15 Spin configurations for structures Γ_4 and Γ_1, with respect to S_1, S_2, S_3, S_4 spins of Fe^{3+} (blue arrows). The weak-ferromagnetic component ***F*** is represented by green arrow. 25
1.16 Magnetic diagram of *R*FeO_3. Adapted from [56]. 26
1.17 Spin configurations for the Γ_4 configuration assuming (a) four-sublattice model and (b) two-sublattice model. The weak-ferromagnetic component ***F*** is represented by green arrow. 26
1.18 Precessional motions of the two $k = 0$ magnetic resonances (magnons): (a) FM or σ-mode and (b) AFM or γ-mode. 27
1.19 Magnon selection rules for THz light in the Γ_4 and Γ_2 configurations. The magnetic field component of the THz pulse is polarized along a line whose colour represents the magnon that is excited: FM if red or AFM if blue. Adapted from [56]. 28
1.20 Temperature dependence of the total ordered Fe^{3+} magnetic moment (upper panel) and its M_x and M_z components (lower panel) in $NdFeO_3$ obtained from Rietveld refinement of neutron powder diffraction patterns. Adapted from [70]. (b) Schematic representation of vectors ***F*** and ***G*** rotation with temperature. Two-sublattice model of Fe^{3+} spins represented by $\boldsymbol{S}^A$ and $\boldsymbol{S}^B$ 30
1.21 Magnetization as a function of temperature measured in (a) FC conditions of 100 Oe and (b) detailed view of ZFC and FC curves at low temperatures. Adapted from [71]. Magnetization as a function of magnetic field applied along (c) c-axis and (d) a-axis. Adapted from [77]. 31
1.22 Inelastic neutron scattering spectrum of $NdFe_3$ recorded at different fixed temperatures. Adapted from [84]. 33
1.23 (a) Scheme of a ϕ-scanning rocking curve measurement in a single crystal. Intensity of orthorhombic diffraction peak $(400)_{orth}$ as a function of rocking angle $\delta\phi$, measured at two representative temperatures (outside SRT: 300 K; inside SRT: 92, 88 K) for (b) $ErFeO_3$ and (c) $TmFeO_3$. Adapted from [88, 89]. 35
1.24 Schematic view of order parameter θ across continuous $\Gamma_4 \longrightarrow \Gamma_{24} \longrightarrow \Gamma_2$ transition. 36

2.1. Survey XPS spectrum and several regions of interest for a thin film $NdNiO_3$ with $LaAlO_3$ as a substrate. 41
2.2. Schematic view of the Raman setup available at IFIMUP facilities. 42
2.3. Scheme of μSR setup used in the GPS beamline. 50

2.4. (a) Angular probability of a positron emission, in a simple scheme with one pair of detectors: forward (F) and backward (B). (b) Time evolution of F and B signals, i.e. positron counter, and asymmetry functions for two cases: longitudinal and transverse fields - local field at the muon stopping site is either longitudinal or transverse with respect to initial direction of muon spin. Adapted from [99]. 50
2.5. Schematic illustration of the experimental setup of user-station 3 of FELIX. Adapted from [101]. 51

3.1. Representative SEM images of NNO thin film onto [001]-LAO substrate: (a) surface image and (b) respective cross-section view, with 1 and 2 μm as a scale, respectively. (c) XRD pattern of the NNO/LAO film. (d) Reciprocal space map around the $(002)_{pc}$ diffraction peak of LAO substrate of the NNO/LAO film. 54
3.2. XPS signal recorded in the 848 – 868 eV energy range of NNO/LAO film. Ni^{3+} and Ni^{3+} $2p^{3/2}$ peaks are observed. The solid lines were determined from the best fit of a mix of Gaussian and Lorentzian functions, while the dashed line accounts for the background was simulated with the Shirley function. 55
3.3. (a) Low magnification cross-sectional HAADF-STEM image of NNO film grown on (001)-LAO substrate. (b) Atomic resolution HAADF-STEM image of the same sample. (c) Elemental distribution maps obtained from the STEM image shown in (a). The (d) in-plane ε_{xx} and (e) out-of-plane ε_{yy} components of the strain tensor were obtained from the STEM image shown in (b) by geometrical phase analysis (GPA). (f) Pseudocubic lattice parameters of the NNO film as a function of the interface distance. 57
3.4. Atomic resolution HAADF- STEM image of film, with a red rectangle marking a small region with Ruddlesden-Popper faults. 58
3.5. Temperature dependence of the resistivity of the film measured in cooling and heating runs, where T_{MI}= 143 ± 1K (blue dot) and T_{IM} = 183 ± 1K (red dot) are indicated as extracted from inset $-\frac{dln(R)}{dT}(T)$ upper limit of peak maximum. The lower limit of peak maximum defines the temperature below which the film is purely insulator, 68 ± 2K (blue star) and 88 ± 2K (red star) for cooling and heating run, respectively. 58
3.6. Temperature dependence of (a) magnetic moment measured in heating, using an applied magnetic field of 100 Oe in field cooling conditions. (b) Residuals ($\frac{H}{M} \propto \frac{1}{\chi}$ data minus Curie-Weiss predicted trend) with inset showing the inverse of susceptibility as a function of temperature. Dashed line marked the T_{IM} obtained from heating run, coinciding with T_N ± 6 K (shaded region). 60
3.7. Temperature dependence of the unpolarized Raman spectra measured in (a) heating and (b) cooling runs, in the full spectral range. 61
3.8. (a) Representative unpolarized Raman spectra of the NNO film, measured in heating run, along with the result of the spectral deconvolution. Spectral components of P$2_1/n$ phase are represented in pink and of P*bnm* phase in green. Temperature dependence of (b) wavenumber and (c) structural volume fraction, i.e., normalized intensity of the Raman modes observed in the 280 to 340 cm^{-1} range. M-modes: 300 + 321 cm^{-1} (the P$2_1/n$ monoclinic phase) and O-mode: 305 cm^{-1} (P*bnm* orthorhombic phase). Dashed lines represent the structural transition temperatures, above which the Raman bands associated with the monoclinic phase disappear. Shaded regions represent: P*bnm* phase in green, the coexistence the two structural phases in yellow and P$2_1/n$ phase in pink. 62

3.9. Diagram of structural and electronic phases as a function of temperature on (a) heating run and (b) cooling run. Upper caption: M = monoclinic, O = orthorhombic. Middle caption: I = insulator, M = metallic. Lower caption: AFM = antiferromagnetic. The circle and the star define the upper and lower limit of the MIT. Monoclinic and orthorhombic volume fraction given by pink and green data respectively. Diagram combining electronic and structural hysteresis, given by (c)resistivity curves and by (d) $-\frac{dln(R)}{dT}(T)$ and monoclinic volume fraction, both on heating (red data) and cooling (blue data) runs. 64
3.10. Raman spectra measured in cooling run, at temperatures around the T_{MI} = 143 K, demonstrating the experimental sensitivity to the structural phases. Spectral components of P$2_1/n$ phase are represented in pink and of P*bnm* phase in green. 66

4.1. Polarized Raman spectra of $NdFeO_3$ at ambient conditions. The measurement configurations are given in Porto's notation, in (a) for the vibration modes of A_g symmetry and in (b) for the vibration modes of $B_{1,2,3g}$ symmetries. X, Y and Z correspond to the orthorhombic axes in the P*bnm* space group. 70
4.2. Vibrational patterns of the Raman-active modes in $NdFeO_3$, described in Table 4.1. Label: Nd atoms (green symbols), Fe atoms (blue symbols) and O atoms (red octahedra cage). 71
4.3. Raman phonon wavenumbers of *R*FeO_3 as a function of the rare earth R^{3+} ionic radius. The data for all rare-earth was take from Weber *et al.* [124], with the exception of Nd (this work, blue data). All lines are guides to the eye only. The setting used in this figure is P*nma* space group, for an easier comparison with Weber *et al.* [124]. 72
4.4. Reflectivity spectra of $NdFeO_3$ recorded at 300 K and 4 K, for the polarizations: (a) E||a-B_{3u}, (b) E||b–B_{2u} and (c) E||c–B_{1u}. The blue solid line was determined by the best fit of Eq. 2 to the experimental reflectivity. 73
4.5. The spectra of the real ϵ' and imaginary parts ϵ'' of the dielectric function calculated from the reflectivity data analysis, recorded at 300 K and 4 K, for (a) ***E***||a, (b) ***E***||b and (c) ***E***||c. 75
4.6. Vibrational patterns of the infrared-active modes in $NdFeO_3$, described in Table 4.1. Label: Nd atoms (green symbols), Fe atoms (blue symbols) and O atoms (red octahedra cage). 75
4.7. Scheme of the magnon selection rule in $NdFeO_3$. The crystallographic axes refer to the P*bnm* setting. The green arrows represent the magnetic field component H^{ω} of the THz radiation. Ferromagnetic vector ***F*** is represented by the red arrow, while the blue arrows represent the normal equilibrium orientations of the canted spins assuming the two sublattice model. 77
4.8. Raman scattering selection rules for different configurations represented by Porto's notation in the Γ_4, Γ_{24} and Γ_2 configurations. Incident and scattered polarization vectors are represented by red and blue arrows, respectively. The setup is always in backscattering configuration, so both incident and scattered light propagate along the same direction. 79
4.9. Extinction coefficient spectra $\kappa(\omega)$, calculated from the absorbance THz spectra of $NdFeO_3$ recorded at representative temperatures, for the (a) H^{ω}||a and (b) H^{ω}||c polarization configurations. (c) Temperature dependences of the wavenumbers of the σ- and γ-modes, observed in the two THz spectra polarizations (closed symbols) and in unpolarized Raman scattering spectra (open symbols) published in Ref.[81]. (d) Temperature dependence of the magnons intensities in the THz spectra. Dashed lines are a guide for the eyes. 80

4.10. Room temperature unpolarized Raman spectra of $NdFeO_3$ single crystal, recorded in the six possible measurement configurations. Note that for unpolarized Raman measurements the incident beam is always polarized. 82

5.1. Magneto-optical images recorded for different fixed temperatures evidencing magnetic domains. The contrast varies between bright and dark domains for ***M***||c and the absence of contrast when ***M***||a. Arrows indicate regions with different weak ferromagnetic moment directions. 87
5.2. (a) Stack of RUS spectra scanned over 1360 to 1870 kHz, recorded in a heating run from 2 to 300 K. Spectra have been offset up the left axis in proportion to the temperature at which they were collected, and this temperature scale is shown on the right axis. Temperature dependence of f^2 (upper panel) and Q^{-1} (lower panel) obtained from fitting an asymmetric Lorentzian function to resonance peaks with frequencies near (b)(e) 1416, (c)(f) 1436 and (d)(g) 1855 kHz (RT values). Red/blue symbols represent heating/cooling data. The SRT temperature range is highlighted in green. 88
5.3. Temperature evolution of (a),(c) real χ' and (b),(d) imaginary χ" parts of AC magnetic susceptibility measured along a-axis and c-axis, respectively. The SRT temperature range is highlighted in green. 89
5.4. (a)-(c)Lattice parameters in the *Pbnm* setting obtained from neutron powder diffraction [70] and XRD [74]. (d) Same data presented as pseudocubic parameters, using cubic structure as a reference. 92
5.5. (a) Variation of e_4 determined from lattice parameters given in Figure 5.4. The red curve is a fit of Equation 5.3 to values derived from the lattice parameters of XRD [74] and neutron data [70]: y_0 = 0.0276, A = -8.03E-6, Θ_s= 116 K. (b) Variation of e_{ty} with fit of Equation 5.3 to data at T > 170 K, extrapolated to lower temperatures. Fit parameters for the data derived from neutron data [70]: y_0 = -0.0079, A = 4.48E-6, Θ_s fixed at 116 K. (c) Variation of unit cell volume. Red curve is fit of Equation 5.3 simultaneously to data at T > 170 K and T < 105 K. Fit parameters for the data derived from XRD data[74]: y_0 = 233.478, A = 0.0079, Θ_s= 265 K. (d) Variations of $sin(2\theta)$ (right axis) calculated from neutron data [70] and THz spectroscopic data [77]; and changes of tetragonal shear strain Δe_{ty}(left axis). Vertical dashed lines at 105 and 170 K mark approximate limits of the SRT interval....93
5.6. (a) Temperature dependence of f^2 of 1416 kHz resonance peak and fit of Equation 2.5 representing elastic softening effects as T$\rightarrow$ 0 K. Fit performed in 210-300 K range with Θ_s fixed at 265 K and extrapolated to T$\rightarrow$ 0 K. Inset shows magnification below 80 K, where softening below $\sim$25K is highlighted. (b) Temperature dependence of Q^{-1} for several resonance peaks in a broad spectral range, showing how the maximum losses are frequency-independent. Another small frequency-independent peak at $\sim$35 K is shown in the inset. 95
5.7. Temperature dependence of f^2 of 1165 kHz resonance peak of $SmFeO_3$, published in [134]. Inset shows the variation of unit cell volume of $SmFeO_3$, with fitting Equation 2.5 with parameters: y_0= 230.663, A = 0.00469, Θ_s= 258 K. Fixing Θ_s, the same model was used to perform a fit to the RUS data f^2 in 480-750 K range and extrapolated to 0 K. 96
5.8. Comparison between Q-1 of resonance frequency 1416 kHz relative to a non-linear baseline, ΔQ^{-1}(left-axis), and $sin^4(2\theta)$ (right-axis) calculated from neutron data [70] and THz spectroscopic data [77]. 98
5.9. Temperature dependence of (a) $1/f^2$, which scales with elastic compliance S, for resonance peak 1416 kHz; modulus of AC magnetic susceptibility $|\chi|$ measured along (b) a-axis and (c) c-axis, for frequency 14132 Hz. 99

6.1. Group-subgroup relation between non-magnetic P*bnm* space group and magnetic monoclinic space group of SRT, obtained using k-SUBGROUPSMAG tool from Bilbao Crystallographic Server. $m\Gamma$ stems for the magnetic irrep, referred in the text simply as Γ. 102
6.2. Schematic view of the spin structures for the different magnetic configurations of $NdFeO_3$ in the ac-plane. 103
6.3. Representative time-dependent asymmetry, recorded at 200 K, for detector pairs: (a) Up-Down (UD) and (c) Forward-Backward (FB); (b),(d) respective fast Fourier transform. Fitting curve (red) of asymmetry data using Equation 6.2. 104
6.4. Fourier transform of time-dependent μSR signal of NdFeO3 for several fixed temperatures, with corresponding fits from Eq.6.2, for detector pairs: (a) Up-Down (UD) and (b) Forward-Backward (FB). 105
6.5. Temperature evolution of (a) frequency, (b) asymmetry and (c) relaxation of the spectral oscillating components. These parameters were obtained from the fit of Equation 6.2 to the time-dependent μSR signal. Vertical dashed lines define the SRT region. UD- close symbols; FB- open symbols. 106
6.6. Schematic representation of oscillating components frequency in case of (a) structural symmetry-lowering during SRT - splitting of components - and (b) structural symmetry kept during SRT - coexistence of two orthorhombic phases Γ_2 + Γ_4. 109

7.1. XMCD spectra of Nd $M_{4,5}$ absorption edges recorded at different fixed temperatures. 113
7.2. Temperature dependence of Nd M_4 absorption edge signal squared obtained from XMCD analysis (left-axis) and the Fe-sublattice magnons wavenumber variation from the average value across the SRT (right-axis). The dashed lines are guide for the eyes. 113
7.3. Extinction coefficient spectra of $NdFeO_3$, in different polarization configurations of the THz radiation at 200 K: (a) and (e) without applied magnetic field; under magnetic field along (b) a-axis and (f) c-axis; for $\boldsymbol{B}_{ext}$||a: magnetic field dependence of (c) wavenumber and (d) intensity; for $\boldsymbol{B}_{ext}$||c: magnetic field dependence of (g) wavenumber and (h) intensity. Dashed lines are a guide for the eyes. ***F*** is the ferromagnetic vector. 115
7.4. Extinction coefficient spectra of $NdFeO_3$, in different polarization configurations of the THz radiation in the SRT region (140 and 120 K): (a) and (e) without applied magnetic field; under magnetic field along (b) a-axis and (f) c-axis; for $\boldsymbol{B}_{ext}$||a: magnetic field dependence of (c) wavenumber and (d) intensity; for $\boldsymbol{B}_{ext}$||c: magnetic field dependence of (g) wavenumber and (h) intensity. Inset of (d) represents the magnetic field dependence of the angle θ between the ***F*** vector and the a-axis, obtained using Equation 7.1. Dashed lines are a guide for the eyes. ***F*** is the ferromagnetic vector. 117
7.5. Magnetic field dependence of the σ- and γ-modes wavenumber and intensity, respectively, for the applied field parallel to the (a)-(b) a-axis and (c)-(d) c-axis, seen in unpolarized Raman spectra at 110 K. Inset of (a) shows the polynomial (2nd order) dependence of the squared wavenumber with the magnetic field, following the model of Ref.[156] 118
7.6. Magnetic field dependence of the wavenumber of σ- and γ-modes observed in THz (closed symbols) and Raman (open symbols) spectroscopies at (a) 14 K and (b) 4 K for $\boldsymbol{B}_{ext}$||a. Inset of (a) and (b) show the polynomial (2nd order) dependence of the squared wavenumber with the magnetic field, following the model of Ref.[156], and the γ-mode intensity, respectively. Magnetic field dependence of the wavenumber of σ- and γ-mode observed in THz and Raman spectroscopies at (c) 50 K, (d) 14 K and (e)-(f) 4 K for $\boldsymbol{B}_{ext}$||c. Inset of (c) and panel (f) show the magnetic field dependence of the γ-mode intensity at 50 and 4 K, respectively. Dashed lines are guide for the eyes. 120

7.7. Magnetic field dependence of the Nd^{3+} shifts wavenumbers, measured for $\boldsymbol{B}_{ext}$||a at (a) 14 K and (b) 110 K. 122
7.8. Magnetic field dependence of the Nd^{3+} shifts wavenumbers, measured for $\boldsymbol{B}_{ext}$||c at (a) 4K, (b) 14 K and (b) 110 K. 123
7.9. Magnetic field dependence Nd^{3+} crystal-field excitations: (a) unpolarized Raman spectra, (b) wavenumbers and (c) wavenumber difference measured at 14 K with $\boldsymbol{B}_{ext}$||a 124
7.10 Magnons frequency vs external magnetic field $\boldsymbol{B}_{ext}$||c at 14 K. Red line is the fit to the σ-mode using Eq.7.5. The fit parameters obtained for σ-mode were imposed in the γ-mode fitting equation (Eq.7.4), represented by the blue line. 126
7.11 Magnetization as a function of the magnetic field applied along (a) a-axis and (b) c-axis. 127
7.12 Derivative of magnetization as a function of the magnetic field applied along (a) a-axis and (b) c-axis. The stars symbols mark the end of induced spin-reorientation, i.e, when Γ_2 phase is stabilized for $\boldsymbol{B}_{ext}$||a or when Γ_4 phase for $\boldsymbol{B}_{ext}$||c. 128
7.13 Magnetization as a function of magnetic field applied along (a) a-axis and (b) c-axis. (c) Derivative magnetization along c-axis, where the symbols mark the spin-flop (SF) transition. Insets in (b) and (c) are zoomed region for curves between12 and 18 K, where SF transition is sharp. 128
7.14 ($\boldsymbol{B}$,T) phase diagram of $NdFeO_3$ for (a) $\boldsymbol{B}_{ext}$||a and (b) $\boldsymbol{B}_{ext}$||c. Close circles represent data measured with THz spectroscopy, open circles with Raman spectroscopy and triangles mark the magnetic transition obtained from magnetization analysis. Colours: Γ_4: red; Γ_{24}: green, Γ_2: purple, Spin-flop: yellow and Ferromagnetic (FM) phase: blue. 130

A.1. Polarization selection rules for Raman modes. First column is the Porto's notation and "x" represents that the mode can be observed in that configuration. Orange table shows the selection rules for the P*nma* setting and blue table for the P*bnm*. Bottom table presents the direct relation of Raman and IR modes between the two settings. 164
A.2. Classification of magnetic point and space groups in triclinic, monoclinic and orthorhombic systems related to different magnetic modes. Columns denote magnetic classes and rows the site-symmetry magnetic point groups. Adapted from [87]. 165
A.3. Group-subgroup relation between magnetic space groups. Adapted from k_SUBGROUPSMAG tool from Bilbao Crystallographic Server. 165
A.4. (a) Representative unpolarized Raman spectra of the NNO film, measured in cooling run, along with the result of the spectral deconvolution. Spectral components of P$2_1/n$ phase are represented in pink and of P*bnm* phase in green. Temperature dependence of (b) wavenumber and (c) structural volume fraction, i.e., normalized intensity of the Raman modes observed in the 280 to 340 cm^{-1} range. M-modes: 300 + 321 cm^{-1} (the P$2_1/n$ monoclinic phase) and O-mode: 305 cm^{-1} (P*bnm* orthorhombic phase). Dashed lines represent the structural transition temperatures, above which the Raman bands associated with the monoclinic phase disappear. Shaded regions represent: P*bnm* phase in green, the coexistence the two structural phases in yellow and P$2_1/n$ phase in pink. 166
A.5. Stack of RUS spectra scanned over 1360 to 1870 kHz, recorded in cooling run, from 2 to 300 K. Spectra have been offset up the left axis in proportion to the temperature at which they were collected, and this temperature scale is shown on the right axis. . 168
A.6. Representative extinction spectra recorded at 4, 140 and 200 K for the THz polarization (a) H^{ω}||a and (b) H^{ω}||c, at different fixed magnetic field strengths (0-7T) applied along the a-axis. 172

A.7. Representative extinction spectra recorded at 4, 50, 120 and 200 K for the THz polarization (a) H^{ω}||a,c and (b) H^{ω}||b, at different fixed magnetic field strengths (0-7T) applied along the c-axis. 173
A.8. Representative extinction spectra recorded at 4, 50, 120 and 200 K for the THz polarization (a) H^{ω}||a,c and (b) H^{ω}||b, at different fixed magnetic field strengths (0-7T) applied along the c-axis. 174
A.9. Unpolarized Raman spectra recorded at 4, 14 and 110 K for (a)-(b)$\boldsymbol{B}_{ext}$||a and (c)-(d)$\boldsymbol{B}_{ext}$||c, where the spectral ranges show the Nd-shifts phonons. 175

List of Abbreviations

AFM Antiferromagnetic

FM Ferromagnetic

FTIR Fourier transform infrared spectroscopy

LAO $LaAlO_3$

MIT Metal-to-insulator transition

NA Numerical Aperture

NFO $NdFeO_3$

NNO $NdNiO_3$

IR Infrared

RSM Reciprocal Space Map

SF Spin-flop

SRT Spin reorientation transition

STEM Scanning Transmission Electron Microscopy

μSR Muon spin rotation spectroscopy

TMO Transition-metal oxide

XPS X-Ray Photoelectron Spectroscopy

XRD X-Ray Diffraction

1. Introduction

In recent years, the rapid progress of information systems, such as artificial intelligence and data-driven technologies, has introduced significant challenges, including massive energy consumption, the handling of increasingly large datasets, and the need for more efficient computational performance. These demands mirror an urgent necessity for new devices capable of efficiently collecting, processing, and distributing information. The nanotechnology industry is under growing pressure to develop materials that are not only more versatile and cost-effective, but also capable of maintaining or even enhancing its performance. Experimental physics and material science researches are reducing the gap between academia and industry, by studying functional materials which possess properties that can be tuned by external parameters (temperature, pressure, electric or magnetic field, among others), making such materials particularly appealing for industry's applications. The goal is to master the engineering of materials physical properties by design, fulfilling in this way the industrial demands.

ABO_3 perovskite oxides materials are one of the most promising families of functional compounds as they allow the control of a wide variety of physical properties. Specially, when the B-site is occupied by a transition-metal cation, making the material a transition-metal oxide (TMO). The covalent-bond nature involving $3d$ shells from the transition-metal and $2p$ shells from oxygen results in strong polarizability, a desirable property in ferroelectrics, and partially filled $3d$ shells of the transition-metal lead to strong-correlation physics often associated with exotic magnetic behaviour [1]. Several phenomena such as Mott insulators, charge, spin and orbital orderings, metal–insulator transitions, multiferroicity and superconductivity are often associated to TMOs [2].

Many TMOs are ferroic materials, i.e., they possess a spontaneous and switchable internal alignment [1, 3]. The ferroic * properties such as ferromagnetism, ferroelectricity or ferroelasticity, are particularly relevant for technological applications, as they can be tuned

*In this thesis the terminology "ferroic" will be extended to include non-primary orderings such as antiferromagnetism, as it is often used in magnetoelectric multiferroics that combine ferroelectricity and antiferromagnetism [4].

by external stimuli and even coupled, allowing the control and enhancement of physical properties in a material [1]. The key factor determining ferroic behaviour in ABO_3 perovskites is inherently connected to the occupation valence state of both A- and B-sites. For instance, the rare-earth ferrites family, $R\mathrm{FeO}_3$, possess rich ferroic interactions that are tunable by changing the rare-earth cation ($4f$-electrons), which will consequently modify the electronic orbital overlap with the transition metal $3d$-electrons [5]. Another oxide family well known for its tunable interactions is the rare-earth nickel oxides (nickelates), $R\mathrm{NiO}_3$, where the structural parameter associated with rare-earth size is capable of controlling the electronic and magnetic transitions [6]. Again, this family of perovskites sheds light on the impact of the interplay between $4f$ - $3d$ shells.

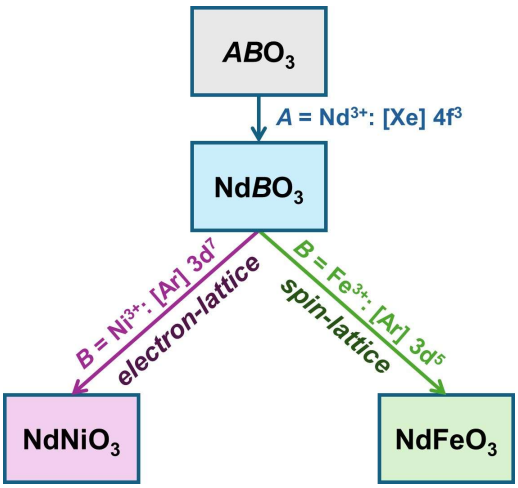


FIGURE 1.1: Schematic representation of the dominant interactions in ABO_3 materials with A-site occupied by Nd^{3+} cation and B-site by either Ni^{3+} or Fe^{3+} cations. The respective electronic configurations of each cation is also presented.

This thesis aims at exploiting different interactions and their impact on the physical properties that arise from the substitution of *B*-site cation (*B* = Ni or Fe) in neodymium-based perovskite oxides, as schematic illustrated by Figure 1.1. The simple change of the transition metal cation implies major differences in $3d$ valence states: for Ni^{3+} the valence state is $3d^7$, while for Fe^{3+} is $3d^5$. The occupation of the valence state in the two materials by itself has tremendous impact on the electronic properties, despite having the same crystallographic structure at room temperature: while $NdFeO_3$ presents all $3d$ orbital partially filled, conferring it only insulator properties, the uneven filling of e_g states in $NdNiO_3$ promotes a metallic state at room temperature. Furthermore, the interaction between $3d$ electrons of transition metals and $4f$ electrons of neodymium, differentiates the physical properties also in comparison with other rare-earth cations of the two families: nickelates and ferrites.

1.1. Perovskite structure: ABO_3

Perovskite structure was discovered in 1839 for a mineral of formula $CaTiO_3$ [7]. The name perosvkite was later given to any compound with a general formula or derivation of ABX_3, where usually A-site is occupied by a cation larger than the one occupying the B-site, and the X-site by an anion [7].The focus of this work are perovskite oxides materials,i.e, with oxygen anion at the X-site, and with the A-cation occupied by a rare-earth element (La to Lu) and the B-cation by a transition metal. The greatest interest on perovskite-type structures comes from the vast diversity incorporated different chemical elements and its implication on the physical properties of the materials. Depending on the size and electron structure, different structural distortions can be induced, making it possible to engineer several physical properties.

The ideal perovskite structure, depicted in Figure 1.2, adopts the cubic $Pm\bar{3}m$ crystallographic space group. One defining feature of this structure is the corner sharing BO_6 octahedra, where B-site cation occupies the octahedra centers and the A-cation the dodecahedra centers. This point of view is interesting because we can easily define the main structural distortions associated with symmetry-lowering.

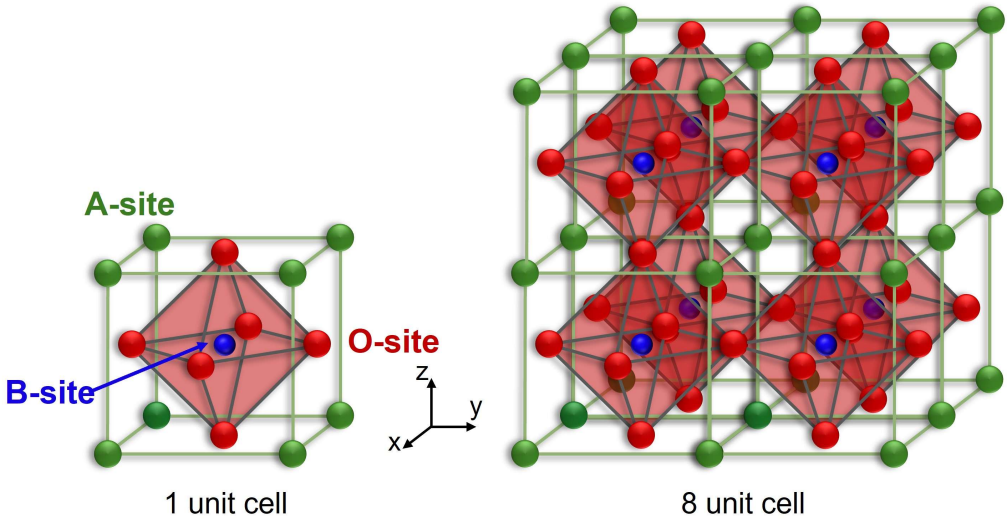


FIGURE 1.2: Ideal perovskite structure with $Pm\bar{3}m$ symmetry, with primitive unit cell Z=1.

Given the atoms coordination (12th for A-site and 6th for B-site), the ideal cubic structure can only be preserved for a certain ratio between the ionic radius of each ion site. If the A-cation as a ionic radius large enough to fill the cavity in between the BO_6 octahedra, the cubic symmetry is stabilized, otherwise the system will distort in order to minimize the cavity size, and the cubic symmetry will be lost. Goldschimidt tolerance factor t establish

the stability of a perovskite structure depending on the A and B cations, and it is expressed by [8]:

$$t = \frac{(r_A + r_O)}{\sqrt{2}(r_B + r_O)} \tag{1.1}$$

where r_i is the corresponding ionic radius of the i- site (i = A, B or O). For the ideal cubic perovskite structure t = 1, but empirically this is rarely observed, and instead the cubic symmetry is stabilized when t ranges between 0.9 - 1.0 [7]. If t > 1, the hexagonal symmetry is preferred, while for 0.71 < t < 0.9 the symmetry lowers favouring orthorhombic arrangement [7]. However, the tolerance factor only takes into consideration the geometric nature of a crystal, neglecting its covalent bonds and interaction mechanisms. Therefore, it only assesses whether the crystal may possess a perovskite structure but is no measurement of the crystallographic space group.

Due to the large number of different elements combinations into the crystalline structure, very often the perovskite structure deviates from the ideal cubic symmetry by distorting in order to better accommodate the mismatch of cations radii. Basic distortions are often represented by few symmetry-adapted distortion modes, as we will see in subsection 1.1.1. Three main types of distortions can be found: (i) cations displacements, (ii) BO_6 octahedra distortions and (iii) BO_6 octahedra tilting [9]. In some cases these distortions coexist.

(i) Cation displacement

A and B-site cations can be displaced from their cubic symmetry positions, according to the covalence character with the surrounding oxygens [10]. Three possible displacements of B-cation from the center of BO_6 octahedra can occur: towards one of the octahedra corners, resulting in an tetragonal unit cell; towards one edge of the cub-octahedron, giving an orthorhombic unit cell; towards one diagonal of the cub-octahedron, forming a rhombohedric unit cell. Such kind of displacements are associated with the appearance of a spontaneous polarization, therefore these distortions are often find in ferroelectric perovskites such as $BaTiO_3$ [11].

(ii) BO_6 distortions

Symmetry-lowering due to octahedra distortions depends on the bonding structure of B-cation and taking into account the octahedron as a non-rigid body, namely when the B-site is occupied by a transition metal with odd number of *d* electrons [10]. Orbital ordering (e.g. Jahn-Teller) or charge ordering effects (e.g. charge disproportionation) operate to lift the orbital degeneracy, changing the shape of octahedra by elongation/contraction or by alternating the size of neighboring octahedra. Further insight on this last BO_6 distortion type due to charge ordering is given in section 1.2.

(iii) BO_6 tilting

Most common type of perovskite distortions and by far the ones with a greater effect on the lattice parameters [12]. Assuming the octahedra as rigid bodies, when an octahedron rotates in some particularly way it causes tilting of its neighbouring octahedra [10, 12]. Octahedra are connected by the vertices having as degrees of freedom the rotations along the pseudo-cubic axis [100], [010] and [001] with respect to the aristotype P$m\bar{3}m$ space group, either in the same direction (in-phase rotation) or opposite direction (anti-phase rotation). Such titling allow variations of the A-O bondings while keeping the B-site position unchanged. Glazer introduced a tilt system notation for perovskite materials [12]. The tilt magnitude is represented by a set of three letters which refer to the pseudo-cubic axis: in the case of unequal tilting system *abc*, or in the case of some equal tilting, for instance same tilt magnitude around [100] and [010], it is written *aac*. To each letter, a superscript is attributed to indicate whether successive octahedra along that axis are: in-phase (+), anti-phase (-) or have no tilt (0) about that axis. The aristotype perovskite structure has no octahedra tilts, therefore, according to Galzer's notation, is described by $a^0a^0a^0$. The tilt system $a^0b^-b^-$ has no rotation around [100] pseudocubic axis, but has anti-phase rotations with same magnitude around [010] and [001].

Some tilt systems are equivalent to structural space groups. Howard and Stokes develop a group theory analysis that only considers octahedra tilts [13], resulting in a group-subgroup relationship presented in Figure 1.3.

Several tilting systems with different A-site cations were compared taking into consideration ionic and covalent A-O bondings models, and the structure that minimizes the energy

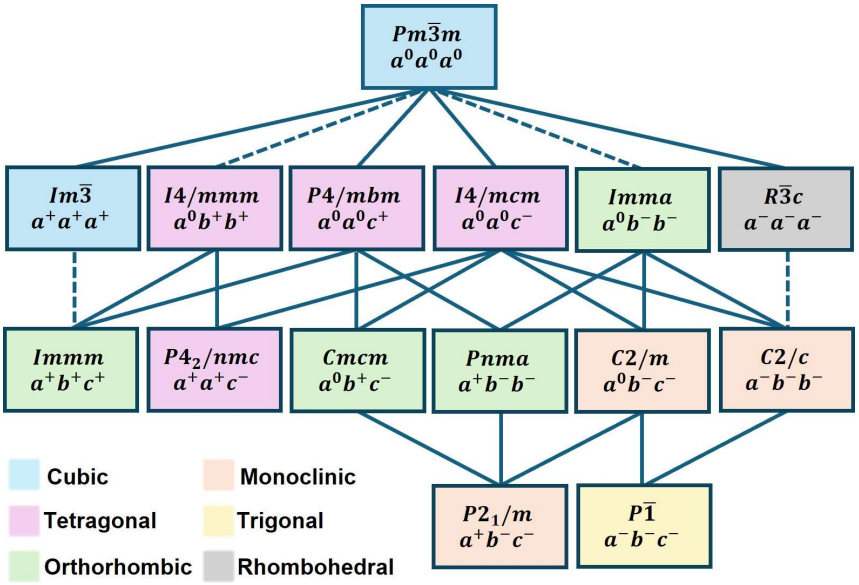


FIGURE 1.3: Scheme presenting the space group relationships associated with tilt system. Solid lines indicate second order phase transitions while dashed lines first order phase transitions. Adapted from [13].

is the orthorhombic $a^+b^-b^-$ tilt system [14], also known as P*nma* space group. This particular symmetry prevails over others in perovskite materials, because their anti-phase and in-phase tilts, which are native instabilities of the ideal cubic perovskite structure, present relatively weak competition and a small anisotropy energy, favouring this tilting configuration [15].

1.1.1 P*nma* or P*bnm* setting

As discussed above, most perovskites crystallizes in the P*nma* space group, which is the case rare-earth orthonickelates and orthoferrites. In the literature, a non standard setting P*bnm* is widely used instead of the standard P*nma*. The two settings are related by a cyclic permutation $(x,y,z)_{Pnma} \longrightarrow (y,z,x)_{Pbnm}$. For sake of simplicity when comparing with literature, the non-standard setting P*bnm* will be adopted in this thesis. Following Glazer's notation, the tilt scheme $a^+b^-b^-$ for P*nma* is equivalent to $a^-a^-c^+$ for P*bnm* [10]. Accordingly, the symmetry-lowering distortions to the P*bnm* structure consist in in-phase and anti-phase BO_6 octahedra rotations: in-phase around [001] and anti-phase around [110] pseudocubic axis, with respect to the P$m\bar{3}m$ ideal structure. Lowering the symmetry requires a redefinition of the lattice parameters, as the P*bnm* causes a fourfold increase of the primitive unit cell to Z = 4 [10]. Maintaining the ideal cubic metric, for P*bnm*

the lattice parameters can be written in terms of a pseudocubic cell:

$$a_o = \sqrt{2}a_{pc}, b_o = \sqrt{2}b_{pc}, c_o = 2c_{pc} \tag{1.2}$$

where a_{pc}, b_{pc} and c_{pc} are the pseudocubic parameters and a_o, b_o and c_o the orthorhombic parameters. It immediately follows that $V_o = 4V_{pc}$.

This structural symmetry lowering impacts the local symmetry of each atom position in the unit cell. These are described by the respective Wyckoff positions, shown in Table 1.1 for the two space groups. In the cubic structure, A and B- cations occupy the vertices and center of the cube, respectively, having symmetry inversion sites, while the oxygens are at the center of the cube faces. In the orthorhombic structure, the B-cation remains in a site with symmetry inversion center, but the A-cations now occupy a site with a mirror plane symmetry. The oxygens are now divided into two different sites: the two O1 are called the apical oxygens that have the same symmetry as A-cation, and the four O2 are called basal oxygens that have no constrains, being invariant only under the identity operator.

TABLE 1.1: Wyckoff positions in the setting groups P$m\bar{3}m$ and P*bnm* of a ABO_3 perovskite. Adapted from WYCKPOS tool from Bilbao Crystallographic Server.

Space group	Atom	Multiplicity	Wyckoff letter	Site symmetry
P$m\bar{3}m$	A	1	a	m$\bar{3}$m
	B	1	b	m$\bar{3}$m
	O	3	c	4/mm.m
P*bnm*	A	4	c	.m.
	B	4	b	$\bar{1}$
	O1	4	c	.m.
	O2	8	d	1

The tilt angles are most accurately obtained from atomic positions than from the unit cell dimensions [10]. Estimating tilt angles directly from cell dimensions assumes rigid and regular octahedra structures, however, in real crystals this is not exactly true. In fact the octahedra are not rigid structures, and consequently, the coexistence of two anti-phase tilts actually imposes a deformation of the otherwise regular octahedron [12], which is the case of P*bnm* structure. To overcome the incomplete description of the symmetry-lowering from P$m\bar{3}m$ to P*bnm* structure by only considering BO_6 tilts, crystallographic distortions can be expressed by calculating the atomic displacements with respect to the high-symmetry phase, i.e, distortion modes [16]. The symmetry-adapted distortion modes of the P*bnm* structure are shown in Figure 1.4. The two primary order parameters are obviously the two tilts, that are described by symmetry-modes M_3^+, corresponding to $[001]_{pc}$

rotation, and R_4^+, corresponding to $[110]_{pc}$ rotation. The symmetry-lowering allows A-cations displacements in the ab-plane, as demonstrated by the anti-polar modes R_5^+ and X_5^+, making this displacements secondary order parameters. The coupling of X_5^+, which exhibits a large amplitude, with the tilt modes M_3^+ andR_4^+, plays a key role in stabilization the P*bnm* structure [15, 17]. Lastly, another secondary order parameter M_2^+ is responsible for the deformation of the BO_6 cage. The amplitude of this distorted-mode is usually negligible in materials with no Jahn-Teller distortion [16].

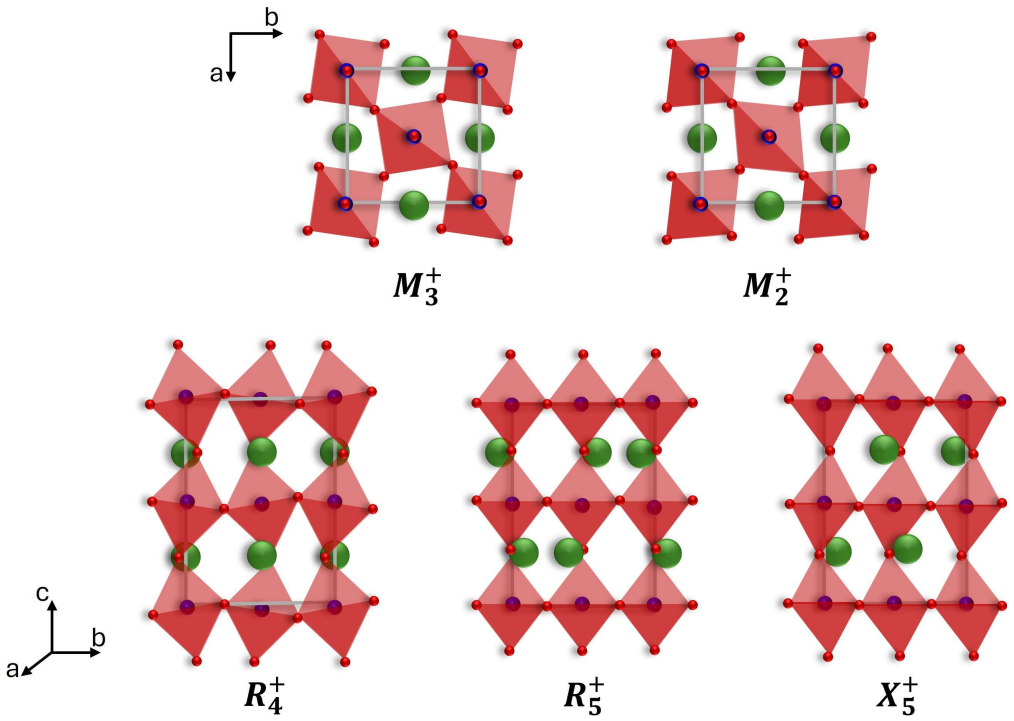


FIGURE 1.4: Symmetry-adapted distortion modes of the orthorhombic P*bnm* space group with respect to the P$m\bar{3}m$ structure. Adapted from [16].

1.1.2 Magnetic ordering in perovskites

In P*bnm* perovskites, the isotropic exchange is the main interaction between the nearest-neighbors spins. The orthorhombic unit cell contains four B-site cations, and different magnetic interactions between those atoms explain the five possible collinear spin structures:

- F-type: all spins pointing in the same direction, see Figure 1.5(a)
- A-type: spins pointing in opposite directions in consecutive planes, creating ferromagnetic layers that are antiferromagnetic between them, see Figure 1.5(b)

- C-type: spins pointing in opposite directions in consecutive lines, creating ferromagnetic lines that are antiferromagnetic between them, see Figure 1.5(c)
- G-type: all neighbouring spins are pointing in opposite directions, see Figure 1.5(d)
- E-type: in the layer, two of the spin nearest-neighbours are pointing in the same direction while the other two nearest-neighbours are pointing in opposite direction, spins in the consecutive layers are antiparallel, see Figure1.5(e)

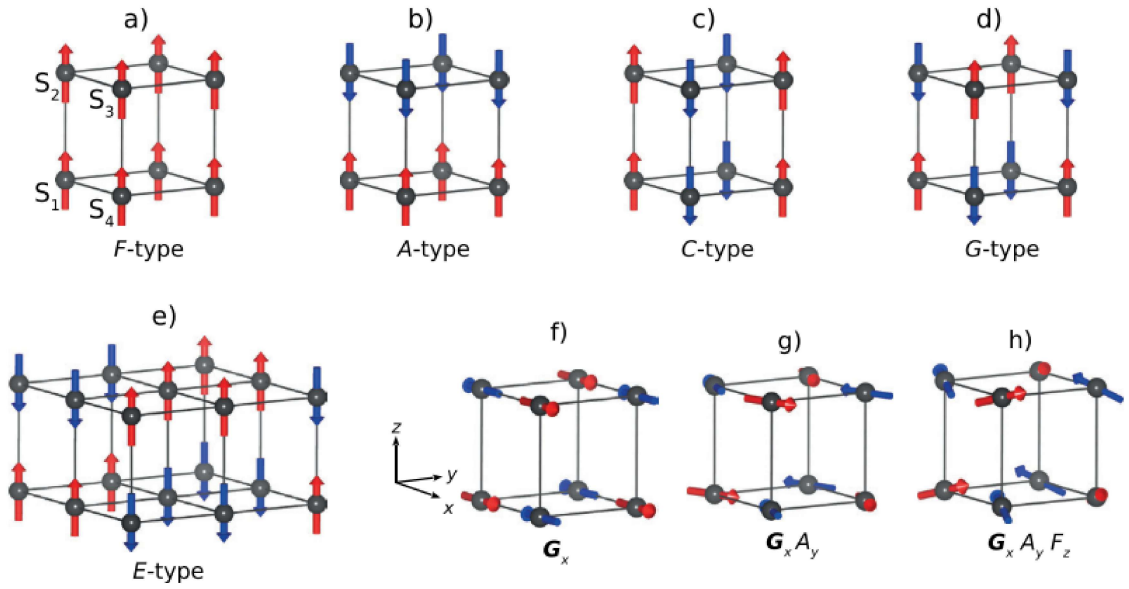


FIGURE 1.5: Types of magnetic orders emerging from the interactions between the four magnetic B-sites atoms of P*bnm* unit cell: collinear orders from (a)-(e) and non-collinear orders from (f)-(h). Adapted from [5].

The net magnetic moment generated by one unit cell is described by the following four spin vectors components, $\boldsymbol{S}_i$, that form a base [5]:

$$\begin{aligned} \boldsymbol{F} &= \boldsymbol{S}_1 + \boldsymbol{S}_2 + \boldsymbol{S}_3 + \boldsymbol{S}_4 \\ \boldsymbol{A} &= \boldsymbol{S}_1 - \boldsymbol{S}_2 - \boldsymbol{S}_3 + \boldsymbol{S}_4 \\ \boldsymbol{C} &= \boldsymbol{S}_1 + \boldsymbol{S}_2 - \boldsymbol{S}_3 - \boldsymbol{S}_4 \\ \boldsymbol{G} &= \boldsymbol{S}_1 - \boldsymbol{S}_2 + \boldsymbol{S}_3 - \boldsymbol{S}_4 \end{aligned} \tag{1.3}$$

where $\boldsymbol{F}$ corresponds to a ferromagnetic ordering and the other three to antiferromagnetic components. Taking into account the spin direction along each axis, a combination of this elementary orders is used to compose more complex magnetic structures. An example is demonstrated in Figure1.5(f)-(g). The Bertaut's notation is usually used to describe this non-collinear orders [5, 18, 19]. The $G_xA_yF_z$ structure can be understood as a G-type order along x direction, a A-type along y direction and a F-type along z direction.

Furthermore, as two directions have an antiferromagnetic order, the net magnetization is along the third direction that has a ferromagnetic order, in this case along z.

In the following, let us consider the ABO_3 perovskite belonging to the orthorhombic space group P*bnm*, where A and B sites are occupied by magnetic ions. The magnetic moments of spin vectors $\mathbf{S}_i, i = 1, ..., 8$ can be divided into two sublattices systems: $\mathbf{S}_i, i = 1, ..., 4$ from B-cation and $\mathbf{S}_i, i = 5, ..., 8$ from A-cation. The system transforms under the group generators: two screw axis $2_{1,x}$ and $2_{1,y}$, and the inversion operator $\bar{1}$ as discussed in [19]. Let us check how these operators act on the B-cation spins, which are placed in the four equivalent symmetry centers with Wyckoff position (4b): $\left(\frac{1}{2}, 0, 0\right)$, $\left(\frac{1}{2}, 0, \frac{1}{2}\right)$, $\left(0, \frac{1}{2}, \frac{1}{2}\right)$ and $\left(0, \frac{1}{2}, 0\right)$. The linear spin combinations presented in Eq. 1.3 are the basis of irreducible representations of $m'm'm$ point group [19]. The (x,y,z) components of each vector can be subject to the symmetry operators $2_{1,x}$, $2_{1,y}$ and $\bar{1}$, and the component will either transform into itself or its symmetric. For instance, let us consider the G_x and G_y components subjected to $2_{1,x}$:

$$\begin{aligned} 2_{1,x}G_x &= 2_{1,x}(S_{1x} - S_{2x} + S_{3x} - S_{4x}) = S_{4x} - S_{3x} + S_{2x} - S_{1x} = -G_x \\ 2_{1,x}G_y &= 2_{1,x}(S_{1y} - S_{2y} + S_{3y} - S_{4y}) = -S_{4y} + S_{3y} - S_{2y} + S_{1y} = +G_y \end{aligned} \tag{1.4}$$

Table 1.2 summarizes the transformation properties for each component of the base vectors under the group generators operators. The results of Table 1.2 can be rearrange by

TABLE 1.2: Transformation properties of the base vector of B-cation [19].

Vectors	**Operators**								
	$2_{1,x}$			$2_{1,y}$			$\bar{1}$		
	x	y	z	x	y	z	x	y	z
F	+	-	-	-	+	-	+	+	+
A	+	-	-	+	-	+	+	+	+
C	-	+	+	+	-	+	+	+	+
G	-	+	+	-	+	-	+	+	+

grouping components with the same transformation properties. For instance, A_x,G_y and C_z all transform under the three operators according to (+++). This set defines the Γ_1 representation. For the B-cations (4b), all components transform into themselves under the $\bar{1}$ operator, and only four representations are possible: $\Gamma_1(+++)$, $\Gamma_2(+-+)$, $\Gamma_3(-++)$ and $\Gamma_4(--+)$.

Considering now how these operators act on the A-cation spins, which are placed in the four equivalent symmetry sites with Wyckoff position (4c): $\left(x, y, \frac{1}{4}\right)$, $\left(-x, -y, -\frac{1}{4}\right)$,

$\left(\frac{1}{2}+x,\frac{1}{2}-y,-\frac{1}{4}\right)$ and $\left(\frac{1}{2}-x,\frac{1}{2}+y,\frac{1}{4}\right)$. Table 1.3 summarizes the transformation properties. In this case, eight representations are possible, $\Gamma_{1,\ldots,8}$, and note that for instance, only one component (C_z) transforms according the $\Gamma_1(++)$ representation.

TABLE 1.3: Transformation properties of the base vector of A-cation [19].

Vectors	**Operators**								
	$2_{1,x}$			$2_{1,y}$			$\bar{1}$		
	x	y	z	x	y	z	x	y	z
F	+	-	-	-	+	-	+	+	+
A	-	+	+	-	+	-	-	-	-
C	-	+	+	+	-	+	+	+	+
G	+	-	-	+	-	+	-	-	-

In this thesis, we will focus on a perovskite materials where the B-site is occupied by a metal-transition, such as Fe or Ni, and the A-site by a rare-earth element, such as Nd. Table 1.4 combines the irreducible representations of two-cation sites, considering the P*bnm* space group, and presents the respective magnetic groups.

TABLE 1.4: Magnetic irreducible representations (irrep) and the corresponding magnetic space groups derived from P*bnm* [19].

Representation	**Generators**			**Transition metal**	**Rare-earth**	**Magnetic group**
	$2_{1,x}$	$2_{1,y}$	$\bar{1}$	(4b)	(4c)	
Γ_1	+	+	+	$A_xG_yC_z$	C_z	P*bnm*
Γ_2	+	-	+	$F_xC_yG_z$	F_xC_y	P*bn'm'*
Γ_3	-	+	+	$C_xF_yA_z$	C_xF_y	P*b'nm'*
Γ_4	-	-	+	$G_xA_yF_z$	F_z	P*b'n'm*
Γ_5	+	+	-	.	G_xA_y	P*b'n'm'*
Γ_6	+	-	-	.	A_z	P*b'nm*
Γ_7	-	+	-	.	G_z	P*bn'm*
Γ_8	-	-	-	.	A_xG_y	P*bnm'*

For rare-earth orthoferrites, the magnetic representation notation is widely used, as it gives a deep insight into the magnetic structure and allowed magnetic excitations [18–21].

1.2. Rare-earth nickelates

Rare-earth nickelates, being perovskites have the chemical formula RNiO$_3$ where R = La–Lu. They are one of the central families of TMOs due to exhibiting strong correlations between lattice, spin and charge/orbital degrees of freedom, enabling the control of phase

transitions and property tailoring [6, 22]. These have stimulated intense research in order to fully understand the interplay between electronic, structural, and magnetic order parameters underlying their metal-to-insulator transition (MIT).

1.2.1 Phase diagram of RNiO$_3$

Nickelates present a rich landscape of structural and physical properties promoted by R substitution along the rare-earths. Besides LaNiO$_3$ that remains a paramagnetic metal with R$\bar{3}c$ symmetry, with temperature all nickelates undergo three transitions: structural, magnetic and electronic. Figure 1.6 displays the phase diagram parametrized by temperature and R size. As the R substitution progresses from Lu to La, the A-site ionic radius

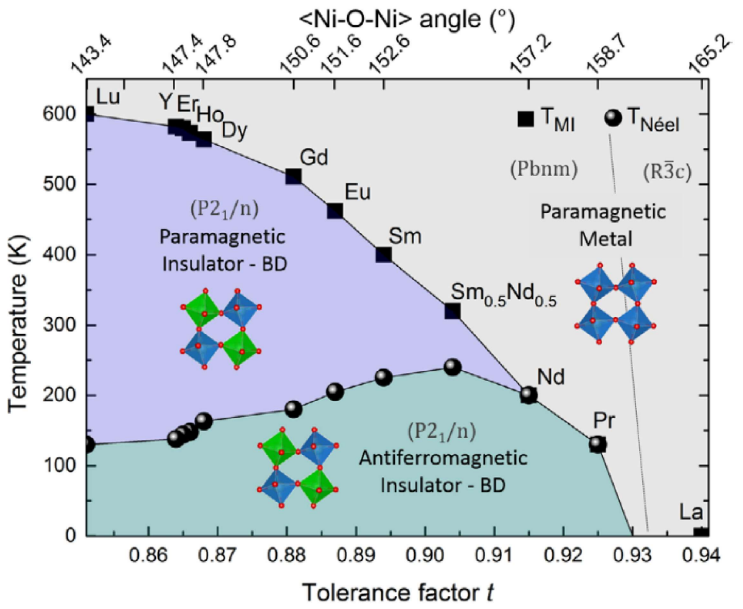


FIGURE 1.6: Phase diagram of RNiO$_3$ along the rare-earth substitution. Squares and circles correspond to MIT and magnetic transition, respectively. Adapted from [6].

increases, reducing the distortion of lattice structure by bringing the Ni-O-Ni bond angle closer to 166°, and therefore increasing the tolerance factor. For less distorted structures compounds as NdNiO$_3$ and PrNiO$_3$, the three transitions occur simultaneously.

1.2.1.1 Electronic transition

The metal-to-insulator phase transition is perhaps the most notable feature of the nickelates family. The temperature at which the MIT occurs is related to the degree of orthorhombic distortion throughout the rare-earth substitution. Before addressing this electronic transition, one should understand the complexity behind nickelates electronic configuration. The oxidation state of Ni^{3+} is defined by 7 electrons on the d shell, resulting in a d^7 low spin configuration $t_{2g}^6 e_g^1$. The two e_g states should be equally occupied. Considering the orthorhombic structure with a regular NiO_6 cage, a small charge transfer δ facilitates the relocation of electrons from the O p band to the Ni d states. The negative charge transfer model explains the predominant Ni electronic configuration of d^8L, where *L* indicates a hole in the oxygen band [23]. With the staring configuration of d^8L in the metallic phase, the following mechanism describes the charge transfer during the transition into an insulator phase [6]:

$$d^8L + d^8L \longrightarrow d^8L^2 + d^8 \tag{1.5}$$

The two undistinguished nickel sites in the metallic phase become inequivalent in the insulator phase. The nickel site with d^8 configuration can be seen as Ni^{2+} oxidation state, been surrounded by a larger oxygen cage, while the d^8L^2 configuration can be compared to Ni^{4+}, having a small cage surrounding it (see Figure 1.7). This is the so-called bond-disproportionation. As depicted in Figure 1.6, the transition temperature strongly depends

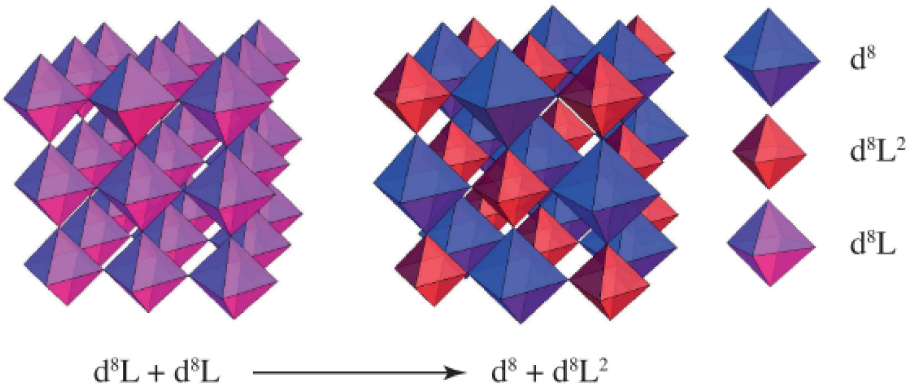


FIGURE 1.7: Illustration of the MIT characteristic of $RNiO_3$, where the insulator phase has two inequivalent nickel sites. Adapted from [24].

on the rare-earth size, increasing with the decreasing ionic radius. This affects the Ni-O-Ni bond angle, and consequently changes the overlap between transition metal d and oxygen p orbitals, thus modifying the MIT temperature in the 100 - 600 K range.

1.2.1.2 Structural transition

With the exception of $LaNiO_3$, $RNiO_3$ adopt the orthorhombic P*bnm* space group between 700 K and the T_{MI} [6]. For temperatures below the MIT, as mentioned in the previous subsection, two inequivalent Ni sites result from the two oxygen octahedra sizes. This gives rise to the monoclinic symmetry, described by the $P2_1/n$ space group [25, 26]. Experimentally, the MIT in $RNiO_3$ is accompanied by the structural transition [6, 25, 27]. The theoretical explanation for simultaneity of electronic and structural transition was proposed by Mercy *et al.*, concluding that the metal-insulator transition of nickelates is structurally triggered [28]. The charge ordering mechanism described before suggests the appearance of a breathing distortion of the oxygen octahedra, promoting the stabilization of the insulator phase. However, the mechanism behind the occurrence of the MIT is more complex. To shed light into this mechanism, one needs to analyse the energy wells of the main atomic distortion individually. Figure 1.8(a) shows the three main atomic motions that lower the ideal perovskite structure P$m\bar{3}m$ to P*bnm* and then to $P2_1/n$, for *R*= Sm, Gd and Y, and for the spin arrangements (ferromagnetic and antiferromagnetic). The main two distortions responsible for the P*bnm* space group are the oxygen rotations(tilts) $[001]_{pc}$ and $[110]_{pc}$, that correspond respectively to the symmetry-adapted modes M_3^+ and R_4^+, already mentioned in Figure 1.4. These distortions are going to be renamed from hereafter in order to better mirror the rotation axis: M_3^+ is equivalent to M_z, and R_4^+ to R_{xy}. They present a typical double-well shape of the energy that becomes more pronounced with the decrease of *R* cation size, but are nearly independent on the spin arrangements (see example of $YNiO_3$ where the two blue lines are indistinguishable). The symmetry-adapted distortion responsible for the stabilization of $P2_1/n$ structure is the octahedra breathing distortion,B_{OC}. Contrary to the other distortions, B_{OC} energy is stable and extremely stiff in a single-well line. By making the *R* cation smaller, the well becomes even more stiff, in contradiction with the increase of T_{MI}. By changing the magnetic order to AFM, the curvature slightly decreases but the single-well is preserved, which cannot explain the symmetry lowering to the monoclinic phase. In conclusion, Figure 1.8(a) resumes why B_{OC} and the magnetic order are insufficient to promote the MIT.

A trigger mechanism was then proposed, based on the coupling between oxygen rotations and octahedra breathing distortions, assuming the following Landau model [28]:

$$\begin{aligned} E =& \gamma_R(T - T_{0R})Q_R^2 + \beta_R Q_R^4 + \lambda_{BR} Q_B^2 Q_R^2 + \gamma_M(T - T_{0M})Q_M^2 + \\ & \beta_M Q_M^4 + \lambda_{BM} Q_B^2 Q_M^2 + \alpha_B Q_B^2 + \beta_B Q_B^4 + \lambda_{MR} Q_M^2 Q_R^2 \end{aligned} \tag{1.6}$$

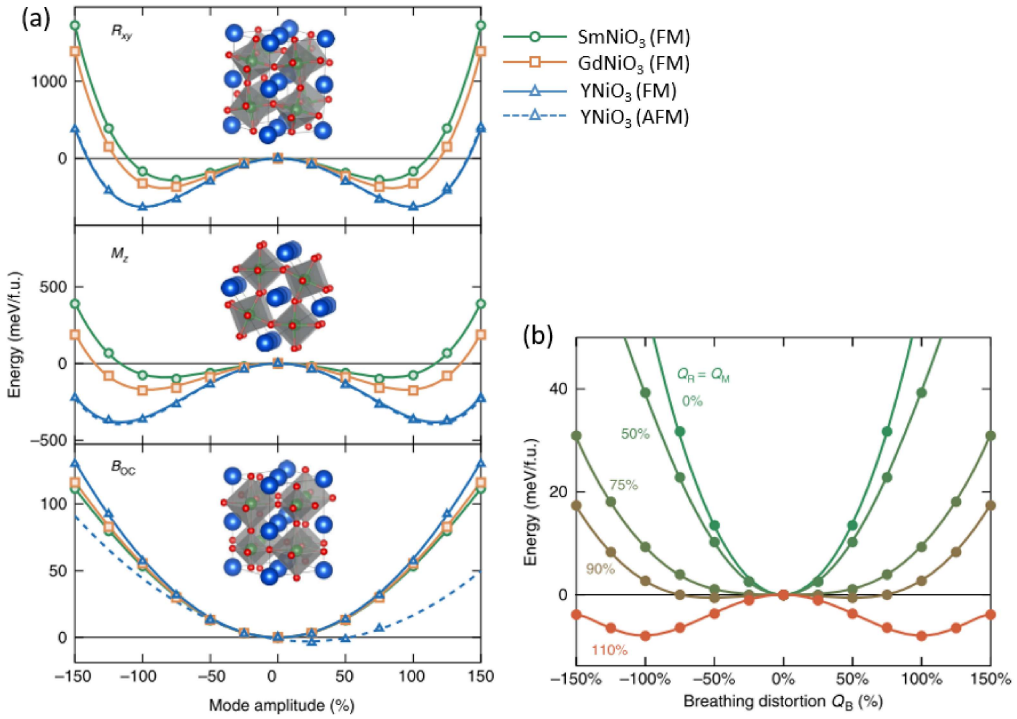


FIGURE 1.8: (a) Main atomic distortions that promote the P*bnm* and then P$2_1/n$ phases, having as a starting point P$m\bar{3}m$. R_{xy}: $[110]_{pc}$ anti-phase rotation of octahedra cages around x- and y-axis, M_z: $[001]_{pc}$ in-phase rotation of octahedra cages around z-axis, B_{OC}: breathing of the oxygen octahedra. Energy wells associated to the freezing of individual distortion of increasing amplitude in the cubic cell are shown for different *R* cations and either a ferromagnetic (full line) or E′-type antiferromagnetic (dashed line, only for *R* = Y) spin arrangement: $SmNiO_3$ (green), $GdNiO_3$ (orange) and $YNiO_3$ (blue). (b) Energy wells as a function of breathing distortion's amplitude for fixed amplitudes of oxygen rotations (R_{xy} and M_z) for the case of $YNiO_3$ with ferromagnetic spin arrangement. Adapted from [28].

where it is assumed only the temperature dependence of the oxygen rotations, R_{xy} and M_z appear at T_{0R} and T_{0M}, respectively. Q_R, Q_M and Q_B are the amplitudes of R_{xy}, M_z and B_{OC}, respectively. After stabilizing in the P*bnm* phase, a renormalization of the B_{OC} energy curvature can be made by grouping the Q_B^2 terms of Eq. 1.6:

$$\widetilde{\alpha_B} = \alpha_B + \lambda_{BM} Q_M^2 + \lambda_{BR} Q_R^2 \tag{1.7}$$

The free energy of the system can be seen as a cooperative bi-quadratic coupling terms between B_{OC} and the rotations R_{xy} and M_z [28]:

$$E \approx \lambda_{BM} Q_M^2 Q_B^2 + \lambda_{BR} Q_R^2 Q_B^2 \tag{1.8}$$

indicating that those two oxygen rotations trigger the appearance of B_{OC}. This result evidences the concurrence of both structural and electronic phase transitions. Figure 1.8(b)

highlights how the stable single-well of B_{OC} energy progressively softens until becoming a double-well with the increasing amplitude of R_{xy} and M_z rotations. To sum-up, the MIT of nickelates arises from the softening of an oxygen-breathing distortion, structurally triggered by oxygen-octahedra rotation motions.

1.2.1.3 Magnetic transition

As depicted by the circles in Figure 1.6, there is a third transition occurring with lowering temperature: Néel transition from paramagnetic to antiferromagnetic phase. In opposition to the MIT, *R* size does not impact as much the Néel transition temperature. Nevertheless, the nature of the transition is not the same for set *R* =Pr-Lu. For *R* =Pr and Nd, the first order magnetic transition occurs simultaneously to both electronic and structural transitions ($T_{MI} = T_N$); while for other rare-earths, the magnetic phase transition is of second order and occurs for $T_N < T_{MI}$ [29, 30]. Figure 1.9(a) illustrates the Ni magnetic moment temperature evolution for a discontinuous transition, for *R* =Pr and Nd, and for a continuous transition, *R* =Sm and Eu [29]. Below T_N, the antiferromagnetic arrangement is characterized by the wave vector $q_0 = (¼, ¼, ¼)_{pc}$, indicating a periodicity of 4 unit cells (Figure 1.9) [31]. This type of arrangement is labelled E'-AFM order (see subsection 1.1.2).

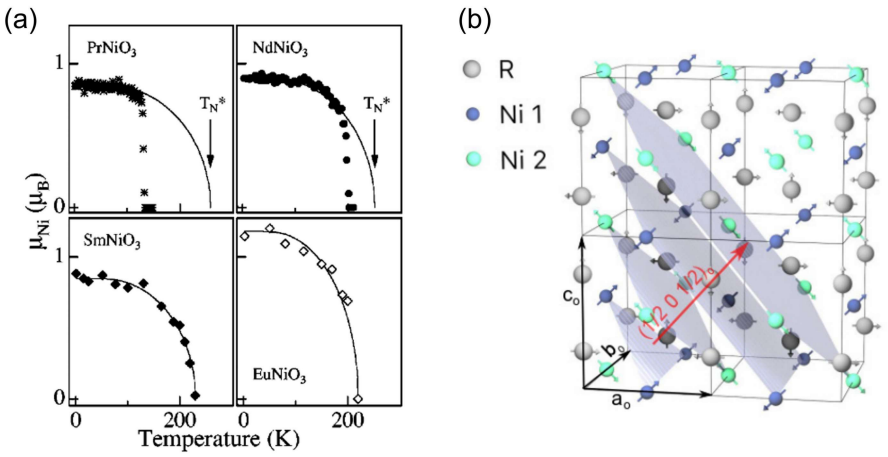


FIGURE 1.9: (a) Temperature evolution of Ni magnetic moment for *R* =Pr, Nd, Sm and Eu. Lines represent the Brillouin fitting function. Adapted from [29]. (b) Antiferromagnetic arrangement of the nickelates magnetic structure. The red arrow highlights the Bragg vector $(½\ 0\ ½)_{orth}$ in orthorhombic notation, which corresponds to $q_0 = (¼, ¼, ¼)_{pc}$ in pseudocubic notation. Adapted from [6].

1.2.2 The case of $NdNiO_3$

The synthesis of bulk $RNiO_3$ is challenging, usually requiring extreme conditions such as high temperatures and/or high oxygen pressures [22, 32, 33]. Furthermore, the presence of an unstable nickel oxidation state (Ni^{3+}) leads to oxygen nonstoichiometric samples, which affects greatly the transport, magnetic and structural properties of the nickelates [22, 34]. Recently, the synthesis of high-quality single-crystals was possible, but their size is still restricted to the micrometer scale [35]. To overcome these challenges, nickelates are widely produced as thin films, using several deposition techniques that ensure good crystalline samples [6]. In comparison with the bulk counterparts, thin films are much more versatile. The choice of dimensionality, substrate and even the possibility of combining different compounds into a heterostructure allows the control of physical properties [6]. Taking as example $NdNiO_3$ films, there is an effect of epitaxial strain on the electronic and magnetic transition temperatures [36–38]. However in this thesis, we will not focus on tuning the properties of $NdNiO_3$ through epitaxy; the choice of dimensionality and substrate used are linked only to the phase stabilization of $NdNiO_3$.

As previously mentioned, $NdNiO_3$ and $PrNiO_3$ stand up from the other rare-earths due to the simultaneity of three transitions. Following the discussion of subsection 1.2.1.2, the amplitude of oxygen rotations R_{xy} and M_z increases with the R cation size decrease. This will promote the MIT at relatively high temperatures and well above the T_N. Yet, for large cations R= Nd and Pr, the oxygen rotations amplitude is not large enough to trigger the MIT. Landau model presented in Eq. 1.6 assumes a FM order, and it is sufficient to explain the MIT for small R, but, for large cations, the magnetism plays an important role. The E'-AFM order is compatible with the B_{OC} distortion, shifting linearly its single-well as shown in Figure 1.8(a) for $YNiO_3$, but not being sufficient to open a gap in the cubic phase by itself. However, applying the magnetic order to the P*bnm* phase, i.e. combining the oxygen rotations with the E'-AFM spin arrangement, promotes the occurrence of MIT for large R cations. Therefore, for $NdNiO_3$ and $PrNiO_3$, $T_{MI} = T_N$, with the transition being abrupt, typical of first order nature [30].

With $NdNiO_3$ (NNO) being one of the materials investigated in this thesis, a more detailed state-of-art of regarding its properties will now be presented. NNO is a metallic paramagnet with orthorhombic P*bnm* symmetry [22, 30, 32]. Bulk NNO undergoes an electronic phase transition into an insulating state below $T_{MI} \simeq 200$ K [32, 39]. In the 90s, although

structural changes were observed below the MIT by X-ray diffraction [32], neutron diffraction [40] and Raman scattering [41], no evidence for the structural symmetry breaking was found and the orthorhombic P*bnm* space group was assumed for the insulating phase. Later, it was proposed the monoclinic $P2_1/n$ space group for $T < T_{MI}$, based on symmetry arguments, and both electron diffraction and Raman scattering experiments [42]. The monoclinic symmetry of the insulating phase was afterwards unambiguously confirmed by high-resolution synchrotron powder diffraction [26]. At $T_N = T_{MI}$, the spin structure of NNO changes from paramagnetic to antiferromagnetic with E-type ordering [43].

1.2.2.1 Percolations effects: electronic and magnetic

The electronic transition of NNO is set to be first-order, attested by the hysteresis between heating and cooling resistivity curves [44]. It has been proposed and experimentally confirmed coexistence and percolation of metallic and insulating domains in the hysteretic region [36, 44–48]. Thus, there is a local distribution of the critical temperature across this region due to the nucleation of insulating domains [45–47]. Nonetheless, the critical temperature of MIT is typically defined as the temperature of the maximum in $-\frac{dln(R)}{dT}(T)$ [36]. Due to the first-order nature of MIT, is not unusual to find a distinction between critical temperatures obtained in heating and cooling runs, T_{IM} and T_{MI}, respectively [45, 49].

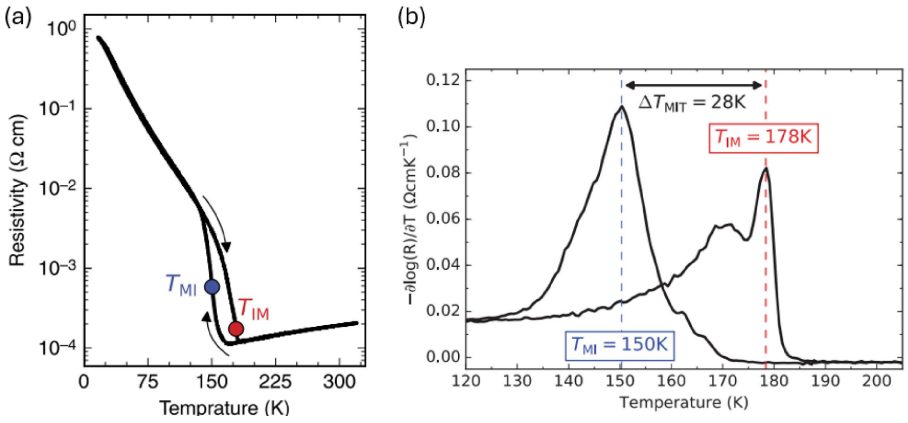


FIGURE 1.10: (a) Resistivity versus temperature of 30 u.c. NNO film deposited on $NdGaO_3$ substrate, where T_{IM} (red dot) and T_{MI} (blue dot) are extracted from peaks of (b). (b) Plot $-\frac{dln(R)}{dT}(T)$ during heating and cooling cycles. Adapted from [45].

Figures 1.10 help to visualize where both critical transitions are marked in the resistivity curve, in spite T_{IM} not being far from the MIT vicinity, the T_{MI} is marked almost at the middle of hysteresis. The abrupt changes in resistivity curve occur at higher temperatures than the ones marked by $T_{IM/MI}$, indicating that percolation of nanoscale insulating domains

is already taking place. In fact, the peak in $-\frac{dln(R)}{dT}(T)$ is correlated with the volume fraction of insulating phase, V_{ins} [36]. Figures 1.11 indicate that the peak associated with T_{MI} corresponds to a volume fraction $V_{ins} \sim \frac{2}{3}$. Note that, using the definition $T_{IM/MI} = \left(-\frac{dln(R)}{dT}\right)_{max}$, the electronic critical transition temperature is marked when the volume fraction of insulating domains is already 65% . This is valid for NNO ceramics and films, with thickness above 30 nm, and follows the predicted percolation threshold of a three-dimensional cubic lattice [36]. For thinner films, with the dimensionality being reduced and approaching a 2D-system, the percolation threshold changes from $\frac{2}{3}$ to $\frac{1}{2}$ [36].

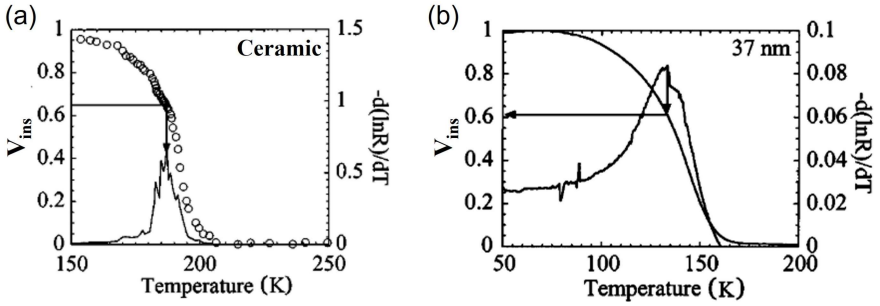


FIGURE 1.11: Volume fraction of insulating phase (left axis) and derivative of logarithm of resistivity (right axis) as a function of temperature for (a) NNO ceramic and (b) NNO thin film on $NdGaO_3$ substrate. Peak maximum (T_{MI}) coincides with percolation threshold $V_{ins} = \frac{2}{3}$. Adapted from [36].

In Figure 1.11(b), the derivative is almost zero in the metallic phase ($V_{ins} = 0$), and tends to a constant value when the system becomes fully insulator ($V_{ins} = 1$). As previously referred, when $T_{IM/MI}$ takes place, the system has 65% of insulating volume. In fact, the deviation of $-\frac{dln(R)}{dT}(T)$ from zero indicates that there are some domains with insulating character and therefore the electronic transition is already taking place. Following this discussion, in Chapter 3, we decided to define the limits of the MIT, and redefine the transition temperature:

- MIT upper limit, temperature from which the derivative of the logarithm of resistivity departs from zero. This is the T_{IM} for heating runs and T_{MI} for cooling runs.
- MIT lower limit, temperature at which the logarithm of resistivity reaches a constant value.

This new definition will allow a more accurate comparison with the structural transition temperature, and more direct parallelism between electronic and structural percolation phenomena.

The size of electronic domains during the MIT nucleation is estimated to be of the nano-size scale, as this explains the unusual shape of the resistance-temperature curves when the transport measurement area is reduced to dimensions comparable with this domain size [47].

The percolation of nano-sized magnetic domains was also detected by resonant magnetic X- ray scattering (RMXS), using nano-probe measurements in a 26 nm- NNO thin film, deposited in a substrate of $NdGaO_3$ [50]. Figure 1.12(a) shows the magnetic textures evolution with temperature (130 - 180 - 130 K). The AFM order parameter is determined from $(¼, ¼, ¼)_{pc}$ diffraction peak intensity [50]. From the resistivity curve depicted in Figure 1.12(b), the T_{MI} (= T_N) is 180 K. One possible explanation for the inhomogeneity in AFM domain distribution at temperatures below T_N could be the phase separation between AFM-insulating and paramagnetic-metallic phases. Note that RMXS measurements performed with nano-probes and macroscopic beam follow the same magnetic hysteresis loop (see Figure 1.12(c)).

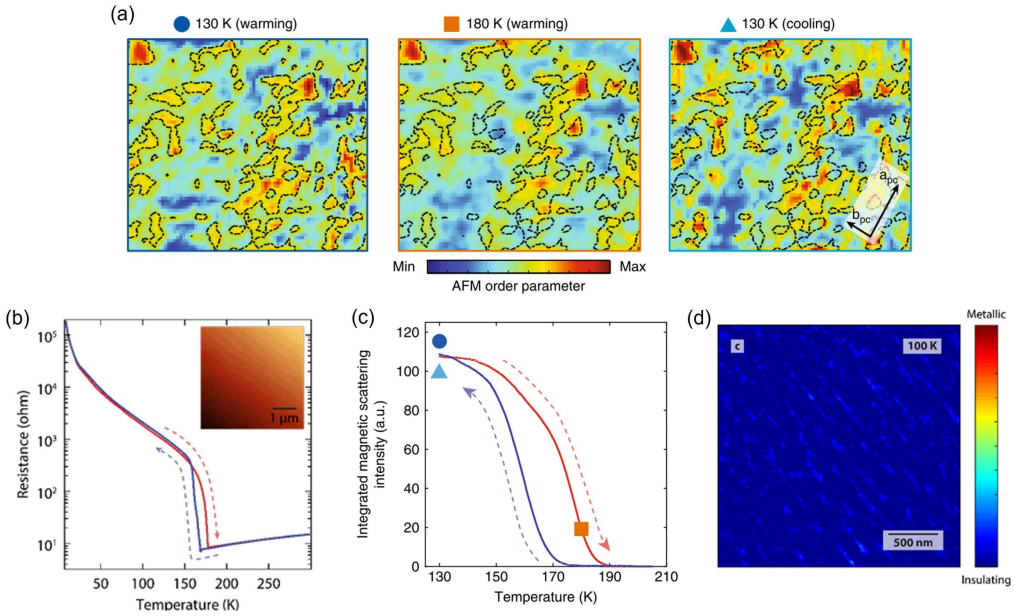


FIGURE 1.12: (a) Magnetic texture evolution with temperature, where black dashed lines are the contour of AFM domains at 130 K. Measurements using RMXS nano-probes.(b) Macroscopic resistivity curve. (c) RMXS measurements where $(¼, ¼, ¼)_{pc}$ diffraction peak intensity is measure with nano-probes (symbols) and macroscopic X-ray beam (lines). (d) XPEEM mapping at 100 K. Adapted from [50].

To verify the magnetic percolation hypothesis, where AFM-insulating and paramagnetic-metallic domains would coexist, X-ray photoemission electron microscopy (XPEEM) measurements were performed to probe electronic domains. However, these measurements were only performed at 100 K (Figure 1.12(d)), and no metallic domains were observed

[50]. The authors concluded that at a temperature so far away from T_N, the absence of metallic domains implies the absence of paramagnetic domains, and therefore the textured AFM domain landscape could not be own to the electronic domains nucleation. The origin of this magnetic inhomogeneity was ascribed to a distribution of different magnetic domains (twinning) in a homogeneous insulating state [50].

Nonetheless, the magnetic percolation cannot be entirely excluded: the temperature evolution of electronic domains should have been investigated at the same temperatures as the RMXS mapping were recorded; and the different penetration depths of each technique have to be taken into account. Actually, both techniques just probe the sample's surface, and it is known that the physical properties probed at the surface can be distinct from the ones probed in the "bulk" sample, due to local lattice distortions at the free boundary [45]. Differences in temperature for MIT-bulk and MIT-surface were already reported for NNO thin films [45].

Despite the strong correlation between lattice and charge degrees of freedom known for the nickelates family, there is a gap in the current literature exploring a possible structural percolation across the MIT. In this thesis, one of the main outcomes is to investigate structural domain evolution across the MIT, using a macroscopic technique to get information from the "bulk properties" of the sample.

1.3. Rare-earth orthoferrites

Rare-earth ferrites are perovskites with the formula $R\mathrm{FeO_3}$ (R = La–Lu). This class of materials has attracted considerable interest due to their remarkable magnetic properties [5, 20, 51]. In some $R\mathrm{FeO_3}$, such as R= Gd and Dy, the magnetic interactions between rare-earth and iron sublattice give rise to multiferroic properties at low temperatures [52, 53]. Room temperature multiferroicity was even claimed for $\mathrm{SmFeO_3}$ [54], but some concerns have been raised regarding those results [55]. The strong spin-lattice coupling characteristic of this materials' family has recently gain even more relevance [52, 56, 57], as it opens the possibility of accessing non-equilibrium transient magnetic states by driving optical phonons into a non-linear regime using ultrafast THz pulses [56, 58–60] . The coherent excitation of phonons, and the consequent lattice distortions, modify the energy landscape of the material and allow new phases for ultrashort timescales, otherwise thermodynamically unstable [59–61].

1.3.1 Phase diagram of *R*FeO_3

Figure 1.13(a) shows the phase diagram of *R*FeO_3. The two interacting magnetic sublattices- Fe^{3+} and R^{3+} - are responsible for the diversity of phase diagram. The Fe^{3+} sublattice orders at much higher temperatures than the R^{3+} sublattice [20]. The magnetic orderings indicated in Figure 1.13(a) only concern Fe-Fe interactions. The Néel transition occurs in the temperature range 620-740 K, with the *R* cation progress from Lu to La [5]. The geometric factor seems to play a role as the transition temperature decreases almost linearly with the decrease of *R* cation size. Using the Bertaut's notation, where $x||a$, $y||b$ and $z||c$, all rare-earth orthoferrites adopt a $G_xA_yF_z$ antiferromagnetic ordering of the Fe^{3+} spins, represented by the blue region of Figure 1.13. This ordering is also identified by the orthorhombic magnetic P*b'n'm* space group (see Table 1.4). Due to canting of the iron sublattice originated by the Dzyaloshinskii–Moriya interaction, a weak-ferromagnetic component ***F*** arises along the c−axis, as shown in Figure 1.13(b), while the antiferromagnetic vector ***G*** is along the a-axis [59, 62, 63]. This magnetic phase is usually referred as Γ_4 [20].

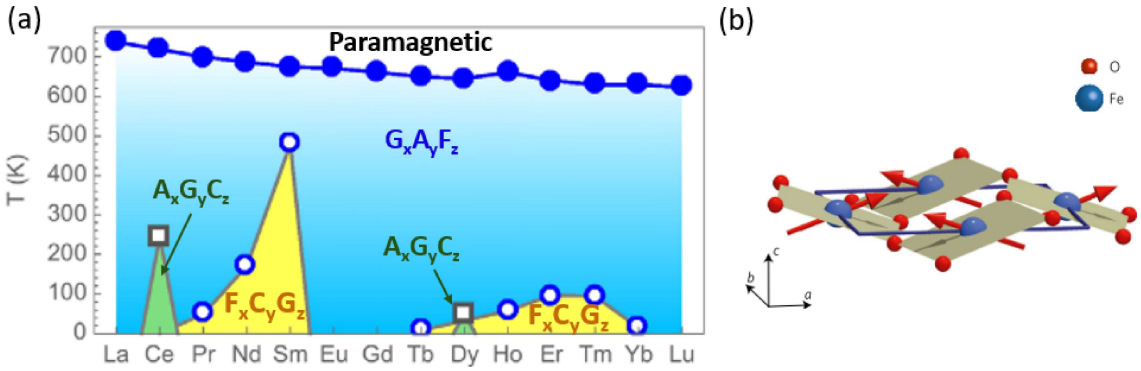


FIGURE 1.13: (a)Phase diagram of *R*FeO_3 along the rare-earth substitution. Filled circles mark the Néel transition temperature, establishing $G_xA_yF_z$ magnetic state. Open circles and squares correspond to the spin reorientation transitions $G_xA_yF_z \rightarrow F_xC_yG_z$ and $G_xA_yF_z \rightarrow A_xG_yC_z$, respectively. Adapted from [5]. (b) Magnetic ordering of Fe^{3+}, with the canting induced out of the ab-plane, giving rise to a small ferromagnetic component along c-axis. Adapted from [59].

The Γ_4 phase persists down to the lowest temperature for magnetically inert rare-earth atoms, *R*= La, Eu, Gd and Lu [20, 56]. The majority of R^{3+} ions are magnetically active and can therefore interact with the Fe^{3+} sublattice [21]. With decreasing temperature, this interaction will promote the rotation of the iron sublattice, called spin reorientation, giving rise to new antiferromagnetic orderings, depending on the rare-earth cations. Most *R*FeO_3 (*R*= Pr, Nd, Sm, Tb, Ho, Er, Tm and Yb), after the spin reorientation transition (SRT), stabilize in the $F_xC_yG_z$ phase (or P*bn'm'* space group), also known as Γ_2, where

the ferromagnetic component ***F*** is along a-axis. This phase is represented by the yellow region in Figure 1.13(a). The other two compounds, $CeFeO_3$ and $DyFeO_3$, stabilize in a different magnetic configuration with the irons spin arrangement described by $A_xG_yC_z$, known as Γ_1, in which the net magnetization is zero. This magnetic phase corresponds to the green regions of the diagram depicted in Figure 1.13(a).

1.3.1.1 Spin reorientation transition model

Below the ordering temperature of the iron sublattice, the *R*FeO_3 family crystallizes in the magnetic P*b'n'm* orthorhombic space group, with unit cell being described by 4 atoms of Fe^{3+} with spins S_1, S_2, S_3, S_4 and 4 atoms of R^{3+} with spins S_5, S_6, S_7, S_8. The system magnetic term of the Hamiltonian is written as [21]:

$$H = H^{Fe} + H^{Fe-R} + H^{R} \tag{1.9}$$

where the first term represents Fe-Fe magnetic interactions, the second term Fe-*R* and the third R^{3+} interactions. Each Hamiltonian term can be decomposed into more interaction terms. The Hamiltonian for Fe^{3+} is written as [21]:

$$H^{Fe} = H_{iso} + H_{anti} + H_{symm} + H_{an} \tag{1.10}$$

where the first, second and third terms represent the isotropic, anti-symmetric and anisotropic-symmetric exchange interactions, respectively, and the fourth the anisotropy energy of Fe^{3+} ions. The H^{Fe-R} term is expressed by three exchange interaction terms between Fe^{3+} and R^{3+} ion, the isotropic, anti-symmetric and anisotropic-symmetric [21]:

$$H^{Fe-R} = \widetilde{H}_{iso} + \widetilde{H}_{anti} + \widetilde{H}_{symm} \tag{1.11}$$

Comparing the order of magnitude of terms in Eq. 1.9, it follows $H^R \ll H^{Fe-R} < H^{Fe}$. The H^R has the same interaction terms and anisotropy energy as Eq. 1.10, but refereeing to R^{3+} ions. The isotropic and anisotropic exchange terms of rare-earths are rather small comparing with those of H^{Fe-R} and H^{Fe}, and thus, the H^R term can be neglected. In fact, the spin reorientation occurs at much higher temperatures than the ordering temperature of R^{3+}, making the anisotropy energy of these ions negligible small to induce the SRT. This argument clearly evidences the H^{Fe-R} role on the temperature induced SRT in rare-earth orthoferrites. The anisotropic exchanges between the two cation sublattices are the mechanism behind this transition, which give rise to different types of spin reorientation:

absent, rotational or abrupt [21]. As previously mentioned, the SRT is absent for the ferrites with non-magnetic R^{3+} and for those cases, the Γ_4 phase is kept in the entire temperature range.

Rotational spin reorientation ($\Gamma_4 \longrightarrow \Gamma_2$)

The rotational spin reorientation is the most frequent and comprises the continuous rotation of the weak net ferromagnetic moment in the ac-plane, while the relative angles between Fe^{3+} spins remain rigid, as depicted in Figure 1.14. With decreasing temperature, the SRT can be seen as a rotation of the easy-axis from a-axis to c-axis in the temperature range between T_1 and T_2, upper and lower limits, respectively. Note that the definition of easy-axis corresponds to the crystallographic direction along which the Fe^{3+} magnetic moments prefer to align due to magnetocrystalline anisotropy [21]. Across the rotation, an intermediate spin structure Γ_{24} is assumed, resulting from superimposing $\Gamma_4(G_x A_y F_z)$ and $\Gamma_2(F_x C_y G_z)$ phases. While R^{3+} ions are paramagnetic, they can be polarized in the exchange field caused by the Fe^{3+} ions, developing a net moment that can either be parallel(+) or antiparallel (-) to the net Fe^{3+} moments, as shown in Figure 1.16. For T > T_1, the four R^{3+} spins are co-linear and align along the c-axis, splitting into two pairs when T < T_1 with the resulting net moment of the R^{3+} being always align with the one from the Fe^{3+} ions. For compounds with antiparallel alignments of the R^{3+} spins (R = Nd, Sm, Er and Tm), there is a compensation temperature at which the R^{3+} net moment cancels the Fe^{3+} moment, and the net magnetization of the system is zero.

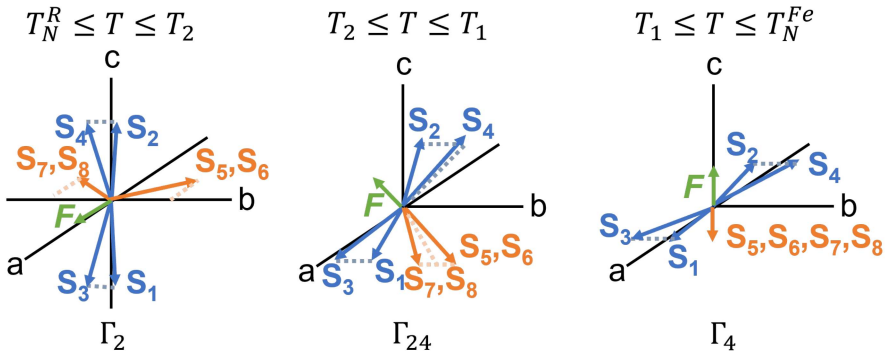


FIGURE 1.14: Spin configurations for different magnetic phases, with rotational SRT $\Gamma_4 \longrightarrow \Gamma_2$, with respect to the S_1, S_2, S_3, S_4 spins of Fe^{3+} (blue arrows). The R^{3+} are also represent in the scheme by S_5, S_6, S_7, S_8 (orange arrows). The weak-ferromagnetic component ***F*** is represented by green arrow.

Abrupt spin reorientation ($\Gamma_4 \longrightarrow \Gamma_1$)

For compounds such as $DyFeO_3$ and $CeFeO_3$, the spin reorientation is abrupt and characterized by a sharp decrease of the magnetization across the transition [64, 65]. At T > T_1, the spin structure of the Fe^{3+} ions is also described by Γ_4, but with decreasing temperature the system abruptly changing to a Γ_1 structure, where the net moments of two Fe^{3+} spin pairs cancel out and the net magnetization becomes zero, as shown in Figure 1.15. The intermediate spin structure Γ_{14} is never reached due to its free-energy $F(\Gamma_{14})$ being higher than $F(\Gamma_4)$ and $F(\Gamma_1)$, making this configuration unstable [21]. $HoFeO_3$ has a singular SRT: the intermediate phase is a mixture of two metastable spin structures Γ_{24} and Γ_{12} [66].

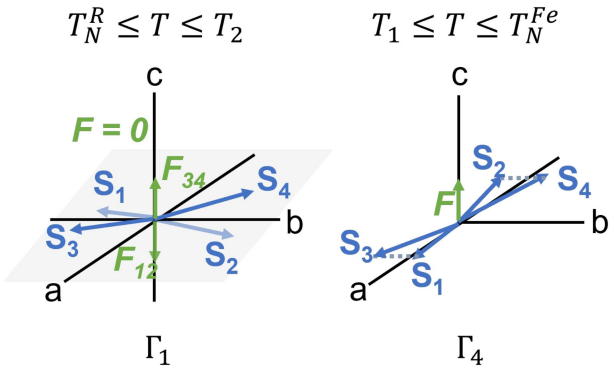


FIGURE 1.15: Spin configurations for structures Γ_4 and Γ_1, with respect to S_1, S_2, S_3, S_4 spins of Fe^{3+} (blue arrows). The weak-ferromagnetic component ***F*** is represented by green arrow.

The ordering temperature of magnetic rare-earth cations is typically below 10 K [20, 67]. Below T_N^R, the R^{3+} spins cooperatively order, leading to a further magnetic symmetry breaking, marked by black region in Figure 1.16.

1.3.1.2 Magnetic ressonances: magnons

Assuming a two-sublattice model, instead of a four-sublattice model, the four original Fe^{3+} ions form two sublattice A and B.

$$\begin{aligned} \boldsymbol{S}^A &= \boldsymbol{S}_1 + \boldsymbol{S}_3 \\ \boldsymbol{S}^B &= \boldsymbol{S}_2 + \boldsymbol{S}_4 \end{aligned} \tag{1.12}$$

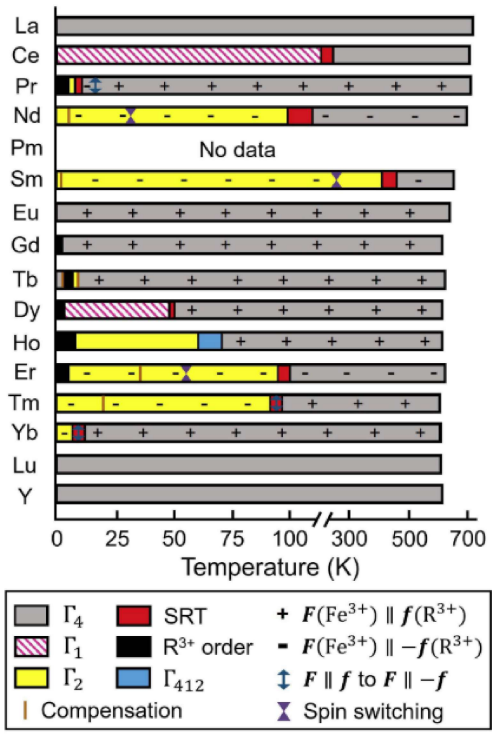


FIGURE 1.16: Magnetic diagram of RFeO$_3$. Adapted from [56].

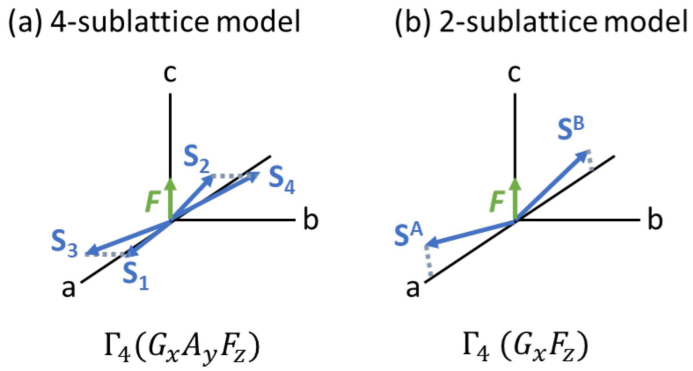


FIGURE 1.17: Spin configurations for the Γ_4 configuration assuming (a) four-sublattice model and (b) two-sublattice model. The weak-ferromagnetic component $\boldsymbol{F}$ is represented by green arrow.

Taking into account the R^{3+} moments makes the system Hamiltonian rather complex, as demonstrated by Eqs.1.9 and 1.11. To simplify, the nearest-neighbour exchange Fe-R interactions will be neglected and the system Hamiltonian is reduced to $H = H^{Fe}$ (Eq.1.10). Expanding the Fe-Fe interaction terms and restricting it to the Fe spins nearest-neighbours (nn), Eq.1.10 can be written as [51]:

$$H = 2J\sum_{nn} \boldsymbol{S}_i^A \cdot \boldsymbol{S}_i^B + \sum_{nn}(\boldsymbol{D} \cdot \boldsymbol{S}_i^A \times \boldsymbol{S}_i^B) + \sum_i \boldsymbol{K}_{eff} \cdot \left[(\boldsymbol{S}_i^A)^2 + (\boldsymbol{S}_i^B)^2\right] \tag{1.13}$$

where J is the isotropic Heisenberg constant, $\boldsymbol{D} = (d_x, d_y, d_z)$ the antisymmetric DM exchange vector, $\boldsymbol{S}_i = (S_x, S_y, S_z)$ is the spin of the $i-th$ Fe^{3+} ion of the sublattice A or B, and $\boldsymbol{K}_{eff}$ is the effective anisotropy. Neglecting the b-component of spins in the two-sublattice model, illustrated in Figure 1.17, and considering the spin rotation confined to the ac-plane [68–71], the anisotropy is set to be $\boldsymbol{K}_{eff} = (K_x, 0, K_z)$. Therefore, Eq.1.13 can be expressed by [51]:

$$\begin{aligned} H =& 2J \sum_{nn} \boldsymbol{S}_i^A \cdot \boldsymbol{S}_i^B + d_y \sum_{nn} (S_{z,i}^A S_{x,i}^B - S_{x,i}^A S_{z,i}^B) \\ & - K_x \left[\sum_i (S_{x,i}^A)^2 + \sum_i (S_{x,i}^B)^2 \right] \\ & - K_z \left[\sum_i (S_{z,i}^A)^2 + \sum_i (S_{z,i}^B)^2 \right] \end{aligned} \tag{1.14}$$

At the Brillouin zone center ($k = 0$), the solution for Eq.1.14 are two magnetic resonances, also called magnons, at frequencies:

$$\begin{aligned} \hbar\omega_\sigma &= \left[24JS \left[2(K_x - K_z)S \right] \right]^{1/2} \\ \hbar\omega_\gamma &= \left[24JS \left(6d_y S \tan\beta + 2K_x S \right) \right]^{1/2} \end{aligned} \tag{1.15}$$

where β is the canted angle and $S = 5/2$ is spin quantum number of Fe^{3+}. One magnon is assigned to the quasi-ferromagnetic (FM) resonance, also known as σ-mode, featuring a precession of the $\boldsymbol{F}$ vector around its equilibrium position (Figure1.18(a)). The other magnon is assigned to the quasi-antiferromagnetic resonance, also known as γ-mode, where the $\boldsymbol{F}$ vector remains along its equilibrium orientation, but with oscillating amplitude (Figure1.18(b)).

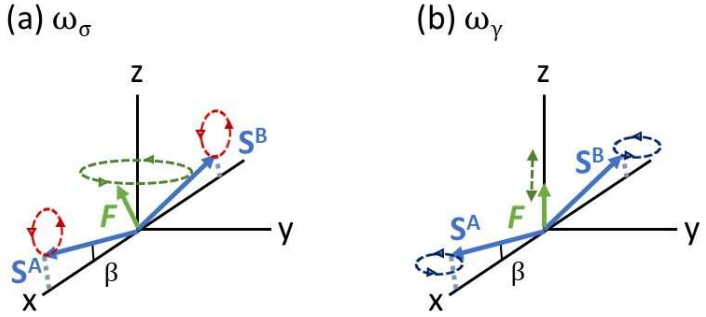


FIGURE 1.18: Precessional motions of the two $k = 0$ magnetic resonances (magnons): (a) FM or σ-mode and (b) AFM or γ-mode.

These magnetic resonances at the zone centre can be excited by inelastic neutron scattering and, due to being optically active, they absorb energy in the THz-range, so are also excited by inelastic light scattering [51, 72, 73].

THz radiation is widely used to probe magnons. The magnetic field component of the THz radiation, H^{ω}, couples linearly to the these magnetic modes, trough the magnetic-dipole interaction [51]. This light-matter interaction is described by a torque $\mathbf{T}_i = \gamma \mathbf{S}_i \times \mathbf{H}^{\omega}$, where γ is the gyromagnetic ratio and i =A or B sublattices. This torque deviates the two sublattice spins $\boldsymbol{S}^A$ and $\boldsymbol{S}^B$ from their equilibrium positions, initiating the precession that is responsible for the two magnons described above. The excitation of magnons depends however on the orientation of the magnetic field component of the THz radiation. THz-magnon selection rules are defined by the general rule: the FM-mode (σ-mode) is excited when $H^{\omega} \perp \boldsymbol{F}$ and the AFM-mode (γ-mode) is excited when $H^{\omega} || \boldsymbol{F}$. Figure 1.19(a) illustrates all possible configurations for the magnon excitation, depending on the direction propagation vector of the THz radiation and the orientation of the magnetic field component with respect to the crystallographic axis. Note that, the $\boldsymbol{F}$ vector orientation differs for Γ_4 and Γ_2 configurations, making the selection rules for each phase different.

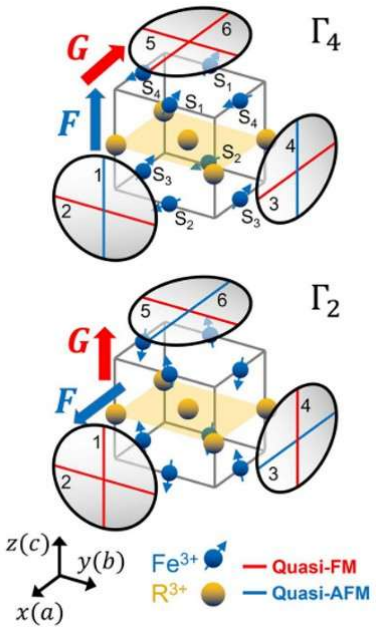


FIGURE 1.19: Magnon selection rules for THz light in the Γ_4 and Γ_2 configurations. The magnetic field component of the THz pulse is polarized along a line whose colour represents the magnon that is excited: FM if red or AFM if blue. Adapted from [56].

Among RFeO$_3$, Nd and Sm ferrites are particular interesting for presenting SRT in a wider temperature range, that occurs at relatively high temperatures in comparison with other

rare-earths (starting at 480 K for $SmFeO_3$ and at 170 K for $NdFeO_3$). Following the main goal of this thesis, we will focus on the case of $NdFeO_3$.

1.3.2 The case of $NdFeO_3$

$NdFeO_3$ is one of the ferrites with a rotational-type spin-reorientation transition ($\Gamma_4 \longrightarrow \Gamma_2$). In this compound, the SRT occurs between T_1 =170-180 K and T_2 =100-110 K, which was probed by several experimental techniques: X-ray and neutron diffraction [70, 74, 75], magnetization [71, 76, 77], Mossbauer spectroscopy [68, 78], THz and Raman spectroscopies [79–81], among others.

1.3.2.1 Magnetic ordering of Fe^{3+} ions

The Fe^{3+} sublattice of $NdFeO_3$ orders antiferromagnetically well above room temperature. The first reported Néel temperature was T_N = 760 K, obtained from neutron diffraction studies [69]. Posterior and more accurate magnetization and Mossbauer measurements set T_N^{Fe} at a slightly lower temperature of 687 K [68, 78]. Below T_N, the Fe^{3+} spins are slightly canted, as shown in Figure 1.17. This configuration is described by the $\Gamma_4(G_xA_yF_z)$ irreducible representation, with a canting angle β = 8.5 mrad [68, 78]. In this configuration, the ferromagnetic vector ***F*** is along the c-axis, while the antiferromagnetic vector ***G*** is along the a-axis. Through the canting angle, the relationship between the two magnetic vectors is such that ***F*** is 120 times smaller than ***G*** [70], being too small to have measurable contribution even for high-resolution neutron diffraction studies [70, 75, 82, 83].

The reorientation of Fe^{3+} spins in the ac-plane occurs in the $T_2 < T < T_1$ range, where T_2 =100-110 K and T_1 =170-180 K [70, 71, 77]. The 10 K variations correspond to different temperature calibrations of the experimental setups. Neutron studies confirm the antiferromagentic G_x configuration above T_1 and G_z configuration below T_2 [70, 75, 82, 83]. Across the SRT, the Rietveld refinement of the Fe^{3+} magnetic moments assumes a mixed G_xG_z ordering [70, 75]. Figure 1.20(a) shows the total magnetic moment in the upper panel, and M_x and M_z components associated with ***G*** vector in the lower panel. Above T_1= 180 K, only M_x component is detected, and below T_1 it starts to decrease at the expense of M_z component until T_2 = 100 K [70]. Two interesting features of the analysis presented in Figure 1.20(a): the total Fe^{3+} magnetic moment, μ_{Fe}^{total}, is practically

temperature-independent; outside the SRT $\mu_{Fe}^{x} \sim \mu_{Fe}^{z}$, and the smooth temperature evolution of M_x,M_z during the reorientation is compatible with the its continuous rotational nature (illustrated in the scheme of Figure 1.20(b)).

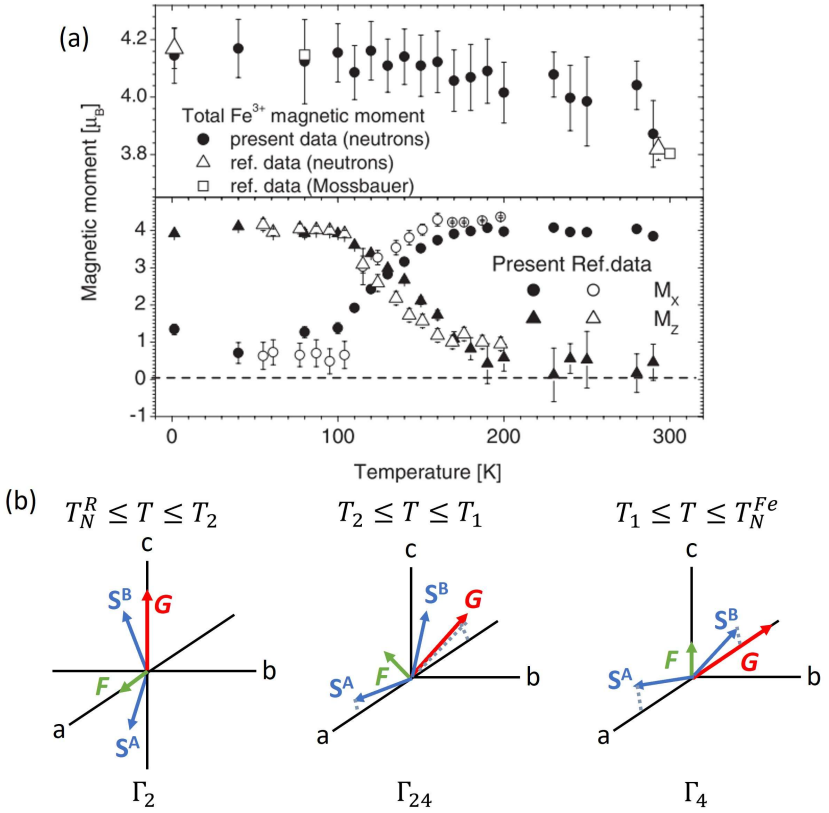


FIGURE 1.20: Temperature dependence of the total ordered Fe^{3+} magnetic moment (upper panel) and its M_x and M_z components (lower panel) in $NdFeO_3$ obtained from Rietveld refinement of neutron powder diffraction patterns. Adapted from [70]. (b) Schematic representation of vectors ***F*** and ***G*** rotation with temperature. Two-sublattice model of Fe^{3+} spins represented by $\boldsymbol{S}^A$ and $\boldsymbol{S}^B$.

Although the ***F*** is too small to be measurable by neutron diffraction experiments, its contributions to the macroscopic magnetization of $NdFeO_3$ can be easily probed by a conventional magnetometry. Figure 1.21(a) shows the temperature dependence of the magnetization measured in a crystal of $NdFeO_3$, along a-axis (M_a) and c-axis(M_c), in field-cooled (FC) conditions of 100 Oe. Above T_1 = 170 K, the ***F*** is along c-axis, making the net magnetization being along c-axis and the $M_a(T)$ negligibly small. At 170 K, a kink in both M_a and M_c curves marks an onset of a SRT. During the transition, $M_a(T)$ increases while $M_c(T)$ decreases, as a result of the ***F*** vector rotation towards the a-axis. The SRT is completed at T_2 = 107 K [71].

Isothermal magnetization curves measured along c- and a- axis, see Figure 1.21(c)-(d), evidence the changes described above from the magnetic hysteresis loops perspective. At T > 170 K, the hysteresis loops along c-axis show some coercivity, that decreases

with decreasing temperature, until it totally disappears at T < 110 K. The complete inverse behaviour takes place for hysteresis loop measured along a-axis, where no loop is detected at T > 170 K, and the coercivity gradually increases below 170 K, until a rectangular shape is achieved [77]. This results corroborates the continuous rotation of the weak-ferromagnetic component of $NdFeO_3$ from c- to a-axis with decreasing temperature as evidenced by the magnetization curves of Figure 1.21(a) and as illustrated by the scheme of Figure 1.20(b).

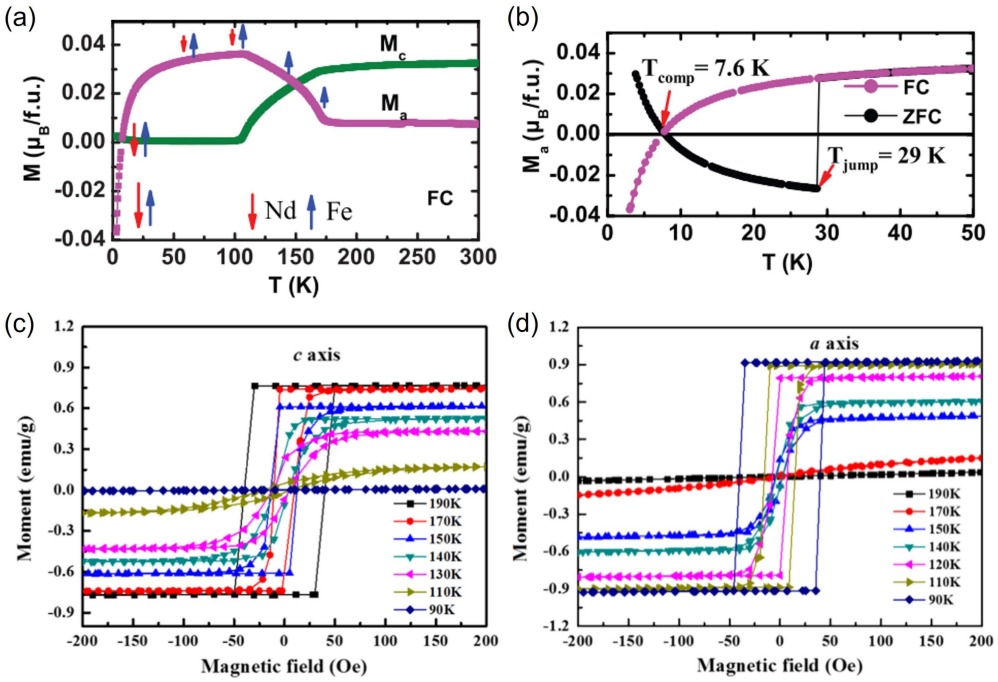


FIGURE 1.21: Magnetization as a function of temperature measured in (a) FC conditions of 100 Oe and (b) detailed view of ZFC and FC curves at low temperatures. Adapted from [71]. Magnetization as a function of magnetic field applied along (c) c-axis and (d) a-axis. Adapted from [77].

Let us now focus on the temperatures below SRT. After reaching a maximum at T_2, $M_a(T)$ curve immediately decreases as temperature falls, as demonstrated in Figure 1.21(a). This seems to be in opposition to the Fe^{3+} magnetic moment obtained from G_x component that remains constant below T_2 (see Figure 1.20(a)). In fact, it is assumed that, with decreasing temperature, the exchange interaction between the two magnetic sublattices, Fe^{3+} and Nd^{3+}, increases and consequently the weak-ferromagnetic component of the Nd^{3+} sublattice aligns in the opposite direction with respect to the Fe^{3+} ***F*** vector. This antiparallel alignment is responsible for the decrease of the system total magnetization [71]. Eventually, the effective moment of the Nd^{3+} and Fe^{3+} becomes equal in opposite directions and $M_a(T)$ becomes zero at the compensation point T_{comp} =7.6 K [71].

The intriguing behaviour of $M_a(T)$ at low temperatures is reported in Figure 1.21(b), with results obtained in zero-field cooled (ZFC) and FC conditions, both measured in heating with 100 Oe applied field. Yuan *et al.* argue that the compensation temperature occurs due to the antiparallel alignment of Nd^{3+} and Fe^{3+} ferromagnetic vectors, and the reversal sign of magnetization due to the different temperature evolution of each sublattice, where with increasing temperature, the Nd^{3+} magnetization weakens must faster than the Fe^{3+} magnetization, facilitates the reversal [71]. In the ZFC case, $M_a(T)$ exhibits a jump at 29 K, where the sign of the magnetization suddenly changes. Such jump does not occur when the system is cooled with an applied magnetic field (FC condition) as the spins of both sublattices become pinned. At T_{jump} = 29 K, a spin-flip transition occurs to a more energetically favourable state with the direction of $M_a(T)$ aligned with the applied magnetic field [71]. Larger magnetic fields move this T_{jump} to lower temperatures, and for 5000 Oe, in ZFC conditions, this spin-flip is completely suppressed [71].

1.3.2.2 Magnetic ordering of Nd^{3+} ions

In $NdFeO_3$, specific heat measurements demonstrated that the Nd^{3+} ions order cooperatively at T_N^{Nd} = 1.05 K [67]. Nonetheless, the magnetization curves shown in the previous section point for a non-cooperative ordering of the Nd^{3+} ions at higher temperatures, i.e., the paramagnetic Nd^{3+} order in the anisotropic field created by the Fe^{3+} ions [71]. Such non-cooperative ordering of Nd^{3+} ions, just below the spin-reorientation of the Fe moments, is demonstrated by the magnetization curves and by the response of Nd magnetic ground state measured through inelastic neutron scattering [84].

Figure 1.22 presents inelastic neutron spectra of $NdFeO_3$ measured at different temperatures. The 170 K spectrum shows that the magnetic response is quasielastic (centred at 0 meV), while below 100 K an inelastic peak is observed at Δ= 0.49 meV, due to the Zeeman splitting of Nd ground state double, evidencing the coupling between rare-earth and iron sublattices [84]. From this experiment, it is concluded that the molecular field at the Nd ions is fluctuating above SRT and becomes static when SRT is set (below T_2) [84].

Another evidence for this non-cooperative ordering of Nd^{3+} ions is the appearance of new diffraction peaks related only with Nd magnetic moments, as it is reported by neutron diffraction data, where (100) magnetic peak emerges just below 25 K [85]. The temperature dependence of this peak intensity has a slope change at T_N^{Nd}, marking the crossover

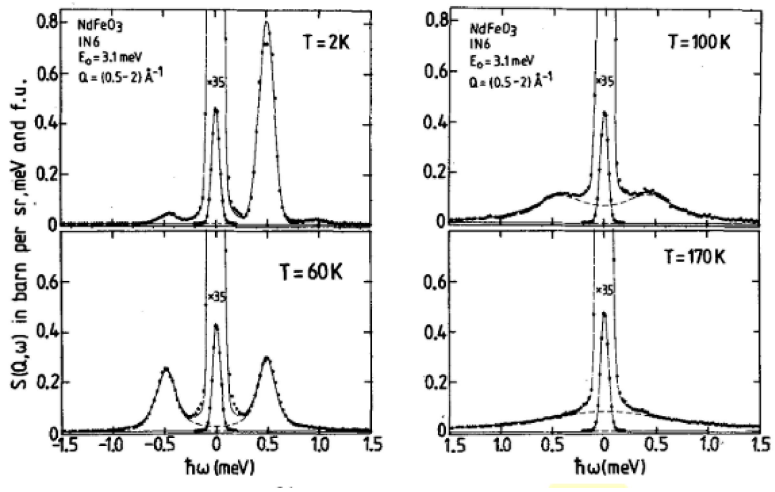


FIGURE 1.22: Inelastic neutron scattering spectrum of $NdFe_3$ recorded at different fixed temperatures. Adapted from [84].

from the Nd polarization under Nd-Fe exchange to a proper long-range ordering due to Nd-Nd interactions [85]. C-type ordering (C_y) for Nd^{3+} ions was confirmed by neutron diffraction [82, 83].

1.3.2.3 Structural and magnetic symmetries considerations across SRT

The crystal structure of rare-earth orthoferrites is well established outside the spin reorientation temperature range, T > T_1 and T < T_2, being described by the orthorhombic space group P*bnm*. As previously mentioned, the magnetic modes ascribed to this structural symmetry have to be one of the irreducible representations listed on Table 1.4. In particular, for $NdFeO_3$, at T > T_1 the Fe^{3+} ions configuration is $G_xA_yF_z$ that is compatible with the magnetic space group P*b'n'm*, described by Γ_4 irrep of the magnetic point group *m'm'm* [86, 87]. At T < T_2, the configuration is $F_xC_yG_z$, compatible with the magnetic space group P*bn'm'*, Γ_2 irrep of the magnetic point group *mm'm'* [86, 87]. During the spin reorientation transition, the Fe^{3+} ions configuration is usually presented as sum of **G** and **F** vectors: $(G_x, 0, G_z) + (F_x, 0, F_z)$, also labelled as Γ_{24}. Both vectors present a continuous rotation around b-axis as Figure 1.20(b) shows. In the neutron data presented in Figure 1.20(a), the SRT range was analysed considering a mixture of Γ_4 and Γ_2. However, there is no experimental evidence that indicates a coexistence of phases during SRT and furthermore, the continuous rotation of **G** and **F** vectors cannot be explained by a simple coexistence, as it would restrict, for instance, the **F** vector to have just one component: either $(F_x, 0, 0)$ for Γ_2, or $(0, 0, F_z)$ for Γ_4, but could never explain the $(F_x, 0, F_z)$ for Γ_{24}. Across the reorientation transition, many authors assume that the P*bnm* symmetry is maintained [70, 74, 75].

Yet, by definition an orthorhombic magnetic space group with ferromagnetism is incompatible with the ferromagnetic component pointing along more than one of the main axis [86, 87]. See Appendix A.2 for more detail. Therefore, theoretically, the symmetry must lower to a monoclinic space group during the SRT [86, 87]. Nonetheless, high-resolution synchrotron powder X-ray diffraction measurements in $NdFeO_3$ sample, performed in the 10 - 750 K range, do not evidence any structural symmetry breaking during SRT, leading the authors to consider the orthorhombic symmetry [74].

The absence of measurable structural distortions associated with a symmetry-lowering across SRT is a common feature of other rare-earth orthoferrites with the same magnetic transition sequence ($\Gamma_4 \longrightarrow \Gamma_{24} \longrightarrow \Gamma_2$). For cases such as $ErFeO_3$ and $TmFeO_3$, X-ray diffraction measurements in single crystals show smoothly changes in the lattice parameters with temperature but do not exhibit anomalies near T_1 and T_2 [88, 89]. After the lattice parameters failed to detect distortions across the SRT, a more accurate method was employed in both $ErFeO_3$ and $TmFeO_3$ samples: rocking curve in the ac-plane around the b-axis by an angle ϕ [88, 89]. The idea is to search for the formation of structural domains, because if the crystal symmetry lowers, then a multidomain polycrystal state is expected [88, 89]. If distortions are present in the SRT, it would happen in the ac-plane: the c-axis would tilt with respect to the a-axis by an angle Δ. Two possible distortions of this type have tilting angles $+\Delta$ (type-I domains) and $-\Delta$ (type-II domains), as illustrated in Figure 1.23(a) [88]. In terms of ϕ scanning rocking curve, this would imply a splitting of the diffraction peak into two peaks in the curve, or at least its widening in the case of Δ being comparable to the resolution of the device. Figures 1.23(b) and 1.23(c) present the rocking curves measured for $ErFeO_3$ and $TmFeO_3$, at two representative temperatures: inside and outside SRT.

Neither for $ErFeO_3$ nor for $TmFeO_3$, a splitting/ broadening of the diffraction peak $(400)_{orth}$ was detected, with the experimental setup resolution being 0.06° and 0.01°, respectively [88, 89]. For $ErFeO_3$, there is a small intensity difference between to two measured temperatures, while for $TmFeO_3$, the peak measured at 88 K seems to be a slightly more asymmetric than the one at 300 K. Although the authors recognise small differences in the intensity/shape of the diffraction peaks recorded inside the reorientation temperature interval, they assign these changes to the apparatus accuracy [88, 89]. Actually, the absence of width changes is the main reason why those authors concluded that no distortion occurs in the spin-reorientation region that lowers the orthorhombic symmetry in the two compounds, and that the SRT is purely magnetic [88, 89].

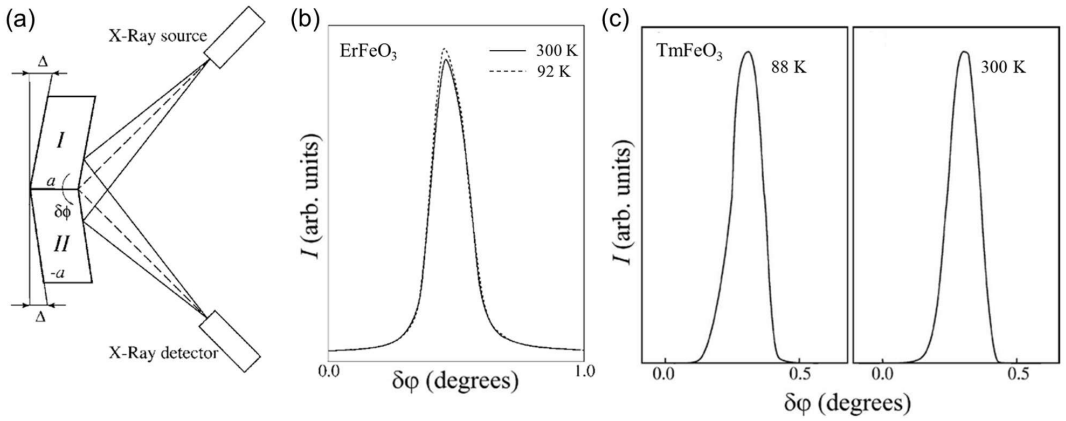


FIGURE 1.23: (a) Scheme of a ϕ-scanning rocking curve measurement in a single crystal. Intensity of orthorhombic diffraction peak $(400)_{orth}$ as a function of rocking angle $\delta\phi$, measured at two representative temperatures (outside SRT: 300 K; inside SRT: 92, 88 K) for (b) $ErFeO_3$ and (c) $TmFeO_3$. Adapted from [88, 89].

Nonetheless, from symmetry point of view, the continuous rotation of vectors ***G*** and ***F*** in the ac-plane during the spin reorientation cannot be explain by the orthorhombic symmetry. During the rotation the ferromagnetic component is no longer along one of the main crystallographic directions, hence the two orthorhombic space groups P*bn'm'* and P*b'n'm* are not suitable to describe this magnetic structure [87]. Appendix A.2 presents the symmetry arguments that justify the choice of monoclinic $P2_1'/n'$ space group for the magnetic structure in the spin-reorientation region. This choice relies on the common subgroup relation between P*bn'm'* and P*b'n'm* [87].

Assuming the same crystallographic system for structural and magnetic structures, the monoclinic space group $P2_1/n$ defines the crystal structure symmetry of $NdFeO_3$ in the SRT temperature range. The transition from P*bnm* to $P2_1/n$ results on a splitting of the Wyckoff positions, as presented in Table 1.5. If a structural transition from the orthorhombic to a monoclinic symmetry occurs, then a small deviation of angle β from 90° is expected, but has yet to be confirmed [74, 87].

Phenomenologically, the Landau-type description for the continuous spin reorientation is given by free energy, where θ (angle between ***F*** vector and c-axis) is the primary order parameter [90]:

$$G = G_0 + K_1 sin^2(\theta) + K_2 sin^4(\theta) \tag{1.16}$$

where G_0 is the isotropic energy, K_1 and K_2 are the anisotropic constants. With the reorientation process being a second order transition, to minimize the free energy with respect

to the order parameter requires $\frac{\partial G}{\partial \theta} = 0$ and $\frac{\partial^2 G}{\partial \theta^2} > 0$, from which the solutions are [90]:

$$\begin{cases} \theta = 0°, T > T_1 \\ sin^2(\theta) = -\dfrac{K_1}{2K_2}, T_2 \leq T \leq T_1 \\ \theta = 90°, T < T_2 \end{cases} \tag{1.17}$$

A representation of θ evolution across different magnetic phases is given in Figure 1.24.

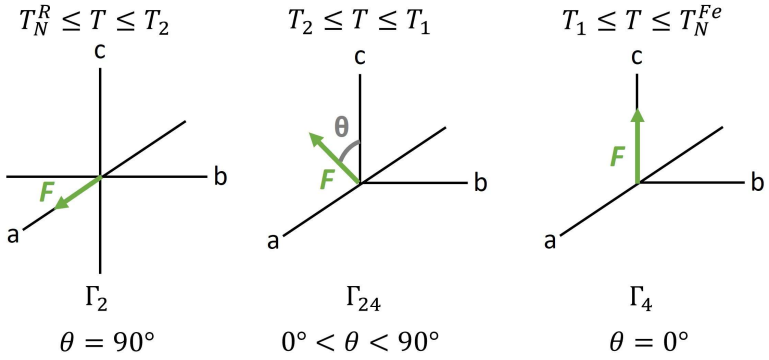


FIGURE 1.24: Schematic view of order parameter θ across continuous $\Gamma_4 \longrightarrow \Gamma_{24} \longrightarrow \Gamma_2$ transition.

From the Landau description it becomes clear that the primary order parameter is magnetic [90]. In this case, any distortion that occurs during SRT will be a secondary parameter, so even if there is a coupling between magnetic and structural parameters, the distortions promoted by the magnetic order will be small. Such small distortions can pass unnoticed to conventional diffraction experiments, as they might be in the range of the apparatus resolution (typically second or third decimal place).

In this regard, the splitting of the Fe site into two non-equivalent Wyckoff positions is particularly interesting as it unveils new opportunities to detect the symmetry-breaking during the SRT in $NdFeO_3$ and on other rare-earth ferrite with the same magnetic phase sequence, exploring for instance, experimental techniques based on local probes.

TABLE 1.5: Wyckoff positions splitting in the transformation P*bnm* $\longrightarrow$ P$2_1/n$. Adapted from WYCKPOS tool from Bilbao Crystallographic Server.

Orthorhombic P*bnm*			$\longrightarrow$	**Monoclinic** P$2_1/n$		
Site	**Wyc. pos.**	**Sym.**		**Site**	**Wyc. pos.**	**Sym.**
Nd	4c	.m.		Nd	4e	1
Fe	4b	$\bar{1}$		Fe1	2c	$\bar{1}$
				Fe2	2d	$\bar{1}$
O1	4c	.m.		O1	4e	1
O2	8d	1		O2	4e	1
				O3	4e	1

1.4. Aim of the thesis

The aim of this thesis is to investigate how *B*-site substitution in neodymium-based perovskite oxides, specifically $NdNiO_3$ and $NdFeO_3$, influences their ferroic behaviour. Although both compounds share a similar crystallographic framework, the different valence occupancies of the *B* cation - $3d^7$ for Ni^{3+} and $3d^5$ for Fe^{3+}- lead to markedly different electronic, magnetic, and even structural responses, driven by the interaction between $3d$ transition metal and $4f$ rare-earth electrons.

Following the literature review presented in Chapter 1, several open questions were identified regarding the two compounds.

For $NdNiO_3$, a redefinition of the boundaries of the MIT is needed, particularly due to its first-order nature, in order to establish a proper correlation with the structural changes. Percolative phenomena through the nucleation of electronic and magnetic domains have been identified in nickelates, $NdNiO_3$ in particular. Although theoretical models attribute the MIT to the softening of the breathing distortion B_{OC}, triggered by the octahedra rotations (R_{xy} and M_z), there is still a gap in the experimental literature that identifies a structural percolation concomitant with the electronic one.

Chapter 3 addresses this open question by investigating the coexistence of structural domains across the MIT. A $NdNiO_3$ thin film deposited on an oriented $LaAlO_3$ substrate is studied for this purpose. The MIT is confirmed via electric resistivity measurement, the para-to-antiferromagnetic transition by magnetization measurements and the orthorhombic-to-monoclinic transition by Raman spectroscopy. A correlation between percolation mechanism of electronic and structural domains across temperature is established, highlighting the strong electron-lattice coupling in $NdNiO_3$.

Regarding $NdFeO_3$, the major open question lies in the lack of experimental evidence for

a symmetry-breaking across spin reorientation transition (SRT), in fact, a long-standing issue in the rare-earth orthoferrite family.

Before addressing this issue, it is essential to have a complete description of optically active phonon and magnon excitations of $NdFeO_3$. Chapter 4 provides this characterization through Raman, FTIR, and THz spectroscopies, supported by group theory and density functional theory (DFT) calculations.

The magnetostructural nature of $NdFeO_3$ is explored in Chapter 5, through the investigation of domain wall dynamics—structural character being probed via resonant ultrasound spectroscopy (RUS), and magnetic character via magneto-optical imaging and AC magnetic susceptibility. This Chapter indirectly points to a symmetry-breaking across the spin reorientation, and sheds light on why it has not been successfully probed experimentally, in spite of being theoretically predicted.

Chapter 6 provide direct evidence of symmetry lowering to the monoclinic phase during the SRT in $NdFeO_3$, using local magnetic probes through muon spin spectroscopy (μSR). Symmetry considerations regarding the Wyckoff positions in the different structural/magnetic phases are confronted with the analysis of μSR results.

Another open question concerns the decrease in net magnetization observed just below T_2 in $NdFeO_3$. It has been hypothesized that this arises from a non-cooperative alignment of Nd^{3+} ions, but experimental evidences are missing. Furthermore, the influence of $3d$–$4f$ coupling on the magnetic dynamics of the spin structure is yet to be studied. Chapter 7 addresses these issues by investigating the cross-talk between the Nd^{3+} and Fe^{3+} magnetic sublattices, using temperature-dependent X-ray magnetic dichroism spectroscopy and THz spectroscopy. The effect of external magnetic field on magnons, probed via Raman and THz spectroscopies, and on the net magnetization, probed by a magnetometry, is also explored. These studies culminate in the construction of ($\boldsymbol{B}$,T) phase diagrams.

Finally, Chapter 8 summarizes the main findings of this thesis and discusses the broader implications of $3d$–$4f$ interactions in rare-earth perovskites oxides.

All experimental techniques and corresponding analysis methods are briefly described in Chapter 2.

To sum up, this thesis will provide new experimental insights into ferroic interactions in complex oxides with inequivalent magnetic sublattices, offering new perspectives for future research, including the ultrafast control of phase transitions.

2. Experimental Techniques

This chapter addresses the experimental techniques used during the preparation and characterization of the samples. Experiments were carried out by the author of this thesis, except when stated otherwise.

2.1. Sample processing techniques

2.1.1 $NdNiO_3$ thin film

$NdNiO_3$ film deposited by metal-organic chemical vapour deposition (MOCVD) technique onto a [001]- $LaAlO_3$. This sample was produced by Dr. Cecilia Girardot from Grenoble Institute of Technology - CNRS, Grenoble, France. Deposition procedure is described in detail elsewhere [27]. Due to sample age, a careful comparison was carried out with the characterization results in a equivalent $NdNiO_3$ film published in Ref.[27]. The chemical and morphological presented in section 3.1 ensures that the film aged well.

2.1.2 $NdFeO_3$ crystals

$NdFeO_3$ crystals were provided by the group of Prof. Marian Mihalik, from the Experimental Physics Slovak Academy of Sciences, Kosice, Slovak Republic. The crystals were grown by a vertical floating zone method, described with detail in [91]. Single-domain platelets were oriented and polished, assisted by Laue diffraction patterns to ensure the desired orientation. Crystal orientation was carried out by PhD student Miroslav Lebeda from the Institute of Physics of the Czech Academy of Sciences, Prague, Czechia.

2.2. Characterization techniques

2.2.1 X-ray diffraction

X-ray diffraction (XRD) is a technique used to obtain the crystallographic structure (lattice parameters and atomic positions), phase composition and strain of materials. The diffraction of X-rays by the periodic atomic planes relies on the Braggs's law. In-house X-rays are produced in a X-ray tube, consisting of a cathode and an anode. The cathode is heated until electrons are ejected, and then are accelerated in a high voltage towards the anode. Due to high energy collision with the anode, a spectrum of X-ray radiation is emitted.

The in-house measurements at room temperature were performed in a Panalytical MPD diffractometer in Bragg-Bentano geometry. A Cu anode was used to produce x-ray K$\alpha_{1,2}$ radiation with λ_1 = 1.540598 Å, λ_2 = 1.544426 Å. The diffractometer is equipped with a X'Celerator detector, with a Ni filter to minimize the Kβ radiation and a secondary monochromator. An acceleration voltage of 50 kV and a current of 40 mA was used. The calibration and alignment of the diffractometer were made by polycrystalline silica as external standard. Diffraction patterns are recorded in the 10-70° 2θ range, with a step size of 0.017° and 100 s/step.

XRD measurements were carried out in collaboration with PhD student Abderrazzak Bassou and Prof. Pedro Tavares, at Centro de Química, University of Trás-os-Montes and Alto Douro in Vila Real, Portugal.

2.2.2 X-ray photoelectron spectroscopy (XPS)

X-ray Photoelectron Spectroscopy (XPS) is a surface-sensitive technique used to determine the elemental composition, chemical state, and electronic structure of materials. XPS is based on the photoelectric effect, where X-rays irradiate a sample, causing the ejection of core electrons. The kinetic energy of the emitted electrons is measured and afterwards the binding energy is determined.

The measurements were performed at Materials Centre of the University of Porto (CEMUP), using a monochromatic Al-Kα radiation (1486.6 eV, operating at 15 kV) from a Kratos AXIS Ultra HAS. A calibration was done using the carbon peak C$1s$ as a reference (285 eV). The analysis was performed with CASAXPS software, where the peaks were fitted using

a mix of Gaussian and Lorentzian functions, and the background was simulated with the Shirley function.

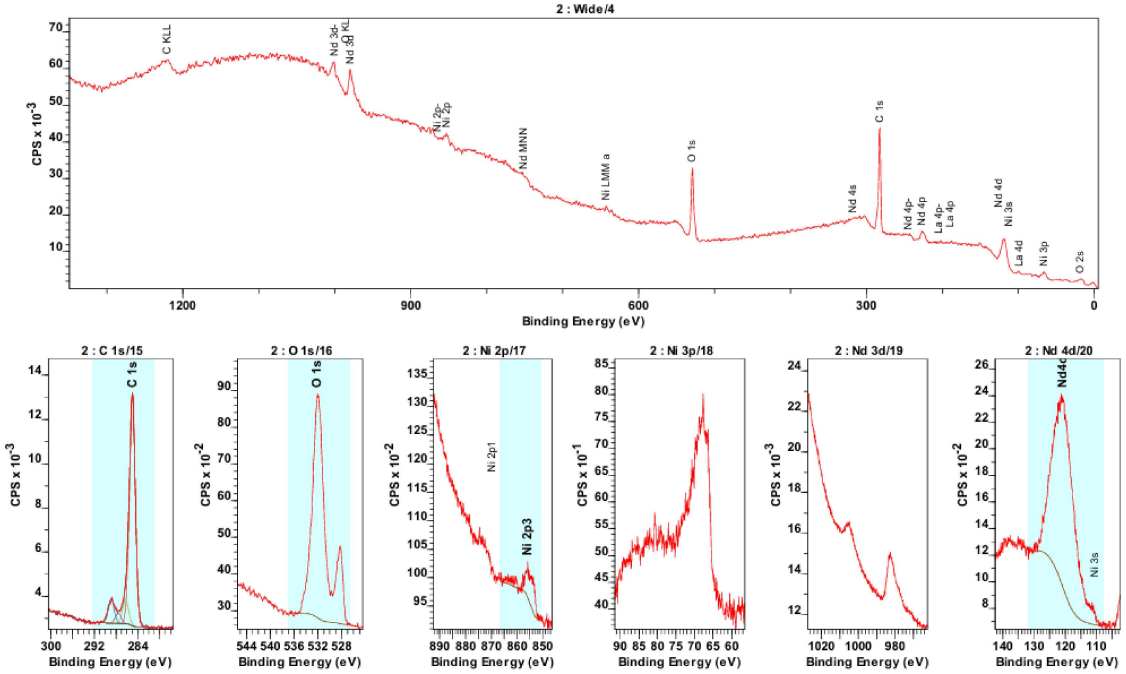


FIGURE 2.1: Survey XPS spectrum and several regions of interest for a thin film $NdNiO_3$ with $LaAlO_3$ as a substrate.

2.2.3 Scanning Transmission Electron Microscopy (STEM)

Scanning transmission electron microscopy (STEM) is a high-resolution imaging and analytical technique used to study structure and composition of materials at atomic scales. This technique consists on a beam of highly focused electrons shining through a sample and the transmitted beam is collected by a detector on the other side. Different types of detectors collect signals, including annular dark-field (ADF) and bright-field (BF) detectors for imaging, and electron energy loss spectroscopy (EELS) or energy-dispersive X-ray spectroscopy (EDS) detectors for elemental analysis. STEM technique requires extremely thin samples to allow electron transmission, hence a cross-sectional lamella of the sample was prepared by a dual-beam FEI Helios focused ion beam (FIB) following the standard lift-out procedure. Room temperature aberration corrected STEM (AC-STEM) and EDS studies were carried out with a double corrected FEI Titan G^3 Cubed Themis equipped with a Super-X EDX System, operated at 200 kV.

The STEM/EDS measurements and analysis are part of the collaboration with INL, Braga, Portugal, and were performed by Dr.Ihsan Çaha and Dr. Leonard Francis.

2.2.4 Raman scattering spectroscopy

Raman scattering is the inelastic scattering of light by a materials. This technique is used to probe excitations such as vibrational (phonons), magnetic and electronic. In this thesis, we will mainly explore the vibrational spectroscopic feature of the Raman effect which can provide insight on the symmetry and structural properties of materials.

The Raman setup used for room temperature and temperature-dependent measurements is a Renishaw inVia Qontor spectrometer, available at IFIMUP. Laser sources with different wavelengths can be used as incident monochromatic radiation, in this thesis a He-Ne laser for 633 nm and a diode-pumped laser for 532 nm were used. The incident radiation is linearly polarized. The Rayleigh line is removed with spectral cut-offs filters, depending on the laser source. The Raman spectra is measure in a back-scattering geometry, and it can be unpolarized or analysed with crossed and parallel polarization configurations (only possible for 532 nm laser). The diffraction gratings were 1800 lines/mm for the 633 nm and of 2400 lines/mm for the 532 nm. At room conditions, a lens 100x with NA of 0.85 was used, while for temperature-dependent measurements a lens of 50x with NA of 0.5. A schematic view of this setup is shown in Figure 2.2.

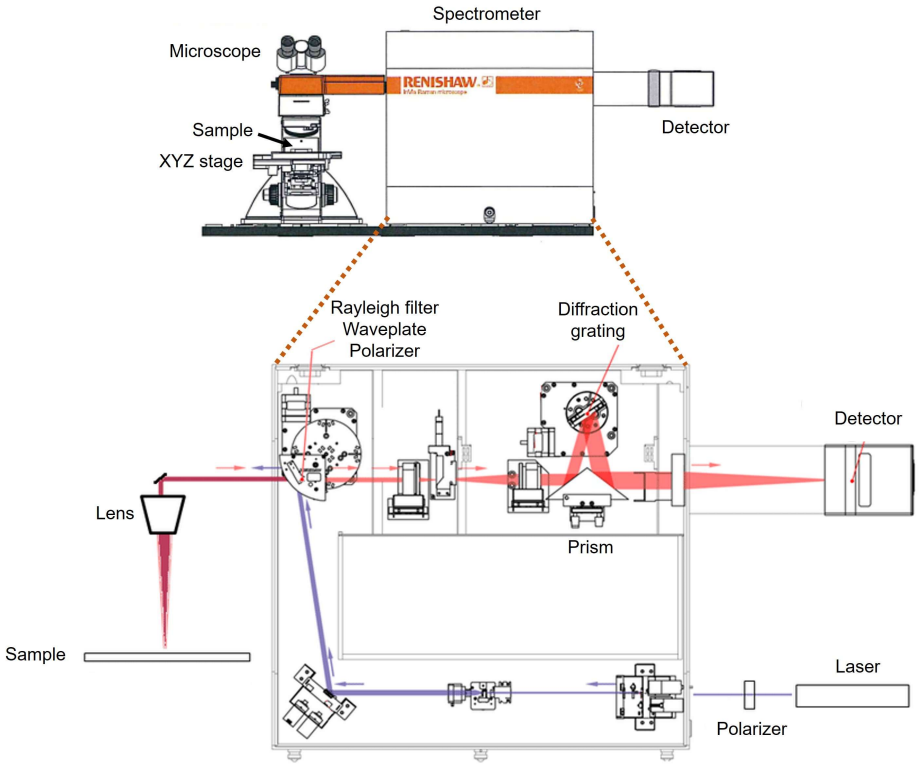


FIGURE 2.2: Schematic view of the Raman setup available at IFIMUP facilities.

For the temperature studies, the sample was placed in one of the two temperature controllers attached to the setup: a closed-cycle helium cryostat (ranging from 9 to 300 K) and/or in a Linkam THS600 stage (ranging from 80 to 900 K), with temperature stability of 0.2 K and 0.1 K, respectively.

For magnetic field-dependent unpolarized Raman measurements, a home-made experimental setup based on free beam propagation of optical excitation and collection was used. A long working distance objective of 50x with a numerical aperture NA = 0.35 was used to focus the excitation beam (λ = 515 nm) down to a spot size of 1 µm and to collect Raman scattering signal. The sample was placed on piezoelectric motors allowing for the laser focus. This set-up was inserted in a closed metallic tube filled with helium exchange gas, allowing temperature control, and then placed in the middle of superconducting solenoids that produce magnetic fields up to $|\boldsymbol{B}_{ext}| = \mu_0|\boldsymbol{H}_{ext}|$ = 14 T. The Raman scattering light was analysed by a grating spectrometer equipped with a LN2 cooled silicon Charge Coupled Device (CCD). To correct temperature uncertainties in the sample due to laser power, the temperature was afterwards determined according to the ratio between intensities of Stokes and anti-Stokes scattering peaks [92, 93]:

$$\frac{I_{Anti}}{I_{Stokes}} = \left(\frac{\nu_{laser} + \Delta\nu}{\nu_{laser} - \Delta\nu}\right)^4 e^{-\frac{hc\Delta\nu}{k_B T}} \tag{2.1}$$

where $\Delta\nu = \frac{\nu_{Anti} + \nu_{Sotkes}}{2}$ is the average wavenumber of Stokes and anti-Stokes scattering peaks.

These measurements were performed at Laboratoire National des Champs Magnétiques Intenses, CNRS, Grenoble, France, in collaboration with Dr.Dipankar Jana and Dr. Clément Faugeras.

The Raman spectra were analysed using the IgorPro software. A sum of damped harmonic oscillators was fitted to the experimental spectra accordingly to the following equation [93]:

$$I(\omega, T) = [1 + n(\omega, T)] \sum_{i=1}^{N} A_{0j} \frac{\omega \Omega_{0j}^2 \Gamma_{0j}^2}{(\Omega_{0j}^2 - \omega^2)^2 + \omega^2 \Gamma_{0j}^2} \tag{2.2}$$

where $I(\omega, T)$ is the intensity, $n(\omega, T)$ the Bose-Einstein factor, A_{0j}, Ω_{0j}, Γ_{0j} are the strength, wavenumber, and damping coefficient of the $j-th$ oscillator, respectively.

2.2.5 Fourier Transform Infrared spectroscopy (FTIR)

Lattice vibrations of materials, namely of solids, lie in the IR range of the electromagnetic spectrum. Fourier Transform Infrared spectroscopy is a technique used to probe polar phonons, that simultaneously detects a broadband signal and transforms it into a frequency-dependent spectrum. Taking advantage of a Michelson interferometer, which is based on the principle of creating interference patterns by changing the optical path difference of two interfering beams, the initial beam is split into two parts, with one of them being reflected by a moving mirror. The intensity signal originated from the two beams interference is associated with the optical path difference. After detection this signal is Fourier-transformed and a frequency-dependent spectrum is obtained. Using a combination of light sources, beam-splitters and detectors, one can chose to study the far-IR (FIR), mid-IR (MIR) or near-IR (NIR) range. In this thesis, most IR-phonons are in the FIR range, however the MIR range is necessary to obtain information regarding the high-frequency electronic contributions to permittivity.

The near-normal incidence IR reflectivity spectra are measured by a Fourier-transform IR spectrometer Bruker IFS 113v in the frequency range of 20 - 3000 cm^{-1} (0.6 – 90 THz) at room temperature. For the low-temperature measurements, the spectral range is reduced by the transparence of cryostat windows to 20 - 650 cm^{-1}. A pyroelectric deuterated triglycine sulfate detector is used for the room-temperature measurements, whereas a more sensitive He-cooled (operating temperature 1.6 K) Si bolometer is used as a detector for the low-temperature experiments. An Oxford Instruments Optistat optical cryostat with polyethylene windows is used for the low-temperature IR measurements down to 4 K.

Data analysis was performed in the WASF software. The IR spectra were fitted using a generalized-oscillator model with the factorized form of the complex permittivity assuming 4-parameter model [94]:

$$\epsilon(\omega) = \epsilon'(\omega) + i\epsilon''(\omega) = \epsilon_\infty \prod_j \frac{\omega_{LOj}^2 - \omega^2 + i\omega\gamma_{LOj}}{\omega_{TOj}^2 - \omega^2 + i\omega\gamma_{TOj}} \tag{2.3}$$

where ω_{TOj} and ω_{LOj} stand for transverse and longitudinal frequencies of the j-th polar phonon, respectively, and γ_{TOj} and γ_{LOj} are the corresponding damping constants [94]. The high-frequency permittivity, ϵ_∞, originating from electronic absorption processes, was obtained from the room-temperature frequency-independent reflectivity tail above the phonon

frequencies and was assumed temperature independent. The complex permittivity, $\epsilon(\omega)$, is related to the reflectivity, $R(\omega)$, by

$$R(\omega) = \left\| \frac{\sqrt{\epsilon(\omega)} - 1}{\sqrt{\epsilon(\omega)} + 1} \right\|^2 \tag{2.4}$$

These parameters were fitted so that the normal incidence reflectivity matches the experimental data.

FTIR measurements and analysis were done in collaboration with Dr. Veronica Goian and Dr. Stanislav Kamba, from the Institute of Physics of the Czech Academy of Sciences, Prague, Czechia.

2.2.6 Time-domain THz spectroscopy

THz time-domain spectroscopy (THz-TDS), or simply refereed as THz spectroscopy, makes use of optoelectronically generated electromagnetic transients and it is an important tool to probe low-frequencies excitation, such as magnons. The THz transients are produced by femtosecond (fs) laser pulses. In a typical THz-TDS setup, the train of laser pulses is sent to a beam splitter to follow two paths: one moving mirror serving as delay line, and the other one, going through the THz emitter, and subsequently to the sample. Finally, the two beams interfere at the detector, and thereby the THz signal is treated by the lock-in amplifier. After detection, the spectrum is calculated by Fourier-transform, passing to the frequency-domain. The spectral resolution in THz-TDS is defined by the inverse of the optical delay time. One fundamental feature of this experimental technique is the access to the phase of the propagated electromagnetic wave, avoiding the need for use of Kramers-Kronig relations for the evaluation of the complex dielectric function. This allowed to directly calculate the complex permittivity and subsequently the reflectivity.

Temperature-dependent THz-TDS measurements were performed in the transmission geometry with a custom-made time-domain THz spectrometer, with a spectral region of 5–50 cm^{-1}. A femtosecond Ti:sapphire laser oscillator (Coherent, Mira) produces a train of femtosecond optical pulses, which generate linearly polarized broadband THz pulses radiated by a photo-conducting switch TeraSED (Giga-Optics). A gated detection scheme based on electrooptic sampling with a 1 mm thick (110) ZnTe crystal as a sensor allows to measure the time profile of the electric field of the transmitted THz pulse. An Oxford

Instruments Optistat optical cryostat with mylar windows is used for the low-temperature THz measurements.

For measurements with external magnetic field, broadband terahertz pulses were generated and detected using commercial fiber-coupled photoconductive switches operating with a femtosecond optical fiber laser system (TeraSmart, Menlo Systems GmbH). The oriented samples were placed in an Oxford Instruments Spectromag He-bath cryostat with mylar windows and a superconducting coil, allowing measurements in a temperature range 2 – 300 K with an applied magnetic field in the range $|\boldsymbol{B}_{ext}| = \mu_0|\boldsymbol{H}_{ext}|$ = 0 - 7 T. The measurements used the Voigt geometry – external static magnetic field applied perpendicularly to the light propagation direction, and the Faraday geometry – external static magnetic field applied parallel to the light propagation direction.

THz-TDS measurements and analysis (PKGRaph software) were done in collaboration with Dr. Christelle Kadlec, Dr. Filip Kadlec and Dr. Stanislav Kamba, from the Institute of Physics of the Czech Academy of Sciences, Prague, Czechia.

2.2.7 Electric and magnetic properties

Electric resistivity

The electrical resistivity measurements were performed using the standard four-probe in-line technique, with a cooling/heating rate of 2 K/min in the temperature range 30–300 K (closed-cycle APD Cryogenics cryostat). A current was applied in the outer electrodes using the current source of a Keithley 617 electrometer and measured with a Tektronix DMM4040 Precision Multimeter. The voltage was measured in the inner electrodes with HP 34401A Precision Multimeter.

These measurements were carried out by PhD student Bruna Silva and Prof. Bernado Almeida, Department of Physics, University of Minho, Portugal.

Quantum Design Magnetic Properties Measurement System (MPMS)

This system offers the sensitivity of a SQUID (Superconducting Quantum Interference Device) magnetometer and provides multiple measurement modes, including DC, VSM, and AC susceptibility, achieving a sensitivity of $\leq 10^{-8}$ emu. The samples used were firmly attached to the MPMS insert, with temperature controlled by liquid helium flux and control magnetic field up to $\pm$ 7 T. Magnetization measurements, M(T), were performed

in the temperature range from 5 to 300 K, in zero-field-cooled (ZFC) and field-cooled conditions (FC), with an applied magnetic field of 100 Oe.

MPMS measurements were performed at IFIMUP, University of Porto.

Dynacool Quantum Design Physical Property Measurement System (PPMS)

Isothermal magnetic hysteresis loops measurements, M(H), were performed in the PPMS vibrating sample magnetometer under a sweeping magnetic field from 0 – 9 T, at fixed temperatures in the 4 – 300 K range.

AC magnetic susceptibility measurements, where also performed on the Quantum Design Dynacool-9T PPMS instrument with the ACMSII option, in selected fixed temperatures ranging from 2 to 300 K. A single-crystalline piece of $NdFeO_3$ of mass 0.04774 mg with a flat (010) face was used, with the crystal oriented either with the a- or c- axis aligned along the applied magnetic field. Data were collected while heating, after cooling the sample under an applied small DC magnetic field from room temperature down to 2 K. The driving AC magnetic field amplitude was 250 Oe and the frequency range was between 200 and 10 000 Hz. At each temperature a three-point measurement process that utilizes internal calibration coils was used in order to increase measurement accuracy.

This measurements were carried out by Dr.Rui Vilarinho in collaboration with Prof. José Paixão, Department of Physics, University of Coimbra, Portugal.

2.2.8 X-ray magnetic circular dichroism

X-ray Magnetic Circular Dichroism (XMCD) is a element-specific technique that uses the polarization properties of X-ray synchrotron radiation to probe microscopic magnetic properties. XMCD uses circular polarized photons with energy near the absorption edge, and it is simply the difference between left and right circularly polarized X-ray absorption spectrum (XMCD = XAS_{left}-XAS_{right}). One relevant feature of this technique comes from the fact that the magnetic absorption cross-section is proportional to the mean value of the macroscopic magnetization, ***M*** [95, 96], being widely used for the characterization of ferromagnetic materials or weak-ferromagnets. Another relevant feature is the element-specific nature of the technique that allows to isolate the magnetic contributions of different magnetic specimens in a material. Most prominent magnetic materials have elements inner core binding energies of $3d$, $4d$, $4f$, and $5d$ orbitals, therefore the photon

energies to probe these absorption edges are in the soft X-ray regime (200 eV - 2 keV) [97].

These experiments were done in total electron yield (TEY) mode, in a oriented single crystal of $NdFeO_3$, with c-axis out-of-plane. The X-ray photon energy ranged between 950 - 1040 eV to probe $M_{4,5}$ edges($3d \rightarrow 4f$ transition) of Nd. XMCD spectra were obtained at several fixed temperatures and during the measurements a magnetic field of 3 T was applied parallel to the c-axis and to the X-ray propagation direction, to ensure saturation of the magnetic moments.

XMCD experiments were performed at DEIMOS beamline from SOLEIL synchrotron, Gif-sur-Yvette, France, under the supervision of beamline scientist Dr. Fadi Choueikani.

2.2.9 Resonant ultrasound spectroscopy (RUS)

Resonant ultrasound spectroscopy (RUS) is an experimental technique used to determine elastic properties of materials by analysing their natural vibrational frequencies [98]. Elastic properties are particularly sensitive to structural changes due to external conditions such as temperature, pressure, electric or magnetic fields. Solid-to-solid structural phase transitions or even other transition types in materials with some degree of elastic coupling, such as magnetoelastic coupling, imply modifications on the elastic constants and therefore can be probed by RUS technique. The setup involves the measurement of acoustic resonances of mm-sized samples held lightly between two piezoelectric transducers. One transducer generates mechanical vibrations, typically in the frequency range 100 kHz – 2 MHz, and the second one acts as a detector. The resonance frequency depends on the shape, density and elastic moduli of the sample. Shape of the sample usually remains unchanged and changes in the density are considered small and continuously following the thermal expansion. Hence, the evolution of resonance frequencies due to varying external parameters can be considered direct measurements of effective elastic constant. Usually, this effective elastic constant involves a linear combination of all the elastic constants of the material.

Data treatment involves the fitting of individual peaks in the primary spectra with an asymmetric Lorentzian function assuming a driven harmonic oscillator [98]:

$$y(f) = y_0 + \frac{A}{(f - f_0)^2 + B} \tag{2.5}$$

where y_0 defines the baseline, f_0 the resonance frequency and A, B are constants defining the Lorentzian shape. The asymmetric Lorentzian implies different $\frac{A}{B}$ ratios for $f > f_0$ and $f < f_0$. From the fitting analysis, two quantities can be extracted: f_0^2 which is proportional to the elastic constant to the corresponding acoustic mode and $\Delta f = \sqrt{B}$ which is the full width half maximum (FWHM) that is related to the acoustic loss, being expressed in terms of the inverse mechanical quality factor $Q^{-1} = \frac{\Delta f}{f_0}$. Anomalies in both factors f_0^2 and Q^{-1} are indication of a coupling mechanisms between mechanical strain and a physical phenomenon [98].

For the low temperatures measurements, the sample sits directly between the transducers and the holder is lowered into a helium cryostat. Few mbars of helium are added to the sample chamber to assist thermal equilibrium between sample and cryostat.

The RUS measurements were performed by Dr. Rui Vilarinho and Prof. Joaquim Agostinho Moreira in collaboration with Prof. Michael Carpenter, Earth Science Department, University of Cambridge, UK.

2.2.10 Muon-spin rotation spectroscopy (μSR)

Muon-spin rotation spectroscopy (μSR) is a technique that exploits the magnetic interaction of muon spins implanted on the sample with the surrounding environment and hence allows the characterization of properties on the implanted spot. This technique uses spin-polarized muons, with spins aligned in a known direction, that are implanted in the sample. If there is a magnetic field at the point where a muon stops in a material, then the muon spin will undergo a Larmor precession around the direction of the local field [99]. Muons are radioactive particles with a mean life-time of 2.2 μs and when a muon decays, a positron (e^+) and two neutrinos (ν) are emitted:

$$\mu^+ \longrightarrow e^+ + \bar{\nu}_\mu + \mu_e \tag{2.6}$$

Due to the muon precession, after its decay, positrons are not isotropically emitted, instead they are emitted preferentially along the direction of the muon spin at the moment of decay. Each muon decays at a different time giving rise to a positron whose detection contributes to a data point at a particular time *t*. The muon spectrometer consists in an array of positron detectors placed around the sample to measure the time evolution of the muon spin polarization, which gives information on the local magnetic field.

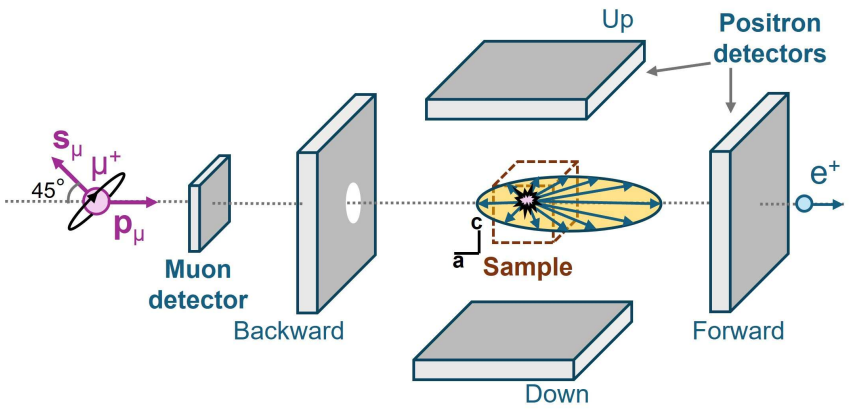


FIGURE 2.3: Scheme of μSR setup used in the GPS beamline.

The muon polarization, $P(t)$, can be extracted from the asymmetry between a pair of positron detectors, $A(t) \propto P(t)$. Positron detectors of Figure2.3 are divided into two pairs: Forward-Backward (FB) and Up-Down (UP). Assuming the simplest case, only one pair of detectors, as Figure 2.4 illustrates, the asymmetry is a function of the positron counter, $N_{F,B}$, of the detector pair and can be written as [99]:

$$A(t) = \frac{N_F(t) - \alpha N_B(t)}{N_F(t) + \alpha N_B(t)} \tag{2.7}$$

with α being a experimental balancing factor between the two detectors. Figure 2.4(b) demonstrates how the local field direction at the muon stopping site affects the asymmetry function.

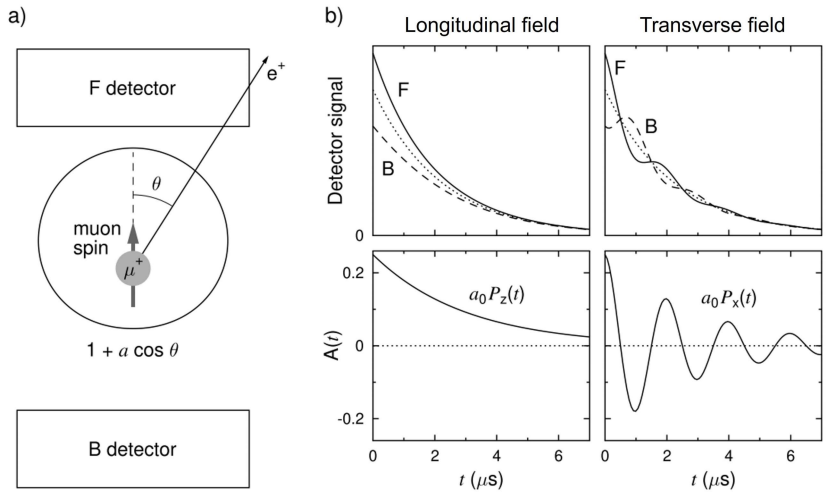


FIGURE 2.4: (a) Angular probability of a positron emission, in a simple scheme with one pair of detectors: forward (F) and backward (B). (b) Time evolution of F and B signals, i.e. positron counter, and asymmetry functions for two cases: longitudinal and transverse fields - local field at the muon stopping site is either longitudinal or transverse with respect to initial direction of muon spin. Adapted from [99].

An oriented $NdFeO_3$ single crystal with a-axis out-of-plane was placed in the cryostat, in a way that the propagation of the muon beam was parallel to the a-axis (see Figure 2.3). Muons with 100% spin polarization and a kinetic energy of 4 MeV were implanted in the crystal, with the spin polarization making 45° with a-axis. Zero-field measurements were undertaken at the GPS instrument at fixed temperatures between 4 and 200 K.

The time evolution of the muon spin polarization was determined from the asymmetry of the decay positrons and analysed with the MUSRFIT software [100]. At each recorded temperature, time-dependent total asymmetry of each detector pair (FB and UD) was fitted using a combination of oscillatory (i), non-oscillatory ($nosc$) and background (bgr) components given by the Equation 6.2, that will be presented and analysed in Chapter 6.

The μSR spectroscopy measurements were performed at GPS beamline of the Swiss Muon Source (SμS),Paul Scherrer Institute (PSI), Villigen, Switzerland, under the supervision of beamline scientist Dr. Hubertus Luetkens.

2.2.11 Magneto-optical microscopy

Magneto-optical microscopy taking advantaged of the Faraday effect allows the direct visualization of magnetic domains in materials that possess a net magnetization. This technique is available at FELIX -Free Electron Lasers for Infrared Experiments- laboratory, Radboud University, Nijmegen, Netherlands. The measurements were performed under the supervision of Dr. Carl Davies and Prof. Andrei Kirilyuk.

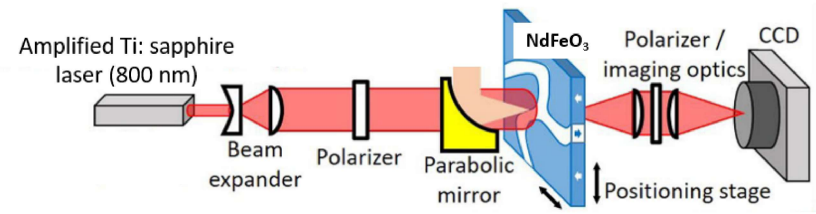


FIGURE 2.5: Schematic illustration of the experimental setup of user-station 3 of FELIX. Adapted from [101].

A thin section of the $NdFeO_3$ crystal was prepared with 100 μm thickness and cut perpendicularly to the c-axis (ab-plane). The sample was mounted in a He-flow cryostat. The femtosecond laser pulses delivered by the amplified Ti:sapphire laser (800 nm) in user-station 3 of FELIX provided illumination. The light transmitted through the sample

is gathered by an objective lens, filtered by an analyser and imaged using a CCD camera. Through the magneto-optical Faraday effect, the axis of the linearly polarized light rotates in opposite directions depending on whether the magnetization points parallel or anti-parallel to the sample normal. The filtering by the analyser therefore visualizes the two different equilibrium magnetic domains as light or dark regions.

3. Structural percolation across MIT in $NdNiO_3$

Rare-earth nickelates, $RNiO_3$ (R = Pr–Lu), are quantum materials that exhibit strong correlations between lattice, spin and charge/orbital degrees of freedom, enabling the control of phase transitions and property tailoring [6, 22]. They still stimulate research in order to fully understand the interplay between electronic, structural, and magnetic order parameters underlying their metal-to-insulator transition (MIT). Among them, $NdNiO_3$ stands out because it lies at the border of a region of interest in the phase diagram where the MIT and Néel transition dissociate by further increasing the octahedra rotation angle [6, 22]. For the case of $NdNiO_3$, the amplitude of these rotations is insufficient to stabilize the oxygen-breathing distortion B_{OC}, responsible for the MIT [28]. E'-type AFM ordering helps to promote the occurrence of the MIT, and therefore, $T_N = T_{IM}$ [6, 28, 30, 32, 37, 102]. Due to the first-order nature of the electronic transition, there is a formation/growth of nanoscale insulating domains in the metallic matrix, typical of electronic percolative processes across the MIT [36, 45–48]. The structural symmetry of metallic and insulating phases has been assigned to orthorhombic and monoclinic symmetries, respectively, by synchrotron x-ray diffraction experiments [26]. However, those experiments were limited to temperatures outside the MIT temperature range [26]. The coexistence of structural phases during the MIT was ascertained through temperature dependent Raman scattering spectroscopy [27, 103, 104], but only in heating ramps and the correlation between electronic and structural percolative effects is yet to be done.

The main objective of this Chapter is to fill this gap, through a single study of the electronic, magnetic, and structural phase sequence, in a wide temperature range encompassing the phase coexistence and hysteresis. The study was performed in a high quality $NdNiO_3$ thin film deposited onto [001]-oriented $LaAlO_3$ substrate by MOCVD deposition technique. To this end, we report the results obtained from temperature dependent resistivity, magnetization, and Raman scattering measurements towards characterizing that phase sequence

and disentangling the actual correlation between those phases. A redefinition of the transition temperature limits of both electronic and structural transformations is given. Structural analysis and volume phase fractions are then presented and discussed to correlate electronic and structural processes, contributing to a more general insight into percolative phenomena in $NdNiO_3$ thin films. The results are published in *Physical Review B* [49].

3.1. Morphological, chemical, and structural characterization

The $NdNiO_3$ thin film exhibits a smooth and defect-free surface, as can be observed in the SEM image shown in Figure 3.1(a). From the cross-section image, shown in Figure 3.1(b), we conclude that the film exhibits a high degree of homogeneity and excellent adhesion to the substrate, as no internal defects or granular structure were detected.

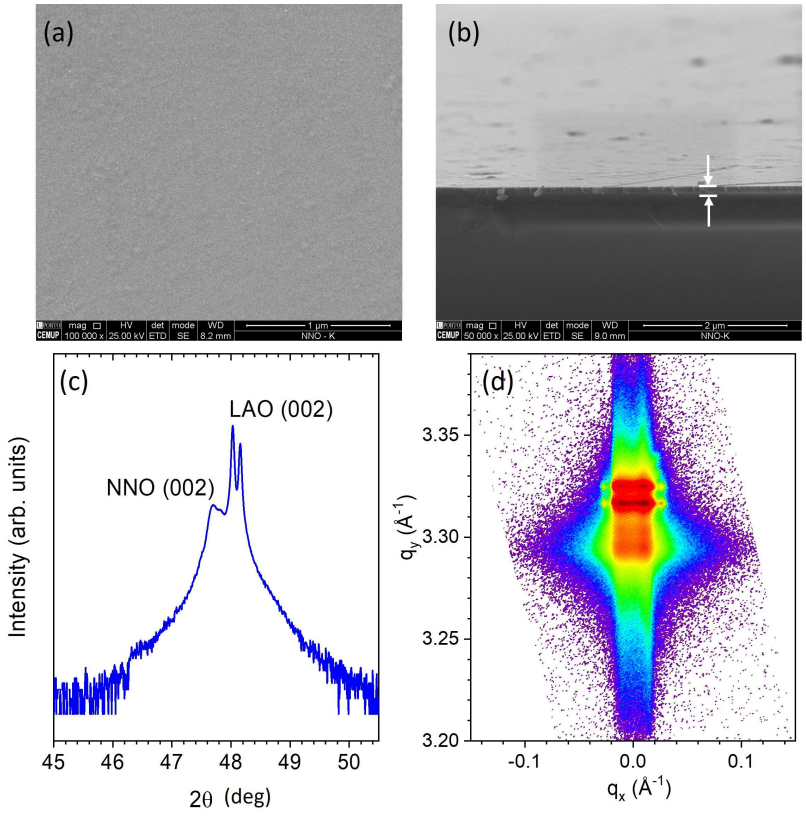


FIGURE 3.1: Representative SEM images of NNO thin film onto [001]-LAO substrate: (a) surface image and (b) respective cross-section view, with 1 and 2 µm as a scale, respectively. (c) XRD pattern of the NNO/LAO film. (d) Reciprocal space map around the $(002)_{pc}$ diffraction peak of LAO substrate of the NNO/LAO film.

The preferential growth direction of the NNO thin film is ascertained by the superposition of both NNO and LAO pseudocubic (002) diffraction peaks. To better enhance the visualization of NNO film peak, otherwise overshadowed by the $(002)_{pc}$ LAO substrate

peak, the XRD pattern of Figure 3.1(c) was recorded with a tilt offset of 0.25° applied to the Bragg-Brentano condition. The NNO film preferential growth orientation is along the c-axis, perpendicular to the substrate, as confirmed from the analysis of the reciprocal space maps (RSMs) around the pseudocubic (002) diffraction peak of the LAO substrate, shown in Figure 3.1(d). The estimated c parameter is 7.627 ± 0.004 Åis in good agreement with the reported values for thin films deposited on the same substrate [36, 105, 106]. No secondary phases were found from the XRD pattern.

The electronic transition temperature is influenced by the amount of oxygen deficiency in $NdNiO_{3-\delta}$ samples, and can even be suppressed in heavily oxygen deficient samples [34, 48]. Nonetheless, the transition temperature is kept almost constant for $\delta < 0.2$ [34]. Hence, it is important to determine the Ni oxidation state of the thin film, with which it is possible to estimate the oxygen vacancies from Ni^{2+} and Ni^{3+} percentage, by XPS analysis. Figure 3.2 shows the XPS signal corresponding to the region of Ni^{3+} Ni^{2+} $2p^{3/2}$ peaks, ranging from 848 to 868 eV. The binding energies peaks at around 853 and 855 eV are assigned to Ni^{2+} $2p^{3/2}$ and Ni^{3+} $2p^{3/2}$, respectively, while the ones in the 860 - 863 eV range are assigned to satellites peaks [107].

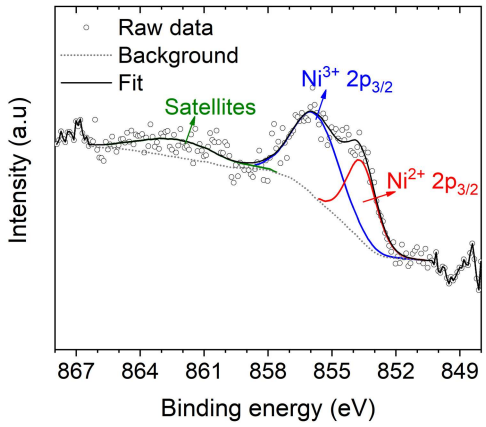


FIGURE 3.2: XPS signal recorded in the 848 – 868 eV energy range of NNO/LAO film. Ni^{3+} and Ni^{3+} $2p^{3/2}$ peaks are observed. The solid lines were determined from the best fit of a mix of Gaussian and Lorentzian functions, while the dashed line accounts for the background was simulated with the Shirley function.

From the XPS analysis, the corresponding areas of Ni^{2+} and Ni^{3+} $2p^{3/2}$ peaks were determined (see Table 3.1) and the calculated ratio $\frac{Ni^{2+}}{Ni^{3+}}$ is 0.62. This ratio has to be consider an approximation, as the accurate determination of $\frac{Ni^{2+}}{Ni^{3+}}$ is prevented by experimental uncertainty of the XPS equipment and the difficulties in fitting procedure. Furthermore, the oxidation state of Nd could not be verified due to binding energy superposition of its $3d$ and

$4f$ orbitals with the Ni $3s$. Similar difficulties have already been reported by other authors [38, 108]. From the calculated percentage of Ni oxidation state in the sample, oxygen vacancy is approximately δ = 0.19, assuming the general formula $Nd^{3+}Ni^{3+}_{1-x}Ni^{2+}_{x}O^{2-}_{3-\delta}$.

TABLE 3.1: Results from the XPS analysis, namely the percentage of Ni^{2+} and Ni^{3+} of the sample is calculated based on the peak areas, from which the oxygen vacancy is estimated.

	Position (eV)	**Area (a.u.)**	**Percentage**	δ
Ni^{3+}	855.7	1358	62 %	0.19
Ni^{2+}	853.6	841	38 %	

3.1.1 STEM

As a complement to the structural analysis of the film already described, the atomic-scale structural analysis was carried out by scanning transmission electron microscopy (STEM). A cross-sectional lamella of the sample was prepared by a focused ion beam (FIB), and the film was studied by atomic resolution STEM imaging and STEM-EDS (energy dispersive x-ray analysis). The high-angle annular dark-field (HAADF) STEM images shown in Figures 3.3(a) and 3.3(b) confirm cube-on-cube growth of 85.45 ± 0.01 nm thick NNO film on a [001]-LAO substrate, with a flat, atomically sharp interface. The NNO film is continuous, and no structural defects or dislocations were observed. The interfacial chemical sharpness was investigated by EDS in the STEM mode. Figure 3.3(c) depicts the EDS maps, disclosing the spatial distribution of Nd (green), Ni (yellow), La (red), and Al (violet) elements from the NNO thin film, and from the LAO substrate. EDS images confirm the interface sharpness without atomic inter diffusion, and with a uniform distribution of Ni and Nd in the NNO film. The strain state of the film was determined by geometrical phase analysis (GPA) of the HAADF images (see Figures 3.3(d) and 3.3(e)). The deformation of the in-plane component of the strain tensor ε_{xx}, shown in Figure 3.3(d), is virtually zero, confirming the good in-plane match between film and substrate. While the in-plane pseudocubic lattice parameter a_{pc} of the NNO film keeps a nearly constant value of 3.818 Å(see Figure 3.3(f)), the out-of-plane pseudocubic c_{pc} parameter shows a strong variation in the deeper atomic layers of the film, decreasing almost 7.5% in the first 15 atomic layers, and relaxes to 3.80 Å as the atomic layer moves away from the interface. The deformation of the out-of-plane component of the strain tensor ε_{yy}, depicted in Figure 3.3(e), provides evidence for a uniform deformation of the atomic planes parallel to the interface

as it is ascertained by the fringes parallelly aligned with the substrate/film interface. The film exhibits small regions with Ruddlesden-Popper faults (see Figure 3.4), often reported in rare-earth nickelates [38]. Although the Ruddlesden-Popper faults decrease the resistance in the insulating phase and show increase in resistivity on the metallic state, they do not preclude the presence of hysteresis at the MIT or the linear temperature dependence of resistivity in the metallic phase [38]. Such phases were also reported in previous studies, concluding that they do not affect the physical properties of the NNO [38]. Moreover, the concentration of Ruddlesden-Popper faults in the NNO sample here studied is below the detection limit of the Raman spectroscopy and XRD techniques. So, the presence of such defects will not hamper the main outcomes of this work.

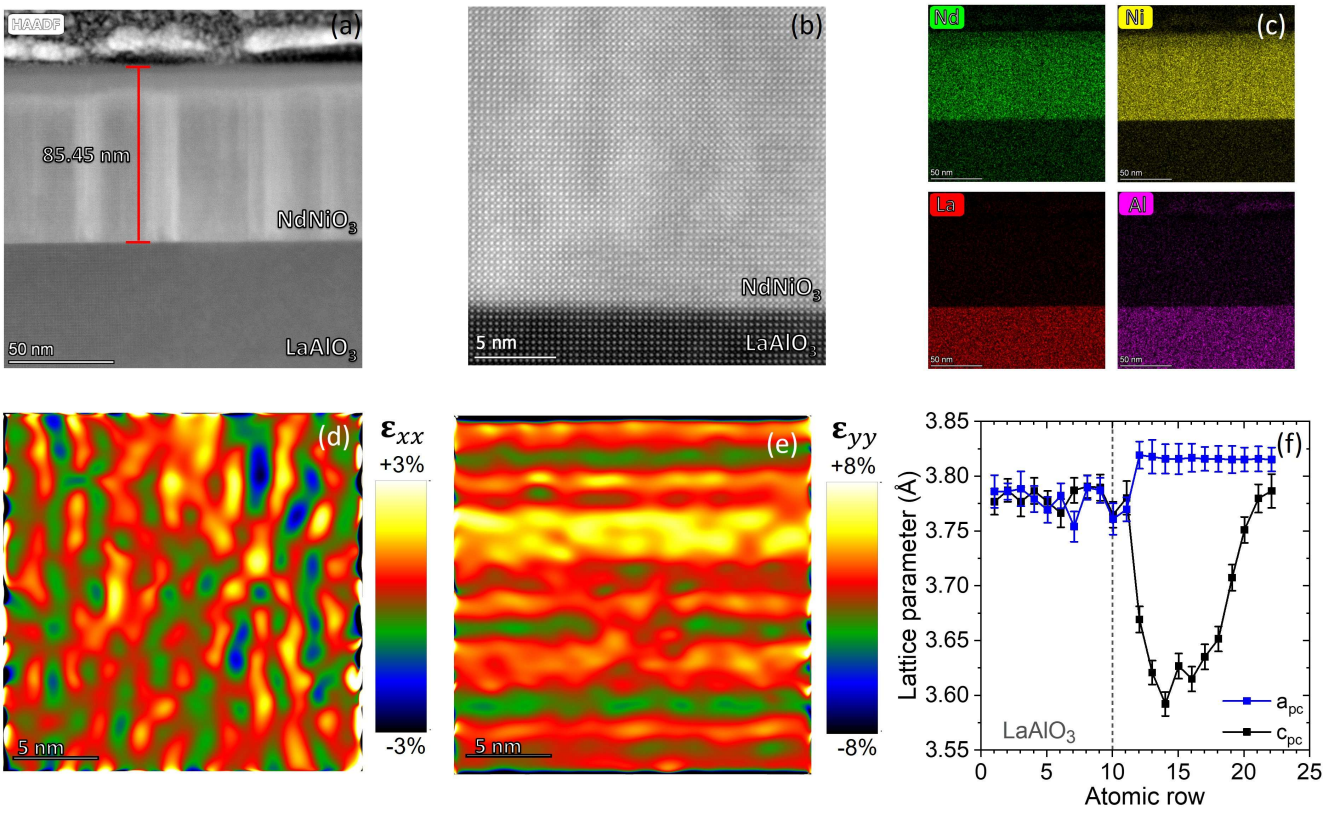


FIGURE 3.3: (a) Low magnification cross-sectional HAADF-STEM image of NNO film grown on (001)-LAO substrate. (b) Atomic resolution HAADF-STEM image of the same sample. (c) Elemental distribution maps obtained from the STEM image shown in (a). The (d) in-plane ε_{xx} and (e) out-of-plane ε_{yy} components of the strain tensor were obtained from the STEM image shown in (b) by geometrical phase analysis (GPA). (f) Pseudocubic lattice parameters of the NNO film as a function of the interface distance.

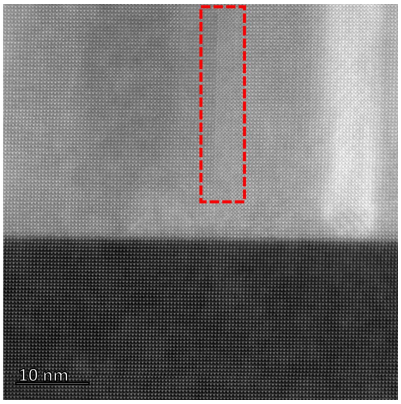


FIGURE 3.4: Atomic resolution HAADF- STEM image of film, with a red rectangle marking a small region with Ruddlesden-Popper faults.

3.2. Metal-to-insulator phase transition

The electronic phase transition was probed by measuring electric resistivity as a function of temperature on the NNO film, in cooling and heating runs, as presented in Figure 3.5.

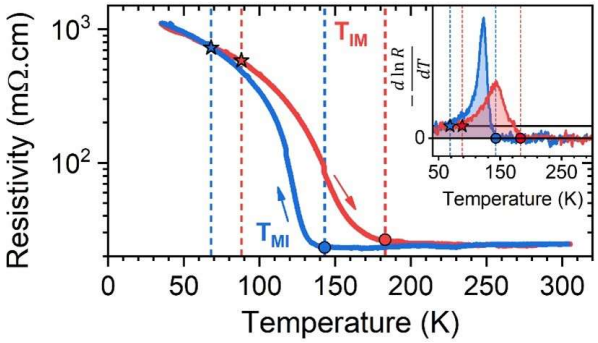


FIGURE 3.5: Temperature dependence of the resistivity of the film measured in cooling and heating runs, where T_{MI}= 143 ± 1K (blue dot) and T_{IM} = 183 ± 1K (red dot) are indicated as extracted from inset $-\frac{dln(R)}{dT}(T)$ upper limit of peak maximum. The lower limit of peak maximum defines the temperature below which the film is purely insulator, 68 ± 2K (blue star) and 88 ± 2K (red star) for cooling and heating run, respectively.

Qualitatively, the sample exhibits a typical resistivity curve of NNO, with a variation of 2 orders of magnitude and a thermal hysteresis between heating and cooling runs[38, 44, 45, 109]. The resistivity hysteretic thermal behavior comes from the coexistence of metallic and insulating states [36, 45, 48].

Due to electronic states coexistence, the critical temperature has to be considered as a local property [45–47]. Yet, it is still common to define a macroscopic temperature for the MIT. Following the discussion and methodology presented in Chapter 1, the upper and lower limits of MIT must be defined, as they differentiate pure electronic regime from a

mixing of two electronic regimes. The upper temperature limit is defined by temperatures T_{MI} and T_{IM}, for cooling and heating runs, respectively. These temperatures were directly obtained from the inset of Figure 3.5 and are identified by circles. Note that $T_{MI} < T_{IM}$, as expected [45]. The lower temperature limits were also determined and are identified by stars. Thus, the electronic transition occurs from 143 ± 1 K to 68 ± 2 K on cooling, and from 88 ± 2 K to 183 ± 1 K on heating. The electronic states coexist in a temperature span of 75 K on cooling and 95 K on heating, with a 40 K difference between upper limits and 20 K between lower limits, emphasizing the first-order nature of this transition.

3.3. Magnetic phase transition

Following the literature, in NNO samples, the magnetic phase transition, from paramagnetic to antiferromagnetic E-type phase, is simultaneous with MIT, therefore assuming heating runs T_N=T_{IM} [22, 26, 28, 40].

The temperature dependence of the sample magnetization was measured in a heating run, with an applied field of 100 Oe, after cooling with the same field and it is shown in Figure 3.6(a). The low magnetic moment of NNO combined with the diamagnetism response of the LAO substrate, results in a low total magnetization value, in comparison with the one reported for a ceramic [110].

Inset of Figure 3.6(b) shows the applied magnetic field strength divided by the magnetization $\frac{H}{M} \propto \frac{1}{\chi}$, whose anomalous temperature evolution is better ascertained by the residuals plot. These residuals correspond to the difference between $\frac{1}{\chi}$ data and linear fit (red curve) assuming a Curie-Weiss model (paramagnetic contribution), which was then extrapolated to low temperatures. The magnetic phase transition is marked by a clear temperature anomalous behaviour of the $\frac{1}{\chi}$ plot, and also by the deviation of residuals from zero, as expected, at a temperature that coincides with the upper temperature limit of the MIT (T_{IM} = 183 ± 1 K), within an experimental error of ± 6 K (blue area in Figure 3.6(b)). The anomaly observed in both Figure 3.6(a)-(b) at around 50 K is associated with oxygen contamination of the SQUID magnetometer chamber.

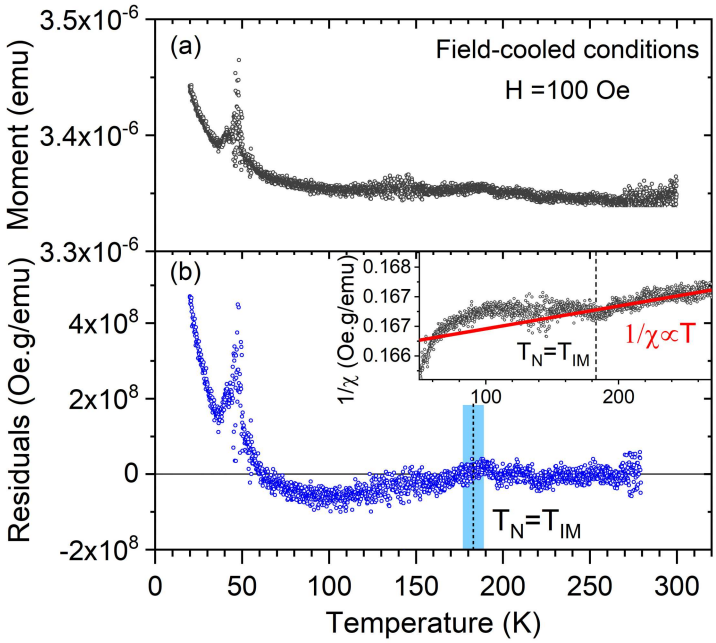


FIGURE 3.6: Temperature dependence of (a) magnetic moment measured in heating, using an applied magnetic field of 100 Oe in field cooling conditions. (b) Residuals ($\frac{H}{M} \propto \frac{1}{\chi}$ data minus Curie-Weiss predicted trend) with inset showing the inverse of susceptibility as a function of temperature. Dashed line marked the T_{IM} obtained from heating run, coinciding with $T_N \pm 6$ K (shaded region).

3.4. Structural phase transition

The unpolarized Raman spectra of the film, in the 100–600 cm^{-1} spectral range, are presented in Figures 3.7, recorded at different fixed temperatures in heating and cooling runs. The room temperature Raman signature of the film exhibits typical spectral profile consistent with the P*bnm* symmetry for NNO, as reported elsewhere [27, 42, 110]. Note that bands observed at 123 and 152 cm^{-1} (room temperature values) are assigned to LAO substrate modes [111]. The results here presented are in excellent agreement with the ones already published for NNO films deposited onto [001]-LAO substrate, confirming the good structural quality of the sample [27, 41]. Moreover, no hints of secondary phases could be detected by a Raman scanning procedure over the sample surface. Regardless of the measurement direction, the Raman signature at the temperature extremes is reproducible, for example, the spectra measured at 70 K during both heating and cooling are similar.

The structural analysis will focus on the heating results at 280-340 cm^{-1} range, shown in Figure 3.8 (a). The band observed at 305 cm^{-1} is characteristic of the orthorhombic phase (hereafter designated by O-band). This band is assigned to a rotation (along the

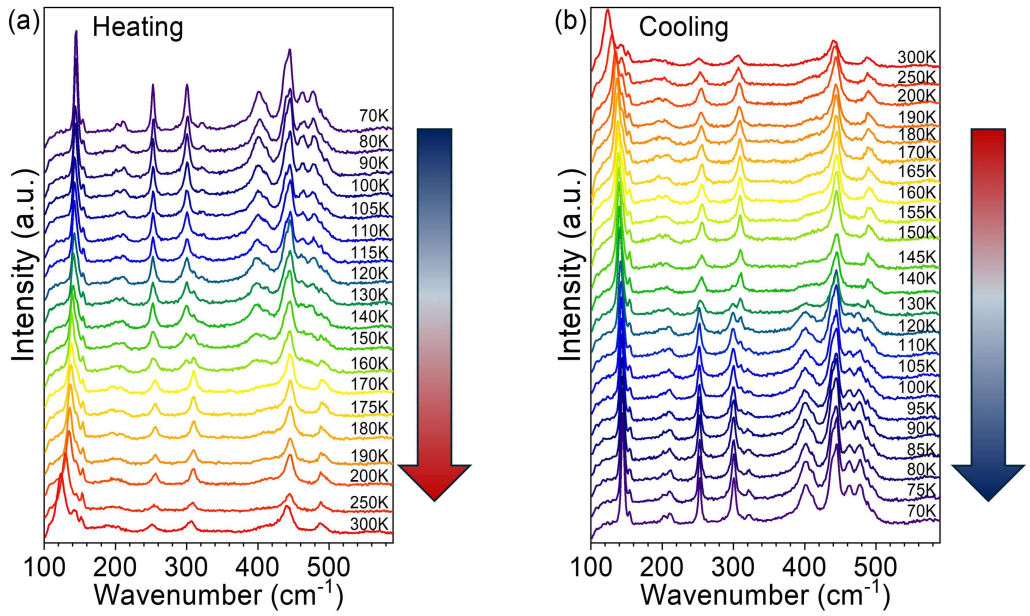
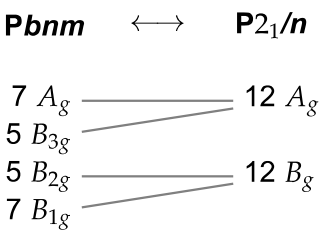


FIGURE 3.7: Temperature dependence of the unpolarized Raman spectra measured in (a) heating and (b) cooling runs, in the full spectral range.

$[110]_{pc}$ direction) of the oxygen octahedra, also referenced as R_{xy} mode [112]. The Raman signature recorded at 70 K is typically found for the monoclinic phase, as it is ascertained by the bands located at 300 and 321 cm^{-1} (hereafter designated by M-bands). The M-band located at 300 cm^{-1} is assigned to the symmetry breaking octahedra breathing mode, B_{OC} [112].

The symmetry changes associated with the structural phase transition are ascertained by the appearance/disappearance of bands on the temperature dependent Raman spectra (Figure3.8 (a)) and Raman modes wavenumber (Figure3.8 (b)), specifically visible in the 280–340 cm^{-1} range. These changes along with others in the 350–550 cm^{-1} range (Figure 3.7) are identified as the fingerprint of the structural transition from P$2_1/n$ to P*bnm* symmetry [27, 42, 103, 113]. Note that, in Figure 3.7(a), the disappearance of two M-bands and consequent substitution by the O-band cannot be ascribed to a splitting, as the modes are all non-degenerated [42, 114]:



On heating, the O-band only starts to be observed at 110 K and its intensity increases

up to 180 K, while the M-bands intensity consistently decreases until they disappear at 180 K, as shown in Figure 3.8 (a). For sake of consistence with the electronic transition analysis, for the structural case, two critical transition temperatures are also marked (limits of yellow region in Figures 3.8): lower temperature limit when O-band appears and upper temperature limit (T_S) when M-bands disappear.

The softening of the modes wavenumbers with increasing temperature, presented in 3.8 (b), follows the expected thermal expansion behaviour [115].

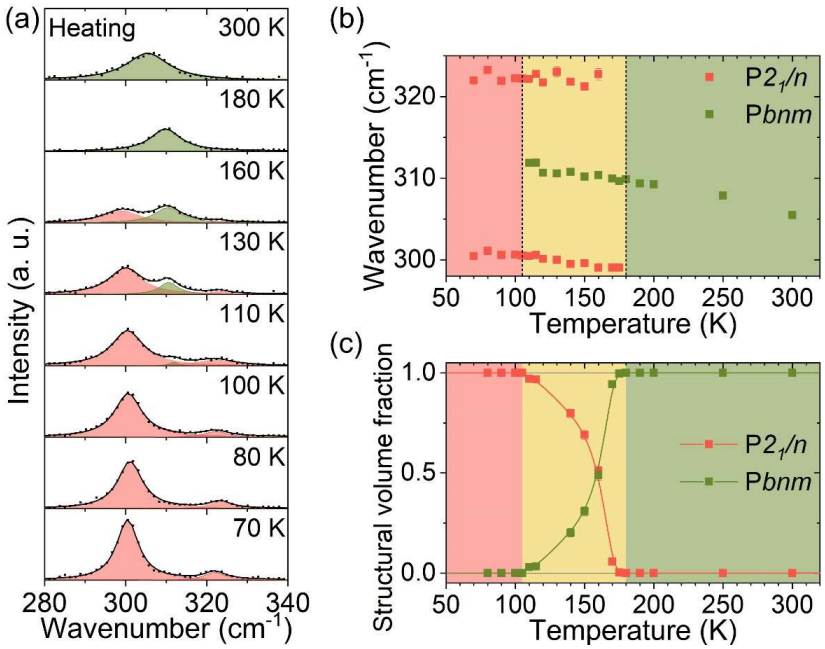


FIGURE 3.8: (a) Representative unpolarized Raman spectra of the NNO film, measured in heating run, along with the result of the spectral deconvolution. Spectral components of P$2_1/n$ phase are represented in pink and of P*bnm* phase in green. Temperature dependence of (b) wavenumber and (c) structural volume fraction, i.e., normalized intensity of the Raman modes observed in the 280 to 340 cm^{-1} range. M-modes: 300 + 321 cm^{-1} (the P$2_1/n$ monoclinic phase) and O-mode: 305 cm^{-1} (P*bnm* orthorhombic phase). Dashed lines represent the structural transition temperatures, above which the Raman bands associated with the monoclinic phase disappear. Shaded regions represent: P*bnm* phase in green, the coexistence the two structural phases in yellow and P$2_1/n$ phase in pink.

The same behaviour was also found in other Raman spectroscopy experiments on NNO single crystals, with the coexistence of orthorhombic and monoclinic bands between 138 and 174 K [103]. The oxygen octahedra breathing mode (M-band at 300 cm^{-1}) has been ascribed to the Ni-O bond length disproportionation and, consequently, to two different oxygen octahedra cages. Its disappearance with increasing temperature shows evidence for a higher symmetry where all oxygen octahedra have the same size, hence, are symmetrically equivalent [28]. The M-bands disappearance is also observed in the 350–550 cm^{-1} range (Figure 3.7). In this spectral range, below 180 K, the disappearance

of the bands at 400, 460, and 475 cm^{-1} is very likely associated with the $P2_1/n$ symmetry, showing clear evidence for structural changes in the sample at this temperature. There is a 75 K temperature interval in which the O-bands and M-bands are simultaneously observed, evidencing a coexistence of the orthorhombic and monoclinic structural phases.

An analogous analysis is presented for cooling results in the Appendix section A.3. The Raman transformations described above are fully reversible on cooling, in such a way that the signatures of the orthorhombic profile are already observed at 80 K and are fully recovered above 160 K (= T_S), as it can be observed in Figure A.4(a)-(c) of Appendix section A.3. Comparing cooling and heating runs, there is a 20 K hysteresis for the upper temperature limit T_S.

From the integrated intensity of the deconvoluted Raman M- and O-bands, the corresponding structural volume ratio could be determined and its evolution with temperature is shown in Figure 3.8 (c). The monoclinic volume fraction was calculated from sum of intensities of the M-bands at 300 and at 321 cm^{-1}, normalized to the total intensity in the 280–340 cm^{-1} spectral range. The same procedure was used to calculate the orthorhombic volume fraction, in this case taking into account the intensity of the 305 cm^{-1} band, normalized to the total intensity. A similar analysis for the cooling run is shown in Figure A.4 (c) of Appendix section A.3.

3.5. Discussion

Based on the experimental results, combined diagrams including the temperature dependence of the resistivity curve and the structural volume fractions are presented in Figures 3.9 (a) and 3.9(b), for heating and cooling runs, respectively. These diagrams evidence the electronic and structural phase coexistence temperature intervals and help us to understand the correlation between charge-lattice orders in NNO.

The pure insulating antiferromagnetic phase with the monoclinic symmetry is found from 35 K up to 88 K, on the heating run, see Figure 3.9(a). On further heating, the coexistence of metallic and insulating phases occurs, conveyed by the light-pink region. Interestingly, from a structural point of view, a purely monoclinic symmetry is kept up to 105 K. This means that between 88 - 105 K, the NNO film keeps the monoclinic symmetry while already exhibiting insulating/metallic phase coexistence, i.e., there are hints for electronic percolation while there is no structural percolation. The antiferromagnetic order

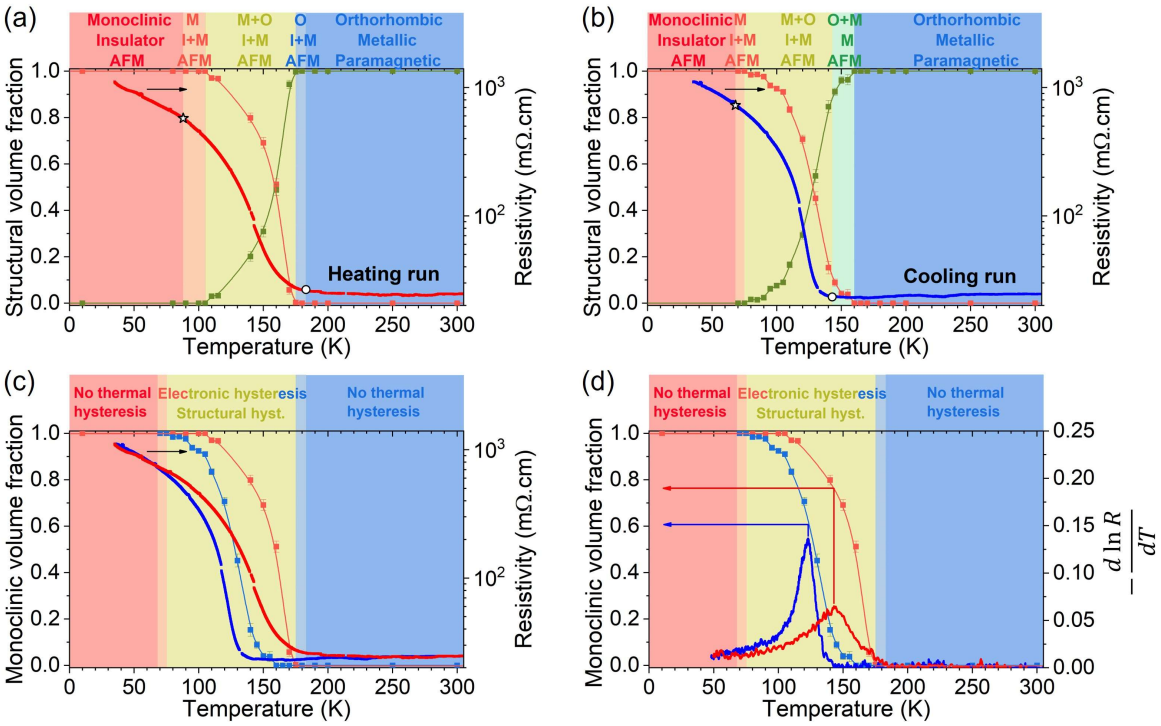


FIGURE 3.9: Diagram of structural and electronic phases as a function of temperature on (a) heating run and (b) cooling run. Upper caption: M = monoclinic, O = orthorhombic. Middle caption: I = insulator, M = metallic. Lower caption: AFM = antiferromagnetic. The circle and the star define the upper and lower limit of the MIT. Monoclinic and orthorhombic volume fraction given by pink and green data respectively. Diagram combining electronic and structural hysteresis, given by (c)resistivity curves and by (d) $-\frac{dln(R)}{dT}(T)$ and monoclinic volume fraction, both on heating (red data) and cooling (blue data) runs.

is preserved in this temperature range. Between 105 and 175 K, both insulating/metallic and monoclinic/orthorhombic phases coexist, as indicated by the yellow region in Figure 3.9(a). Just above 175 K the film reaches a purely orthorhombic structure, although the coexistence of metallic and insulating phases still persists up to 183 K. Above this temperature, the sample becomes metallic and paramagnetic, adopting the orthorhombic symmetry, as has been reported [30, 32].

Despite thermal hysteresis, the phase sequence is completely reversible, which has been confirmed by the analysis of cooling run presented in Figure 3.9(b). The monoclinic signatures start to be observed below 160 K, while the NNO film still remains fully metallic and paramagnetic (if one assumes $T_N = T_{MI}$ also for the cooling run, as we experimentally show for the heating run). Below 143 K (i.e., 17 K below the onset of structural phase coexistence), the insulating/metallic domains coexistence starts and the NNO film becomes antiferromagnetic. Between 143 and 75 K, all electronic and structural phases coexist. Below 75 K, the Raman spectra present only monoclinic signatures while the pure insulating state is only reached below 68 K, i.e., 7 K below the total structural transformation into

the monoclinic symmetry. Hysteretic properties described above (better seen in Figure 3.9(c)) confirm the first-order nature of both electronic and structural phase transitions. These transitions are faster on cooling than on heating, meaning that the dynamics underlying the phase transitions is dependent on the temperature ramp.

Due to the first-order nature of the phase transition in NNO, nucleation processes of mixed insulating/metallic phases are intrinsic to the hysteretic temperature range. According to Catalan *et al.*, the maximum of $-\frac{dln(R)}{dT}(T)$ should occur at the critical threshold for the loss of metallic connectivity in the percolative lattice, which corresponds to an insulating volume fraction of $\frac{2}{3}$ [36]. In order to better understand the thermal evolution of the structural phases and its correlation with the electronic states, the temperature dependence of the monoclinic volume ratio and $-\frac{dln(R)}{dT}(T)$ were plotted in Figure 3.9 (d), on heating and cooling ramps. The main outcome is the correlation between electronic and structural states, since the monoclinic volume fractions taken at this percolation threshold critical temperature are 0.61 and 0.76, on cooling and heating runs, respectively (see Figure 3.9 (d)). These values are close to the expected value of $\frac{2}{3}$, as the insulating phase exhibits monoclinic symmetry. Therefore, we conclude that monoclinic domains correspond to insulating domains. This result gives clear evidence for the direct correlation between electronic and structural phases in NNO and agrees with the theoretical prediction that in NNO the magnetic phase transition and structural symmetry lowering due to bond disproportionation are concomitant to trigger the MIT [28].

Nonetheless, significant differences between the temperature interval limits where pure electronic phases coexist with pure structural ones cannot still be fully understood in the framework of the percolative effects. Possible interpretations concern different structural and electronic dynamics, the different time length scale of the microscopic mechanisms involved on those transitions, or even the probing time length scale of each experimental technique. One could argue that the detection limit of the structural phases is directly correlated with the uncertainty of the bands intensity. As an example, the measurements done in cooling at 155 K, 150 K and 145 K (all above the T_{MI} = 143 K) are shown in Figure 3.10. It can be seen that the Raman M-band at 300 cm^{-1} is already present, as demonstrated by its intensity above the measurement uncertainty. Furthermore, in every plot showing the structural volume fraction, the error bars are all below 2 %. We are confident that the sensitivity of the Raman spectroscopy results allows to determine the percentage of each structural phase with an error below 2 %, therefore the temperature differences between the structural and electronic transitions deserve to be further investigated.

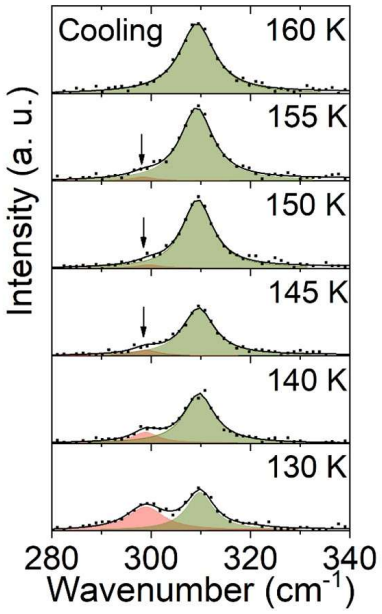


FIGURE 3.10: Raman spectra measured in cooling run, at temperatures around the T_{MI} = 143 K, demonstrating the experimental sensitivity to the structural phases. Spectral components of P$2_1/n$ phase are represented in pink and of P*bnm* phase in green.

3.6. Summary

This chapter presents an experimental study of the electronic and structural properties of an 85 nm thin film of NNO deposited onto [001]-LAO substrate by MOCVD technique. The concurrence of electronic, magnetic, and structural transitions in NNO is confirmed. Our results point for a structural percolative process throughout the metal-to-insulator phase transition, emphasising the correlation between symmetry breaking oxygen-breathing distortion (B_{OC}) and the occurrence of metal-to-insulator transition. From Raman scattering experiments, the monoclinic and orthorhombic phases' coexistence was fully characterized, and their volume fractions determined as a function of temperature. At the critical threshold of the insulating domain percolation, the monoclinic volume fraction attains the predicted $\frac{2}{3}$ for a three-dimensional lattice, evidencing a structural percolative process. Moreover, the simultaneity of electronic and magnetic phase transitions is experimentally confirmed, reinforcing the magnetic order as the key ingredient to promote the MIT in NNO. The differences between temperature interval limits where pure electronic states coexist with pure structural phases still need further investigation.

4. Optically active lattice and magnetic excitations of $NdFeO_3$

Ultrafast phase transition control lies at the forefront of condensed matter physics, by enabling the manipulation of matter on ultrashort timescales. Triggered by ultrashort and intense laser pulses, the electronic, structural, and/or magnetic states of materials can be modified and allow the access to transient phases and hidden states that are inaccessible under equilibrium conditions [56, 58–60, 116, 117].

In $NdNiO_3$, the modification of magnetic and structural orders using ultrashort X-ray pulses, although in different timescales, had implications in the electronic transition, reinforcing structural and magnetic dynamics orders conspire to induce an metal-to-insulator transition [118]. However, this study just modified pre-existent states, no other hidden phase was reported. Orthoferrites had had a renewed interest in the recent years, due to possibility of not only modify pre-existent states, but also inducing new polar and/or magnetic transient states [56, 59, 60, 117]. Particularly, the manipulation of magnetic domains and photo-induced magnetic transitions between equilibrium and nonequilibrium states has been possible due to the excitation of polar phonons[56, 60, 117]. Orthoferrites' coupling between magnetism and structure is a key point for the ultrafast phase transition studies [59, 60]. $NdFeO_3$ is a good candidate for induced transient studies, as some of its phonons revealed to be sensitive to the spin reorientation transition [81] . Yet, it is fundamental to have a deep knowledge of all lattice and magnetic excitations at equilibrium conditions. For $NdFeO_3$, optical Raman-active phonons and magnons have been experimentally characterized, but the group analysis is still rather incomplete [79, 119]. The infrared (IR)-active phonons of this compound have yet to be systematically studied, as the few publications available only present a rather incomplete characterization [120, 121].

This chapter presents a complete characterization of the optically-active lattice and magnetic excitations of $NdFeO_3$ at the Brillouin zone centre, by means of polarized Raman, infrared and THz spectroscopies. To complement the experimental results, first-principles

calculations * were performed to confirm the mode symmetry and identify the vibrational motion of each phonon. Such motions are valid for a large number of materials sharing the P*bnm* perovskite structure. Regarding the magnetic excitations, theoretical and experimental selection rules are here presented. Some of the results reported in this Chapter are published in *Scientific Reports* [122].

4.1. Lattice excitations

4.1.1 Group theory analysis of the phonons

In the temperature range where the P*bnm* space group describes the crystallographic structure of $NdFeO_3$, the atoms Wyckoff positions are the ones presented in Table 1.1. At the Γ point, group theory analysis gives the following decomposition into irreducible representations:

$$\Gamma_{phonons}\,(Pbnm) = 7A_g + 7B_{1g} + 5B_{2g} + 5B_{3g} + 8A_u + 8B_{1u} + 10B_{2u} + 10B_{3u} \qquad (4.1)$$

All zone-centre phonons are non-degenerated, and the $8A_u$ phonons are optically silent. The optical phonons transforming according to an even irreducible representations are Raman-active ($\Gamma_{Raman} = 7A_g + 7B_{1g} + 5B_{2g} + 5B_{3g}$), while those transforming according to the odd representations are IR-active ($\Gamma_{IR} = 7B_{1u} + 9B_{2u} + 9B_{3u}$). Three phonons ($1B_{1u} + 1B_{2u} + 1B_{3u}$) are acoustic phonons. As the Fe sits in the centre of inversion, its motions only participate in the polar phonons.

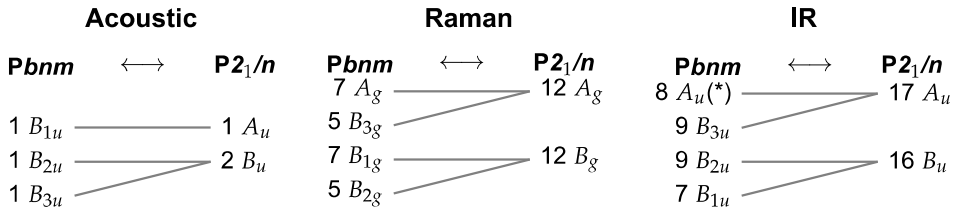
The theoretical arguments presented in Chapter 1 point for a symmetry-lowering to the monoclinic $P2_1/n$ space group across the SRT. The atoms Wkycoff positions for this symmetry are presented in Table 1.5, and the decomposition into irreducible representations at the Γ point is:

$$\Gamma_{phonons}\,(P2_1/n) = 12A_g + 12B_g + 18A_u + 18B_u \qquad (4.2)$$

The zone-centre phonons remain all non-degenerated. Raman-active phonons are now $\Gamma_{Raman} = 12A_g + 12B_g$), and IR-active phonons are $\Gamma_{IR} = 17A_u + 16B_u$. Three phonons ($1A_u + 2B_u$) are acoustic.

*performed by Dr. J. Íñiguez-González (University of Luxembourg) and Dr. H.Zhao (Jilin University).

The group-subgroup transformation P*bnm* $\longleftrightarrow$ P$2_1/n$ can be described by the relation between high and low symmetries irreps:



From the relation diagram between the two space groups, it is demonstrated that the number of phonons remains constant for both acoustic and Raman-active phonons: 3 acoustic and 12 Raman-active. For the IR-active modes, it is worth mentioning that only 25 phonons are optically active in the P*bnm* structure, note that A_u phonons are marked with (*) because, in this symmetry, they are optically silent. With symmetry lowering, those phonons become active, and transform into A_u IR-phonons, therefore the number of IR-active phonons differs between high and low symmetries: 25 for P*bnm* and 33 for P$2_1/n$.

In the following sections, Raman- and IR- active phonons of $NdFeO_3$ will be probed and the respective mode assignment given. Those studies will be restricted to temperatures where the P*bnm* space group is set.

4.1.2 Raman active modes

Figure 4.1(a) and 4.1(b) show, respectively, the polarized Raman spectra of phonons with symmetry A_g and B_g, recorded at room temperature.

The fitting procedure described in Chapter 2, uses Equation 2.2 to accurately determine the observed Raman-active phonons wavenumber. This information is presented in Table 4.1, along with the calculated wavenumbers and main atomic motions obtained from DFT calculations. Due to thermal expansion, the phonons wavenumber shifts to lower values, thus a comparison of values obtained by DFT calculations (T = 0 K) with the ones recorded at 300 K might not be trivial. To overcome this issue, phonon wavenumber recorded at 10 K (in a ceramic sample [81]), were also included in Table 4.1.

In general, there is a good agreement between the frequency of observed phonons with the predicted values from DFT calculations. At 300 K, 7A_g phonons are observed in the 100–500 cm^{-1} spectral range, while 5 B_{1g}, 5 B_{2g} and 5 B_{3g} phonons are detected in the

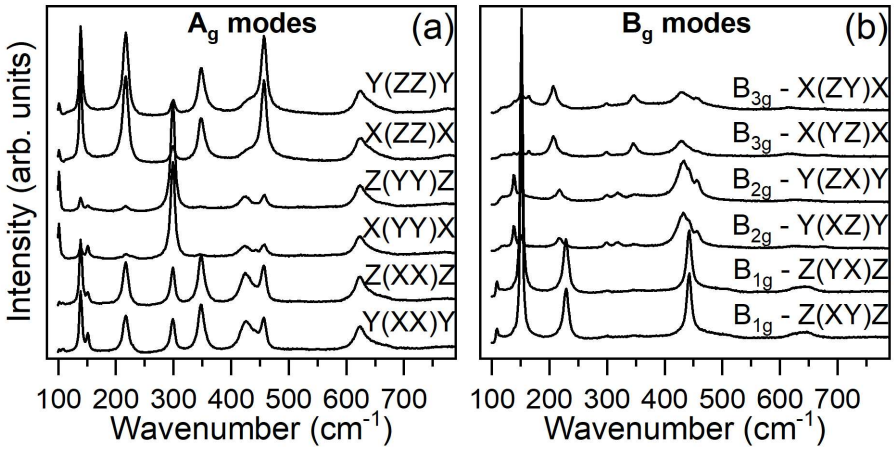


FIGURE 4.1: Polarized Raman spectra of $NdFeO_3$ at ambient conditions. The measurement configurations are given in Porto's notation, in (a) for the vibration modes of A_g symmetry and in (b) for the vibration modes of $B_{1,2,3g}$ symmetries. X, Y and Z correspond to the orthorhombic axes in the P*bnm* space group.

TABLE 4.1: Experimental and theoretical band positions, the corresponding symmetry assignment and main atomic motions (identified from DFT calculations) of the observed Raman-active modes in $NdFeO_3$. The values at 10 K were taken from [81].

Symmetry	DFT (cm^{-1})	Experimental (cm^{-1})		Main atomic motion
		10 K [81]	300 K	
A_g	104.6	–*	101.2	Nd(y), in-phase in x-y, out-of-phase in z
	141.4	142.2	138.9	Nd(y), out-of-phase
	231.5	217.8	216.8	$[001]_{pc}$ FeO_6 rotation, in-plane
	307.5	305.0	298.7	O1 x-y plane
	359.8	357.0	348.7	$[110]_{pc}$ FeO_6 rotation, in-phase
	418.6	422.1	425.8	O1-Fe-O2 stretching, in-phase
	456.2	460.4	457.2	O1-Fe-O2 scissor-like bending
B_{1g}	110.0	109.0	109.3	Nd(x), in-phase in x-y, out-of-phase in z
	157.3	153.9	151.4	Nd(y), out-of-phase
	251.9	233.7	228.6	$[110]_{pc}$ FeO_6 rotation, in-phase
	346.0	320.8	—	O1-x-y plane
	443.6	448.2	442.5	O1-Fe-O2 scissor-like bending
	500.8	504.5	—	O2-Fe-O2 scissor-like bending, in-phase
	619.8	620.4	628.0	Fe-O2 stretching in-phase
B_{2g}	140.9	139.6	138.3	Nd(z) out-of-phase in x-y, z
	315.4	305.8	299.2	O1-Fe-O2 in-phase
	426.6	431.5	431.4	Octahedra squeezing in z
	439.9	436.8	443.1	O2-Fe-O2 scissor-like bending, out-of-phase
	650.4	643.0	647.5	FeO_6 breathing
B_{3g}	160.7	155.4	150.9	Nd(z) in-phase in x-y, out-of-phase in z
	231.5	217.8	216.8	$[001]_{pc}$ FeO_6 rotation, out-of-phase
	357.5	357.0	346.5	$[001]_{pc}$ FeO_6 rotation, out-of-phase
	425.3	426.2	431.5	Fe-O2 stretching, out-of-phase
	593.8	596.3	618.4	Fe-O1 stretching

100–700 cm^{-1} range. At 10 K, we were successful to detect all the predicted B_{1g}, B_{2g} and B_{3g} phonons. However, one of the A_g modes, indicated with * , was not detected. Probably this mode still exits at 10 K, but its wavenumber is below the spectral range detection limit used (< 100 cm^{-1}). The broad feature observed in the 600–700 cm^{-1} range in Figure 4.1(a) is assigned to second order processes, as reported in other rare-earth orthoferrites [123, 124] and in agreement with the lack of predicted A_g modes in that frequency range (Table 4.1). The small features observed in Figure 4.1(b) for the B_{1g}

modes, between 300 and 400 cm^{-1} are bands arising from leakage of strong A_g modes, due to polarizer/sample misalignments.

Figure 4.2 presents a schematic view of the main atomic motion of the Raman-active modes, which is compatible with the published literature for other perovskite-compounds with P*bnm* symmetry [125].

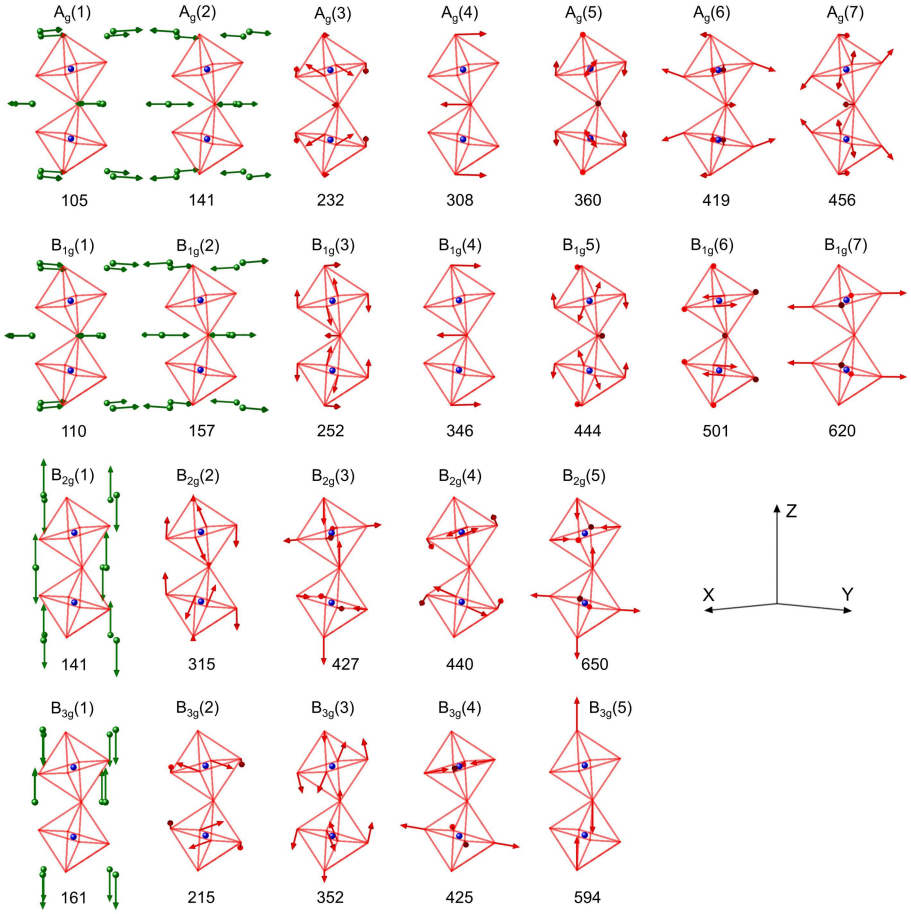


FIGURE 4.2: Vibrational patterns of the Raman-active modes in $NdFeO_3$, described in Table 4.1. Label: Nd atoms (green symbols), Fe atoms (blue symbols) and O atoms (red octahedra cage).

The characterization of Raman-active phonons of $NdFeO_3$ at room temperature was already presented by Singh *et al.*, but there are some concerns regarding the analysis presented by those authors [119]. First, the theoretical model used to compute the Raman-active modes wavenumbers gives large differences between the calculated and experimental values, with the experimental values being very close to the ones presented in our work. In this regard, the first-principles calculations presented in this thesis are more suitable to describe $NdFeO_3$ phonons. Second, Singh *et al.* only provide the main atomic motions for the A_g and B_{1g} modes [119], whereas we provide the eigenmodes for all

symmetries. Third, the authors assign three Raman-active modes to the FeO_6 breathing atomic motion: $A_g(3)$,$B_{1g}(3)$ and $B_{1g}(7)$ [119]. However, as Figure 4.2 demonstrates, the only breathing atomic motion is $B_{2g}(5)$. Both $A_g(3)$ and $B_{1g}(3)$ are FeO_6 rotations, and $B_{1g}(7)$ corresponds to a Fe-O2 stretching.

The Raman analysis in $NdFeO_3$ complements the study already done for the other rare-earth orthoferrites [124]. Figure 4.3 presents the wavenumber of selected Raman-active phonons as a function of the ionic radius, combining the data from Weber *et al.* [124] with the ones here reported. As it can be ascertained from the figure, our data fits very well the ionic radius trend of the Raman-active phonon wavenumbers in the $RFeO_3$ family, with *R* = Dy – La.

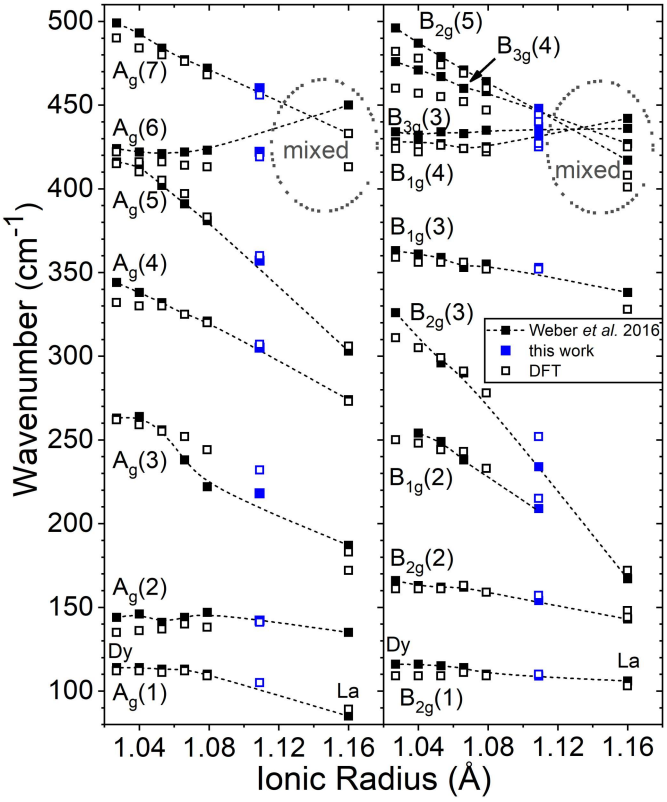


FIGURE 4.3: Raman phonon wavenumbers of $RFeO_3$ as a function of the rare earth R^{3+} ionic radius. The data for all rare-earth was take from Weber *et al.* [124], with the exception of Nd (this work, blue data). All lines are guides to the eye only. The setting used in this figure is P*nma* space group, for an easier comparison with Weber *et al.* [124].

4.1.3 Infrared active modes

Figures 4.4(a)-(c) shows the IR reflectivity spectra recorded at 300 and 4 K, for the IR electric vector ***E*** polarized along the a-, b- and c-axis, respectively, in the 5–700 cm^{-1} spectral range. The solid blue lines were determined by the best fit of Equations 2.3

and 2.4 to the experimental spectra. To perform the fits, high frequency contributions to the dielectric function, ϵ_∞, were determined: 5.36 for ***E***||a, 5.53 for ***E***||b, and 5.34 for ***E***||c. These values are compatible with the refractive index usually found in rare-earth orthoferrites [51].

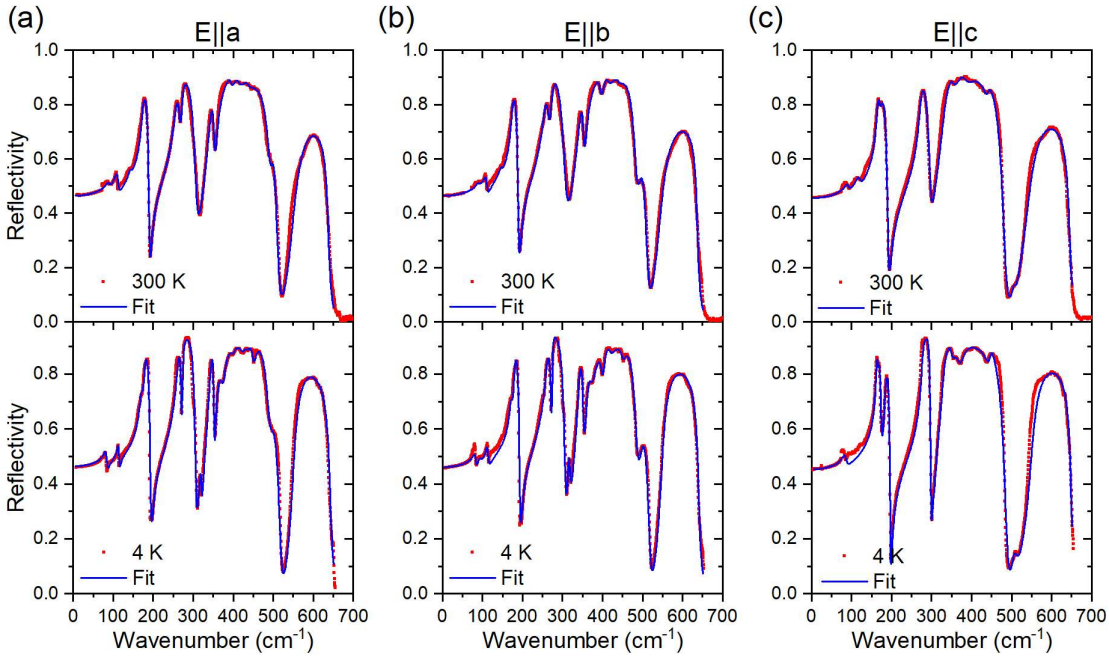


FIGURE 4.4: Reflectivity spectra of $NdFeO_3$ recorded at 300 K and 4 K, for the polarizations: (a) E||a-B_{3u}, (b) E||b–B_{2u} and (c) E||c–B_{1u}. The blue solid line was determined by the best fit of Eq. 2 to the experimental reflectivity.

The room temperature reflectivity spectra are described by a total of 13 B_{3u} (***E***||a), 13 B_{2u} (***E***||b) and 11 B_{1u} (***E***||c) excitations, i.e., slightly more than expected from factor-group analysis in Equation 4.1. Among these excitations, we found an excellent agreement between the calculated transversal optical phonon frequencies (from DFT calculations) and the experimental ones at 4 K, as presented in Table 4.2. While we succeeded at observing all the predicted polar phonons at 4 K, the bands are broader and overlap at 300 K, preventing us to resolve all modes at this temperature. The remaining redundant excitations are assigned to crystal-field excitations and leakages from other polarizations due to small misalignments of the samples (see Appendix A.4).

Figure 4.5 shows the spectra of the real ϵ' and imaginary parts ϵ'' of the dielectric function, calculated from Equation 2.3. Frequencies peaks in $\epsilon''(\omega)$ spectra roughly correspond to the frequencies of the transversal optical phonons. According to our calculations, the translational modes of Nd^{3+} and Fe^{3+} cations are observed in the 110–200 cm^{-1} spectral range, while the internal vibrations of the FeO_6 octahedra are found to be in the 220–650

TABLE 4.2: Experimental and theoretical (only for transversal phonons) band positions, the corresponding symmetry assignment of the observed transversal and longitudinal IR-active modes in $NFeO_3$.

Symmetry	Transversal (cm^{-1})			Longitudinal (cm^{-1})		Main atomic motion
	DFT	4 K	300 K	4 K	300 K	
B_{1u} (***E***||c)	167.3	167.5	165.0	174.4	170.8	Nd(z); Fe(y) out-of-phase in z, in-phase in x-y
	176.4	183.1	172.6	197.0	191.8	Nd(z) in-phase in x; Fe+O1 x-y plane
	271.8	276.5	272.0	298.2	297.0	O2(z) out-of-phase in z, in-phase in x-y; Fe(xyz)
	301.7	303.6	—	304.8	—	Fe(x) out-of-phase in z
	337.6	329.5	330.7	350.0	354.8	$[001]_{pc}$ FeO_6 rotation, out-of-phase
	503.8	505.4	506.6	510.8	507.8	O2-Fe-O2 scissor-like bending, out-of-phase; Fe(yz)
	535.9	549.3	540.9	648.1	644.5	Fe-O1 stretching
B_{2u} (***E***||b)	110.3	112.3	109.6	113.7	111.3	Nd(x) in-phase in z, out-of-phase in x-y; Fe(x)
	189.3	179.8	174.1	193.7	190.3	Nd(y) against Fe
	242.9	259.6	255.4	271.7	266.8	O1-Fe-O2 in-phase; Fe(y)
	282.4	275.3	272.3	307.2	307.8	O1 against Fe in x-y plane, in-phase
	302.4	315.6	—	318.6	—	O2-Fe-O2 scissor-like bending; Fe(xyz)
	322.1	340.3	342.7	352.4	353.0	O2-Fe-O2 scissor-like bending; Fe(xyz)
	405.6	401.8	397.0	419.2	413.8	O1 against Fe in x-y plane
	503.7	492.7	490.9	518.0	512.0	Fe-O2 stretching in-phase; Fe(z)
	520.8	548.1	543.3	639.7	636.1	Fe-O2 stretching, out-of-phase; Fe(yz)
B_{3u} (***E***||a)	115.0	113.8	110.2	114.9	112.3	Nd(x) in-phase in z, out-of-phase in y; Fe(y)
	177.2	178.3	173.5	194.0	190.6	Nd(x) against FeO_6 octahedra
	256.4	260.8	256.6	260.8	267.4	$[110]_{pc}$ FeO_6 rotation in-phase; Fe(xyz)
	277.3	274.1	271.7	307.2	308.4	O1-Fe-O2 scissor-like bending; Fe(xyz)
	312.2	319.2	—	321.1	—	O1 x-y plane, out-of-phase; Fe(z)
	342.5	340.9	341.5	352.4	353.0	O1 x-y plane; Fe(yz)
	370.3	376.5	358.4	400.3	395.5	O1-Fe-O2 scissor-like bending; Fe(xy)
	448.3	452.4	439.2	489.7	493.3	O1-Fe-O2 scissor-like bending; Fe(y)
	543.8	550.6	549.3	642.1	637.3	Fe-O1 stretching out-of-phase; Fe(x)

cm^{-1} range [126]. Figure 4.6 presents a schematic view of the main atomic motion of the IR-active modes of Table 4.2, which had not been reported up to now, within the best of our knowledge.

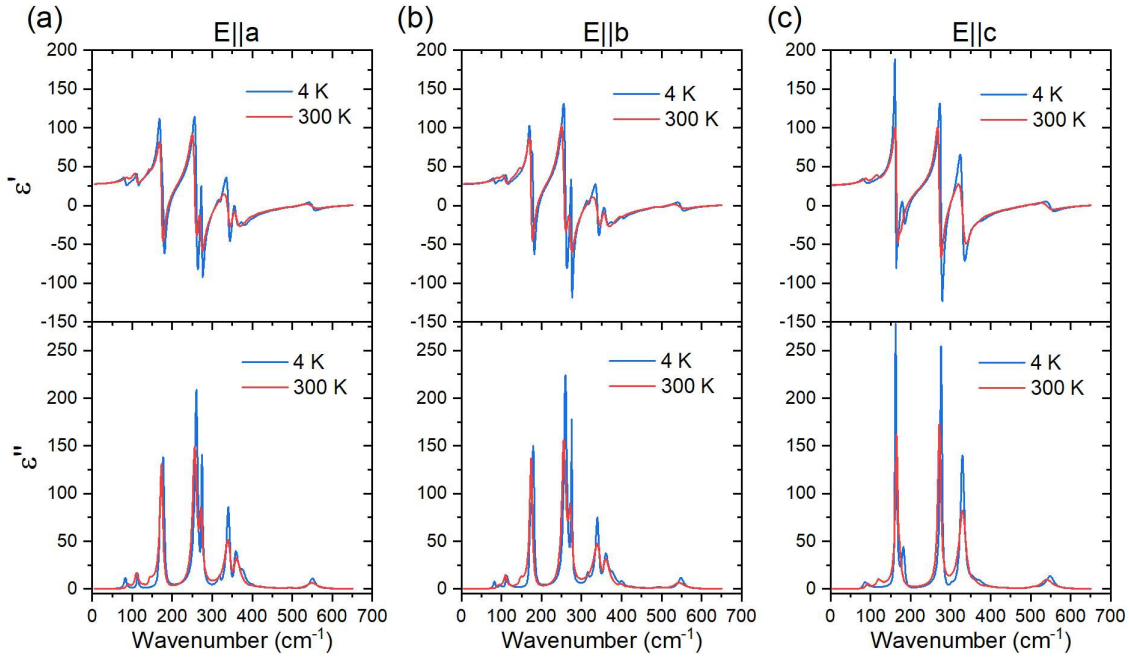


FIGURE 4.5: The spectra of the real ϵ' and imaginary parts ϵ'' of the dielectric function calculated from the reflectivity data analysis, recorded at 300 K and 4 K, for (a) ***E***||a, (b) ***E***||b and (c) ***E***||c.

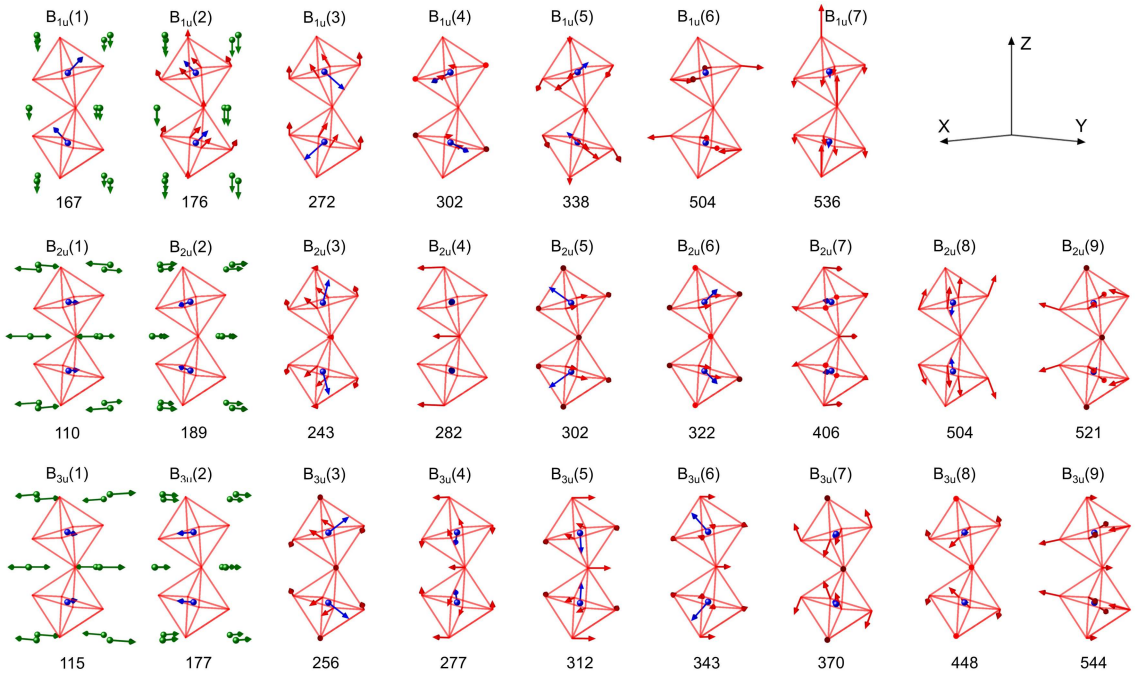


FIGURE 4.6: Vibrational patterns of the infrared-active modes in $NdFeO_3$, described in Table 4.1. Label: Nd atoms (green symbols), Fe atoms (blue symbols) and O atoms (red octahedra cage).

4.2. Magnetic excitations

4.2.1 Magnon selection rules

Similarly to lattice excitations (phonons), the magnetic excitations (magnons) also have their own set of optical-selection rules. Inelastic light scattering spectroscopies are widely used to probe magnon excitations [51, 56]. Depending on the setup measurement of each technique, for instance, reflection or transmission of scattered light, the light-matter interaction will be affected in different ways, and hence, the selection rules may also differ. The scattering techniques here present are THz and Raman spectroscopies, which have different measurements geometries (described in Chapter 2), thus for each technique a set of magnon selection rules will be now presented.

For THz spectroscopy

Figure 4.7 shows a schematic view of THz selection rules for magnons of $NdFeO_3$, across the different magnetic configurations. This scheme was constructed based on the already reported selection rules shown in Figure 1.19. It considers a two Fe-sublattice model, where the two vectors S_1 and S_2 correspond to the magnetic moments of two nearest neighbour Fe^{3+} cations and the ferromagnetic vector $\boldsymbol{F} \propto S_1 + S_2$ [51, 80, 127]. As illustrated in Figure 1.18, the precessional motion of the two magnons is related to the ***F*** vector: σ-mode or quasi-ferromagnetic (FM) resonance corresponds to the precession of ***F*** vector around its equilibrium position, and γ-mode or quasi-antiferromagnetic (AFM) resonance, to the oscillating amplitude of ***F*** vector along is equilibrium orientation. Therefore, the selection rules will depend on the ***F*** vector orientation, represented in the upper panel, and on the orientation of the THz radiation magnetic field, H^{ω}, represented in the lower panels of Figure 4.7, for the different magnetic configurations.

The σ-mode is optically excited when the magnetic polarization of the THz radiation, H^{ω}, has a component on the perpendicular plane of the precession axis: ab-plane for the Γ_4 phase or bc-plane for the Γ_2 phase [20, 21, 51, 56]. The γ-mode is excited when H^{ω} is parallel to ***F*** vector: H^{ω}||c in the Γ_4 phase, or H^{ω}||a in the a-axis phase [20, 21, 51, 56].

During the spin reorientation, as the ***F*** vector continuously rotates in the ac-plane, selection rules change and can be interpreted as a merge between Γ_4 and Γ_2 selection rules. For Γ_{24} phase, it is even possible two excite simultaneously both magnons if H^{ω}||a,c.

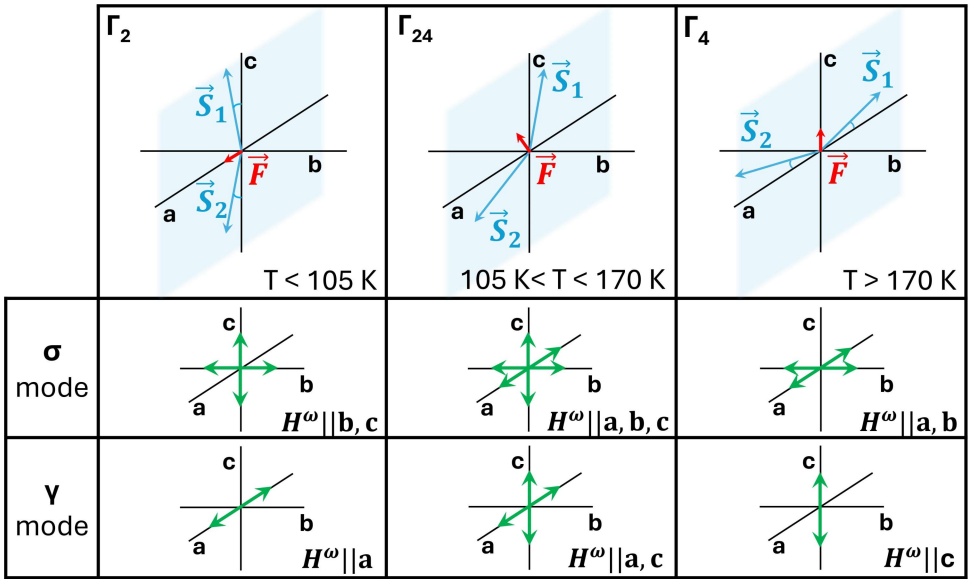


FIGURE 4.7: Scheme of the magnon selection rule in $NdFeO_3$. The crystallographic axes refer to the P*bnm* setting. The green arrows represent the magnetic field component H^{ω} of the THz radiation. Ferromagnetic vector ***F*** is represented by the red arrow, while the blue arrows represent the normal equilibrium orientations of the canted spins assuming the two sublattice model.

For Raman spectroscopy

Beside THz spectroscopy, Raman spectroscopy also allows the detection of excitations on the THz-energy range, and therefore, magnons. The magnons probed by Raman scattering technique obey to different selection rules than the ones probed by THz spectroscopy. The determination of Raman selection rules depends on the Raman tensors of the material magnetic point group [128]. Above SRT, the $NdFeO_3$ adopts the P*b'n'm* space group, Γ_4 configuration, that belongs to the magnetic point group m'm'm. The Raman tensors of this point group are [51, 128]:

$$A_g = \begin{pmatrix} A & iB & 0 \\ iD & E & 0 \\ 0 & 0 & I \end{pmatrix}$$
$$B_g = \begin{pmatrix} 0 & 0 & iC \\ 0 & 0 & F \\ iG & H & 0 \end{pmatrix} \quad (4.3)$$

where $A, ..., I$ are constants. The symmetry of Raman modes A_g is associated with γ-mode and the B_g with σ-mode [51]. Below SRT, Γ_2 configuration, the system adopts another orthorhombic symmetry, P*bn'm'*, which belongs to the magnetic point group mm'm'. The Raman tensors are now define by [128]:

$$A_g = \begin{pmatrix} A & 0 & 0 \\ 0 & B & iH \\ 0 & iW & C \end{pmatrix}$$
$$B_g = \begin{pmatrix} 0 & D & iF \\ E & 0 & 0 \\ iG & 0 & 0 \end{pmatrix} \tag{4.4}$$

The magnons symmetry is kept in the Γ_2 configuration: γ-mode has A_g symmetry and σ-mode has B_g symmetry [51].

For Γ_{24}, we are going to assume that the symmetry is lowered to the monoclinic $P2_1'/n'$ space group, which belongs to the magnetic point group 2'/m'. The Raman tensor is defined as [128]:

$$A_g = \begin{pmatrix} A & B & iC \\ D & E & iF \\ iG & iH & I \end{pmatrix} \tag{4.5}$$

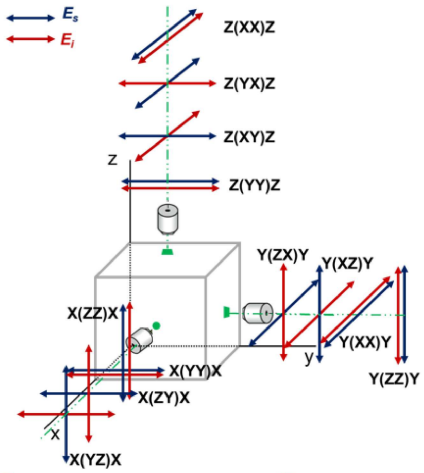
Note that a lowering to the monoclinic structure affects the symmetry of irreps associated with the magnons: both become A_g modes. The following diagram summarizes the magnons irrep relations between orthorhombic and monoclinic magnetic structures:

P*b'n'm* $\longleftrightarrow$ **P2'$_1$*/n'*** $\longleftrightarrow$ **P*bn'm'***

$$\begin{matrix} 1A_g \\ 1B_g \end{matrix} \diagdown\!\diagup \; 2A_g \; \diagup\!\diagdown \begin{matrix} 1A_g \\ 1B_g \end{matrix}$$

Another interesting feature of the monoclinic symmetry is the fact that all the elements of tensor are non-zero, which immediately indicates that any measurement configuration can excite the two magnons.

It is possible to predict if a magnon mode is allow/forbidden for a specific measurement configuration by checking the Raman selection rules. Similarly to THz selection rules, Raman selection rules also differ from Γ_4 to Γ_2 configurations. The intensity of Raman modes is proportional to the Raman tensor, $I \propto |\mathbf{e}_s R \mathbf{e}_i|^2$ [129], where $\mathbf{e}_{i,s}$ are the directions of polarization vector of incident/scattered light. The configuration of polarized Raman scattering experiments are often represented using Porto's notation (see Appendix A for more information). Figure 1.19(b) presents the calculated selection rules for Raman scattering experiment based on the Raman tensors of Equations 4.3, 4.4 and 4.5. By definition the A_g modes are usually symmetric and therefore, only allowed for parallel light polarizations, but in the case of magnetic point groups with time reversal, Raman tensors can have asymmetric and/or purely imaginary elements. This modifies the polarization selection rules, and allows A_g to be excited by cross-polarization, e.g. **Z(XY)Z** in the Γ_4 phase.



	Γ_2		Γ_{24}	Γ_4	
Porto's notation	A_g (γ-mode)	B_g(σ-mode)	A_g (σ-mode and γ-mode)	A_g (γ-mode)	B_g(σ-mode)
Y(XX)Y or Z(XX)Z	X	--	X	X	--
X(YY)X or Z(YY)Z	X	--	X	X	--
X(ZZ)X or Y(ZZ)Y	X	--	X	X	--
Z(XY)Z or Z(YX)Z	--	X	X	X	--
Y(XZ)Y or Y(ZX)Y	--	X	X	--	X
X(YZ)X or X(ZY)X	X	--	X	--	X

FIGURE 4.8: Raman scattering selection rules for different configurations represented by Porto's notation in the Γ_4, Γ_{24} and Γ_2 configurations. Incident and scattered polarization vectors are represented by red and blue arrows, respectively. The setup is always in backscattering configuration, so both incident and scattered light propagate along the same direction.

Next sections focuses on the experimental results obtained from the temperature-dependent THz absorption experiments and room-temperature Raman experiments.

4.2.2 Temperature evolution of magnons by TDS-THz spectroscopy

Figures 4.9(a) and 4.9(b) show representative zero-field extinction coefficient spectra, $\kappa(\omega)$, calculated from the THz absorption spectra, for the magnetic field H^{ω} of the THz radiation polarized along the a- and c-axes, respectively. In both cases, the propagation direction of the incident THz radiation was kept parallel to the b-axis. Figures 4.9(c) and 4.9(d) show the temperature dependence of the magnons wavenumber and intensity, observed in THz absorption. For completeness, we also present the wavenumber of the σ-mode observed in Raman scattering already published elsewhere [81].

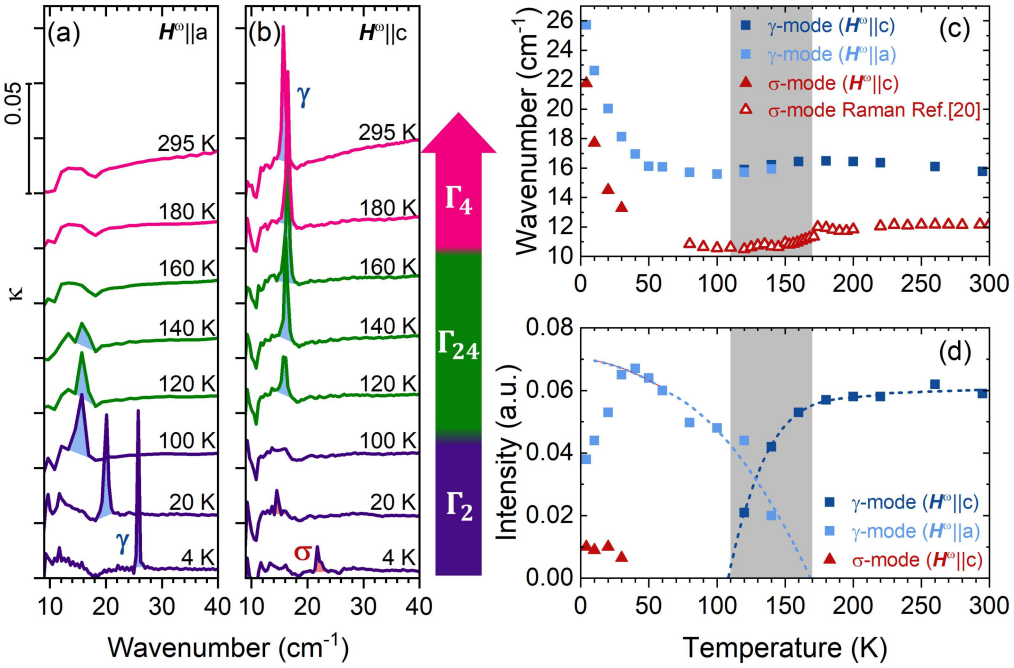


FIGURE 4.9: Extinction coefficient spectra $\kappa(\omega)$, calculated from the absorbance THz spectra of $NdFeO_3$ recorded at representative temperatures, for the (a) H^{ω}||a and (b) H^{ω}||c polarization configurations. (c) Temperature dependences of the wavenumbers of the σ- and γ-modes, observed in the two THz spectra polarizations (closed symbols) and in unpolarized Raman scattering spectra (open symbols) published in Ref.[81]. (d) Temperature dependence of the magnons intensities in the THz spectra. Dashed lines are a guide for the eyes.

At room temperature, the prominent peak observed at 15.8 cm^{-1} in the extinction coefficient spectrum, $\kappa(\omega)$, recorded with H^{ω}||c configuration (see Figure 4.9(b)) is assigned to the γ-mode. The expected σ-mode could not be observed in the $\kappa(\omega)$ spectrum recorded with H^{ω}||a configuration (see Figure 4.9(a)) likely due to its weak intensity or proximity to the detection limit (10 cm^{-1}), but previous Raman scattering results revealed the σ-mode at 12 cm^{-1} at room temperature (see Figure 4.9(c)) [81].

For H^{ω}||c, the γ-mode intensity weakly depends on temperature in the 295 - 180 K range, whereas its wavenumber increases by about 1 cm^{-1} (see Figures 4.9(c) and 4.9(d)). The peak intensity continuously decreases on further cooling and eventually vanishes below 120 K. In contrast, for H^{ω}||a, the γ-mode only appears below 140 K (see Figure 4.9(a)) and its intensity increases on cooling, as can be seen in Figure 4.9(d). The continuous intensity drop of the γ-mode observed in the H^{ω}||c on cooling, and the simultaneous intensity increase in the H^{ω}||a spectra in the 160 – 100 K range, are evidences for the continuous rotation of the ferromagnetic vector ***F*** across the spin reorientation transition range. Below 100 K, the γ-mode narrows and shifts to higher wavenumbers (see Figures 4.9(b) and 4.9(c)), in such a way that at 4 K, it peaks at 25.8 cm^{-1}. This hardening and intensity decrease below 40 K were reported before [80]. The proximity to Nd^{3+} ordering temperature increases the Fe-Nd competition given rise to an unstable magnetic state, resulting on the weakening of the γ-mode intensity [80]. The σ-mode appears in the $\kappa(\omega)$ spectra recorded in the H^{ω}||c polarization configuration below 50 K. The peak position up shifts from 13.5 cm^{-1} (40 K) to 21.8 cm^{-1} (4 K). Combining THz and Raman spectroscopic results, shown in Figure 4.9(c), we observe that, from room temperature to 170 K, the σ-mode wavenumber is temperature independent. On further cooling, this mode partially softens in the 170 - 110 K range, and afterwards it hardens as the temperature approaches 4 K.

4.2.3 Room temperature magnons signature by Raman spectroscopy

Figure 4.10 shows the unpolarized Raman spectra recorded at room temperature, in all the possible measurement configurations. Due to setup limitations it was not possible to polarize the scattered light, but the incident light is always polarized, therefore its direction is identified in the figure.

One has to take in mind that ”collected” light will always have contributions from parallel and cross polarizations, e.g. k||a, E_i||c has simultaneous **X(ZZ)X** and **X(ZY)X** which by the selection rules presented in Figure 4.8, would excite γ-mode and σ-mode, respectively. Although this spectrum presents mainly the signal of σ-mode, this is related to polarizability value of each element in the Raman tensor.

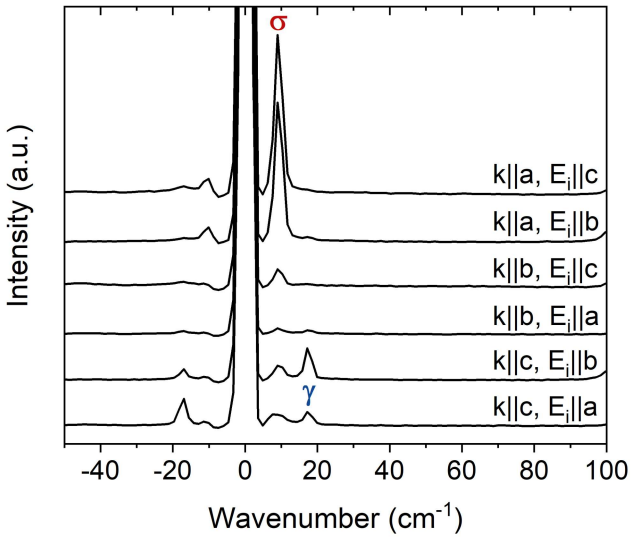


FIGURE 4.10: Room temperature unpolarized Raman spectra of $NdFeO_3$ single crystal, recorded in the six possible measurement configurations. Note that for unpolarized Raman measurements the incident beam is always polarized.

4.2.4 Crystal-field excitations

Due to the crystal-field interaction, the ground state of Nd^{3+}, ${}^{9/2}I_4$, splits into 5 Kramers doublets and they can be observed in IR reflectivity spectra [130]. Following the current literature, Table 4.3 presents the excitation assignment to the crystal-field excitations in $NdFeO_3$ [131], along with the experimental values obtained from the reflectivity spectra fitting at 300 K and 4 K. The first doublet can be seen in all polarizations at 4 K, while the second doublet is only visible for ***E***||a and ***E***||b (cf. Figures 4.4(a)-(c)).

TABLE 4.3: Theoretical and experimental values of some crystal-field (CF) excitations of $NFeO_3$. Note that each CF excitation has two calculated values representing the up and down spin energies (due to Zeeman effect).

CF calculated (cm^{-1})[130]	4 K			300 K		
	E||a	**E||b**	**E||c**	**E||a**	**E||b**	**E||c**
81.8 - 85.9	82.8	82.4	84.5	88.7	—	91.4
360.5 - 368.4	357.2	360.2	—	—	357.8	—

4.3. Summary

In this Chapter a comprehensive study of the optical lattice and magnetic excitations in $NdFeO_3$ is given. From the group theory analysis of phonons and magnons, the selection rules are defined and compared with experimental THz, IR and Raman spectroscopic data.

The polarized Raman scattering and IR spectroscopies studies, along with the first-principles simulations, allow us the mode and symmetry assignments of the observed phonons. In this sense, this work complements the understanding of optical phonons in rare-earth orthoferrites. The temperature dependence of the magnons probed by THz spectroscopy follows the predicted selection rule changes across the SRT, which is already an indication of the symmetry-breaking of $NdFeO_3$, that will be further investigated in the next Chapter.

The overall results presented in this Chapter provide a more complete description and understanding of the optically-active excitations in $NdFeO_3$, that can be extrapolated to other orthoferrites.

5. Magnetic and structural domain walls dynamics in $NdFeO_3$

Magnetic phase transitions in $NdFeO_3$ are accompanied by subtle structural changes, as previously demonstrated through temperature dependent Raman scattering spectroscopy, as well as X-ray and neutron diffraction experiments [70, 74, 81]. During the spin reorientation transition, it has been reported that the b(T) lattice parameter exhibits a broad minimum around 160 K (near T_1), while both a(T) and c(T) decrease monotonically with decreasing temperature [70, 74]. Notably, the variation in the b parameter over the 1.5–1200 K range is approximately one-tenth of the changes observed in the a and c parameters, which results in the absence of clear anomalies in the unit cell volume [70, 74]. The lack of pronounced distortions in the lattice parameters and cell volume—typically associated with structural symmetry lowering—led the scientific community to assume that the magnetic transition in orthoferrites is isostructural in nature [70, 74, 88, 89]. However, the anomalous temperature dependence of certain phonon modes associated with FeO_6 octahedral rotations near the SRT temperature boundaries points to the presence of magnetostructural coupling via spin-phonon interaction in $NdFeO_3$ [81]. Still, this coupling does not appear strong enough to directly reveal a symmetry breaking at the SRT.

The case of NdNiO3 contrast with $NdFeO_3$, as it undergoes the same P$bnm \rightarrow$ P$21/n$ transition, in which the number of Raman-active modes remains constant, yet the phonons associated with orthorhombic and monoclinic symmetries are distinguishable by their frequencies. Their temperature dependence exhibits a discontinuity, making it straightforward to assign each phonon to a specific phase (see Chapter 3). For $NdFeO_3$, assuming the same structural transition, no discontinuity is observed in the phonon behaviour across the SRT boundaries, making symmetry assignment more challenging [81]. This discrepancy may be explained by the nature of the transition: first-order in $NdNiO_3$, but predicted to be second-order in $NdFeO_3$, which would inherently lack discontinuities.

The experimental indication of a monoclinic structure emerging during the SRT is particularly compelling, especially since $NdFeO_3$ shares a similar structural and magnetic

phase sequence with other rare-earth orthoferrites [5]. If symmetry lowering indeed occurs, monoclinic domains should form, and their dynamical behaviour becomes accessible for investigation. In this context, resonant ultrasound spectroscopy (RUS) provides an alternative approach to probing elastic properties, while anelastic behaviour offers insights into domain wall dynamics and magnetoelastic coupling [132, 133]. From the perspective of magnetic domains, magneto-optical imaging via the Faraday effect, alongside AC magnetic susceptibility, can be used to probe their dynamics.

Our goal is to contribute to a deeper understanding of the mechanisms underlying magnetoelastic coupling in orthoferrites. The results presented offer strong evidence for a symmetry lowering during the spin reorientation process—an effect not previously observed experimentally—and help clarify why conventional structural techniques have failed to detect this distortion. These findings are part of an article submitted to *Advance Functional Materials*.

5.1. Magneto-optic imaging of domain walls

Figure 5.1 shows the temperature evolution of magnetic domain walls in $NdFeO_3$, including SRT interval. The sample was cut parallelly to the ab-plane (c-axis out-of-plane in the P*bnm* setting). These images were obtained using the magneto-optic Faraday effect, which is sensitive to the magnetization component parallel to the transmitted light direction; i.e. the out-of-plane magnetization component. Consequently, the images show a strong contrast for the out-of-plane component of magnetization. At 200, 185 and 175 K, as the weak ferromagnetic moment (***M***) aligns along the c-axis, dark and bright regions are observed, corresponding to magnetic domains with opposite magnetization directions, $[001]$ and $[00\bar{1}]$, respectively. These results are compatible with the 180° type magnetic domains. Planar interfaces remaining temperature independent are ferroelastic domain walls owe their origin to octahedral tilting that establish the orthorhombic symmetry. Two different configurations of magnetic domain walls are visible: either coinciding exactly with the planar ferroelastic domain walls or embedded within the elastic domains, with a strongly curved shape. Images obtained at 165 and 110 K show that the magnetic domain walls undergo significant changes in configuration, as the magnetization ***M*** rotates towards the a-direction. Segments of the walls became displaced from the ferroelastic domain walls, and the strongly curved walls developed straight boundaries at a steep angle to these. The overall contrast fades within the SRT interval as the direction of net

magnetization rotates from $\langle 001 \rangle$ to $\langle 100 \rangle$, i.e., from out-of-plane to in-plane. The image obtained at 100 K shows very little contrast, consistent with net magnetic moments having completed the rotation to $\langle 100 \rangle$.

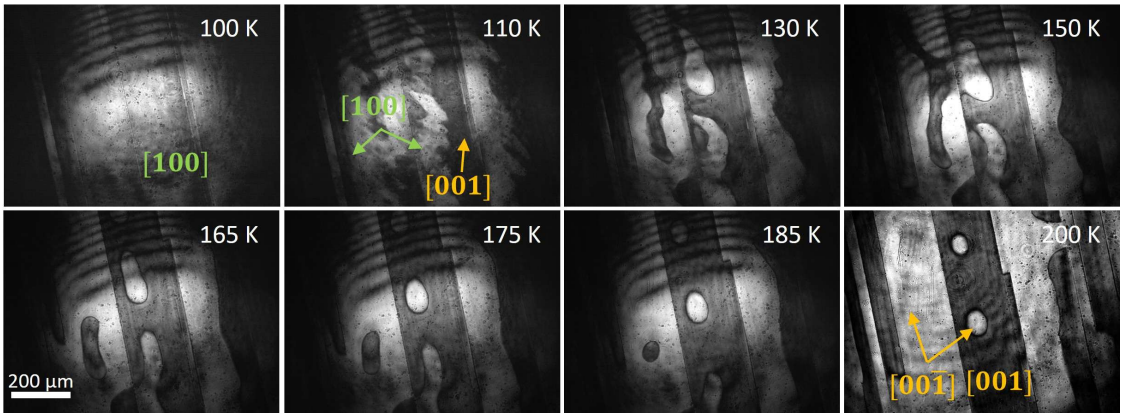


FIGURE 5.1: Magneto-optical images recorded for different fixed temperatures evidencing magnetic domains. The contrast varies between bright and dark domains for ***M***||c and the absence of contrast when ***M***||a. Arrows indicate regions with different weak ferromagnetic moment directions.

5.2. Magnetoelastic properties

Figure 5.2(a) shows the RUS spectra recorded through a heating run in the 2 – 300 K range and stacked in proportion to the temperature at which they were recorded. The spectra recorded in cooling are similar (see Appendix A.5). Observed resonance peaks were analysed in both runs. Due to presenting similar temperature evolutions, only a few were selected as representative examples, capturing the essential physics. Figure 5.2(b)-(d) presents the temperature evolution of the square frequency, f^2, and Figure 5.2(e)-(g) the acoustic losses, Q^{-1} , of representative resonance peaks with frequencies of 1416, 1436, and 1855 kHz, values at room temperature.

In detail, f^2(T) increases (elastic stiffening) with decreasing temperature from 300 to 180 K, as expected for normal crystalline materials. Softening by $\sim$ 1-1.5 % occurs through the interval $\sim$ 170-150 K. A single peak in Q^{-1}(T) is observed in the SRT interval. This pattern is closely similar to that seen previously in RUS data for the SRT in $SmFeO_3$ [134]. Some resonance peaks show a slight thermal hysteresis of f^2 values between cooling and heating, in the interval $\sim$ 110-135 K (Figure 5.2(b)-(d)). Below 80 K, the f^2(T) recovers the stiffness trend, reaching a maximum at 20 K. On further cooling, the f^2(T) softens on approaching 2 K. Below 100 K, Q^{-1}(T) is weakly dependent on temperature, but presents a small anomaly at 40 K, see Figure 5.2(e)-(g), which will be address in section 5.4.

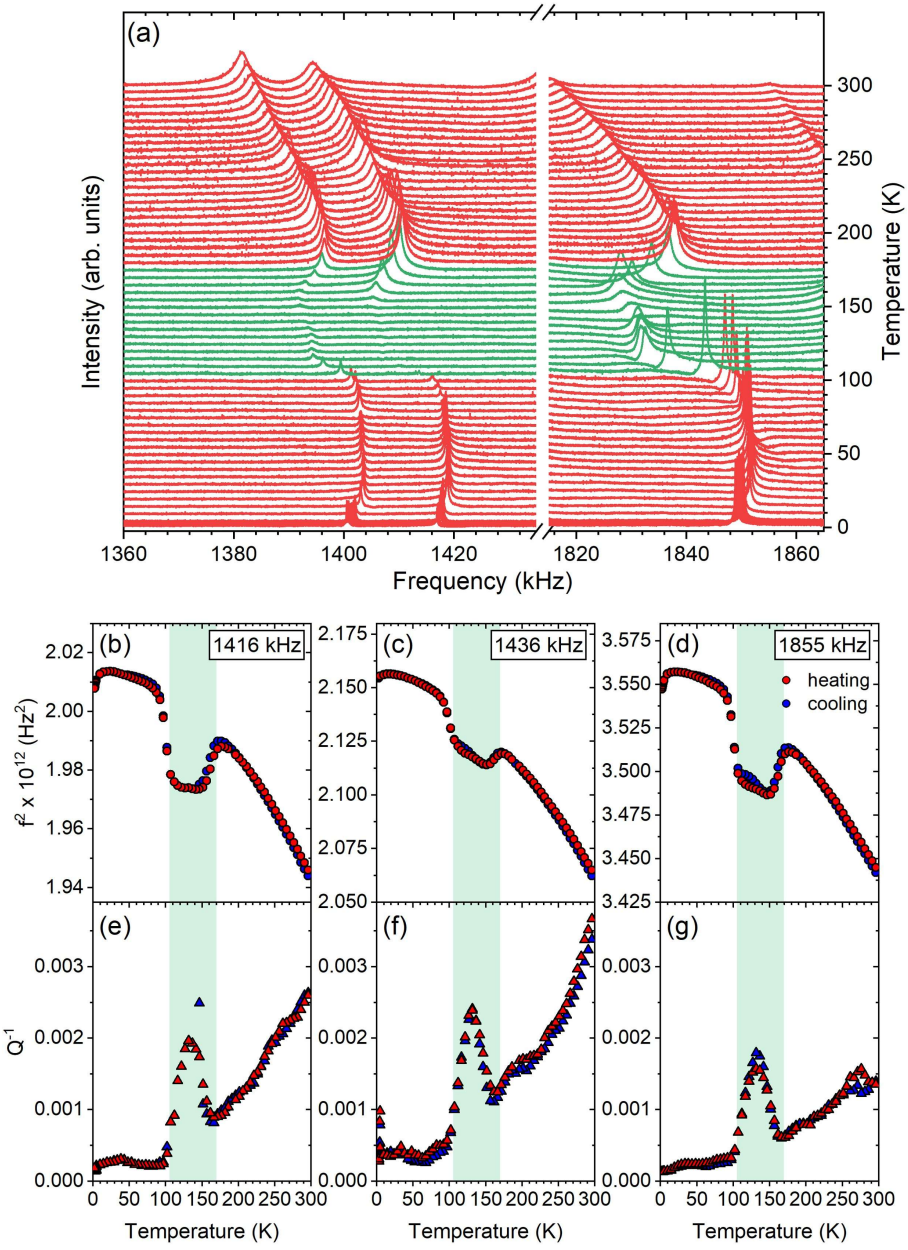


FIGURE 5.2: (a) Stack of RUS spectra scanned over 1360 to 1870 kHz, recorded in a heating run from 2 to 300 K. Spectra have been offset up the left axis in proportion to the temperature at which they were collected, and this temperature scale is shown on the right axis. Temperature dependence of f^2 (upper panel) and Q^{-1} (lower panel) obtained from fitting an asymmetric Lorentzian function to resonance peaks with frequencies near (b)(e) 1416, (c)(f) 1436 and (d)(g) 1855 kHz (RT values). Red/blue symbols represent heating/cooling data. The SRT temperature range is highlighted in green.

5.3. AC magnetic susceptibility

During the SRT, magnetic domain walls can acquire a component of ferroelastic strain contrast across them, not observable in our magneto-optical Faraday images. However, the close correlation between the elastic/anelastic and magnetic susceptibility losses should exist if the material presents magnetoelastic coupling. This correlation is confirmed by AC magnetic susceptibility measurements. Figure 5.3 shows the temperature dependence of real (χ') and imaginary (χ") parts of the complex AC magnetic susceptibility, for fixed frequencies in the 200 Hz -10 kHz range measured in a crystal along the a-axis (Figure 5.3(a)-(b)) and the c-axis (Figure 5.3(c)-(d)), with an applied DC magnetic field of 250 Oe along the respective measurement AC-driven field.

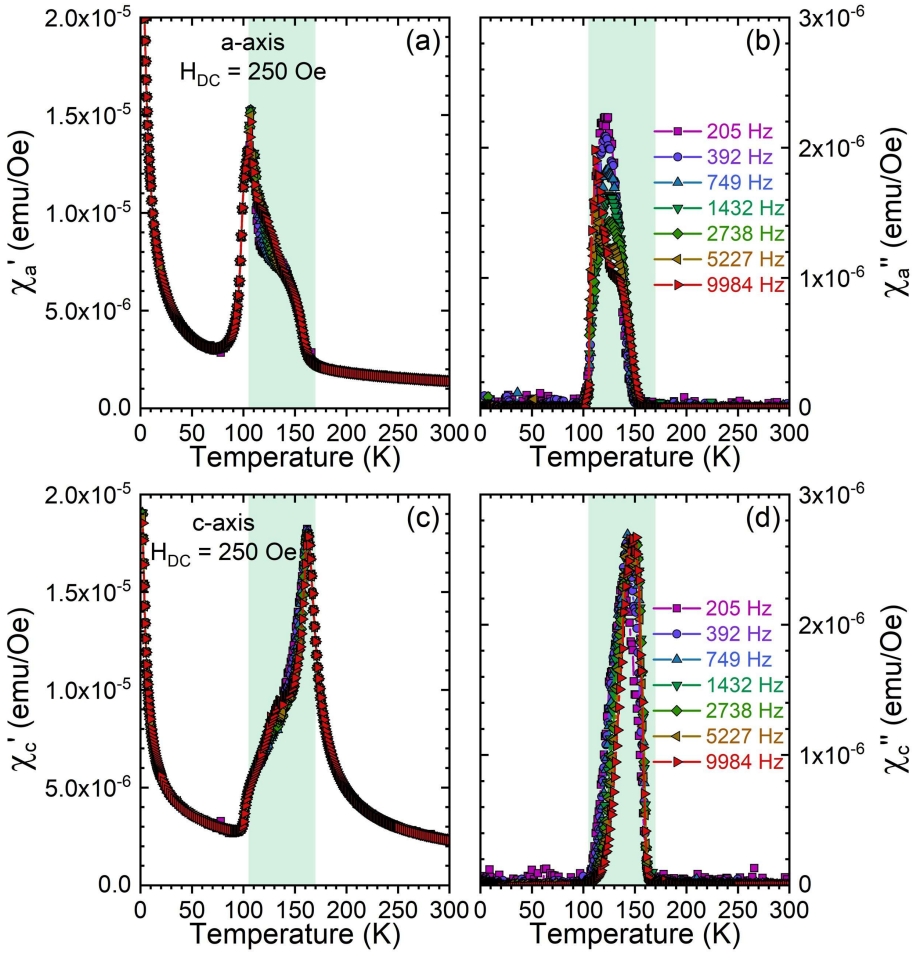


FIGURE 5.3: Temperature evolution of (a),(c) real χ' and (b),(d) imaginary χ" parts of AC magnetic susceptibility measured along a-axis and c-axis, respectively. The SRT temperature range is highlighted in green.

χ'(T) is smooth with temperature from 300 K to T_1 = 170 K, and no dispersion is observed in this range. On approaching T_1 from above, χ_c'(T) increases and peaks at 165 K, marking

the onset of SRT. Both χ_a'(T) and χ_c'(T) exhibit dispersion in the SRT interval. On further cooling and approaching T_2 = 105 K, χ_a'(T) shows a maximum peaking at this temperature, while χ_c'(T) decreases smoothly. $\chi_{a,c}$'(T) increases monotonically below T_2 no maximum could be observed down to 2 K, and dispersion is negligible.

χ"(T) shows a sharp and broad frequency dependent anomaly in the SRT interval. On cooling, the onset of SRT is marked by the steep increase of χ_c"(T) at 165 K, while χ_a"(T) only increases below 155 K. On the other hand, χ_a"(T) shows a frequency-independent peak at 105 K. In the SRT interval, the anomalies of both χ_a"(T) and χ_c"(T) are not symmetric with respect to the mid-point of SRT interval. It should be stressed that dispersion is more pronounced in the a-direction.

The aforementioned frequency dispersion observed in both the real and imaginary parts of the AC magnetic susceptibility points to a relaxation process, only activated during the spin reorientation range.

5.4. Discussion

5.4.1 Correlation between elastic and magnetic domain walls

Ferroelastic domain walls observed in Figure 5.1 adopt planar configurations to minimize their elastic strain energy. There is no equivalent shear strain contrast across 180° magnetic domain walls, which can, therefore, be strongly curved. In the magneto-optical images, the magnetic domains are either coincident with the ferrolastic domains, sharing the planar domain walls, or embedded within them, with curved domain walls. 180° walls contain a volume strain gradient, which likely accounts for their strong interaction with the ferroelastic domain walls, as an orientation with the minimum total strain energy for both combined. In areas that are out of range of strain fields from the ferroelastic domain walls, inherited from octahedral tilting, the magnetic domains have strongly curved walls, implying weak or absent coupling to the underlying crystallographic structure.

Across the SRT, magneto-optical images do not reveal the appearance of new ferroelastic domains, as it would be expected due to the symmetry lowering from orthorhombic to monoclinic. However, it is notable that the magnetic domain walls observed between 150 and 110 K have linear segments at a steep angle to the preexisting ferroelastic domain walls. As in the case of orthorhombic to monoclinic transitions in LaP_5O_{14} [135] and NdP_5O_{14} [133], ferroelastic domain walls within the SRT interval should align parallel to

$[001]$ and $[100]$. The $[001]$ is a common direction across $[100]$ walls, so they would not necessarily also become magnetic domain walls. However, a small change in the orientation of the magnetic moments occurs across $[001]$ walls, corresponding initially to a misorientation of $2\Delta\beta$, where $\Delta\beta$ is the change in the unit cell angle β from 90°. If rotation towards the a-axis proceeded in opposite directions on each side of the wall of neighboring domains (i.e. towards $[100]$ on one side and towards $[\bar{1}00]$ on the other side) they become magnetic domain walls with a misorientation of the magnetic moments across them. The misorientation would follow the temperature evolution of θ to give 90° walls at θ = 45° and 180° walls at θ = 90°. There is, therefore, the possibility of generating domain walls that have mixed ferroelastic and magnetic character during the spin rotation process.

5.4.2 Elastic softening and stiffening across SRT

Stepwise data softening at T_1 and stiffness at T_2 (on cooling) observed here for all the measured acoustic resonances of $NdFeO_3$ are closely similar to the pattern previously reported for the longitudinal acoustic waves velocities variations of the elastic constant C_{33}, for the spin reorientation transitions in $TmFeO_3$ [136, 137], $ErFeO_3$ [138, 139] and $YbFeO_3$ [140] single crystals. Additionally, these compounds also present two anomalies (dips) in the temperature evolution of the elastic constant C_{55} at T_1 and T_2, obtained in measurements of transverse acoustic waves velocities [136–140]. This pattern of softening was not observed in the RUS data from either $NdFeO_3$ or $SmFeO_3$ [134]. It is relevant to stress that in a RUS experiment the acoustic resonances involve predominantly shearing motions and the f^2 are expected to scale with different combinations of shear elastic constants C_{44}, C_{55}, C_{66}, C_{11}-C_{12}, C_{22}-C_{23}, C_{33}-C_{13}, etc.

It is well established that the predominant contribution to the temperature dependence of elastic constants at phase transitions arises from the coupling between spontaneous strain components, e_i (i = 1-6), and primary order parameter [141]. A coupling term that is linear in strain and quadratic in the order parameter would be expected to give rise to step-like softening [137], like the ones reported for $NdFeO_3$. For $RFeO_3$ exhibiting spin reorientation transition, the primary order parameter is the angle θ between ***F***, net ferromagnetic moment, and the c-axis (see Appendix A.6) [90].

To correlate strain and order parameter θ, let us first calculate the strain components evolution with temperature. Figure 5.4 shows lattice parameters of $NdFeO_3$ determined

by neutron powder diffraction (Slawinski *et al.* 2005 [70]) and synchrotron X-ray diffraction (Slawinski *et al.* 2007 [74]).

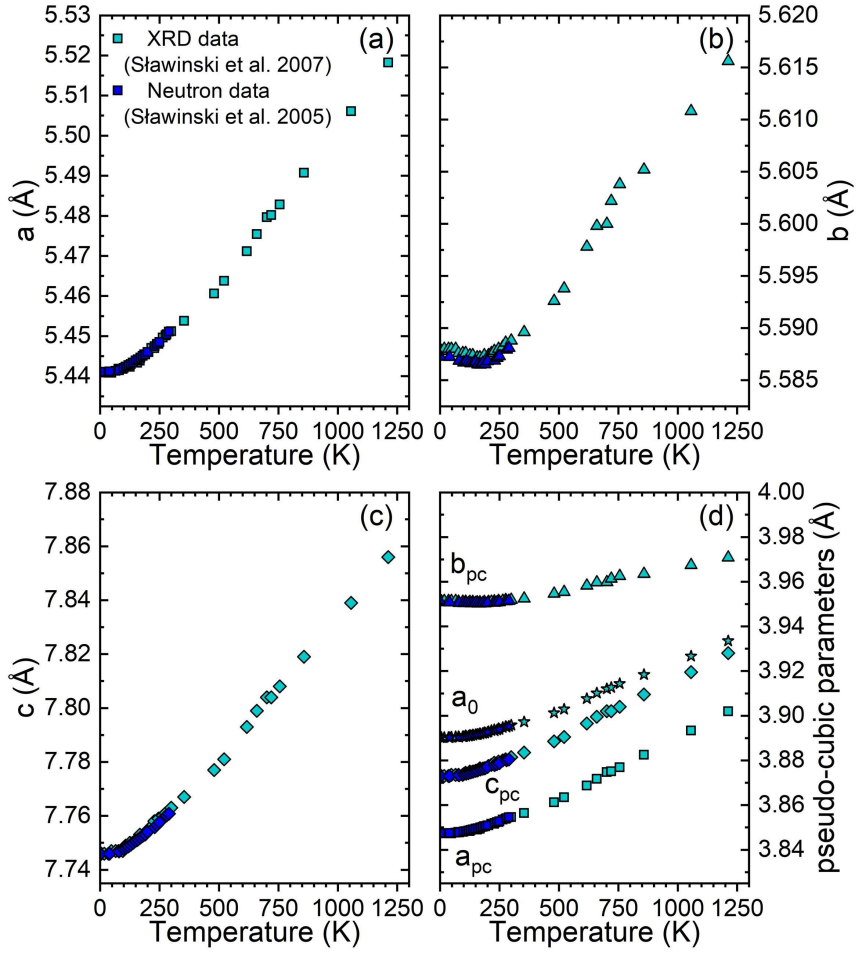


FIGURE 5.4: (a)-(c)Lattice parameters in the *Pbnm* setting obtained from neutron powder diffraction [70] and XRD [74]. (d) Same data presented as pseudocubic parameters, using cubic structure as a reference.

A small anomaly in the b-parameter near T_1 is the only visible hint for a magnetoelastic coupling, see Figure 5.4(b), signifying that there are, nevertheless, measurable spontaneous strains accompanying the SRT. For the purpose of calculating symmetry-adapted strains according to Carpenter *et al.* [141] and McKnight *et al.* [142], we consider the pseudocubic lattice parameters of space group setting P*bnm*: $a_{pc} = \frac{a}{\sqrt{2}}$,$b_{pc} = \frac{b}{\sqrt{2}}$ and $c_{pc} = \frac{c}{2}$. A reference parameter for the cubic structure has been determined as $a_0 = \left(\frac{abc}{4}\right)^{1/3}$ at each temperature (plotted in Figure 5.4(d)). Linear strains were determined as [142]:

$$\begin{aligned} e_1 &= \frac{c_{pc} - a_0}{a_0} \\ e_2 &= \frac{b_{pc} - a_0}{a_0} \\ e_3 &= \frac{a_{pc} - a_0}{a_0} \end{aligned} \tag{5.1}$$

For P*bnm* structure, the unique axis of orthorhombic e_{oy} and tetragonal e_{ty} strains is parallel to b-axis, and those strains are defined as [142]:

$$e_{oy} = e_4 = e_2 - e_3$$
$$e_{ty} = \frac{2e_1 - e_2 - e_3}{\sqrt{3}} \tag{5.2}$$

Symmetry-adapted strain only take into account octahedral tilting, any additional superimposed strain is considered to arise from magnetoelastic coupling. Values of e_4 and e_{ty} derived from the lattice parameter data in Figure 5.4, are shown in Figures 5.5(a) and 5.5(b), respectively.

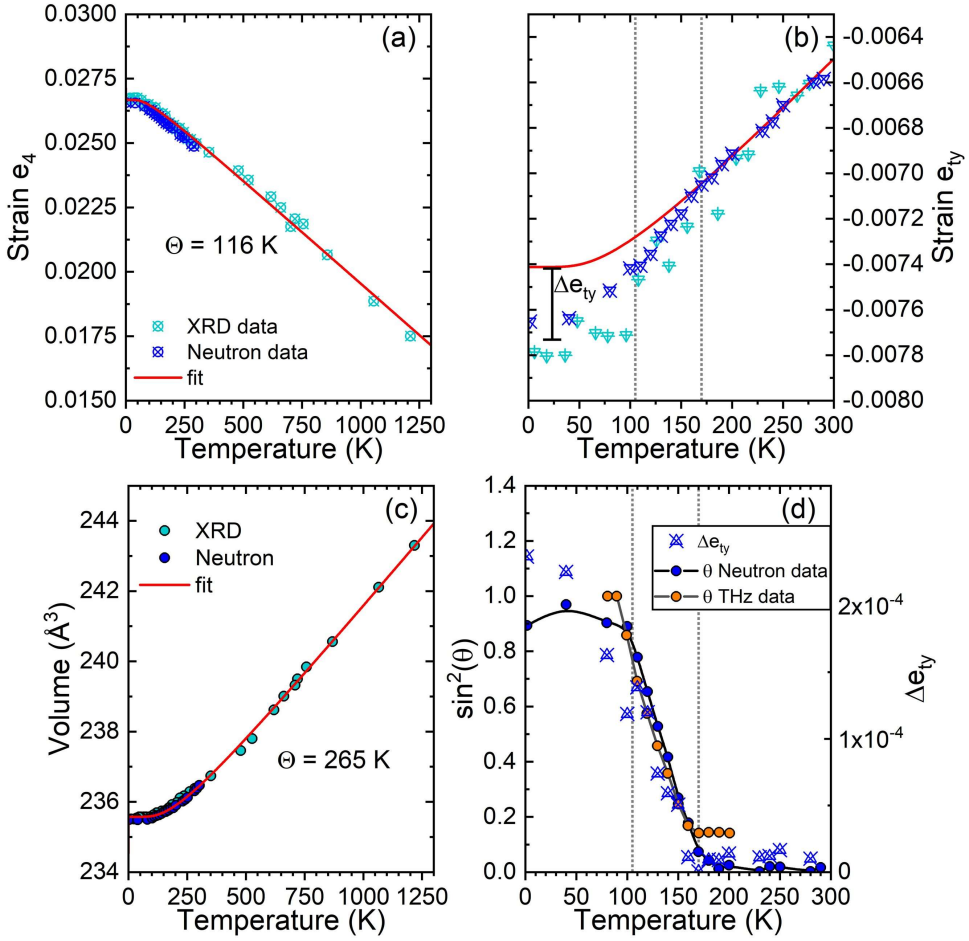


FIGURE 5.5: (a) Variation of e_4 determined from lattice parameters given in Figure 5.4. The red curve is a fit of Equation 5.3 to values derived from the lattice parameters of XRD [74] and neutron data [70]: y_0 = 0.0276, A = -8.03E-6, Θ_s= 116 K. (b) Variation of e_{ty} with fit of Equation 5.3 to data at T > 170 K, extrapolated to lower temperatures. Fit parameters for the data derived from neutron data [70]: y_0 = -0.0079, A = 4.48E-6, Θ_s fixed at 116 K. (c) Variation of unit cell volume. Red curve is fit of Equation 5.3 simultaneously to data at T > 170 K and T < 105 K. Fit parameters for the data derived from XRD data[74]: y_0 = 233.478, A = 0.0079, Θ_s= 265 K. (d) Variations of $sin(2\theta)$ (right axis) calculated from neutron data [70] and THz spectroscopic data [77]; and changes of tetragonal shear strain Δe_{ty}(left axis). Vertical dashed lines at 105 and 170 K mark approximate limits of the SRT interval.

Strain e_4 does not show any overt anomalies associated with the SRT (Figure 5.5(a)), whereas e_{ty} shows a clear break in slope at ~170 K (Figure 5.5(b)), pointing for a magnetoelastic coupling. Therefore, strain e_4 can be used as reference for fitting model considering volume changes only due to octahedra tilting, described by [143–145]:

$$y(T) = y_0 + A\Theta_s \coth(\frac{\Theta_s}{T}) \tag{5.3}$$

where y_0 and A are constants, and Θ_s is the tilting saturation temperature. Changes in e_{ty} due to spin rotation, Δe_{ty}, were calculated as the difference between observed values of e_{ty} and values given by extrapolation of the fit of Equation 5.3 to data in the interval ~170-300 K, fixing Θ_s = 116 K. The variation of Δe_{ty} with temperature is shown in Figure 5.5(d) (right axis), and it is consistent with a linear variation of $sin^2(\theta)$ in the temperature between $T_2 \leq T \leq T_1$. Data for θ was calculated/obtained from literature (see also Appendix A.6) [70, 77]. In Figure 5.5(c), the calculated unit cell volume does not show any obvious slope change that might be associated with the magnetic reorientation.

Strains e_i, i =1-3, couple as $\lambda_i e_i sin^2(\theta)$ (i.e. linear in strain and quadratic in the order parameter), which is confirmed by a linear correlation between $sin^2(\theta)$ and a small tetragonal shear strain, Δe_{ty} in Figure 5.5(d).

Magnetoelastic coupling accompanying spin rotation in $NdFeO_3$ is rather weak in comparison with strain coupling at structural transitions. This is the case of the shear strain due to octahedral tilting in $LaAlO_3$, which varies up to $1.5x10^{-3}$ and gives rise to the softening of the shear modulus by almost 30% [146]. In $NdFeO_3$, the change in tetragonal shear strain, Δe_{ty}, identified in Figure 5.5(d) is only up to $0.2x10^{-3}$, almost an order of magnitude smaller, and, consequently, the elastic softening is only 1%.

Strain e_5 couples linearly with the order parameter, $\lambda_5 e_5 sin(2\theta)$, resulting in a softening of C_{55} as the transition is approached from both sides in a manner that is characteristic of pseudoproper ferroelastic transitions [135]. In a good approximation, e_5 scales with $cos\beta$, but deviations of the monoclinic angle β from 90° have not yet been detected in diffraction measurements [70, 74]. Taking the experimental limit of resolution as $|90-\beta| < 0.006°$, it would give $e_5 < 0.0001$; the fact that the coupling is weak, probably accounts for the absence of any elastic softening attributable to $\lambda_5 e_5 sin(2\theta)$. Instead, the observed stepwise softening/stiffening at the SRT limits confirms that the linear-quadratic term $\lambda_5 e_5 sin^2(2\theta)$ dominates.

To assess whether there are significant differences in elastic properties between the orthorhombic structures on either side of the SRT, a detailed analysis of RUS data is presented in Figure 5.6, for the representative frequency peak 1416 kHz. The data was fitted with the same model of Equation 5.3, assuming the temperature evolution of elastic stiffening scales with changes in volume [143–145].

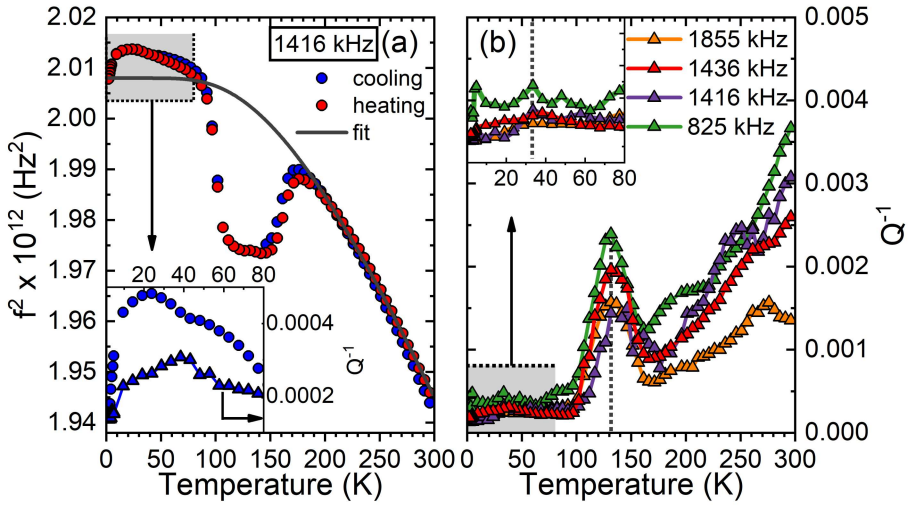


FIGURE 5.6: (a) Temperature dependence of f^2 of 1416 kHz resonance peak and fit of Equation 2.5 representing elastic softening effects as T$\rightarrow$ 0 K. Fit performed in 210-300 K range with Θ_s fixed at 265 K and extrapolated to T$\rightarrow$ 0 K. Inset shows magnification below 80 K, where softening below $\sim$25K is highlighted. (b) Temperature dependence of Q^{-1} for several resonance peaks in a broad spectral range, showing how the maximum losses are frequency-independent. Another small frequency-independent peak at $\sim$35 K is shown in the inset.

The curve in Figure 5.6(a) was determined by the best fit of Equation 2.5 to data between 210-300 K range, with Θ_s fixed at 265 K. The choice for Θ_s was based on the fitting to the volume temperature evolution, assuming that the elastic stiffening with falling temperature occurs due to volume contraction, for which Θ_s = 265 K provides a good description (Figure 5.5(c)). The extrapolation of the fitting curve to 0 K brings the baseline curve away from the experimental data for temperatures below T < T_1 = 170 K.

Indeed, a structural transition from orthorhombic P*bnm* to the monoclinic $P2_1/n$ is predicted during SRT, which should impact the elastic constants. However, below T_2 = 105 K, the orthorhombic structure is recovered; therefore, one would expect a recovering trend of the elastic constants, which is not the case, otherwise, Equation 2.5 would describe the data below T_2. This result contrasts with the one observed in $SmFeO_3$ (SFO), for which f^2(T) is described above (T > T_1^{SFO} = 480 K) and below SRT (300 K< T < T_2^{SFO} = 450 K) by Equation 2.5 (see Figure 5.7).

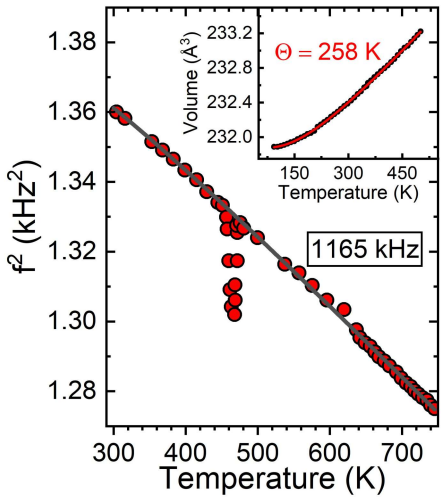


FIGURE 5.7: Temperature dependence of f^2 of 1165 kHz resonance peak of $SmFeO_3$, published in [134]. Inset shows the variation of unit cell volume of $SmFeO_3$, with fitting Equation 2.5 with parameters: y_0= 230.663, A = 0.00469, Θ_s= 258 K. Fixing Θ_s, the same model was used to perform a fit to the RUS data f^2 in 480-750 K range and extrapolated to 0 K.

The main difference between $SmFeO_3$ and $NdFeO_3$ concerns the temperature difference of T_2 and the non-cooperative ordering of the rare-earth ions; while for $NdFeO_3$ there is no difference i.e, $T_2 \approx T_{noncoop}^{Nd} \approx 100$ K, for $SmFeO_3$, the Sm^{3+} ions order non-cooperatively around 100 K but the lower limit of SRT is at 450 K, therefore, $T_2 \gg T_{noncoop}^{Sm}$. The RUS measurements for $SmFeO_3$ were recorded above 300 K, which prevented us from confirming the assumption that below 100 K the $f^2(T)$ would also deviates from the model fit, indicating that the rare-earth magnetism couples with the elastic constants below 100 K. Yet, for $NdFeO_3$, the magnetization data reported in [71] and the XMCD data that will be discussed in the Chapter 7, give us confidence to assign the deviations to the effect of Nd-subalttice non-cooperative ordering, which changes the magnetoelastic coupling below T_2 =105 K.

All resonances soften just below 25 K, though with different magnitudes, depending on the particular resonance peak. The inset of Figure 5.6(a) provides a representative example. Individual resonances depend on different combinations of elastic constants underlying the resonance peak. The mechanism for such softening below 25 K cannot be anything other than a precursor effect of the magnetic instability associated with the cooperative ordering of the Nd^{3+}-sublattice at T_N^{Nd} = 1.05 K [67]. This interpretation is supported by a previous neutron diffraction experiment, focused on the Nd-sublattice magnetism, which evidenced the emergence of the magnetic reflection (100) at 25 K, specifically assigned to the magnetic diffraction from the Nd-spin sublattice, increasing its intensity on cooling

towards T_N^{Nd} [67].

Another anomalous temperature dependence is ascertained for some resonance peaks at 35 K. As can be seen in Figure 5.6 insets, the 1416 kHz resonance peak exhibits anomalous temperature dependence in both f^2 and Q^{-1} . An anomaly in the temperature dependence of the b-parameter, seen as a small peak in b(T) at 40 K, was already reported [70]. The absence of any anomalous temperature dependence in DC and AC magnetic susceptibility at 40 K rules out the magnetic origin of this structural distortion.

5.4.3 Acoustic loss and domain wall mobility

In agreement with the observations for $SmFeO_3$ [134], the increase in loss is limited to the SRT temperature range, and is symmetrical about the midpoint between T_1 and T_2, as illustrated by Figure 5.6(b). The acoustic losses across the spin reorientation process cannot be attributed to pinning/freezing motions of defects on the sample, which could be thermally activated, as the Q^{-1} peaks all at the same temperature, being frequency-independent. This feature rules out possible pinning/freezing defects of the sample that have a relaxational nature. Any contribution from the motion of twin walls observed in Figure 5.1 can also be ruled out, because the ferroelastic domain walls, which arise from symmetry changes due to octahedral tilting in orthorhombic perovskites (such as $SrZrO_3$ [142] and $Ca_{1-x}Sr_xTiO_3$ [147]), are typically immobile under stress and frequency conditions of the RUS experiment. If the domains walls were mobile down to low temperatures, as in the case of $BaCeO_3$ [148], they would cause substantial attenuation outside the SRT interval. Consequently, the acoustic loss mechanism has to involve a defect present only across the SRT interval, where the monoclinic symmetry is predicted, which is coupled to some shear strain such that it moves in response to a dynamic shear stress. This restricts the possibilities effectively to ferroelastic domain walls that arise as a consequence of the loss of point group symmetry $mmm \longrightarrow 2/m$ or magnetic domain walls that acquire a ferroelastic strain component during the rotation of magnetic moments.

The symmetrical pattern loss as $T \longrightarrow T_1$ and $T \longrightarrow T_2$ within the SRT interval suggests a correlation with the temperature dependence of $sin(2\theta)$. Figure 5.8 shows a relationship between $sin(2\theta)$ and the temperature variation in Q^{-1} relative to a non-linear baseline, ΔQ^{-1}, for the resonance peak with frequency 1416 kHz at room temperature.

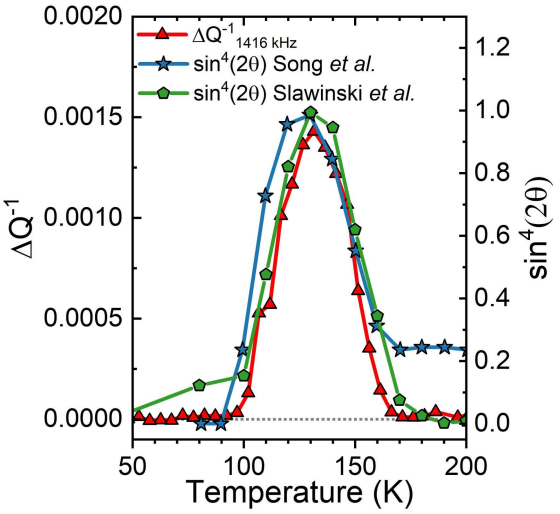


FIGURE 5.8: Comparison between Q-1 of resonance frequency 1416 kHz relative to a non-linear baseline, ΔQ^{-1}(left-axis), and $sin^4(2\theta)$ (right-axis) calculated from neutron data [70] and THz spectroscopic data [77].

Note that $sin(2\theta) = 0$ when θ= 0° and 90°, and maximum when θ= 45°. In fact, ΔQ^{-1} scales closely with $sin^4(2\theta)$. A phenomenological approach considering motion of ferroelastic domain walls in the monoclinic structure is presented in Appendix A.7, and demonstrates that acoustic losses in the SRT are indeed related with changes in elastic constant C_{55}:

$$Q^{-1} \propto e_5^4 \propto sin^4(2\theta) \tag{5.4}$$

Low values of both χ" and Q^{-1} above T_1 and below T_2 indicate that magnetic and ferroelastic domain walls in the orthorhombic structures are immobile. Within the SRT, new ferroelastic domain walls and magnetic domain walls acquire some shear strain contrast and become mobile. In this context, an important consideration may relate to domain wall thicknesses since thick walls are less likely to be pinned by point defects in a crystal than thin walls. The width, w, of ferroelastic walls is typically on the order of only a few unit cells, but they can be substantially wider in the narrow temperature interval below a second order transition [149]. Magnetic domain walls are likely to be $\sim$10-100 times wider than typical ferroelastic domain walls, depending on the degree of magnetic anisotropy. A significant increase in values of w due to mixed ferroelastic/magnetic character and the proximity to two second order transitions would explain why the magnetic domain walls become mobile in the monoclinic structure (SRT temperature range).

5.4.4 Magnetic susceptibility vs elastic compliance

Magnetic susceptibility is a second rank tensor property, $\chi_{ij} = \frac{M_i}{H_j}$, where M_i is the moment induced by the application of a field H_j. The equivalent relationship for elastic compliance, S_{ij} in Voigt notation for a fourth rank tensor, is $S_{ij} = \frac{e_i}{\sigma_j}$, where e_i is a strain induced by stress σ_j. Without considering a specific orientation, $S = \frac{1}{C}$, where C is the related elastic constant. Results from the acoustic resonance peak with frequency 1416 kHz are plotted as $1/f^2$ in Figure 5.9(a), to represent the variation of some combination of single crystal elastic compliances rather than the elastic constants themselves. This shows strikingly close similarity with the variation of modulus of χ in Figure 5.9(b) and 5.9(c), measured along the a-axis and c-axis respectively. Changes in both reflect a common mechanism arising from coupling of M and e with the order parameter, θ, although the magnetic susceptibility has a strong orientation dependence.

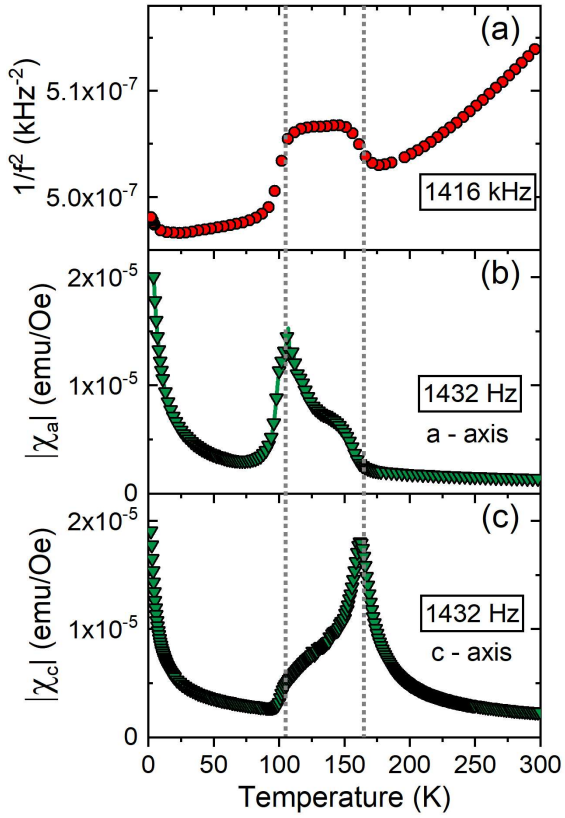


FIGURE 5.9: Temperature dependence of (a) $1/f^2$, which scales with elastic compliance S, for resonance peak 1416 kHz; modulus of AC magnetic susceptibility $|\chi|$ measured along (b) a-axis and (c) c-axis, for frequency 14132 Hz.

Outside the SRT interval a field, H or σ, induces changes in M or e that reflect intrinsic properties of orthorhombic $NdFeO_3$, whether the alignment of M is parallel to $\langle 001 \rangle$ or $\langle 100 \rangle$. In the monoclinic structure there is an additional relaxation of θ due to the coupling

so that changes in M and e are slightly greater than they would otherwise have been. Hence there is an increase in both magnetic susceptibility and compliance values during the spin reorientation process.

5.5. Summary

This Chapter investigates the magnetoelastic coupling and domain wall dynamics of $NdFeO_3$, through a combination of magneto-optical imaging, RUS and AC magnetic susceptibility data. A phenomenological framework in which the elastic constant is a coupling term linear in strain and quadratic in the magnetic order parameter θ, described the observed softening/stiffening of resonance peaks at the spin reorientation transition limits. Correlations between acoustic loss and the imaginary part of the AC magnetic susceptibility provide evidence in particular for domain walls with mixed ferroelastic/magnetic character and theirs mobility during the SRT. Moreover, these results are fully compatible with the symmetry lowering from orthorhombic to monoclinic across the spin reorientation. Lastly, the magnetoelastic behaviour at $T < T_2$ hints for a crosstalk between the Nd- and Fe-sublattices that will be further explored in the following Chapters. Spin-lattice interaction is highlighted in this Chapter and opens new ways to explore the acoustic control of magnetism in $NdFeO_3$.

6. Monoclinic phase across SRT in $NdFeO_3$

In the previous Chapter, it was demonstrated that losses in the elastic constants and AC magnetic susceptibility are caused by the mobility of domain walls during the SRT range, having mixed ferroelastic/magnetic nature. These results are compatible with the symmetry lowering during the SR process. Indeed, the continuous rotation of ***F*** vector in the ac-plane during Γ_{24} phase implies a monoclinic symmetry in this phase, as supported by the arguments presented in Chapter 1 and Appendix A.2.

However, this symmetry lowering across SRT has not been experimentally observed neither in $NdFeO_3$ nor in any other rare-earth ferrites with same transition sequence: $\Gamma_2 \longrightarrow \Gamma_{24} \longrightarrow \Gamma_4$. X-ray/neutron diffraction measurements in several ferrites such as $TmFeO_3$ [89], $ErFeO_3$ [88], and $NdFeO_3$ [70, 74] show smooth changes in the lattice parameters with temperature, but no significant anomaly/ structural distortion was detected near T_1 and T_2. Based on the assumption that in a single crystal if the symmetry lowers then a multidomain polycrystal state is formed, structural texture modifications were investigated in single crystals of $TmFeO_3$ and $ErFeO_3$, but no change was detected in the SR region [88, 89]. Based on the RUS data analysis of $NdFeO_3$, presented in Chapter 5, a plausible explanation for the undetected monoclinic structure is that the distortion amplitude is smaller than the experimental resolution.

In order to verify the hypothesis of a transition P*bnm* $\longrightarrow$P$2_1/n$ in the SR region, local probes can be more appropriated than diffraction techniques to detect in this case, the predicted splitting of Wykcoff positions. To further strength this interpretation, in this Chapter, we propose to prove the symmetry-breaking across the Γ_{24} phase in a single crystal of $NdFeO_3$, using a non-conventional technique: muon-spin rotation spectroscopy. This technique probes the local magnetic fields at the muons' stopping sites. These stopping sites are indirectly associated with the crystallographic structure of the material, therefore, if any structural distortion occurs, the muons should be able to sense it. The findings reported in this Chapter are part of an article in preparation.

6.1. Muon-spin:local magnetic probes

6.1.1 Symmetry considerations

Following the hypothesis of a symmetry lowering , there must be a group-subgroup relation between the two magnetic orthorhombic symmetries at Γ_4 (P*b'n'm*) / Γ_2 (P*bn'm'*) phases and the monoclinic symmetry at Γ_{24} phase. This relation is illustrated in Figure 6.1 and justifies the choice of space group $P2_1'/n'$.

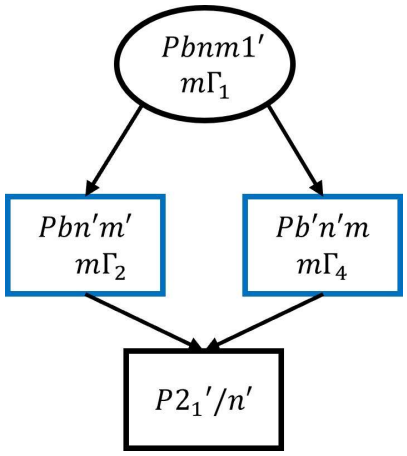


FIGURE 6.1: Group-subgroup relation between non-magnetic P*bnm* space group and magnetic monoclinic space group of SRT, obtained using k-SUBGROUPSMAG tool from Bilbao Crystallographic Server. $m\Gamma$ stems for the magnetic irrep, referred in the text simply as Γ.

The transition from P*b'n'm*/P*bn'm'* to $P2_1'/n'$ results in a splitting of the Wyckoff positions of Fe-sites and O2-sites, as presented in Table 1.5 of Chapter 1. Figure 6.2 illustrates the spin structures from the ac-plane perspective for $NdFeO_3$, where is noticeable the Fe-site splitting into two non-equivalent sites: Fe1 and Fe2.

As local magnetic probes, muons must be able to distinguish between the two non-equivalent iron sites during the monoclinic structure (Γ_{24}), while for the orthorhombic phases (Γ_4 and Γ_2), only one iron site should be sense by the muon-spin.

6.1.2 μSR analysis

Muon-spin rotation spectroscopy (μSR) measurements were performed on an oriented $NdFeO_3$ single-crystal at several fixed temperatures between 5 and 200 K, using GPS instrument at PSI. The time evolution of the muon spin polarization was determined from

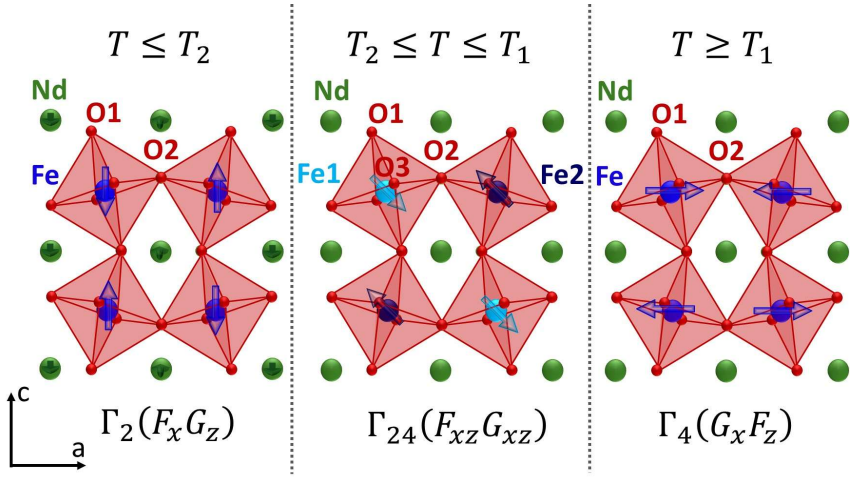


FIGURE 6.2: Schematic view of the spin structures for the different magnetic configurations of $NdFeO_3$ in the ac-plane.

the asymmetry of decaying positrons between two pairs of detectors: Up-Down (UD) and Forward-Backward (FB). See Figure 2.3 for further detail on the measurement geometry.

Figure 6.3 shows the time-dependent asymmetry, $A(t)$, recorded at 200 K for each detector pair (UD, FB) and the respective fast Fourier transform (FFT). In both $A(t)$ curves, the oscillations indicate that at 200 K the magnetic phase of $NdFeO_3$ is ordered, expected as the Fe^{3+} ions order at T_N^{Fe} = 687 K [68], otherwise, in a paramagentic phase, these oscillations would be absent. They are associated with the implanted muon-spin precession frequencies ν, and depend on the distribution of internal magnetic field, B_μ, at the muons stopping sites [99]:

$$\nu = \lambda_\mu \frac{B_\mu}{2\pi} \tag{6.1}$$

where the muon gyromagnetic ratio is λ_μ = 2π x 135.5 MHz.T^{-1}.

These precession frequencies are obtained directly from fitting the time-dependent total asymmetry $A(t)$ of each detector pair, in the 0.002 ≤ t ≤ 0.2 μs time interval. At each recorded temperature, $A(t)$ was fitted using a combination of oscillatory (i), non-oscillatory ($nosc$) and background (bgr) components given by the expression:

$$A(t) = \sum_i A_i e^{-\lambda_i t} \cos(2\pi\nu_i t) + A_{nosc} e^{-\lambda_{nosc} t} + A_{bgr} \tag{6.2}$$

where A is the asymmetry, λ the relaxation and ν the frequency. Note that only the oscillatory components give us information regarding the local magnetic fields at the mu stopping sites in the $NdFeO_3$ sample. The background component, as its name indicates, is a compensation term to describe the background introduced by an unbalanced factor,

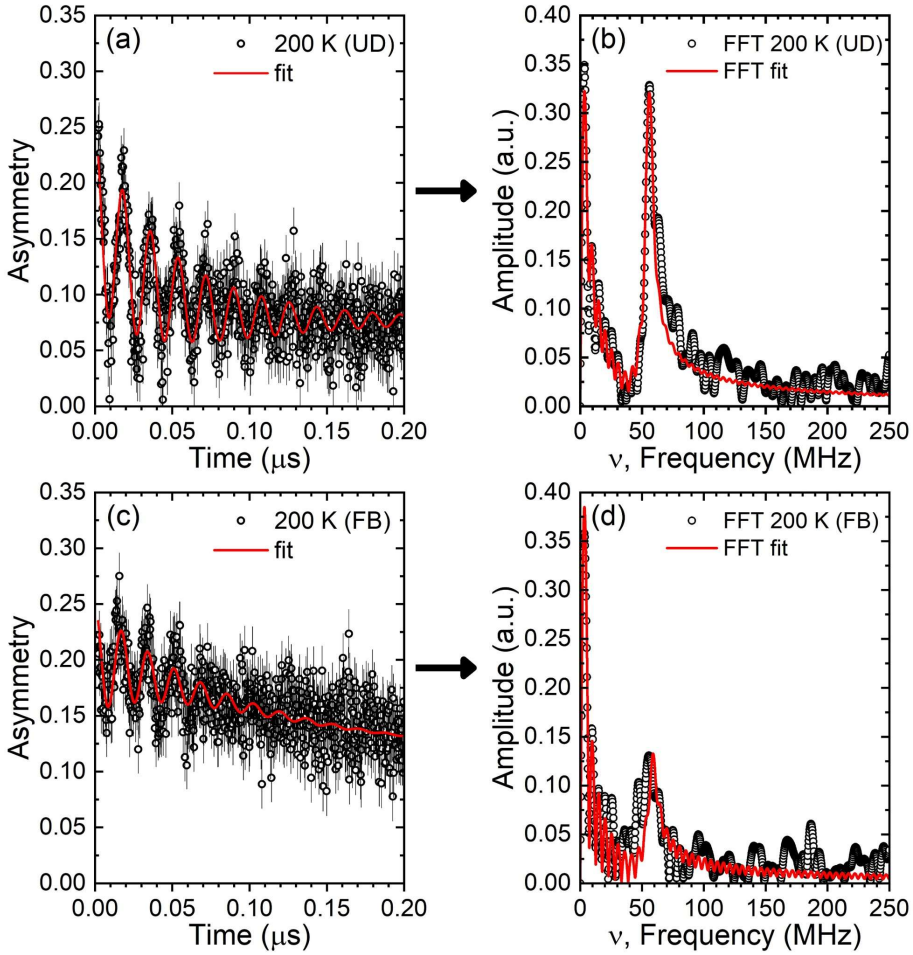


FIGURE 6.3: Representative time-dependent asymmetry, recorded at 200 K, for detector pairs: (a) Up-Down (UD) and (c) Forward-Backward (FB); (b),(d) respective fast Fourier transform. Fitting curve (red) of asymmetry data using Equation 6.2.

α, between the detectors. This factor is calibrated for each detector pair and fixed in the same value for all temperatures: α_{UD} = 0.9 and α_{FB} = 1.17. The non-oscillatory term was included in the fitting model to improve the quality of the fit, but its origin is somehow uncertain and it can be seen as a background signal from the sample. Due to its non-oscillatory nature, this term will not change any conclusion drawn from the precession frequencies.

The FFTs help on the visualization of the sample characteristic precession frequencies, specially when more than one frequency describe the $A(t)$ signal. Following the same procedure presented in Figure 6.3, the FFTs for complete set of temperatures are shown in Figure 6.4(a) for the detector pair UD and in Figure 6.4(b) for the detector pair FB.

Qualitatively, during the Γ_4 phase (T > T_1 = 170 K), $NdFeO_3$ spectral signature is dominated by a single component, more prominent in the UD detector pair but also visible in

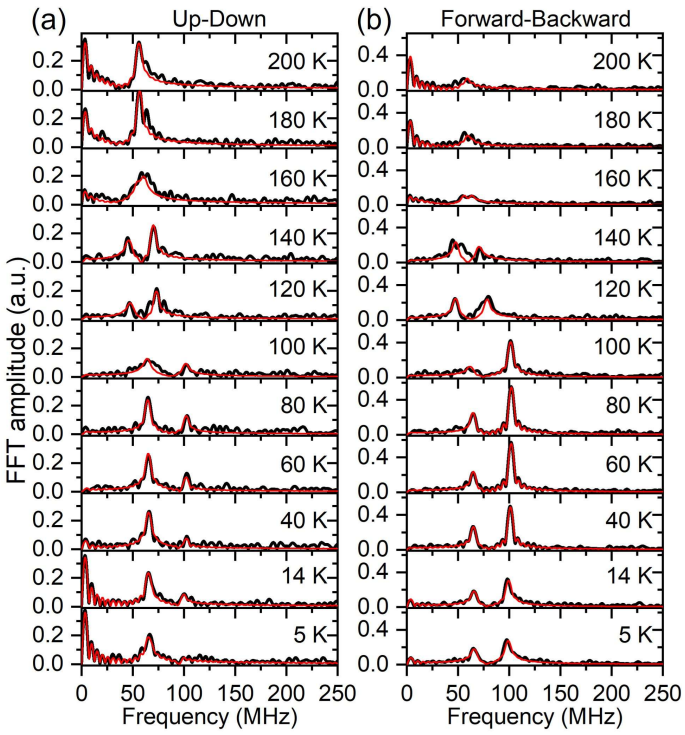


FIGURE 6.4: Fourier transform of time-dependent μSR signal of NdFeO3 for several fixed temperatures, with corresponding fits from Eq.6.2, for detector pairs: (a) Up-Down (UD) and (b) Forward-Backward (FB).

the FB detector pair. Checking the measurement configuration of Figure 2.3, this indicate a preferential muon decaying direction in the c-direction. In the SRT temperature range (105 K < T < 170 K), the spectral signature splits into two with opposite precession frequency trends: one increases (up to 70 MHz) while the other decreases (down to 45 MHz)is divided into two components, where lower frequency component tends to be smaller in amplitude than higher frequency one for UD, and swapping their amplitude trend for FB. At the Γ_2 phase (T < T_2), also two components are visible, with opposite amplitude trends between detector pairs, however, while the lower component peaks at around 65 MHz, a similar value when compared with T > T_1 values, the higher spectral component peaks at $\sim$100 MHz.

Temperature evolution of oscillating components parameters (frequency ν, asymmetry A and relaxation λ), obtained by fitting Equation 6.2 to $A(t)$ signal, are shown in Figure 6.5.

In Figure 6.5(a), it is noteworthy that, for a fixed temperature, frequencies in each of the detector pair (UD- close symbols; FB- open symbols) correspond to the same oscillating components; i.e. as illustrated by FFTs of Figure 6.4, the number and frequencies of the components remain the same and evolve similarly with temperature; only the amplitude varies between detector pairs.

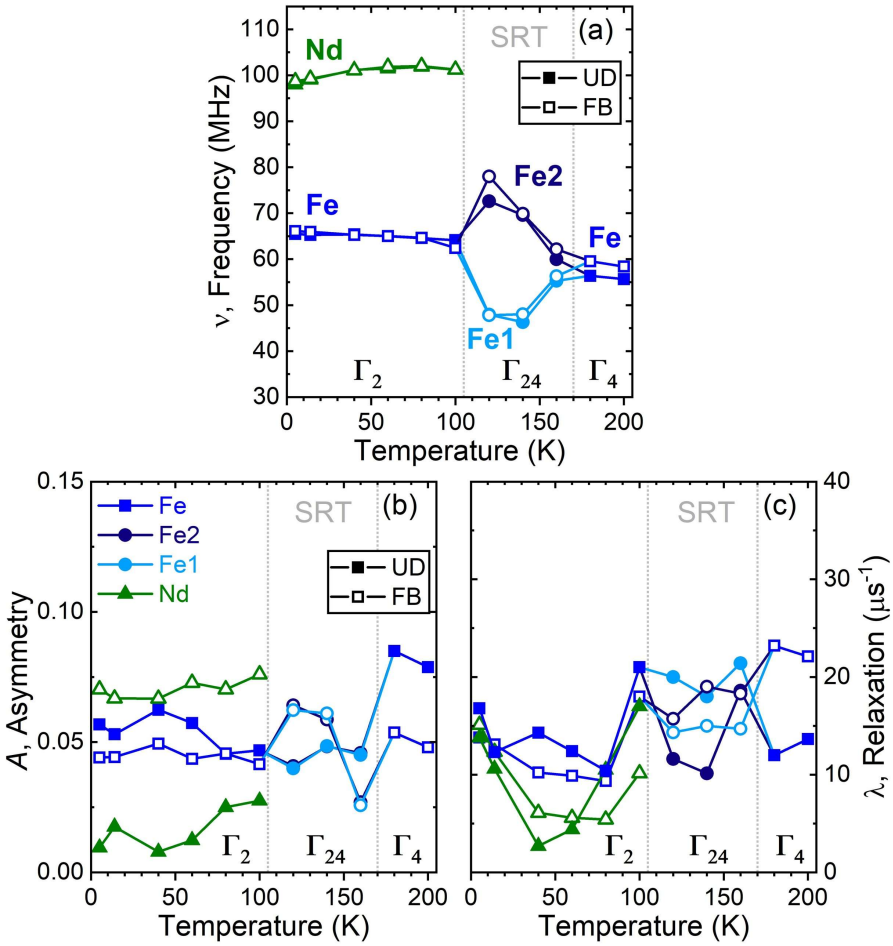


FIGURE 6.5: Temperature evolution of (a) frequency, (b) asymmetry and (c) relaxation of the spectral oscillating components. These parameters were obtained from the fit of Equation 6.2 to the time-dependent μSR signal. Vertical dashed lines define the SRT region. UD- close symbols; FB- open symbols.

According to our interpretation of Figure 6.5(a), we have the following scenario:

- for T > T_1, the μ stops at equivalent sites and probes essentially the same field, so a single oscillating component is observed. In Γ_4 phase, the Fe-sublattice is magnetically order, while the Nd-sublattice remains paramagnetic, hence local magnetic field sense by the muon should come from the Fe ions. So, we assign this single oscillation to a muon stopping sites close to the four equivalent Fe sites, which will contribute with the same exact magnetic field.

- for T_2 < T < T_1, two oscillating components are now observed with different frequencies comparing to the single frequency of Γ_4 phase. If the symmetry is lowered to the $P2_1'/n'$ space group, the four equivalent Fe split into two Fe sites: Fe1 and Fe2, as illustrated in Figure 6.2. The muon stopping site close to the four Fe are no longer equivalent, splitting into two different sites, therefore the muons close to Fe1 will

sense a magnetic field different from the ones stopping close to Fe2: two oscillating components.

- for T < T_2, the μ stopping site at $\sim$65 MHz is recovered, which is consistent with the recovering of four Fe sites equivalence. In the Γ_2 phase, the Fe spins direction is rotated 90° with respect to Γ_4 phase, therefore the strength of the local magnetic field can be different, i.e. oscillation frequency has a slightly different value. Additionally, other component is observed at high frequencies, that we assign to the Nd-sublattice. The fact that this high-frequency component only appears below 100 K is in agreement with the non-cooperative ordering of the Nd^{3+} ions, already observed in magnetization [71] and RUS experiments, and confirmed by the XMCD analysis presented in the next Chapter.

Note that the O-sites also split during SRT, however, contrarily to Nd^{3+} and Fe^{3+}, oxygen is a non-magnetic ion; even if the muon stops near an oxygen, the local magnetic field contributions will never come from this ion, therefore we assume that the muons are ”blind” to the O-sites.

Turning now to the temperature dependence of the components asymmetry, depicted in Figure 6.5(b), the first notable point is the nearly constant trend observed within each magnetic phase. Apart from a slightly higher asymmetry for the Fe site (UD) in the Γ_4 phase, the remaining Fe components remain nearly constant across the entire temperature range. As mentioned previously, this asymmetry could be related to a preferential decay direction along the c-axis, as the UD detectors primarily probe in that direction. This would not be surprising, given that the net magnetic moment of $NdFeO3$ points along the c-axis in the $\Gamma 4$ phase. During the Γ_{24} phase, the asymmetries associated with the two Fe sites (Fe1 and Fe2) were constrained to be equal. By doing so, we assume that the rotation of Fe moments in the ac-plane occurs at a similar rate. In the Γ_2 phase, the preferential decay direction of the Fe-sublattice net magnetic moment cannot be inferred, as both detector pairs exhibit similar asymmetries. However, for the Nd sublattice, the asymmetry is much more prominent in the FB pair, indicating a preferential decay direction along the a-axis. This observation is in good agreement with the net magnetic moment created by Nd^{3+} ions [64].

The relaxation plot in Figure 6.5(c) provides insight into the inhomogeneity of local magnetic fields at the muon stopping sites. Overall, some component relaxations peak near the boundaries of the SRT region, suggesting enhanced magnetic fluctuations or field

inhomogeneity—consistent with a restructuring of the magnetic order. A noticeable increase in relaxation is also observed as the temperature decreases, approaching the Nd ordering temperature.

Remarkably, throughout several fitting attempts prior to arriving at the final result, the temperature dependence of the oscillation frequencies remained unchanged. In fact, from an FFT perspective, the asymmetry and relaxation parameters primarily influence the amplitude and width of the spectral components, which are more prone to slight adjustments during each refinement. However, the sharp nature of the spectral features results in well-defined frequencies. This provides strong confidence in the reliability of the extracted frequency values. Nonetheless, the interpretation of these findings deserves to be further investigated by comparing two hypothesis: splitting of components or coexistence of components.

6.2. Hypothesis: splitting or coexistence?

The lack of experimental evidence for a symmetry-lowering lead some authors to consider the orthorhombic P*bnm* symmetry across the spin reorientation region [70, 74, 75]. This assumption means that the SR range should be a result of coexistence the two orthorhombic magnetic phases: Γ_2 + Γ_4, where no symmetry-lowering should be excepted. Beside the RUS analysis presented in the previous Chapter, which points for the formation of new ferroelastic domains during the SRT linked to a monoclinic structure, the μSR analysis is essential to unravel this issue. By predicting how the component oscillations associated with the muon stopping site evolve in case of: a symmetry-lowering, Figure 6.6(a), or a coexistence of symmetries, Figure 6.6(b).

As argued before, a symmetry-lowering from P*bnm* $\longrightarrow$ P$2_1/n$ results on a splitting of the four equivalent Fe sites into two inequivalent sites. Therefore, the effective magnetic field sensed by the muon must be different if it stops near Fe1 or Fe2, and also different from the stopping site outside the SRT. If instead, a coexistence of the two magnetic phases takes place in the SRT, there shouldn't be reason for a change in the frequency of the oscillating components across the reorientation region, as the muon would sense the same magnetic field of the Γ_2 or Γ_4 phase. The only characteristic would be existence of two oscillating frequencies during SRT, coming from the muons which stop in different magnetic domains (due to a percolation of magnetic states).

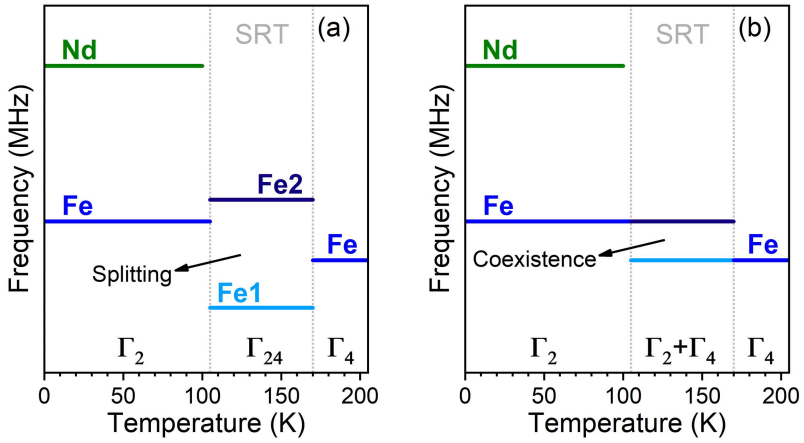


FIGURE 6.6: Schematic representation of oscillating components frequency in case of (a) structural symmetry-lowering during SRT - splitting of components - and (b) structural symmetry kept during SRT - coexistence of two orthorhombic phases Γ_2 + Γ_4.

Comparing the experimental results of Figure 6.5(a) with the schematic models of Figure 6.6, the coexistence of magnetic phases Γ_2 + Γ_4 is immediately discarded due to different frequency values of the oscillating components inside and outside the SRT. Therefore, for $NdFeO_3$ there is indeed experimental evidence for a structural transition to the monoclinic $P2_1/n$ space group (also represented by Γ_{24} irrep) during the reorientation process.

6.3. Summary

To sum up, the μSR data clearly reveal a symmetry lowering across the Γ_{24} phase, evidenced by the splitting of muon stopping sites. This observation is consistent with the splitting of Fe-site Wyckoff positions during the transition from the orthorhombic P*b'n'm* to the monoclinic $P2'1/n'$ space group. Although muons are local magnetic probes, the symmetry of the material significantly influences their stopping sites. The reappearance of a similar precession frequency in the $\Gamma 2$ phase aligns with the restoration of the P*bn'm'* structure, while the emergence of an additional high-frequency precession component is attributed to the increasing magnetic field from the Nd sublattice, which becomes aligned below 100 K, as will be shown in the following Chapter.

The monoclinic structure of $NdFeO_3$ across the SRT is experimentally confirmed for the first time via muon-spin spectroscopy. To support this interpretation, density functional theory (DFT) calculations are being carried out, to determine the most probable muon stopping sites within both the monoclinic and orthorhombic structures. This symmetry breaking should be valid for other rare-earth orthoferrites with the same magnetic phase sequence.

7. Spin structure control in $NdFeO_3$: the role of 4f magnetic anisotropy

In orthoferrites, the interaction between rare-earth and iron cations is the driving mechanism behind the reorientation of Fe^{3+} spins [150, 151]. Without considering the interaction term between these two magnetic sublattices, the Hamiltonian cannot describe the spin reorientation process [150, 152]. The magnetic sequence of phases in orthoferrites depends strongly on the specific rare-earth cation, highlighting the fundamental role of the 4f electron shell. Furthermore, below T_2, a decrease in the net magnetization of $SmFeO_3$ and $NdFeO_3$ has been reported [71, 134]. This effect has been attributed to a non-cooperative ordering of rare-earth cations aligning in the anisotropic field created by Fe^{3+} ions [71]. However, to the best of our knowledge, no experimental results have been published that corroborate this assumption. Specifically for $NdFeO_3$, the Nd^{3+} spins order cooperatively only below T_N^{Nd} = 1.05 K [67]. Although, the neutron diffraction peak (100) - associated solely with Nd^{3+} magnetic moment - becomes noticeable below 25 K [85]. Therefore, the reason for magnetization decrease immediately below T_2 remains an open question.

The possibility of controlling the magnetic structure through external stimuli, such as a magnetic field, is particularly appealing in orthoferrite materials that exhibit a thermal predisposition for spin rotation [153, 154]. For the case of $NdFeO_3$, the field dependence of its magnetic structure has been studied via Fe-spin magnons, typically probed through THz spectroscopy [153], as well as magnetization measurements [71, 154]. All studies emphasize the anisotropic nature of this compound, with a pronounced dependence on the direction of the applied field, even at low field strengths [154]. A magnetically induced spin reorientation from Γ_4 to Γ_2 configuration, was observed above T_2, for applied magnetic field along the a-axis and strength up to 5 T [153]. Surprisingly, at both 140 and 100 K, the reverse transformation from Γ_2 to Γ_4 configuration was not achieved for fields up to 3 T applied along the c-axis [153]. This behaviour has been attributed to the high magnetic susceptibility of the Nd^{3+} ions [73, 153]; when the field is applied along

the c-axis, the magnetic energy is insufficient to drive the system back to Γ_4 structure, and both the Γ_2 and Γ_{24} structures are maintained [153]. Nevertheless, the effects of higher magnetic fields on $NdFeO_3$ magnetic structure remain unexplored, particularly in the low-temperature regime where compensation between the two magnetic sublattices occurs—an area that remains open for further investigation.

This Chapter addresses the crosstalk between $3d$- and $4f$- electron shells in the two magnetic sublattices $NdFeO_3$. X-ray magnetic circular dichroism (XMCD) focused on the Nd^{3+} absorption edge shed light on the non-cooperative ordering of this cation just below the spin reorientation process is completed at T_2. Furthermore, the anisotropic character of $NdFeO_3$ is highlighted by the impact of external magnetic fields on its magnetic structure, following magnetic field dependence of the optically active magnon excitations through polarized THz absorption and unpolarized Raman scattering spectroscopies, in oriented single crystalline samples. For this purpose, we perform an experimental study of the magnetic field-dependent excitations in a wide temperature range that encompasses the different magnetic states of this compound. To ground our interpretation, complementary isothermal magnetization measurements were performed to corroborate the magnetic structure changes induced by the external applied field.

The overall picture here reported is expected to be general for other rare-earth orthoferrites with spin-reorientation transitions and extendable, as well, to other systems with non-equivalent magnetic sublattices. The results reported here are part of an article submitted to Communications Materials, currently Under Review.

7.1. Coupling of the two magnetic sublattices

In Chapter 4, the temperature dependence of the two magnons shows a considerable hardening below T_2 = 105 K, which coincides with the decrease of macroscopic magnetization that has been attributed to the antiparallel alignment of Nd-sublattice in relation to the Fe-sublattice [71]. To experimentally confirm that the Nd^{3+} cations start to align non-cooperatively just below T_2, temperature-dependent XMCD focused on the Nd $M_{4,5}$ absorption edge was performed, and the spectra are shown in Figure 7.1.

The XMCD signal at both Nd absorption edges becomes stronger as the temperature decreases, indicating a growth in the Nd-sublattice magnetization, particularly pronounced below 100 K. The area of M_4 absorption edge at 1005 eV was calculated as a function of

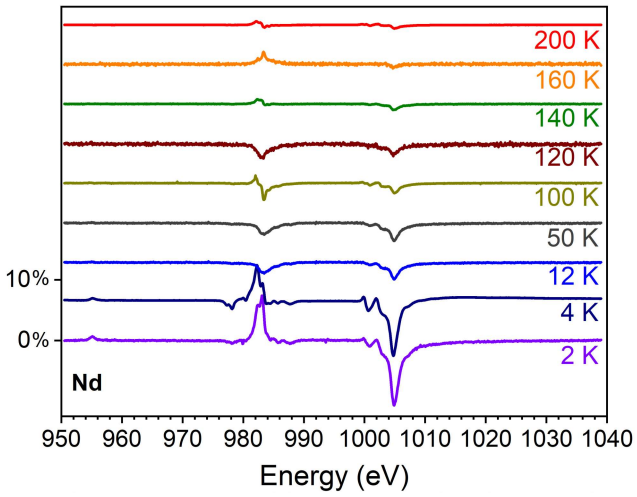


FIGURE 7.1: XMCD spectra of Nd $M_{4,5}$ absorption edges recorded at different fixed temperatures.

temperature and its squared signal is proportional to the net ferromagnetic moment of the Nd-sublattice [96]. Figure 7.2 shows the temperature dependence of Nd M_4 absorption edge signal squared along with the variation $\Delta\omega$ of Fe-sublattice magnons wavenumber. Here, $\Delta\omega = \omega_{avg}^{SRT} - \omega(T)$, where ω_{avg}^{SRT} is the average wavenumber value across the SRT temperature range and $\omega(T)$ the wavenumber at temperature *T*.

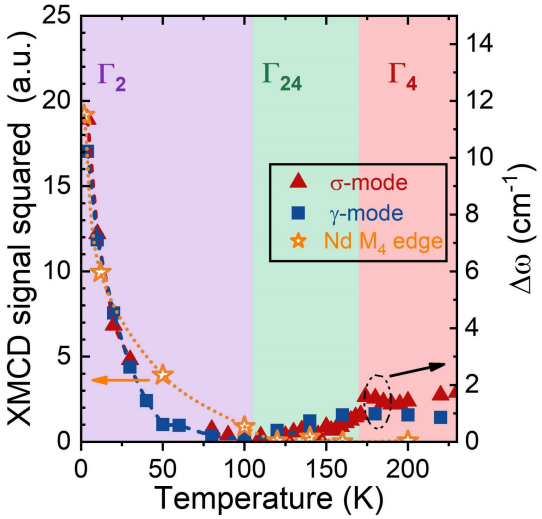


FIGURE 7.2: Temperature dependence of Nd M_4 absorption edge signal squared obtained from XMCD analysis (left-axis) and the Fe-sublattice magnons wavenumber variation from the average value across the SRT (right-axis). The dashed lines are guide for the eyes.

The XMCD squared signal is negligibly small above 100 K and monotonously increases with temperature. This increase is explained by the strong anisotropy of the susceptibility tensor associated with the Nd^{3+} $4f$ electrons, which is larger along the a-axis [88]. So,

as the Fe-sublattice net magnetization rotates towards the a-axis below 100 K, the Nd-sublattice strongly polarizes, giving rise to a strengthening of the XMCD signal [96]. This result confirms, on the one hand, the increase of Nd-sublattice magnetization, as it was assumed [71]. The $\Delta\omega$ of Fe-sublattice magnons follows the XMCD signal growth, giving definitive evidence for the key role played by the magnetic anisotropy of Nd-sublattice that interacts with the Fe-sublattice.

7.2. Magnon behaviour under magnetic field

This section presents the magnetic field dependence of magnons signatures, probed by polarized THz and unpolarized Raman spectroscopies, recorded at different fixed temperatures. We will present the magnon spectra for some representative temperatures and magnetic fields, but the complete set of results can be found in Appendix A.8. Extinction coefficient spectra, $\kappa(\omega)$, were calculated directly from the absorption THz data.

First, focusing on the results at 200 K, Figures 7.3(a) and 7.3(b) show the extinction coefficient spectra, $\kappa(\omega)$, recorded without and with a magnetic field applied along a-axis, respectively, for THz polarizations H^{ω}||a, c. Without magnetic field (see Figure 7.3(a)), the single peak, only observed for the H^{ω}||c polarization geometry, is assigned to the γ-mode (see selection rules in Figure 4.7). As the magnetic field strength $\boldsymbol{B}_{ext}$||a increases, the intensity of the γ-mode for H^{ω}||c decreases, until completely disappearing at 3 T (see Figures 7.3(b) and 7.3(d)). In the 0 – 2 T range, this mode softens around 0.6 cm^{-1}, as shown in Figure 7.3(c). On the contrary, for H^{ω}||a, no magnon could be detected in the absence of an external field, but it is already observed at 1 T and its intensity increases with the magnetic field, until reaching a plateau above 3 T. These results evidence the continuous rotation of the ***F*** vector from the c-axis towards the a-axis when applying magnetic field along the a-axis. According to the selection rules, the ***F*** vector is completely parallel to the a-axis for $|\boldsymbol{B}_{ext}|$> 3 T. The similar study was performed by applying the magnetic field along the c-axis ($\boldsymbol{B}_{ext}$||c). Figures 7.3(e) and 7.3(f) show the $\kappa(\omega)$ spectra recorded without and with magnetic field, respectively, for THz polarization geometries H^{ω}||b, c. In both cases, with and without field, the γ-mode can only be observed for the H^{ω}||c up to 7 T. The wavenumber of the γ-mode increases with the magnetic field strength, as it can be seen in Figure 7.3(g), while its intensity remains almost constant (Figure 7.3(h)). We conclude that the ***F*** vector keeps the c-axis direction, as it is expected as a magnetic field is applied along the ***F*** vector direction, not changing the net magnetization direction.

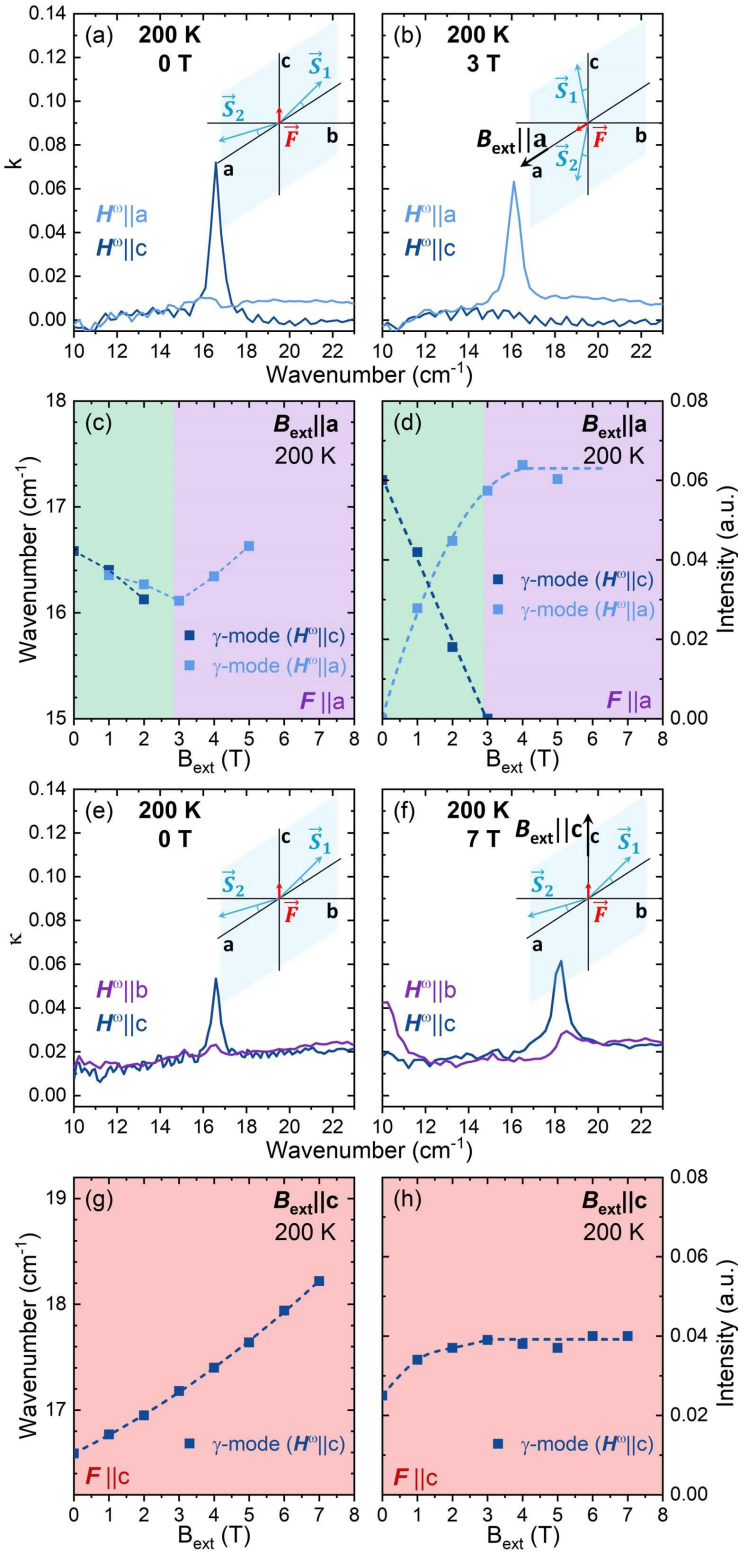


FIGURE 7.3: Extinction coefficient spectra of $NdFeO_3$, in different polarization configurations of the THz radiation at 200 K: (a) and (e) without applied magnetic field; under magnetic field along (b) a-axis and (f) c-axis; for $\boldsymbol{B}_{ext}$||a: magnetic field dependence of (c) wavenumber and (d) intensity; for $\boldsymbol{B}_{ext}$||c: magnetic field dependence of (g) wavenumber and (h) intensity. Dashed lines are a guide for the eyes. ***F*** is the ferromagnetic vector.

The next step is to apply the magnetic field in the SRT region (105 – 170 K), where the ***F*** vector rotates spontaneously, restricted to the ac-plane [71, 76, 79]. Figures 7.4(a) and 7.4(b) show the $\kappa(\omega)$ spectra at 140 K, without and with an applied magnetic field along the a-axis, respectively, for the H$^{\omega}$||a, c polarization configurations. Figures 7.4(e) and 7.4(f) show the $\kappa(\omega)$ spectra recorded at 120 K for $\boldsymbol{B}_{ext}$||c, in the H$^{\omega}$||a,b polarization configurations, without and with an applied magnetic field, respectively.

According to the selection rules, in the SRT temperature range, without an external magnetic field, the γ-mode can only be observed for H$^{\omega}$||a,c THz polarization geometries (see Figure 4.7). This is confirmed in Figure 7.4(a) and Figure 7.4(e), where a single peak is observed in the spectra recorded for H$^{\omega}$||a,c, although with different intensities. As $\boldsymbol{B}_{ext}$||a grows, the intensity of γ-mode observed in the H$^{\omega}$||c spectra decreases, until it disappears at 2 T (see Figure 7.4(b) and Figure 7.4(d)). On the contrary, for H$^{\omega}$||a, the intensity of the γ-mode increases, reaching a plateau above 2 T, and at the same magnetic field strength, the wavenumber reaches a minimum value (see Figure 7.4(c)). There is a relation between the γ-mode intensity and the relative orientation of ***F*** vector, defined by θ (angle between ***F*** vector and a-axis), described by the following equation [155]:

$$I_{\gamma}(\theta) = I_0 \cos^2(\theta) \tag{7.1}$$

where I_0 is the maximum peak intensity, that we assumed to be the mean value measured for $|\boldsymbol{B}_{ext}|$ > 2 T shown in Figure 7.4(d) (i.e., when the ***F*** vector lies along the a-axis), and $I_{\gamma}(\theta)$ is the peak intensity. Inset of Figure 7.4(d) shows the θ dependence on magnetic field (along a-axis). At 140 K, in the absence of an external field, the ***F*** vector makes an angle of 64° with the a-axis, and then decreases on increasing the external field, as evidenced in the inset of Figure 7.4(d). These results provide evidence for a magnetically induced transition at 140 K, in which the ***F*** vector follows the direction of the applied field above the critical value.

The reverse magnetically induced spin reorientation is also possible; i.e. ***F*** rotating towards c-axis and it was observed at 120 K, with the applied magnetic field along the c-axis ($\boldsymbol{B}_{ext}$||c), as shown in Figures 7.4(e) and 7.4(f). The reorientation is completed at 2.5 T, as the intensity of γ-mode, observed for H$^{\omega}$||a, decreases with increasing the magnetic field, and then, vanishing above 2.5 T (Figures 7.4(g) and 7.4(h)). The fact that the spectra recorded with the H$^{\omega}$||b do not exhibit traces of magnon signature confirms the rotation of ***F*** vector towards the c-axis. This result contrasts with the observation of Ref.[153], where no signatures for the reorientation of ***F*** vector could be ascertained at 140 K for

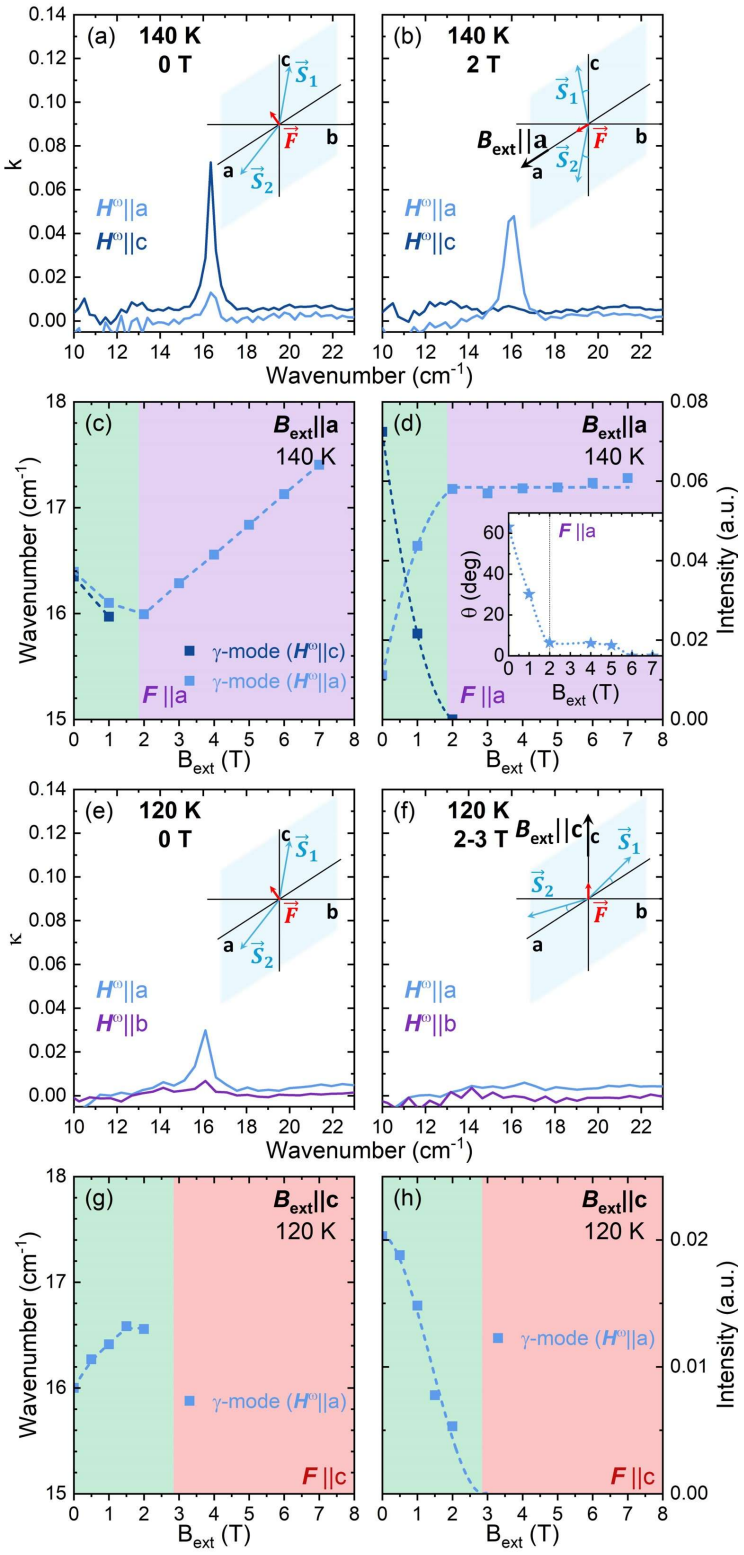


FIGURE 7.4: Extinction coefficient spectra of $NdFeO_3$, in different polarization configurations of the THz radiation in the SRT region (140 and 120 K): (a) and (e) without applied magnetic field; under magnetic field along (b) a-axis and (f) c-axis; for $\boldsymbol{B}_{ext}$||a: magnetic field dependence of (c) wavenumber and (d) intensity; for $\boldsymbol{B}_{ext}$||c: magnetic field dependence of (g) wavenumber and (h) intensity. Inset of (d) represents the magnetic field dependence of the angle θ between the ***F*** vector and the a-axis, obtained using Equation 7.1. Dashed lines are a guide for the eyes. ***F*** is the ferromagnetic vector.

$\boldsymbol{B}_{ext}$||c. Here, we confirm the induced rotation of ***F*** vector towards the c-axis at 120 K, which means that at this temperature the effect of Nd^{3+} anisotropy is still small to avoid the reorientation of Fe-sublattice magnetization.

After studying the effect of magnetic field applied during the SRT temperature range, we investigate this effect on the lowest temperature border of SRT, at 110 K. Figures 7.5(a)-(d) show the magnetic field dependence of both σ- and γ-modes wavenumbers and intensities, observed in unpolarized Raman scattering, under an external magnetic field applied along the a-axis and c-axis. Full set of unpolarized Raman spectra are shown in Appendix A.8.

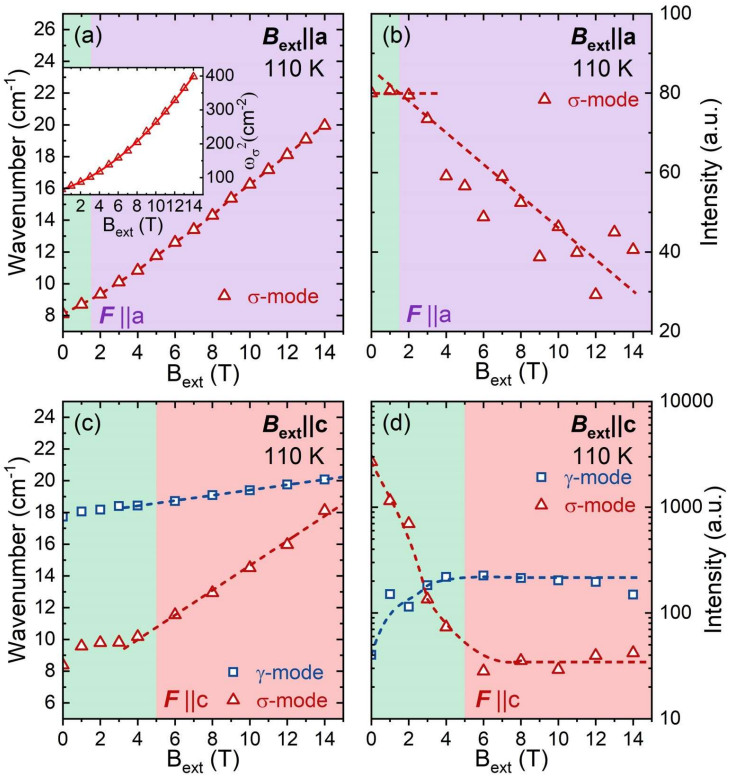


FIGURE 7.5: Magnetic field dependence of the σ- and γ-modes wavenumber and intensity, respectively, for the applied field parallel to the (a)-(b) a-axis and (c)-(d) c-axis, seen in unpolarized Raman spectra at 110 K. Inset of (a) shows the polynomial (2nd order) dependence of the squared wavenumber with the magnetic field, following the model of Ref.[156]

In general overview, the magnons wavenumber increases with increasing the magnetic field strength, independently of the external field orientation. Considering $\boldsymbol{B}_{ext}$||a, Figure 7.5(a), only the σ-mode is observed for all $\boldsymbol{B}_{ext}$ strengths (see Figure A.8(a)). It is relevant to notice that these spectra were not collected in the backscattering geometry, therefore Raman selection rules of Chapter 4 cannot help us to understand why only σ-mode is observed.

The σ-mode wavenumber increases with the magnetic field and its intensity remains constant up to 2 T, and decreases continuously on further magnetic field increase (see Figure 7.5(a)-(b)). This result is a consequence of the ***F*** vector not being completely parallel to the a-axis for $|\boldsymbol{B}_{ext}|$ < 2 T. Nevertheless, due to the proximity of ***F*** vector to the a-axis at 110 K even at low magnetic fields, the wavenumber squared follows the predicted law (quadratic) in the whole magnetic field range, as shown in the inset of Figure 7.5(a).

For $\boldsymbol{B}_{ext}$||c measurements, the $NdFeO_3$ crystal orientation allowed the excitation of the two magnons. The σ-mode wavenumber is almost constant up to 4 T, and above follows a linear trend, as shown in Figure 7.5(c). On the contrary, γ-mode wavenumber follows a linear trend in the whole field range. The intensities of both magnons depict an interesting behaviour, switching their magnitudes at 4 T (see Figure 7.5(d)), indicating the reorientation of ***F*** vector towards c-axis. As mentioned in Chapter4, at 110 K the spontaneous spin reorientation transition is almost complete, and the ***F*** vector lies along the a-axis at 0 T. Intuitively, when applying the magnetic field along c-axis, the rotation of ***F*** vector from a- to c-axis is expected. For this reason, applying $\boldsymbol{B}_{ext}$||c has a stronger impact on the magnons wavenumber than $\boldsymbol{B}_{ext}$||a, as confirmed in Figure 7.5.

In the following, we will focus on the results of applying the external magnetic field in the Γ_2 phase (50, 14 and 4 K), where at 0 T, the ***F*** vector is parallel to the a-axis. Figures 7.6(a)-(b) present the results for $\boldsymbol{B}_{ext}$||a, and Figures 7.6(c)-(f) for $\boldsymbol{B}_{ext}$||c.

Applying the magnetic field in the same direction as the ***F*** vector (i.e. $\boldsymbol{B}_{ext}$||a), will not promote the rotation of the ***F*** vector, therefore no induced reorientation is expected. In fact, Figures 7.6(a)-(b) confirm this assumption at 14 and 4 K, as there is no evidence of a reorientation of the ***F*** vector. At 14 K, as the inset of Figure 7.6(a) shows, the σ-mode wavenumber squared follows the predicted quadratic law with the magnetic field [156]. At 4 K, there is also no indication of ***F*** vector rotation, as the intensity of the γ-mode is practically constant (see inset of Figure 7.6(b)). Although the Fe-sublattice spin structure is described by the Γ_2 irrep at both 14 and 4 K, the magnetic-field dependence of the σ-mode at these temperatures is different: at 14 K the σ-mode wavenumber increases with the magnetic field, while for 4 K it decreases. It is relevant to notice that at 4 K, the magnetic system is near the ordering temperature of the Nd-sublattice (T_N^{Nd} = 1.05 K) [67], and the interplay between Nd- Fe sublattices is expected to be stronger, therefore the Fe-magnons at 4 K might reflect a different magnetic dynamics, as we will discuss later.

On the opposite, for $\boldsymbol{B}_{ext}$||c, the results demonstrate an induced reorientation (Figures

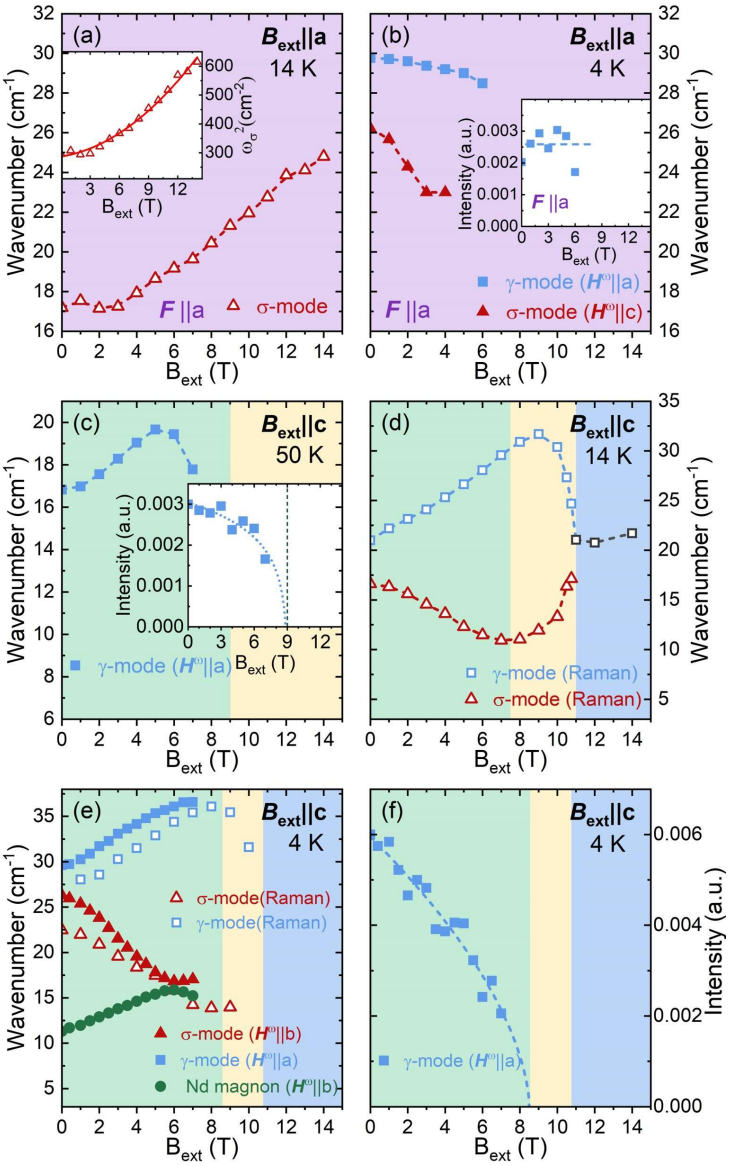


FIGURE 7.6: Magnetic field dependence of the wavenumber of σ- and γ-modes observed in THz (closed symbols) and Raman (open symbols) spectroscopies at (a) 14 K and (b) 4 K for $\boldsymbol{B}_{ext}$||a. Inset of (a) and (b) show the polynomial (2nd order) dependence of the squared wavenumber with the magnetic field, following the model of Ref.[156], and the γ-mode intensity, respectively. Magnetic field dependence of the wavenumber of σ- and γ-mode observed in THz and Raman spectroscopies at (c) 50 K, (d) 14 K and (e)-(f) 4 K for $\boldsymbol{B}_{ext}$||c. Inset of (c) and panel (f) show the magnetic field dependence of the γ-mode intensity at 50 and 4 K, respectively. Dashed lines are guide for the eyes.

7.6(c)-(f)). At 50 K, only the γ-mode could be detected in THz experiments, while at 4 and 14 K both the σ- and γ-modes are observed in THz and/or Raman experiments. The magnetic field dependence of γ-mode wavenumber at 50, 14 and 4 K shares common features: an upshift with increasing magnetic field, followed by a softening. The σ-mode wavenumber shows the opposite trend, softening at first, and after reaching a minimum, inverts the trend. At 50 K, γ-mode intensity decreases with magnetic field, and by extrapolating its behaviour to higher fields, we estimate that it would eventually disappear from the H^{ω}||a configuration at 9 T (see Figure 7.6(c) inset). From the measurements done at H^{ω}||b, shown in Figure A.7(b), we know that the intensity of γ-mode does not increase in this polarization configuration. We conclude that it should appear in H^{ω}||c, in agreement with the magnon behaviour discussed above.

Focusing now on the results at 14 K, shown in Figure 7.6(d), the maximum separation between σ- and γ-modes is achieved around 9 T, after which the magnons energy approach. Above 11 T, only one magnon could be observed. The magnetic field dependence of the two magnons at 14 K is quite different from the one observed at 110 K (see Figure 7.6(c)), where there is strong evidence for the ***F*** vector rotation towards the c-axis. For this reason, the phase sequence at 14 K (and also at 50 K) is different from the one at 110 K. At 4 K, the magnons behave in a similar way compared with 14 K. From the THz data, it was possible to extrapolate the intensity decrease of the γ-mode (Figure 7.6(f)), which hints at a critical field of 9 T. However, the THz experiments were limited to 7 T, and therefore, no further conclusions could be extracted from the intensity analysis. From the Raman experiments, above 9 T there is a drastic decrease in the magnons intensity, see the spectra in Figure A.8(b), making it difficult to follow them above 10 T.

Other low-lying energy excitation, assigned to the Nd-sublattice is observed at 4 K [150]. Its wavenumber follows a similar trend to the applied magnetic field as γ-mode, resulting from the strong coupling between the Fe- and Nd-sublattices. The magnetic anisotropic character of the Nd-sublattice is evidenced when comparing the magnetic field dependence of the magnons at 14 and 4 K.

For $\boldsymbol{B}_{ext}$||a, at 14 and 4 K the magnons trends are opposite (see Figures 7.6(a)-(b)), while for $\boldsymbol{B}_{ext}$||c, the magnons trends are comparable at 14 and 4 K (see Figures 7.6(d)-(e)). These differences according to the temperature and applied magnetic field direction reveal different magnetic structures, underlying the magnetic anisotropy of the $4f$-electrons from Nd-sublattice.

7.3. Other excitations under magnetic field

7.3.1 Nd^{3+} phonons

The increasing role of the Nd-sublattice in the dynamics of $NdFeO_3$, below T_2, is also ascertained from the magnetic field dependence of Nd-oscillations phonon modes (also called Nd-shifts), probed at 110, 14 and 4 K, by unpolarized Raman spectroscopy. The complete set of spectra is shown in Appendix A.8.

A detailed mode assignment of the Raman phonons is presented in Chapter 4. Regarding the Nd-shifts, the modes are assigned to Nd(y) (107 cm^{-1}; A_g symmetry) and Nd(x) (111 cm^{-1}; B_{1g} symmetry), both involving in-phase vibrations of Nd^{3+} cation in the ab-plane, while out-of-phase along the c-direction [122]. Other two modes are assigned to Nd(x) (141 cm^{-1}; A_g symmetry) and Nd(y) (154 cm^{-1}; B_{1g} symmetry), both involving out-of-phase oscillations in the ab-plane [122].

The magnetic field dependence of Nd-shifts wavenumber is presented in Figure 7.7 for $\boldsymbol{B}_{ext}$||a and in Figure 7.8 for $\boldsymbol{B}_{ext}$||c.

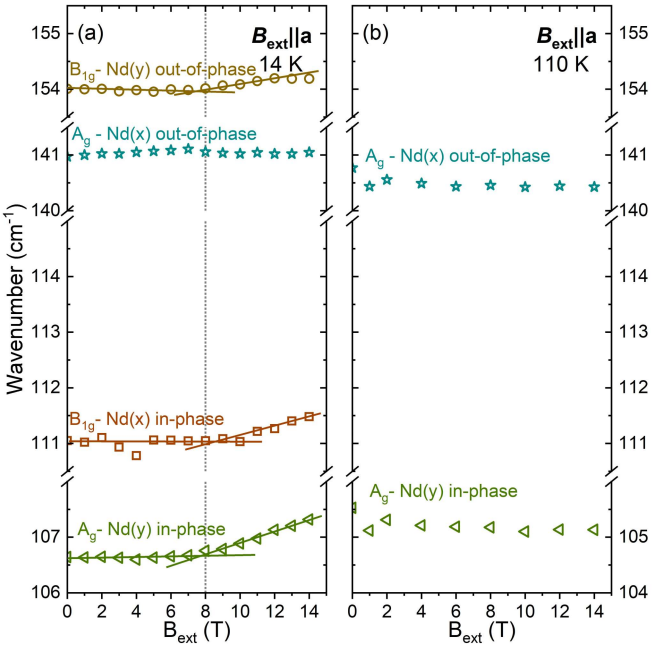


FIGURE 7.7: Magnetic field dependence of the Nd^{3+} shifts wavenumbers, measured for $\boldsymbol{B}_{ext}$||a at (a) 14 K and (b) 110 K.

At 110 K, the field dependence of Nd-shifts wavenumber does not display any significant change in neither of the field directions, as it can be seen in the analysis of Figures 7.7(b) and 7.8(c). The scenario is different at 14 K, where the in-phase Nd-shifts have a

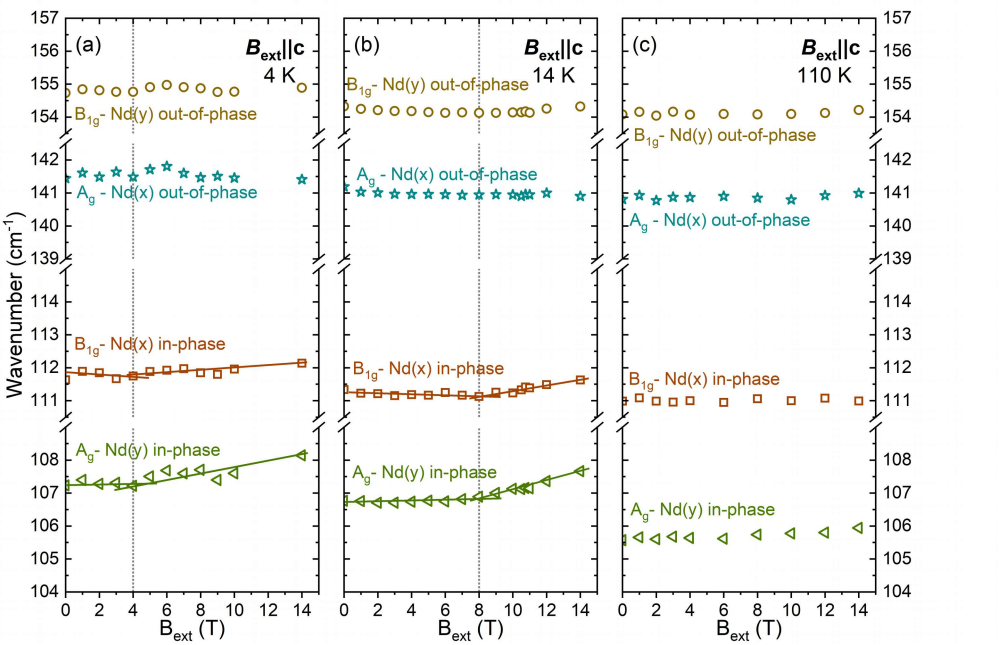


FIGURE 7.8: Magnetic field dependence of the Nd^{3+} shifts wavenumbers, measured for $\boldsymbol{B}_{ext}$||c at (a) 4K, (b) 14 K and (b) 110 K.

slope change at 8 T, independently on the direction of the applied field, as shown in Figures 7.7(a) and 7.8(b). Below 8 T, the wavenumber is almost constant, and afterwards it increases linearly. This slope change does not seem to be related with any magnetic modification sense by Fe^{3+} magnons.

At 4 K, a slight deviation of the in-phase Nd-shifts occurs at 4 T, for $\boldsymbol{B}_{ext}$||c, see Figure 7.8(a). Differences in the field dependences at 14 and 4 K hint for a different contribution of the Nd-sublattice to the magnetoelastic properties of $NdFeO_3$, possibly related with the approach to the ordering temperature of the cation.

7.3.2 Crystal-field excitation of Nd^{3+}

Figure 7.9 present the effect of an external magnetic field on the crystal-field excitation of Nd^{3+} ions. Without magnetic field applied, the band observed at 82 cm^{-1} is assigned to the lowest energy crystal-field excitation [122, 130]. Figure 7.9(a) shows the Raman spectra as a function of applied magnetic field ($\boldsymbol{B}_{ext}$||a), focused on the spectral range where there is a splitting of this crystal-field excitation due to Zeeman effect.

For magnetic field below 3 T, no splitting of the band could be ascertained. The band starts

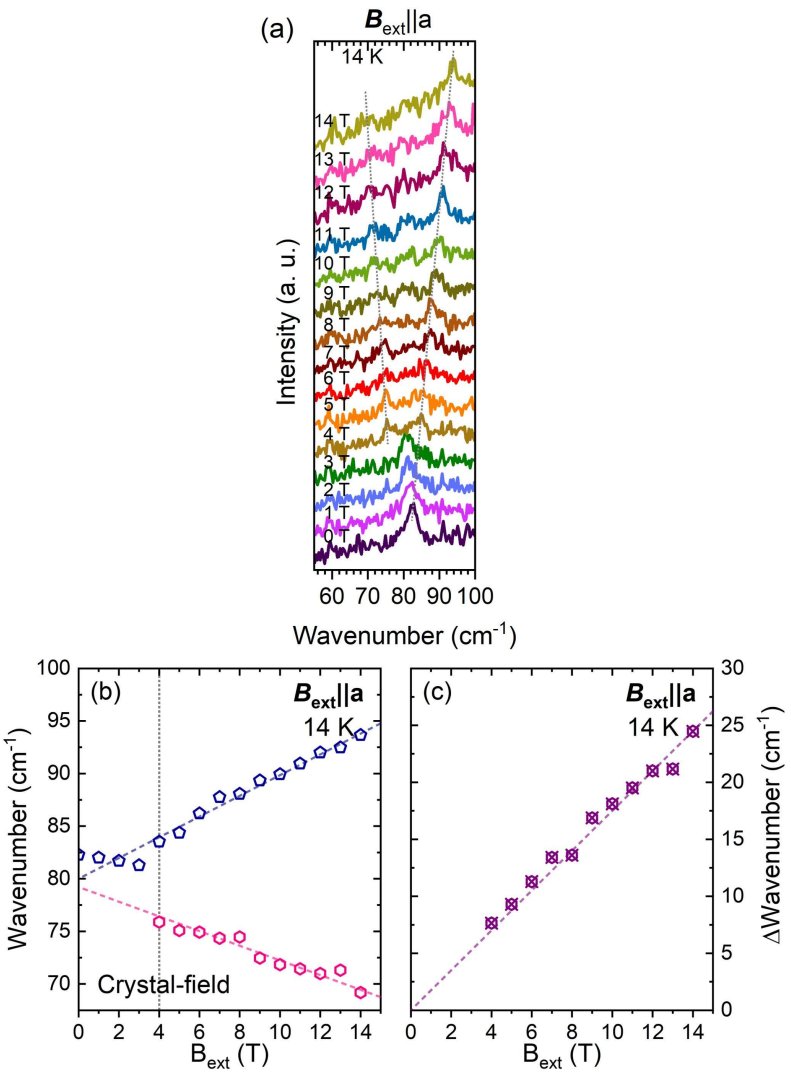


FIGURE 7.9: Magnetic field dependence Nd^{3+} crystal-field excitations: (a) unpolarized Raman spectra, (b) wavenumbers and (c) wavenumber difference measured at 14 K with $\boldsymbol{B}_{ext}$||a.

to split with increasing the external field, as illustrated by the wavenumber field dependence in Figure 7.9(b). Figure 7.9(c) presents the wavenumber difference between the splitting, that follows a linear trend. At 4 T the line splitting is ≈ 8 cm^{-1}, which corresponds to a 1 meV. This value is in good agreement with the one predicted in Ref.[130].

The Zeeman effect correlates the splitting energy (ΔE) with the applied magnetic field as [157]:

$$\Delta E = g\mu_B B \tag{7.2}$$

where μ_B is the Bohr magnetron and g-factor can be determined from the slope of one of branches in Figure7.9(b). Considering $\Delta E = hf = hc\nu$ (c = speed of light, h = Plank's constant and ν=wavenumber in cm^{-1}), Equation 7.2 can be convert into:

$$\nu(B) = \frac{g\mu_B}{hc} B \tag{7.3}$$

The g-factor is directly obtained from slope (m) of the linear magnetic field dependence of the crystal-field levels in Figure 7.9(b), $g = \frac{mhc}{\mu_B}$, and is g = 1.96 ± 0.04. This value is close to the typical values of g-factor experimentally obtained [158].

7.4. Discussion

According to the spectroscopic results previously reported, magnetically induced spin-reorientation is achieved above 100 K whenever the external magnetic field is applied along the easy-axis of $NdFeO_3$. Thus, the $\Gamma_4 \longrightarrow \Gamma_{24} \longrightarrow \Gamma_2$ transition is achieved at 200 K when the applied field is along the a-axis, while the $\Gamma_{24} \longrightarrow \Gamma_2$ transition occurs at 110 K when the field is applied along the c-axis. In 110 – 170 K range, where the SRT occurs naturally without an external field, the system stabilizes in the Γ_2 phase if $\boldsymbol{B}_{ext}$||a or in the Γ_4 phase if $\boldsymbol{B}_{ext}$||c.

Below 100 K, the effect of the external magnetic field on the phase sequence of $NdFeO_3$ is different. For $\boldsymbol{B}_{ext}$||a, there are no evidences for changes in the magnetic structure, keeping the Γ_2 phase down to 14 K. However, for $\boldsymbol{B}_{ext}$||c, the magnons point to a magnetic transition, that is not assigned to a spin-reorientation.

Coming back to Figure 7.6(c)-(e), the γ-mode exhibits similar magnetic field dependence at 50 and 14 K, revealing that the magnetic phase sequence at both temperatures is the same. Further ahead, we will see that this interpretation is valid from 110 K down to T_{comp} 8 K. The partial softening of the σ-mode wavenumber at 14 K, shown in Figure 7.6(d), points for a spin-flop (SF) transition instead of a spin-reorientation. The softening of the ferromagnetic resonance (σ-mode) is a common property of antiferromagnets undergoing a spin-flop transition, at a critical field [156, 158, 159]. The softening of the σ-mode and the hardening of the γ-mode are predicted for a spin-flop model, assuming the two-Fe sublattice model [159]. According to this model, the magnons frequency evolution with magnetic field applied along the easy axis direction is described as follows [159]:

$$\left(\frac{f_\gamma}{g}\right)^2 \sim H_{||c}^2 + H_d^2 + 2\left[1 + \left(\frac{H_{||c}}{H_d}\right)^2\right] B_{ext}^2 \tag{7.4}$$

$$\left(\frac{f_\sigma}{g}\right)^2 \sim H_{||c}^2 - 2\left(\frac{H_{||c}}{H_d}\right)^2 B_{ext}^2 \tag{7.5}$$

where $f_{\gamma,\sigma}$ is the magnon frequency ($f_{\gamma,\sigma} = c\omega_{\gamma,\sigma}$, c the light speed and $\omega_{\gamma,\sigma}$ the wavenumber), g is the gyromagnetic ratio, H_d is the antisymmetric DM exchange field and $H_{||c}$ is the field at which the spin-flop transition would occur without DM interaction [159]. Figure 7.10 presents the magnons frequencies as a function of the external magnetic field for 14 K, and the corresponding fit of Eq.7.5 to the experimental values of σ-mode.

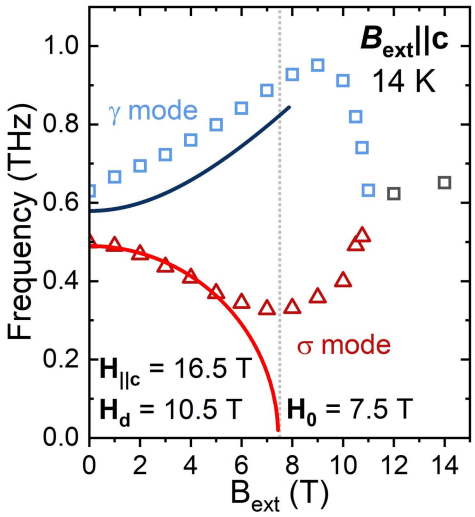


FIGURE 7.10: Magnons frequency vs external magnetic field $\boldsymbol{B}_{ext}$||c at 14 K. Red line is the fit to the σ-mode using Eq.7.5. The fit parameters obtained for σ-mode were imposed in the γ-mode fitting equation (Eq.7.4), represented by the blue line.

The model does not consider the interaction between rare-earth and iron sublattices [159], which becomes stronger at low temperatures, yet Eq.7.5 describes well the partial softening of the σ-mode up to 6 T, as shown in Figure 7.10. The extrapolation to higher fields, allows the determination of parameters H_d= 10.5 T and $H_{||c}$ = 16.5 T and of the spin flop critical field $H_0 = \frac{H_d}{\sqrt{2}}$ = 7.5 T, that occurs when f_σ= 0. Yet, considering the obtained parameters into Eq.7.4, the increasing trend of the γ-mode frequency in the 0-8 T range is reproduced. However, the experimental values are about 20 % above the ones predicted by Eq.7.4. Still, the value obtained for H_d is of the same order of magnitude as the ones published for other orthoferrites [159, 160]. From the σ-mode analysis, there are evidences for a spin-flop transition at 14 K when $\boldsymbol{B}_{ext}$||c. This transition should also occur for other temperatures, namely at 50 K, where the γ-mode behaves similarly to the one at 14 K, pointing for the same magnetic structure.

To support the magnetic structure changes inferred from the spectroscopic analysis, the isothermal magnetization as a function of magnetic field strength and direction were measured, and results are presented in Figure 7.11.

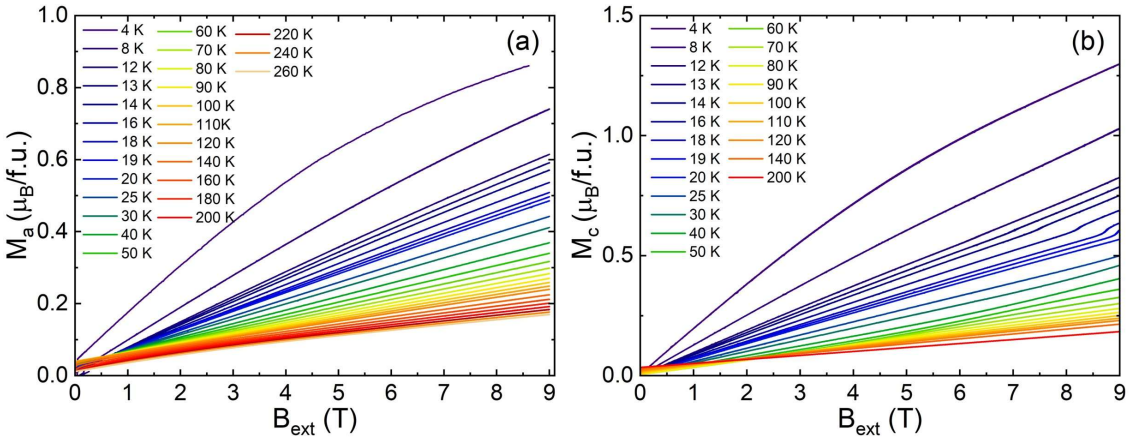


FIGURE 7.11: Magnetization as a function of the magnetic field applied along (a) a-axis and (b) c-axis.

The effect of magnetic structure changes in the magnetization curves is better shown by plotting their derivatives. First, we will focus on the temperatures above 100 K (Figures 7.12(a) and 7.12(b)), where a magnetically induced spin reorientation is predicted. The $\frac{M_a}{dB}$(B) plot, Figure 7.12(a), gives us information regarding the critical field for the spin-reorientation from $\Gamma_4, \Gamma_{24} \longrightarrow \Gamma_2$ phases (marked with a star symbol). Beside this magnetic induced reorientation, no other transition was ascertained in the magnetization curves by applying $\boldsymbol{B}_{ext}$||a. Figure 7.12(b) shows the $\frac{M_c}{dB}$(B) plot where the reorientation from $\Gamma_2, \Gamma_{24} \longrightarrow \Gamma_4$ phases is also marked by the star symbols. These results for both $\boldsymbol{B}_{ext}$||a and $\boldsymbol{B}_{ext}$||c are in good agreement with the spectroscopic ones presented above.

We proceed by examining the magnetization analysis in the 110 - T_{comp} range, illustrated in Figure 7.13.

Figure 7.13(a) shows that the magnetization along the a-axis (M_a) is almost linear with $\boldsymbol{B}_{ext}$||a, up to 9 T, in the T_{comp} < T ≤ 110 K range. This result confirms the absence of magnetic structure changes with applied field along a-axis. Below T_{comp}, M_a(B) presents a curvature that mirror magnetic structure changes, as suggested by the spectroscopic data at 4 K.

When $\boldsymbol{B}_{ext}$||c, the magnetization along the c-axis, M_c, is not linear with the applied field below 110 K, as shown in Figure 7.13(b). The M_c(B) curves exhibit a S-like anomaly at high fields, highlighted in the inset of Figure 7.13(b). The $\frac{M_c}{dB}$(B) is presented in Figure 7.13(c).

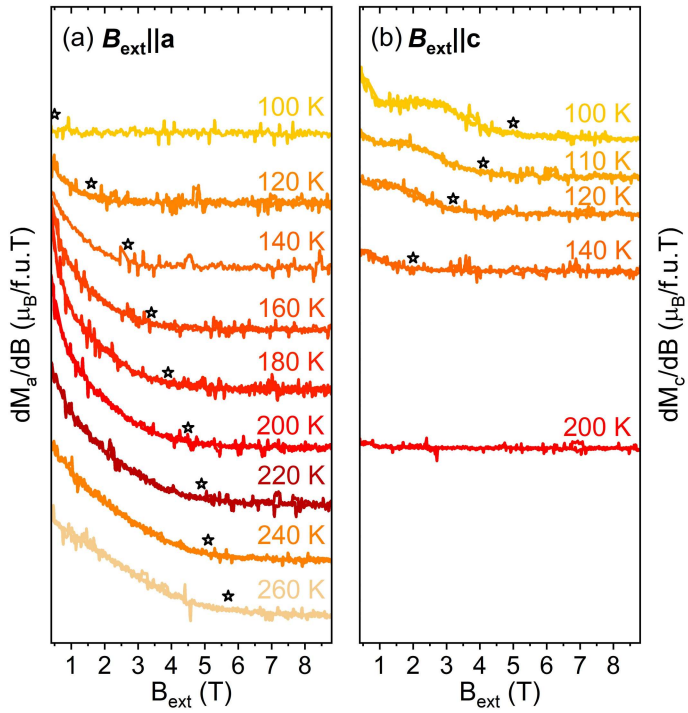


FIGURE 7.12: Derivative of magnetization as a function of the magnetic field applied along (a) a-axis and (b) c-axis. The stars symbols mark the end of induced spin-reorientation, i.e, when Γ_2 phase is stabilized for $\boldsymbol{B}_{ext}$||a or when Γ_4 phase for $\boldsymbol{B}_{ext}$||c.

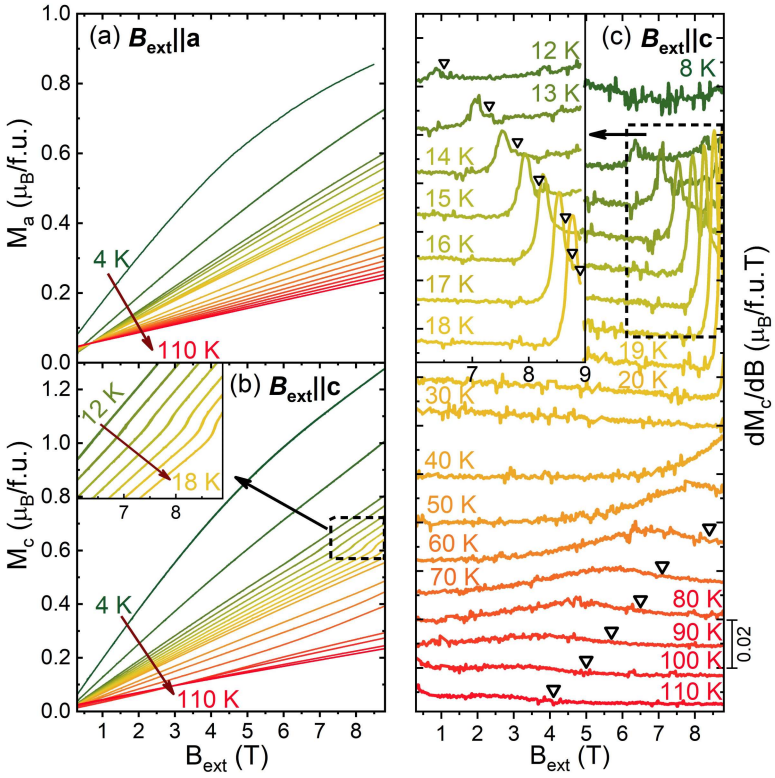


FIGURE 7.13: Magnetization as a function of magnetic field applied along (a) a-axis and (b) c-axis. (c) Derivative magnetization along c-axis, where the symbols mark the spin-flop (SF) transition. Insets in (b) and (c) are zoomed region for curves between12 and 18 K, where SF transition is sharp.

As seen before in Figure 7.12(b), above 110 K the derivative has a broad anomaly, whose amplitude increases and shifts towards higher fields. Between 30-20 K, the anomaly is not observed in the measured range (up to 9 T), reappearing much narrower at 19 K. From 19 to 12 K, the peak shifts towards lower fields, decreasing its amplitude in such a way that at 8 K it is no longer observed. The S-shape anomaly in M_c(B), when the field is applied along the easy-axis (c-axis for temperatures below 110 K), and the linear trend in the M_a(B), are the signature of the spin-flop transition [157, 160, 161], already evidenced by the magnons dependence with field at 14 K for $\boldsymbol{B}_{ext}$||c. The spin-flop process is completed at the field when the linear trend of the magnetization M_c is recovered, giving a good estimation for the critical field, as shown by the symbols in Figure 7.13(c). Interestingly, at 14 K, the value obtained is 7.8 T, in good agreement with the critical field H_0 obtained from the fitting of σ-mode frequency.

Above 110 K, no other transition besides induced spin reorientation occurs, regardless of the applied magnetic field direction, as Figure 7.12 demonstrates. The different field-induced magnetic transitions observed above and below 110 K with $\boldsymbol{B}_{ext}$||c are undoubtedly assigned to the magnetic interaction strengthening between Nd and Fe-sublattices, and clearly show the anisotropic nature of $4f$-electron shell Nd^{3+} ions.

The 4 K case deserves detailed discussion. Although the magnetic field dependences of both σ- and γ-mode resembles the one observed at 14 K (Figure 7.6(d)-(e)), the M_c(B) curves at 4 and 14 K are different (see Figure 7.11(b)). Below 12 K, instead of a S-shaped curve, the M_c(B) curve down bends, also as in the case of M_a(B). It is worth stressing that below $T_{comp} \sim 8$ K at zero-field, the magnetic behaviour of $NdFeO_3$ is dominated by the Nd-sublattice magnetism. The appearance of a Nd- magnon excitation in the THz spectra at 4 K (see Figure 7.6(e)), whose magnetic field dependence follows the one of the γ-mode, corroborates the crosstalk between the two magnetic sublattices. Therefore, we cannot exclude the possibility that the nature of the magnetic phases differs above and below T_{comp}.

7.5. Summary

In this Chapter, we presented a comprehensive temperature/magnetic field dependent experimental study of phase transitions occurring in NdFeO3. These results were obtained from THz and Raman spectroscopies, X-ray magnetic circular dichroism and isothermal magnetization experiments. The one outcome concerns the interplay between the two

magnetic sublattices across the zero-field spin reorientation transition, ascertained by the correlation between the Fe-sublattice magnons and the net magnetization of the Nd-spins sublattice.

The other outcome can be graphically represented by two (***B***, T) phase diagrams for $NdFeO_3$ with $\boldsymbol{B}_{ext}$||a and $\boldsymbol{B}_{ext}$||c, respectively, shown in Figures 7.14(a) and 7.14(b).

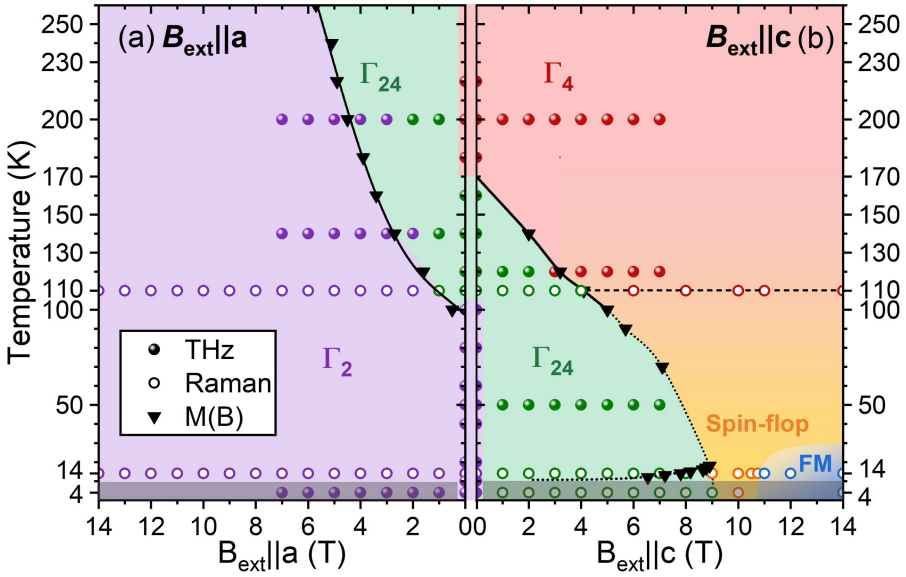


FIGURE 7.14: (***B***,T) phase diagram of $NdFeO_3$ for (a) $\boldsymbol{B}_{ext}$||a and (b) $\boldsymbol{B}_{ext}$||c. Close circles represent data measured with THz spectroscopy, open circles with Raman spectroscopy and triangles mark the magnetic transition obtained from magnetization analysis. Colours: Γ_4: red; Γ_{24}: green, Γ_2: purple, Spin-flop: yellow and Ferromagnetic (FM) phase: blue.

Starting by the description of phase diagram for $\boldsymbol{B}_{ext}$||a, shown in Figure 10(a). The induced SRT from $\Gamma_4 \longrightarrow \Gamma_{24} \longrightarrow \Gamma_2$ configuration is observed above 100 K. Below this temperature no other transition could be ascertained. The critical fields obtained from $\frac{M_a}{dB}$(B)(see Figure 7.12), as a result of the magnetic field induced SRT, allow us to draw a phase-line that is compatible with the THz and Raman spectroscopic results.

Focusing now on the phase diagram for $\boldsymbol{B}_{ext}$||c, shown in Figure 7.14(b), the Γ_4 configuration is kept above 170 K, as excepted. Between 170 - 110 K, the spin reorientation from $\Gamma_{24} \longrightarrow \Gamma_4$ occurs, with the critical field increasing as temperature decreases. Below 110 K and for low magnetic field strength ($|\boldsymbol{B}_{ext}|$ < 1 T), the $\Gamma_2 \longrightarrow \Gamma_{24}$ orientation transition is achieved. On further magnetic field increasing, the Γ_{24} structure is followed by a spin-flop transition (yellow region of Figure 7.14(b)). The fact that this spin-flop transition only occurs for T_{comp} < T ≤ 110 K when applying $\boldsymbol{B}_{ext}$||c sheds light on the anisotropy character of the $4f$-electrons of Nd-spins and on its impact in the Fe-spin structure. The

role of the $4f$-electrons shell is responsible for the different magnetic phase sequence observed above and below 110 K. Around 14 K, we cannot exclude a new magnetic transition, likely assign to a ferromagnetic state, as only one magnon can be detected above 11 T. As aforementioned, although at 4 K the magnon profile seems to be similar to the one at 14 K, the magnetization data does not allow us to draw any conclusions regarding a spin-flop transition at this temperature.

For both phase diagrams, a shadowed region is marked below T_{comp}, as the effect of the ordering of the Nd-sublattice might play an important role at low temperature and modify the magnetic structure. Further studies deserved to be carried out to confirm the magnetic phase sequence at these temperatures.

8. Conclusions

This thesis aimed to investigate the complex interplay between lattice, charge, and spin degrees of freedom in $NdNiO_3$ and $NdFeO_3$, by comparing the different properties that mirror the phase sequence of each material. In this Chapter, we summarize the main findings of each study and present a critical overview of their broader implications. Open questions will be also addressed and a future research plan proposed.

The first part of this thesis was dedicated to the investigation of a $NdNiO_3$ film. Chapter 3 examines the percolative nature of its electronic and structural transitions. Structural percolation is evidenced by the coexistence of orthorhombic P*bnm* and monoclinic $P2_1/n$ domains. Raman spectroscopy is used not only to identify the structural symmetry of the domains, but also to quantify their volume fractions. This quantification reveals a critical monoclinic volume fraction of $\frac{2}{3}$ at the threshold temperature of the insulating domains. The simultaneous emergence of structural and electronic percolation confirms the tight link between the insulating state and symmetry-breaking oxygen octahedra breathing distortions, which stabilize the monoclinic structure. Moreover, the experimental observation of coinciding electronic and magnetic phase transitions reinforces the role of magnetic ordering as a driving force behind the MIT in $NdNiO_3$.

The second part of the thesis explores $NdFeO_3$. Chapter 4 provides a spectroscopic characterization of optically active phonons and magnetic excitations in $NdFeO_3$. Combining group theory analysis, density functional theory and polarized Raman, FTIR and THz spectroscopies, the symmetry and atomic displacement patterns of vibrational modes are systematically identified. The selection rules here presented for both lattice and magnetic excitations serve as a crucial foundation for interpreting more complex phenomena, such as symmetry lowering during spin reorientation and field-induced magnetic transitions, which are addressed in subsequent chapters.

Chapter 5 investigates the magnetoelastic coupling and domain wall dynamics in $NdFeO_3$. Using a phenomenological approach, it is shown that the elastic constants arise from a

coupling term linear in strain and quadratic in the magnetic order parameter θ. The observed softening/stiffening at the boundaries of the SRT is thus attributed to magnetoelastic coupling. Additionally, the mixed elastic and magnetic character of domain walls is particularly relevant within the SRT, with their mobility confined to this temperature range, as evidenced by the losses in RUS and AC magnetic susceptibility. These results open the veil to a symmetry-breaking and by estimating the small amplitude of monoclinic distortions during the reorientation process, this Chapter demonstrates the limitations of conventional diffraction techniques in detecting such weak structural changes, shifting the paradigm in probing subtle distortions.

Chapter 6 main focus is on unravelling symmetry lowering during spin reorientation process in $NdFeO_3$, theoretically predicted but never experimentally proven for any *R*FeO_3. In this thesis, we show that muon spin spectroscopy is a suitable tool to detect symmetry breaking in $NdFeO_3$ during SRT. Actually, muons act as local probes of structural symmetry, by sensing the local magnetic field at their stopping sites, which are closely tied with the crystalline structure. A clear spectral splitting of the muon precession frequencies across the SRT is a hallmark of structural symmetry breaking. We interpret the spectral line splitting, only detected in the SRT, as a manifestation of the splitting of Fe Wyckoff positions: four equivalent Fe sites in the orthorhombic P*bnm* transform into two inequivalent Fe1 and Fe2 sites in the monoclinic $P2_1/n$. The re-emergence of a single precession component at the Γ_2 phase coincides with the recovering of orthorhombic symmetry. Additionally, below 100 K, we assign the new spectral component at higher frequencies to the non cooperative ordering of Nd sublattice, which is demonstrated to occur below T_2 in Chapter 7. The findings presented in Chapter 5 and Chapter 6 show that the SRT in NdFeO3 is undeniably governed by a magnetic and structural dynamics compatible with a symmetry breaking. This realization deepens our understanding of complex magnetic phase transitions in other orthoferrites.

The final part of the thesis, Chapter 7, investigates the anisotropic behaviour of $NdFeO_3$, driven by the $4f$-shell of Nd^{3+} ions. The non-cooperative ordering of Nd sublattice immediately below T_2, hypothesised by several authors but never actually measured, was confirmed using an element selective technique, X-ray magnetic circular dichroism, which allows to measure the magnetization coming solely from Nd^{3+} ions. Furthermore, strong interplay between the two magnetic sublattices is evidenced during the zero-field spin reorientation transition, as shown by the correlations between Fe-spin magnon behaviour and the evolving Nd magnetization.

In addition, another key finding, through THz and Raman spectroscopy, is the ability to magnetically induce the spin reorientation. When an external magnetic field is applied along the a-axis, the system undergoes a $\Gamma_4 \longrightarrow \Gamma_{24} \longrightarrow \Gamma_2$ transition between 260 K and 110 K. For a field along the c-axis, a $\Gamma_{24} \longrightarrow \Gamma_4$ transition is driven in the 170–110 K range. Below 100 K, the magnetic anisotropy of the Nd-sublattice is dominant and impacts the induced magnetic sequence, namely in the $\boldsymbol{B}_{ext}$||c case, where a spin-flop transition occurs down to 12 K, instead of a reorientation. Applying magnetic field along the easy-axis is not a sufficient condition for a spin-flop process, as it was not possible to induce this transition when applying $\boldsymbol{B}_{ext}$||a above 170 K (in the Γ_4 phase), therefore ordering of Nd ions helps to promote a spin-flop in $NdFeO_3$. Phase diagrams for both a- and c-axis field orientations are constructed to summarize these results, providing a reference framework for modeling systems with two inequivalent magnetic sublattices, and highlighting the central role of rare-earth anisotropy in complex magnetic phase sequences.

Having summarized the core findings for each compound individually, a comparative analysis is necessary to understand how the choice of B-site cation influences their physical properties.

The first clear observation is that both compounds share the same crystallographic structure (orthorhombic P*bnm*) at room temperature and undergo a structural transition to the monoclinic $P2_1/n$. However, the nature of this transition differs: it is first-order in $NdNiO_3$, associated with the MIT, and second-order in $NdFeO_3$, coupled to the SRT.

Secondly, the electronic transitions differ fundamentally. $NdFeO_3$ is an insulator, in all the temperature range studied, due to the partially filled $3d$-shells of Fe^{3+} , while $NdNiO_3$ exhibits a temperature-dependent MIT due to the uneven filling of the Ni^{3+} $3d$ orbitals.

Third, the magnetic ordering is remarkably different. Fe^{3+} ions order at much higher temperatures than Ni^{3+}. $NdFeO_3$ is antiferromagnetic at room temperature, whereas $NdNiO_3$ is paramagnetic. Furthermore, the orthoferrites display a much richer sequence of magnetic transitions, including spin reorientation phenomena.

The phase diagram of $RNiO_3$ (Figure 1.6) shows that structural and electronic transitions scale with bond angle,i.e. with *R* cation size, while magnetic transition varies only slightly. Thus, the role of R^{3+} cations in $RNiO_3$ seems to be primarily geometric, modulating the amplitude of octahedral tilts and, so, the superexchange interactions between the $3d$-$3d$

orbitals. Apparently, the coincidence of magnetic transition with structural and electronic transitions in $NdNiO_3$ is fortuitous. For Nd^{3+} and Pr^{3+}, their large size allows magnetic order to assist the MIT, but more generally, the octahedra tilts are sufficient to promote an overlap of $3d$–$3d$ orbitals (Ni–Ni), mediated by O $2p$, driving the MIT. For those two cases, the $4f$–$3d$ coupling offers only a secondary "push". In fact, a 50% doping with Sm - replacing Nd with a smaller cation- is enough to separate both electronic and structural transitions from the magnetic one.

In contrast, the $RFeO_3$ phase diagram (Figure 1.13) reveals that the diversity of magnetic phases is governed by the $4f$-$3d$ orbitals interactions. Geometric effects play a minimal role, as there is no clear correlation between rare-earth ionic size and magnetic phase sequence. Furthermore, non-magnetic cations do not induce spin reorientation of the Fe sublattice, highlighting the decisive influence of $4f$–$3d$ interactions.

In conclusion, comparing the two rare-earth perovskite families, we find that in $RNiO_3$, rare-earth size — and its influence on $3d$–$3d$ interactions — is the determinant key of physical properties in these materials, while $4f$–$3d$ interactions play a secondary role. On the contrary, in $RFeO_3$, the dominant factor is the exchange interaction between rare-earth $4f$ electrons and Fe $3d$ orbitals, which is responsible for the rich and complex magnetic properties observed.

Open questions, future research plan and new perspectives

While this thesis has provided significant insights into the physical properties of $NdNiO_3$ and $NdFeO_3$, several important questions remain open and offer promising directions for future investigation.

Regarding the $NdNiO_3$ analysis, one outstanding issue is the observed mismatch between the temperature intervals in which electronic and structural transitions occur. The coexistence of pure electronic states with structurally distinct phases suggests a more complex coupling mechanism that is not yet fully understood. This apparent decoupling may reflect intrinsic dynamics of the phase transition, or it may be influenced by limitations in experimental resolution or discrepancies in temperature calibration across different measurement setups. The possibility of simultaneously probing both the electronic and structural states under identical thermal conditions would eliminate artefacts arising from equipment-specific calibration offsets and offer a clearer picture of whether the

observed temperature separation is genuine or instrumental. A deeper insight on this behaviour would be essential for disentangling the interplay between symmetry breaking and charge ordering in nickelates.

Recently the interest in orthoferrite family has resurged, driven by their potential to host transient magnetic and polar states in non-equilibrium conditions. In particular, the use of intense terahertz pulses to drive optical phonons into the non-linear regime raises the possibility of dynamically inducing novel ferroic states. Achieving this goal, however, requires a detailed and complete understanding of lattice excitations under equilibrium conditions—an area to which this thesis has contributed and which now serves as a foundation for future ultrafast studies.

In the case of $NdFeO_3$, the interpretation of muon spin spectroscopy analysis should be complemented by density functional theory (DFT) calculations aimed at determining the most probable muon stopping sites within the crystallographic structure. This effort is currently being undertaken in collaboration with PhD student Muhammad Aasim and his supervisor Estelina Silva at IFIMUP. Furthermore, a deeper understanding of symmetry-breaking during SRT - Wyckoff position splitting - and of the additional precession frequency associated with the rare-earth non cooperative magnetic ordering below the reorientation process, would benefit from comparative studies. Investigating another rare-earth ferrite, such as $SmFeO_3$ which exhibits distinct reorientation temperatures and anti-magnetic anisotropy profile, could provide validation for the hypothesis proposed in this thesis regarding the interpretation of μSR data and its sensitivity to structural symmetry lowering and rare-earth sublattice behaviour.

Additionally, the magnetic structure of $NdFeO_3$ at temperatures below the compensation point (T_{comp}) with applied magnetic field, remains unresolved. Due to the proximity of this regime to the Nd ordering temperature T_N^{Nd} = 1.05 K and the increase of competing contributions from the $4f$ -Nd with $3d$-Fe, the system exhibits a rich but not yet fully understood magnetic behaviour. Further experimental studies, such as neutron diffraction, and theoretical efforts will be essential to unravel the precise spin configuration in this temperature range.

Finally, to directly probe the elastic properties of $NdFeO_3$ and assess the proposed softening of specific elastic constants across the spin reorientation transition, a proposal has been submitted and accepted at the European Synchrotron Radiation Facility (ESRF) to perform inelastic X-ray scattering measurements. This experiment aims to map the

dispersion relations of acoustic phonons near the Brillouin zone centre, allowing direct access to the elastic constants, providing a deeper understanding of the anomalies associated with the spin-lattice coupling in $NdFeO_3$.

References

[1] N. A. Spaldin, S.-W. Cheong, and R. Ramesh, “Multiferroics: Past, present, and future,” *Physics Today*, vol. 63, no. 10, pp. 38–43, oct 2010. [Online]. Available: http://physicstoday.scitation.org/doi/10.1063/1.3502547 [Cited on pages 1 and 2.]

[2] H. Y. Hwang, Y. Iwasa, M. Kawasaki, B. Keimer, N. Nagaosa, and Y. Tokura, “Emergent phenomena at oxide interfaces,” *Nature Materials*, vol. 11, no. 2, pp. 103–113, 2012. [Online]. Available: http://dx.doi.org/10.1038/nmat3223 [Cited on page 1.]

[3] N. A. Spaldin, “MATERIALS SCIENCE: The Renaissance of Magnetoelectric Multiferroics,” *Science*, vol. 309, no. 5733, pp. 391–392, jul 2005. [Online]. Available: http://www.ncbi.nlm.nih.gov/pubmed/16020720https://www.sciencemag.org/lookup/doi/10.1126/science.1113357 [Cited on page 1.]

[4] N. A. Spaldin and R. Ramesh, “Advances in magnetoelectric multiferroics,” *Nature Materials*, vol. 18, no. 3, pp. 203–212, mar 2019. [Online]. Available: http://dx.doi.org/10.1038/s41563-018-0275-2http://www.nature.com/articles/s41563-018-0275-2 [Cited on page 1.]

[5] E. Bousquet and A. Cano, “Non-collinear magnetism in multiferroic perovskites,” *Journal of Physics: Condensed Matter*, vol. 28, no. 12, p. 123001, mar 2016. [Online]. Available: https://iopscience.iop.org/article/10.1088/0953-8984/28/12/123001 [Cited on pages xv, xvi, 2, 9, 21, 22, and 86.]

[6] S. Catalano, M. Gibert, J. Fowlie, J. Íñiguez, J.-M. Triscone, and J. Kreisel, “Rare-earth nickelates RNiO3 : thin films and heterostructures,” *Reports on Progress in Physics*, vol. 81, no. 4, p. 046501, apr 2018. [Online]. Available: http://stacks.iop.org/0034-4885/81/i=4/a=046501?key=crossref.c95ab197e6b880dc2da6fd71f5758d81 [Cited on pages xv, 2, 12, 13, 14, 16, 17, and 53.]

[7] R. J. D. Tilley, *Perovskites: Structure-Property Relationships*, 1st ed., L. John Wiley Sons, Ed. UK: John Wiley Sons, Ltd, apr 2016. [Cited on pages 3 and 4.]

[8] V. M. Goldschmidt, "Die Gesetzeder Krystallochemie," *Die Naturwissenschaften*, vol. 21, p. 477, 1926. [Cited on page 4.]

[9] A. M. Glazer, "Simple Ways of Determining Perovskite Structures," *Acta Crystallographica Section B Structural Science*, vol. A31, pp. 756–762, 1975. [Online]. Available: https://journals.iucr.org/paper?a11802 [Cited on page 4.]

[10] R. H. Mitchell, *Perovskites: Modern and Ancient*. Ontario, Canada: Almaz Press Inc., 2002. [Cited on pages 4, 5, 6, and 7.]

[11] G. H. Kwei, A. C. Lawson, S. J. L. Billinge, and S. W. Cheong, "Structures of the ferroelectric phases of barium titanate," *The Journal of Physical Chemistry*, vol. 97, no. 10, pp. 2368–2377, mar 1993. [Online]. Available: https://pubs.acs.org/doi/abs/10.1021/j100112a043 [Cited on page 4.]

[12] A. M. Glazer, "The classification of tilted octahedra in perovskites," *Acta Crystallographica Section B Structural Crystallography and Crystal Chemistry*, vol. 28, no. 11, pp. 3384–3392, nov 1972. [Online]. Available: http://scripts.iucr.org/cgi-bin/paper?S0567740872007976 [Cited on pages 5 and 7.]

[13] H. T. Stokes, E. H. Kisi, D. M. Hatch, and C. J. Howard, "Group-theoretical analysis of octahedral tilting in ferroelectric perovskites," *Acta Crystallographica Section B Structural Science*, vol. 58, no. 6, pp. 934–938, dec 2002. [Online]. Available: https://journals.iucr.org/paper?S0108768102015756 [Cited on pages xv, 5, and 6.]

[14] P. M. Woodward, "Octahedral Tilting in Perovskites. II. Structure Stabilizing Forces," *Acta Crystallographica Section B Structural Science*, vol. 53, no. 1, pp. 44–66, feb 1997. [Online]. Available: https://journals.iucr.org/paper?S0108768196012050 [Cited on page 6.]

[15] P. Chen, M. N. Grisolia, H. J. Zhao, O. E. González-Vázquez, L. Bellaiche, M. Bibes, B. G. Liu, and J. Íñiguez, "Energetics of oxygen-octahedra rotations in perovskite oxides from first principles," *Physical Review B*, vol. 97, no. 2, pp. 1–22, 2018. [Online]. Available: https://journals.aps.org/prb/abstract/10.1103/PhysRevB.97.024113 [Cited on pages 6 and 8.]

[16] J. M. Perez-Mato, D. Orobengoa, and M. I. Aroyo, *Mode crystallography of distorted structures*. International Union of Crystallography, 2010, vol. 66, no. 5. [Online]. Available: https://journals.iucr.org/a/issues/2010/05/00/sh5107/index.html [Cited on pages xv, 7, and 8.]

[17] N. Miao, N. C. Bristowe, B. Xu, M. J. Verstraete, and P. Ghosez, "First-principles study of the lattice dynamical properties of strontium ruthenate," *Journal of Physics: Condensed Matter*, vol. 26, no. 3, p. 035401, jan 2014. [Online]. Available: https://iopscience.iop.org/article/10.1088/0953-8984/26/3/035401 [Cited on page 8.]

[18] E. F. Bertaut, *Magnetism: A treatise on modern theory and materials, vol. III*, G. T. Rado and H. Suhl, Eds. New York: Academic Press, 1963, vol. 3. [Cited on pages 9 and 11.]

[19] ——, "Representation analysis of magnetic structures," *Acta Crystallographica Section A: Crystal Physics, Diffraction, Theoretical and General Crystallography*, vol. 24, no. 1, pp. 217–231, jan 1968. [Online]. Available: https://journals.iucr.org/paper?S0567739468000306 [Cited on pages xiii, 9, 10, and 11.]

[20] R. L. White, "Review of Recent Work on the Magnetic and Spectroscopic Properties of the Rare-Earth Orthoferrites," *Journal of Applied Physics*, vol. 40, no. 3, pp. 1061–1069, mar 1969. [Online]. Available: https://pubs.aip.org/jap/article/40/3/1061/502958/Review-of-Recent-Work-on-the-Magnetic-and [Cited on pages 21, 22, 25, and 76.]

[21] T. Yamaguchi, "Theory of spin reorientation in rare-earth orthochromites and orthoferrites," *Journal of Physics and Chemistry of Solids*, vol. 35, no. 4, pp. 479–500, jan 1974. [Online]. Available: https://linkinghub.elsevier.com/retrieve/pii/S002236977480003X [Cited on pages 11, 22, 23, 24, 25, and 76.]

[22] M. L. Medarde, "Structural, magnetic and electronic properties of RNiO3 perovskites (R = rare earth)," *Journal of Physics Condensed Matter*, vol. 9, no. 8, pp. 1679–1707, 1997. [Online]. Available: https://iopscience.iop.org/article/10.1088/0953-8984/9/8/003 [Cited on pages 12, 17, 53, and 59.]

[23] T. Mizokawa, H. Namatame, A. Fujimori, K. Akeyama, H. Kondoh, H. Kuroda, and N. Kosugi, "Origin of the band gap in the negative charge-transfer-energy compound NaCuO2," *Physical Review Letters*, vol. 67, no. 12, pp. 1638–1641, sep

1991. [Online]. Available: https://link.aps.org/doi/10.1103/PhysRevLett.67.1638 [Cited on page 13.]

[24] J. Fowlie, “Electronic and structural properties of LaNiO3-based heterostructures Electronic and structural properties of LaNiO 3 -based heterostructures,” Ph.D. dissertation, Université de Genève, 2018. [Cited on pages xv and 13.]

[25] J. A. Alonso, J. L. García-Muñoz, M. T. Fernández-Díaz, M. A. Aranda, M. J. Martínez-Lope, and M. T. Casais, “Charge disproportionation in RNiO3 perovskites: Simultaneous metal-insulator and structural transition in YNiO3,” *Physical Review Letters*, vol. 82, no. 19, pp. 3871–3874, 1999. [Online]. Available: https://journals.aps.org/prl/pdf/10.1103/PhysRevLett.82.3871 [Cited on page 14.]

[26] J. L. García-Muñoz, M. A. Aranda, J. A. Alonso, and M. J. Martínez-Lope, “Structure and charge order in the antiferromagnetic band-insulating phase of NdNiO3,” *Physical Review B - Condensed Matter and Materials Physics*, vol. 79, no. 13, pp. 1–5, 2009. [Online]. Available: https://journals.aps.org/prb/pdf/10.1103/PhysRevB.79.134432 [Cited on pages 14, 18, 53, and 59.]

[27] C. Girardot, J. Kreisel, S. Pignard, N. Caillault, and F. Weiss, “Raman scattering investigation across the magnetic and metal-insulator transition in rare earth nickelate R NiO3 (R=Sm, Nd) thin films,” *Physical Review B - Condensed Matter and Materials Physics*, vol. 78, no. 10, pp. 1–7, 2008. [Online]. Available: https://journals.aps.org/prb/abstract/10.1103/PhysRevB.78.104101 [Cited on pages 14, 39, 53, 60, and 61.]

[28] A. Mercy, J. Bieder, J. Íñiguez, and P. Ghosez, “Structurally triggered metal-insulator transition in rare-earth nickelates,” *Nature Communications*, vol. 8, no. 1, pp. 1–6, 2017. [Online]. Available: http://dx.doi.org/10.1038/s41467-017-01811-x [Cited on pages xv, 14, 15, 53, 59, 62, and 65.]

[29] I. Vobornik, L. Perfetti, M. Zacchigna, M. Grioni, G. Margaritondo, J. Mesot, M. Medarde, and P. Lacorre, “Electronic-structure evolution through the metal-insulator transition in RNiO3,” *Physical Review B*, vol. 60, no. 12, pp. R8426–R8429, sep 1999. [Online]. Available: https://link.aps.org/doi/10.1103/PhysRevB.60.R8426 [Cited on pages xv and 16.]

[30] G. Catalan, “Progress in perovskite nickelate research,” *Phase Transitions*, vol. 81, no. 7-8, pp. 729–749, jul 2008. [Online]. Available: http://www.tandfonline.com/doi/abs/10.1080/01411590801992463 [Cited on pages 16, 17, 53, and 64.]

[31] S. Catalano, M. Gibert, V. Bisogni, O. E. Peil, F. He, R. Sutarto, M. Viret, P. Zubko, R. Scherwitzl, A. Georges, G. A. Sawatzky, T. Schmitt, and J. M. Triscone, “Electronic transitions in strained SmNiO3 thin films,” *APL Materials*, vol. 2, no. 11, 2014. [Online]. Available: https://doi.org/10.1063/1.4902138 [Cited on page 16.]

[32] P. Lacorre, J. Pannetier, S. A. I. Nazzal, P. W. Wang, and T. C. Huang, “Synthesis, Crystal Structure and Properties of Metalic PrNiO3: Comparison with Metallic NdNiO3 and Semiconducting SmNiO3,” *Journal of Solid State Chemistry*, vol. 91, pp. 225–237, 1991. [Online]. Available: https://www.sciencedirect.com/science/article/abs/pii/002245969190077U [Cited on pages 17, 18, 53, and 64.]

[33] J. A. Alonso, M. J. Martínez-Lope, M. T. Casais, M. A. G. Aranda, and M. T. Fernández-Díaz, “Metal−Insulator Transitions, Structural and Microstructural Evolution of RNiO 3 (R = Sm, Eu, Gd, Dy, Ho, Y) Perovskites: Evidence for Room-Temperature Charge Disproportionation in Monoclinic HoNiO 3 and YNiO 3,” *Journal of the American Chemical Society*, vol. 121, no. 20, pp. 4754–4762, may 1999. [Online]. Available: https://pubs.acs.org/doi/10.1021/ja984015x [Cited on page 17.]

[34] I. Nikulin, M. Novojilov, A. Kaul, S. Mudretsova, and S. Kondrashov, “Oxygen nonstoichiometry of NdNiO3−δ and SmNiO3−δ,” *Materials Research Bulletin*, vol. 39, no. 6, pp. 775–791, may 2004. [Online]. Available: https://linkinghub.elsevier.com/retrieve/pii/S0025540804000352 [Cited on pages 17 and 55.]

[35] Y. M. Klein, M. Kozlowski, A. Linden, P. Lacorre, M. Medarde, and D. J. Gawryluk, “RENiO 3 Single Crystals (RE = Nd, Sm, Gd, Dy, Y, Ho, Er, Lu) Grown from Molten Salts under 2000 bar of Oxygen Gas Pressure,” *Crystal Growth and Design*, vol. 21, no. 7, pp. 4230–4241, jul 2021. [Online]. Available: https://pubs.acs.org/doi/10.1021/acs.cgd.1c00474 [Cited on page 17.]

[36] G. Catalan, R. M. Bowman, and J. M. Gregg, “Metal-insulator transitions in NdNiO3 thin films,” *Physical Review B*, vol. 62, no. 12, pp. 7892–7900, sep 2000. [Online]. Available: https://link.aps.org/doi/10.1103/PhysRevB.62.7892 [Cited on pages xv, 17, 18, 19, 53, 55, 58, and 65.]

[37] S. Catalano, M. Gibert, V. Bisogni, F. He, R. Sutarto, M. Viret, P. Zubko, R. Scherwitzl, G. A. Sawatzky, and E. Al., "Tailoring the electronic transitions of NdNiO3 films through (111) pc oriented interfaces," *APL Materials*, vol. 3, no. 6, p. 062506, jun 2015. [Online]. Available: http://aip.scitation.org/doi/10.1063/1.4919803 [Cited on page 53.]

[38] Q. Guo, S. Farokhipoor, C. Magén, F. Rivadulla, and B. Noheda, "Tunable resistivity exponents in the metallic phase of epitaxial nickelates," *Nature Communications*, vol. 11, no. 1, p. 2949, dec 2020. [Online]. Available: http://www.nature.com/articles/s41467-020-16740-5 [Cited on pages 17, 56, 57, and 58.]

[39] J. Blasco, M. Castro, and J. Garcia, "Structural, electronic, magnetic and calorimetric study of the metal-insulator transition in NdNiO 3- delta," *Journal of Physics: Condensed Matter*, vol. 6, no. 30, pp. 5875–5889, jul 1994. [Online]. Available: https://iopscience.iop.org/article/10.1088/0953-8984/6/30/009 [Cited on page 17.]

[40] J. L. García-Muñoz, J. Rodríguez-Carvajal, P. Lacorre, and J. B. Torrance, "Neutron-diffraction study of R NiO 3 (R =La,Pr,Nd,Sm): Electronically induced structural changes across the metal-insulator transition," *Physical Review B*, vol. 46, no. 8, pp. 4414–4425, aug 1992. [Online]. Available: https://link.aps.org/doi/10.1103/PhysRevB.46.4414 [Cited on pages 18 and 59.]

[41] M. Zaghrioui, A. Bulou, P. Laffez, and P. Lacorre, "Raman study of metal-insulator transition in NdNiO3 thin films," *Journal of Magnetism and Magnetic Materials*, vol. 211, no. 1, pp. 238–242, 2000. [Online]. Available: https://www.sciencedirect.com/science/article/pii/S0304885399007404 [Cited on pages 18 and 60.]

[42] M. Zaghrioui, A. Bulou, P. Lacorre, and P. Laffez, "Electron diffraction and Raman scattering evidence of a symmetry breaking at the metal-insulator transition of NdNiO3," *Physical Review B - Condensed Matter and Materials Physics*, vol. 64, no. 8, pp. 811 021–811 024, 2001. [Online]. Available: https://journals.aps.org/prb/abstract/10.1103/PhysRevB.64.081102 [Cited on pages 18, 60, and 61.]

[43] J. L. García-Muñoz, J. Rodríguez-Carvajal, and P. Lacorre, "Sudden Appearance of an Unusual Spin Density Wave At the Metal-Insulator Transition in the Perovskites

RNiO 3 (R = Pr, Nd)," *Europhysics Letters (EPL)*, vol. 20, no. 3, pp. 241–247, oct 1992. [Online]. Available: https://iopscience.iop.org/article/10.1209/0295-5075/20/3/009 [Cited on page 18.]

[44] X. Granados, J. Fontcuberta, X. Obradors, L. Mañosa, and J. B. Torrance, "Metallic state and the metal-insulator transition of NdNiO3," *Physical Review B*, vol. 48, no. 16, pp. 11 666–11 672, 1993. [Online]. Available: https://link.aps.org/doi/10.1103/PhysRevB.48.11666 [Cited on pages 18 and 58.]

[45] G. Mattoni, P. Zubko, F. Maccherozzi, A. van der Torren, D. B. Boltje, M. Hadjimichael, N. Manca, S. Catalano, M. Gibert, and E. Al., "Striped nanoscale phase separation at the metal–insulator transition of heteroepitaxial nickelates," *Nature Communications*, vol. 7, no. 1, p. 13141, nov 2016. [Online]. Available: https://www.nature.com/articles/ncomms13141 [Cited on pages xv, 18, 21, 53, 58, and 59.]

[46] D. Preziosi, L. Lopez-Mir, X. Li, T. Cornelissen, J. H. Lee, F. Trier, K. Bouzehouane, S. Valencia, A. Gloter, and E. Al., "Direct Mapping of Phase Separation across the Metal-Insulator Transition of NdNiO3." *Nano letters*, vol. 18, no. 4, pp. 2226–2232, 2018. [Online]. Available: http://www.ncbi.nlm.nih.gov/pubmed/29589952

[47] J. H. Lee, F. Trier, T. Cornelissen, D. Preziosi, K. Bouzehouane, S. Fusil, S. Valencia, and M. Bibes, "Imaging and Harnessing Percolation at the Metal–Insulator Transition of NdNiO 3 Nanogaps," *Nano Letters*, vol. 19, no. 11, pp. 7801–7805, nov 2019. [Online]. Available: https://pubs.acs.org/doi/10.1021/acs.nanolett.9b02815 [Cited on pages 18, 20, and 58.]

[48] Q. Guo and B. Noheda, "From hidden metal-insulator transition to Planckian-like dissipation by tuning the oxygen content in a nickelate," *npj Quantum Materials*, vol. 6, no. 1, p. 72, dec 2021. [Online]. Available: https://www.nature.com/articles/s41535-021-00374-x [Cited on pages 18, 53, 55, and 58.]

[49] M. M. Gomes, B. Manjunath, R. Vilarinho, A. A. Bassou, B. Silva, J. Oliveira, I. Çaha, F. L. Deepak, B. Almeida, A. Almeida, J. Kreisel, P. B. Tavares, J. Íñiguez, and J. A. Moreira, "Structural percolation evolution throughout the metal-to-insulator transition in NdNiO3," *Physical Review B*, vol. 109, no. 22, p. 224109, jun 2024. [Online]. Available: https://link.aps.org/doi/10.1103/PhysRevB.109.224109 [Cited on pages 18 and 54.]

[50] J. Li, J. Pelliciari, C. Mazzoli, S. Catalano, F. Simmons, J. T. Sadowski, A. Levitan, M. Gibert, E. Carlson, J.-M. Triscone, S. Wilkins, and R. Comin, "Scale-invariant magnetic textures in the strongly correlated oxide NdNiO3," *Nature Communications*, vol. 10, no. 1, p. 4568, oct 2019. [Online]. Available: https://www.nature.com/articles/s41467-019-12502-0 [Cited on pages xvi, 20, and 21.]

[51] R. M. White, R. J. Nemanich, and C. Herring, "Light scattering from magnetic excitations in orthoferrites," *Physical Review B*, vol. 25, no. 3, pp. 1822–1836, feb 1982. [Online]. Available: https://link.aps.org/doi/10.1103/PhysRevB.25.1822 [Cited on pages 21, 26, 27, 28, 73, 76, 77, and 78.]

[52] Y. Tokunaga, N. Furukawa, H. Sakai, Y. Taguchi, T.-h. Arima, and Y. Tokura, "Composite domain walls in a multiferroic perovskite ferrite," *Nature Materials*, vol. 8, no. 7, pp. 558–562, jul 2009. [Online]. Available: http://www.nature.com/articles/nmat2469 [Cited on page 21.]

[53] Y. Tokunaga, S. Iguchi, T. Arima, and Y. Tokura, "Magnetic-Field-Induced Ferroelectric State in DyFeO3," *Physical Review Letters*, vol. 101, no. 9, p. 097205, aug 2008. [Online]. Available: https://link.aps.org/doi/10.1103/PhysRevLett.101.097205 [Cited on page 21.]

[54] J.-H. Lee, Y. K. Jeong, J. H. Park, M.-A. Oak, H. M. Jang, J. Y. Son, and J. F. Scott, "Spin-Canting-Induced Improper Ferroelectricity and Spontaneous Magnetization Reversal in SmFe3," *Physical Review Letters*, vol. 107, no. 11, p. 117201, sep 2011. [Online]. Available: https://link.aps.org/doi/10.1103/PhysRevLett.107.117201 [Cited on page 21.]

[55] C.-Y. Kuo, Y. Drees, M. T. Fernández-Díaz, L. Zhao, L. Vasylechko, D. Sheptyakov, A. M. T. Bell, T. W. Pi, H.-J. Lin, M.-K. Wu, E. Pellegrin, S. M. Valvidares, Z. W. Li, P. Adler, A. Todorova, R. Küchler, A. Steppke, L. H. Tjeng, Z. Hu, and A. C. Komarek, "k=0 Magnetic Structure and Absence of Ferroelectricity in SmFeO3," *Physical Review Letters*, vol. 113, no. 21, p. 217203, nov 2014. [Online]. Available: https://link.aps.org/doi/10.1103/PhysRevLett.113.217203 [Cited on page 21.]

[56] X. Li, D. Kim, Y. Liu, and J. Kono, "Terahertz spin dynamics in rare-earth orthoferrites," *Photonics Insights*, vol. 1, no. 2, p. R05, 2022. [Online]. Available: https://www.researching.cn/articles/OJ71e394d50dce845a [Cited on pages xvi, 21, 22, 26, 28, 67, and 76.]

[57] H. J. Zhao, L. Bellaiche, X. M. Chen, and J. Íñiguez, "Improper electric polarization in simple perovskite oxides with two magnetic sublattices," *Nature Communications*, vol. 8, no. 1, p. 14025, apr 2017. [Online]. Available: http://www.nature.com/articles/ncomms14025 [Cited on page 21.]

[58] D. Nicoletti and A. Cavalleri, "Nonlinear light–matter interaction at terahertz frequencies," *Advances in Optics and Photonics*, vol. 8, no. 3, p. 401, 2016. [Online]. Available: https://opg.optica.org/aop/abstract.cfm?uri=aop-8-3-401 [Cited on pages 21 and 67.]

[59] T. F. Nova, A. Cartella, A. Cantaluppi, M. Först, D. Bossini, R. V. Mikhaylovskiy, A. V. Kimel, R. Merlin, and A. Cavalleri, "An effective magnetic field from optically driven phonons," *Nature Physics*, vol. 13, no. 2, pp. 132–136, feb 2017. [Online]. Available: http://www.nature.com/articles/nphys3925 [Cited on pages xvi, 21, 22, and 67.]

[60] D. Afanasiev, J. R. Hortensius, B. A. Ivanov, A. Sasani, E. Bousquet, Y. M. Blanter, R. V. Mikhaylovskiy, A. V. Kimel, and A. D. Caviglia, "Ultrafast control of magnetic interactions via light-driven phonons," *Nature Materials*, vol. 20, no. 5, pp. 607–611, may 2021. [Online]. Available: http://www.nature.com/articles/s41563-021-00922-7 [Cited on pages 21 and 67.]

[61] C. S. Davies, F. G. N. Fennema, A. Tsukamoto, I. Razdolski, A. V. Kimel, and A. Kirilyuk, "Phononic switching of magnetization by the ultrafast Barnett effect," *Nature*, vol. 628, no. 8008, pp. 540–544, apr 2024. [Online]. Available: https://www.nature.com/articles/s41586-024-07200-x [Cited on page 21.]

[62] T. Moriya, "Anisotropic Superexchange Interaction and Weak Ferromagnetism," *Physical Review*, vol. 120, no. 1, pp. 91–98, oct 1960. [Online]. Available: https://link.aps.org/doi/10.1103/PhysRev.120.91 [Cited on page 22.]

[63] I. Dzyaloshinsky, "A thermodynamic theory of "weak" ferromagnetism of antiferromagnetics," *Journal of Physics and Chemistry of Solids*, vol. 4, no. 4, pp. 241–255, jan 1958. [Online]. Available: https://linkinghub.elsevier.com/retrieve/pii/0022369758900763 [Cited on page 22.]

[64] S. J. Yuan, Y. M. Cao, L. Li, T. F. Qi, S. X. Cao, J. C. Zhang, L. E. DeLong, and G. Cao, "First-order spin reorientation transition and specific-heat anomaly in CeFeO3," *Journal of Applied Physics*, vol. 114, no. 11, sep 2013. [Online].

Available: https://pubs.aip.org/jap/article/114/11/113909/139868/First-order-spin-reorientation-transition-and [Cited on pages 25 and 107.]

[65] R. M. Bozorth, V. Kramer, and J. P. Remeika, “Magnetization in Single Crystals of Some Rare-Earth Orthoferrites,” *Physical Review Letters*, vol. 1, no. 1, pp. 3–4, jul 1958. [Online]. Available: https://link.aps.org/doi/10.1103/PhysRevLett.1.3 [Cited on page 25.]

[66] G. Voroboev, A. Kadomtseva, I. Krynetii, and A. Mukhin, “Unusual nature of spin reorientation in HoFeO3,” *Zh. Eksp. Teor. Fiz.*, vol. 95, p. 1049, 1989. [Cited on page 25.]

[67] F. Bartolomé, M. Kuz’min, J. Bartolomé, J. Blasco, J. García, and F. Sapiña, “Low-temperature specific heat of NdMO3(M=Co, Fe, Cr, Ni): Magnetic ordering of Nd,” *Solid State Communications*, vol. 91, no. 3, pp. 177–182, jul 1994. [Online]. Available: https://linkinghub.elsevier.com/retrieve/pii/0038109894902186 [Cited on pages 25, 32, 96, 97, 111, and 119.]

[68] D. Treves, “Studies on Orthoferrites at the Weizmann Institute of Science,” *Journal of Applied Physics*, vol. 36, no. 3, pp. 1033–1039, mar 1965. [Online]. Available: http://aip.scitation.org/doi/10.1063/1.1714088 [Cited on pages 27, 29, and 103.]

[69] W. C. Koehler, E. O. Wollan, and M. K. Wilkinson, “Neutron Diffraction Study of the Magnetic Properties of Rare-Earth-Iron Perovskites,” *Physical Review*, vol. 118, no. 1, pp. 58–70, apr 1960. [Online]. Available: https://link.aps.org/doi/10.1103/PhysRev.118.58 [Cited on page 29.]

[70] W. Sławiński, R. Przeniosło, I. Sosnowska, and E. Suard, “Spin reorientation and structural changes in NdFeO3,” *Journal of Physics: Condensed Matter*, vol. 17, no. 29, pp. 4605–4614, jul 2005. [Online]. Available: https://iopscience.iop.org/article/10.1088/0953-8984/17/29/002 [Cited on pages xvi, xix, 29, 30, 33, 85, 92, 93, 94, 97, 98, 101, 108, and 169.]

[71] S. J. Yuan, W. Ren, F. Hong, Y. B. Wang, J. C. Zhang, L. Bellaiche, S. X. Cao, and G. Cao, “Spin switching and magnetization reversal in single-crystal NdFeO3,” *Physical Review B*, vol. 87, no. 18, p. 184405, may 2013. [Online]. Available: https://link.aps.org/doi/10.1103/PhysRevB.87.184405 [Cited on pages xvi, 27, 29, 30, 31, 32, 96, 107, 111, 112, 114, and 116.]

[72] S. M. Shapiro, J. D. Axe, and J. P. Remeika, “Neutron-scattering studies of spin waves in rare-earth orthoferrites,” *Physical Review B*, vol. 10, no. 5, pp. 2014–2021, sep 1974. [Online]. Available: https://link.aps.org/doi/10.1103/PhysRevB.10.2014 [Cited on page 28.]

[73] N. Koshizuka and K. Hayashi, “Raman Scattering from Magnon Excitations in RFeO 3,” *Journal of the Physical Society of Japan*, vol. 57, no. 12, pp. 4418–4428, dec 1988. [Online]. Available: http://journals.jps.jp/doi/10.1143/JPSJ.57.4418 [Cited on pages 28 and 111.]

[74] W. Sławiński, R. Przeniosło, I. Sosnowska, M. Brunelli, and M. Bieringer, “Anomalous thermal expansion in polycrystalline NdFeO3 studied by SR and X-ray diffraction,” *Nuclear Instruments and Methods in Physics Research Section B: Beam Interactions with Materials and Atoms*, vol. 254, no. 1, pp. 149–152, jan 2007. [Online]. Available: https://linkinghub.elsevier.com/retrieve/pii/S0168583X06010445 [Cited on pages xix, 29, 33, 34, 35, 85, 92, 93, 94, 101, and 108.]

[75] I. Sosnowsk, E. Steichelea, and A. Hewatc, “Reorientation phase transition in NdfeO3,” *Physica B+C*, vol. 136, no. 1-3, pp. 394–396, jan 1986. [Online]. Available: https://linkinghub.elsevier.com/retrieve/pii/S0378436386800997 [Cited on pages 29, 33, and 108.]

[76] S. Yuan, Y. Wang, M. Shao, F. Chang, B. Kang, Y. Isikawa, and S. Cao, “Magnetic properties of NdFeO 3 single crystal in the spin reorientation region,” *Journal of Applied Physics*, vol. 109, no. 7, p. 07E141, apr 2011. [Online]. Available: http://aip.scitation.org/doi/10.1063/1.3562259 [Cited on pages 29 and 116.]

[77] G. Song, J. Jiang, B. Kang, J. Zhang, Z. Cheng, G. Ma, and S. Cao, “Spin reorientation transition process in single crystal NdFeO3,” *Solid State Communications*, vol. 211, pp. 47–51, jun 2015. [Online]. Available: https://linkinghub.elsevier.com/retrieve/pii/S0038109815001064 [Cited on pages xvi, xix, 29, 31, 93, 94, 98, and 169.]

[78] M. Eibschütz, S. Shtrikman, and D. Treves, “Mössbauer Studies of Fe57 in Orthoferrites,” *Physical Review*, vol. 156, no. 2, pp. 562–577, apr 1967. [Online]. Available: https://link.aps.org/doi/10.1103/PhysRev.156.562 [Cited on page 29.]

[79] J. Jiang, Z. Jin, G. Song, X. Lin, G. Ma, and S. Cao, “Dynamical spin reorientation transition in NdFeO 3 single crystal observed with polarized terahertz time domain spectroscopy,” *Applied Physics Letters*, vol. 103, no. 6, p. 062403, aug 2013. [Online]. Available: http://aip.scitation.org/doi/10.1063/1.4818135 [Cited on pages 29, 67, and 116.]

[80] E. Constable, D. L. Cortie, J. Horvat, R. A. Lewis, Z. Cheng, G. Deng, S. Cao, S. Yuan, and G. Ma, “Complementary terahertz absorption and inelastic neutron study of the dynamic anisotropy contribution to zone-center spin waves in a canted antiferromagnet NdFeO3,” *Physical Review B*, vol. 90, no. 5, p. 054413, aug 2014. [Online]. Available: https://link.aps.org/doi/10.1103/PhysRevB.90.054413 [Cited on pages 76 and 81.]

[81] R. Vilarinho, M. C. Weber, M. Guennou, A. C. Miranda, C. Dias, P. Tavares, J. Kreisel, A. Almeida, and J. A. Moreira, “Magnetostructural coupling in RFeO3 (R = Nd, Tb, Eu and Gd),” *Scientific Reports*, vol. 12, no. 1, p. 9697, dec 2022. [Online]. Available: https://www.nature.com/articles/s41598-022-13097-1 [Cited on pages xiii, xviii, 29, 67, 69, 70, 80, and 85.]

[82] R. Przeniosło, I. Sosnowska, and P. Fischer, “Magnetic moment ordering of Nd3+ ions in NdFeO3,” *Journal of Magnetism and Magnetic Materials*, vol. 140-144, pp. 2153–2154, feb 1995. [Online]. Available: https://linkinghub.elsevier.com/retrieve/pii/0304885394012792 [Cited on pages 29 and 33.]

[83] R. Przeniosło, I. Sosnowska, P. Fischer, W. Marti, F. Bartolomé, J. Bartolomé, E. Palacios, and R. Sonntag, “Magnetic moment ordering of Nd3+ and Fe3+ in NdFe03 at low temperature,” *Journal of Magnetism and Magnetic Materials*, vol. 160, pp. 370–371, jul 1996. [Online]. Available: https://linkinghub.elsevier.com/retrieve/pii/030488539600234X [Cited on pages 29 and 33.]

[84] M. Loewenhaupt, I. Sosnowska, and B. Frick, “Spin-reorientation in NdFeO3 and the magnetic excitation spectrum of Nd,” *Journal de Physique Colloques*, vol. 49, no. C8, p. 921, 1988. [Online]. Available: https://hal.archives-ouvertes.fr/jpa-00228611 [Cited on pages xvi, 32, and 33.]

[85] J. Bartolomé, E. Palacios, M. D. Kuz’min, F. Bartolomé, I. Sosnowska, R. Przeniosło, R. Sonntag, and M. M. Lukina, “Single-crystal neutron diffraction study of Nd magnetic ordering in NdFeO3 at low temperature,” *Physical Review*

B, vol. 55, no. 17, pp. 11 432–11 441, may 1997. [Online]. Available: https://link.aps.org/doi/10.1103/PhysRevB.55.11432 [Cited on pages 32, 33, and 111.]

[86] P. Fabrykiewicz, R. Przeniosło, and I. Sosnowska, "Magnetic, electric and toroidal polarization modes describing the physical properties of crystals. NdFeO 3 case," *Acta Crystallographica Section A Foundations and Advances*, vol. 79, no. 1, pp. 80–94, jan 2023. [Online]. Available: https://scripts.iucr.org/cgi-bin/paper?S2053273322009858 [Cited on pages 33, 34, and 164.]

[87] P. Fabrykiewicz, R. Przeniosło, I. Sosnowska, R. Przenioslo, and I. Sosnowska, "Magnetic modes compatible with the symmetry of crystals," *Acta Crystallographica Section A Foundations and Advances*, vol. 77, no. 4, pp. 327–338, jul 2021. [Online]. Available: https://scripts.iucr.org/cgi-bin/paper?S2053273321004551 [Cited on pages xxi, 33, 34, 35, 164, and 165.]

[88] L. T. Tsymbal, V. I. Kamenev, Y. B. Bazaliy, D. A. Khara, and P. E. Wigen, "Structural properties of ErFeO3 in the spin-reorientation region," *Physical Review B*, vol. 72, no. 5, p. 052413, aug 2005. [Online]. Available: https://link.aps.org/doi/10.1103/PhysRevB.72.052413 [Cited on pages xvi, 34, 35, 85, 101, and 113.]

[89] L. T. Tsymbal, Y. B. Bazaliy, V. N. Derkachenko, V. I. Kamenev, G. N. Kakazei, F. J. Palomares, and P. E. Wigen, "Magnetic and structural properties of spin-reorientation transitions in orthoferrites," *Journal of Applied Physics*, vol. 101, no. 12, jun 2007. [Online]. Available: https://pubs.aip.org/jap/article/101/12/123919/343574/Magnetic-and-structural-properties-of-spin [Cited on pages xvi, 34, 35, 85, and 101.]

[90] H. Horner and C. M. Varma, "Nature of Spin-Reorientation Transitions," *Physical Review Letters*, vol. 20, no. 16, pp. 845–846, apr 1968. [Online]. Available: https://link.aps.org/doi/10.1103/PhysRevLett.20.845 [Cited on pages 35, 36, 91, and 169.]

[91] M. Mihalik, M. Mihalik, M. Zentková, K. Uhlířová, M. Kratochvílová, and P. Roupcová, "Magneto-crystalline anisotropy of NdFe0.9Mn0.1O3 single crystal," *Physica B: Condensed Matter*, vol. 536, no. June 2017, pp. 89–92, may 2018. [Online]. Available: https://linkinghub.elsevier.com/retrieve/pii/S0921452617308608 [Cited on page 39.]

[92] H. Fujimori, M. Kakihana, K. Ioku, S. Goto, and M. Yoshimura, "Advantage of anti-Stokes Raman scattering for high-temperature measurements," *Applied Physics Letters*, vol. 79, no. 7, pp. 937–939, aug 2001. [Online]. Available: https://pubs.aip.org/apl/article/79/7/937/114556/Advantage-of-anti-Stokes-Raman-scattering-for-high [Cited on page 43.]

[93] W. Hayes and R. Loudon, *Scattering of Light by Crystals*. New York: John Wiley and Sons, 1978. [Cited on page 43.]

[94] F. Gervais, *Infrared and Millimeter Waves vol 8*, K J Button, Ed. London: Academic Press, 1983. [Cited on page 44.]

[95] F. Hippert, E. Geissler, J. L. Hodeau, E. Lelievre-Berna, and J. Regnard, *Neutron and X-ray Spectroscopy*. Springer, 2006. [Cited on page 47.]

[96] G. van der Laan and T. Hesjedal, "X-ray detected ferromagnetic resonance techniques for the study of magnetization dynamics," *Nuclear Instruments and Methods in Physics Research Section B: Beam Interactions with Materials and Atoms*, vol. 540, no. April, pp. 85–93, jul 2023. [Online]. Available: https://linkinghub.elsevier.com/retrieve/pii/S0168583X23001337 [Cited on pages 47, 113, and 114.]

[97] P. Fischer and H. Ohldag, "X-rays and magnetism," *Reports on Progress in Physics*, vol. 78, no. 9, p. 094501, sep 2015. [Online]. Available: https://iopscience.iop.org/article/10.1088/0034-4885/78/9/094501 [Cited on page 48.]

[98] A. Migliori and J. L. Sarrao, *Resonant Ultrasound Spectroscopy: Applications to Physics, Materials Measurements, and Nondestructive Evaluation*. Wiley, 1997. [Cited on pages 48 and 49.]

[99] S. J. Blundell, R. De Renzi, T. Lancaster, and F. L. Pratt, *Muon Spectroscopy: An Introduction*. Oxford University PressOxford, nov 2022. [Online]. Available: https://academic.oup.com/book/43671 [Cited on pages xvii, 49, 50, and 103.]

[100] A. Suter and B. Wojek, "Musrfit: A Free Platform-Independent Framework for μSR Data Analysis," *Physics Procedia*, vol. 30, pp. 69–73, 2012. [Online]. Available: https://linkinghub.elsevier.com/retrieve/pii/S187538921201228X [Cited on page 51.]

[101] T. Kurihara, K. Hirota, H. Qiu, K. T. N. Phan, K. Kato, G. Isoyama, and M. Nakajima, "Reconfiguration of magnetic domain structures of ErFeO3 by intense terahertz free electron laser pulses," *Scientific Reports*, vol. 10, no. 1, p. 7321, apr 2020. [Online]. Available: https://www.nature.com/articles/s41598-020-64147-5 [Cited on pages xvii and 51.]

[102] J. Torrance, P. Lacorre, A. Nazzal, E. Ansaldo, and C. Niedermayer, "Systematic study of insulator-metal transitions in perovskites RNiO3 (R=Pr,Nd,Sm,Eu) due to closing of charge-transfer gap," *Physical Review B*, vol. 45, no. 14, pp. 8209–8212, apr 1992. [Online]. Available: https://link.aps.org/doi/10.1103/PhysRevB.45.8209 [Cited on page 53.]

[103] I. Ardizzone, J. Teyssier, I. Crassee, A. B. Kuzmenko, D. G. Mazzone, D. J. Gawryluk, M. Medarde, and D. van der Marel, "Raman spectroscopic evidence for multiferroicity in rare earth nickelate single crystals," *Physical Review Research*, vol. 3, no. 3, p. 033007, jul 2021. [Online]. Available: https://link.aps.org/doi/10.1103/PhysRevResearch.3.033007 [Cited on pages 53, 61, and 62.]

[104] P. Majhi, S. Mitra, A. Singh, B. Ghosh, V. R. Reddy, S. Saha, and A. K. Raychaudhuri, "Phase coexistence and resistance relaxation kinetics in NdNiO3 films below the metal-insulator transition temperature," *Physical Review B*, vol. 108, no. 6, p. 064103, aug 2023. [Online]. Available: https://link.aps.org/doi/10.1103/PhysRevB.108.064103 [Cited on page 53.]

[105] P. Laffez, M. Zaghrioui, I. Monot, T. Brousse, and P. Lacorre, "Microstructure and metal–insulator transition of NdNiO3 thin films on various substrates," *Thin Solid Films*, vol. 354, no. 1-2, pp. 50–54, oct 1999. [Online]. Available: https://linkinghub.elsevier.com/retrieve/pii/S004060909900557X [Cited on page 55.]

[106] Y. Kumar, R. J. Choudhary, S. K. Sharma, M. Knobel, and R. Kumar, "Strain dependent stabilization of metallic paramagnetic state in epitaxial NdNiO3 thin films," *Applied Physics Letters*, vol. 101, no. 13, pp. 1–6, 2012. [Online]. Available: https://doi.org/10.1063/1.4754593 [Cited on page 55.]

[107] C. Hu, X. Wang, T. Yao, T. Gao, J. Han, X. Zhang, Y. Zhang, P. Xu, and B. Song, "Enhanced Electrocatalytic Oxygen Evolution Activity by Tuning Both the Oxygen Vacancy and Orbital Occupancy of B□Site Metal Cation in NdNiO 3,"

Advanced Functional Materials, vol. 29, no. 30, p. 1902449, jul 2019. [Online]. Available: https://onlinelibrary.wiley.com/doi/abs/10.1002/adfm.201902449 [Cited on page 55.]

[108] D. Preziosi, A. Sander, A. Barthélémy, and M. Bibes, "Reproducibility and off-stoichiometry issues in nickelate thin films grown by pulsed laser deposition," *AIP Advances*, vol. 7, no. 1, p. 015210, jan 2017. [Online]. Available: http://aip.scitation.org/doi/10.1063/1.4975307 [Cited on page 56.]

[109] S. Heo, C. Oh, J. Son, and H. M. Jang, "Influence of tensile-strain-induced oxygen deficiency on metal-insulator transitions in NdNiO3-δ epitaxial thin films," *Scientific Reports*, vol. 7, no. 1, pp. 1–9, 2017. [Online]. Available: https://www.nature.com/articles/s41598-017-04884-2 [Cited on page 58.]

[110] A. Bassou, P. Machado, M. Gomes, B. Manjunath, R. Vilarinho, B. Silva, J. Oliveira, B. Almeida, A. Almeida, and E. Al., "Thermal stability and decomposition kinetics of NdNiO3−δ at 1 bar of O2," *Materials Today Communications*, vol. 28, no. December 2020, p. 102663, sep 2021. [Online]. Available: https://linkinghub.elsevier.com/retrieve/pii/S2352492821006553 [Cited on pages 59 and 60.]

[111] V. G. Sathe and A. Dubey, "Broken symmetry in LaAlO 3 single crystal probed by resonant Raman spectroscopy," *Journal of Physics: Condensed Matter*, vol. 19, no. 38, p. 382201, sep 2007. [Online]. Available: https://iopscience.iop.org/article/10.1088/0953-8984/19/38/382201 [Cited on page 60.]

[112] A. Schober, "Advanced Raman Spectroscopy of Ultrathin RNiO3 Films," Ph.D. dissertation, University of Luxembourg, 2018. [Cited on page 61.]

[113] T. Shao, Z. Qi, Y. Wang, Y. Li, M. Yang, and C. Hu, "Metal-insulator transition in epitaxial NdNiO 3 thin film: A structural, electrical and optical study," *Applied Surface Science*, vol. 399, pp. 346–350, 2017. [Online]. Available: http://dx.doi.org/10.1016/j.apsusc.2016.12.102 [Cited on page 61.]

[114] H. C. Gupta, M. K. Singh, and L. M. Tiwari, "A lattice dynamical investigation of Raman and infrared wavenumbers at the zone center of the orthorhombic NdNiO 3 perovskite," *Journal of Physics and Chemistry of Solids*, vol. 64, no. 3, pp. 531–533, 2003. [Online]. Available: https://www.sciencedirect.com/science/article/pii/S0022369702003360 [Cited on page 61.]

[115] M. Balkanski, R. F. Wallis, and E. Haro, “Anharmonic effects in light scattering due to optical phonons in silicon,” *Physical Review B*, vol. 28, no. 4, pp. 1928–1934, aug 1983. [Online]. Available: https://link.aps.org/doi/10.1103/PhysRevB.28.1928 [Cited on page 62.]

[116] D. M. Juraschek, M. Fechner, A. V. Balatsky, and N. A. Spaldin, “Dynamical multiferroicity,” *Physical Review Materials*, vol. 1, no. 1, p. 014401, jun 2017. [Online]. Available: http://link.aps.org/doi/10.1103/PhysRevMaterials.1.014401 [Cited on page 67.]

[117] A. Stupakiewicz, C. S. Davies, K. Szerenos, D. Afanasiev, K. S. Rabinovich, A. V. Boris, A. Caviglia, A. V. Kimel, and A. Kirilyuk, “Ultrafast phononic switching of magnetization,” *Nature Physics*, vol. 17, no. 4, pp. 489–492, apr 2021. [Online]. Available: http://www.nature.com/articles/s41567-020-01124-9 [Cited on page 67.]

[118] V. A. Stoica, D. Puggioni, J. Zhang, R. Singla, G. L. Dakovski, G. Coslovich, M. H. Seaberg, M. Kareev, S. Middey, P. Kissin, R. D. Averitt, J. Chakhalian, H. Wen, J. M. Rondinelli, and J. W. Freeland, “Magnetic order driven ultrafast phase transition in <math> <msub> <mi>NdNiO</mi> <mn>3</mn> </msub> </math>,” *Physical Review B*, vol. 106, no. 16, p. 165104, oct 2022. [Online]. Available: https://link.aps.org/doi/10.1103/PhysRevB.106.165104 [Cited on page 67.]

[119] M. K. Singh, H. M. Jang, H. C. Gupta, and R. S. Katiyar, “Polarized Raman scattering and lattice eigenmodes of antiferromagnetic NdFeO 3,” *Journal of Raman Spectroscopy*, vol. 39, no. 7, pp. 842–848, jul 2008. [Online]. Available: https://onlinelibrary.wiley.com/doi/10.1002/jrs.1923 [Cited on pages 67, 71, and 72.]

[120] V. Mathe, K. Patankar, R. Patil, and C. Lokhande, “Synthesis and dielectric properties of Bi1−xNdxFeO3 perovskites,” *Journal of Magnetism and Magnetic Materials*, vol. 270, no. 3, pp. 380–388, apr 2004. [Online]. Available: https://linkinghub.elsevier.com/retrieve/pii/S0304885303007376 [Cited on page 67.]

[121] M. T. Jamil, J. Ahmad, S. H. Bukhari, and H. Ahmad, “Optical phonons and its effect on physical properties of rare-earth orthoferrites R FeO3 (R = La, Nd, Gd, Dy, Er): IR reflectivity measurements,” *International Journal of Modern Physics B*, vol. 32, no. 21, p. 1850229, aug 2018. [Online]. Available:

https://www.worldscientific.com/doi/abs/10.1142/S0217979218502296 [Cited on page 67.]

[122] M. M. Gomes, R. Vilarinho, H. Zhao, J. Íñiguez-González, M. Mihalik, M. Mihalik, A. Maia, V. Goian, D. Nuzhnyy, S. Kamba, and J. A. Moreira, "Lattice excitations in NdFeO3 through polarized optical spectroscopies," *Scientific Reports*, vol. 14, no. 1, p. 15378, jul 2024. [Online]. Available: SSSSSSShttps://www.nature.com/articles/s41598-024-66594-w [Cited on pages 68, 122, and 123.]

[123] M. N. Iliev, M. V. Abrashev, J. Laverdière, S. Jandl, M. M. Gospodinov, Y.-Q. Wang, and Y.-Y. Sun, "Distortion-dependent Raman spectra and mode mixing in RMnO3 perovskites (R=La,Pr,Nd,Sm,Eu,Gd,Tb,Dy,Ho,Y)," *Physical Review B*, vol. 73, no. 6, p. 064302, feb 2006. [Online]. Available: https://link.aps.org/doi/10.1103/PhysRevB.73.064302 [Cited on page 70.]

[124] M. C. Weber, M. Guennou, H. J. Zhao, J. Íñiguez, R. Vilarinho, A. Almeida, J. A. Moreira, and J. Kreisel, "Raman spectroscopy of rare-earth orthoferrites RFeO3 (R=La, Sm, Eu, Gd, Tb, Dy)," *Physical Review B*, vol. 94, no. 21, p. 214103, dec 2016. [Online]. Available: https://link.aps.org/doi/10.1103/PhysRevB.94.214103 [Cited on pages xviii, 70, and 72.]

[125] M. V. Abrashev, J. Bäckström, L. Börjesson, V. N. Popov, R. A. Chakalov, N. Kolev, R.-L. Meng, and M. N. Iliev, "Raman spectroscopy of CaMnO3: Mode assignment and relationship between Raman line intensities and structural distortions," *Physical Review B*, vol. 65, no. 18, p. 184301, apr 2002. [Online]. Available: https://link.aps.org/doi/10.1103/PhysRevB.65.184301 [Cited on page 71.]

[126] E. Haye, E. Andre, F. Capon, S. Barrat, M. De La Pierre, R. Dovesi, and C. Carteret, "Experimental and Theoretical Infrared Signatures of REMO3 (RE = La, Pr, Nd, Sm, and M = Co, Fe) Perovskites," *Journal of Physical Chemistry C*, vol. 122, no. 19, pp. 10 519–10 525, 2018. [Cited on page 74.]

[127] G. F. Herrmann, "Magnetic Resonances and Susceptibility in Orthoferrites," *Physical Review*, vol. 133, no. 5A, pp. A1334–A1344, mar 1964. [Online]. Available: https://link.aps.org/doi/10.1103/PhysRev.133.A1334 [Cited on page 76.]

[128] A. P. Cracknell, "Scattering matrices for the Raman effect in magnetic crystals," *Journal of Physics C: Solid State Physics*, vol. 2, no. 3, p. 314, mar 1969. [Online].

Available: https://iopscience.iop.org/article/10.1088/0022-3719/2/3/314 [Cited on pages 77 and 78.]

[129] R. Loudon, "The Raman effect in crystals," *Advances in Physics*, vol. 13, no. 52, pp. 423–482, oct 1964. [Online]. Available: http://www.tandfonline.com/action/journalInformation?journalCode=tadp20http://www.tandfonline.com/doi/abs/10.1080/00018736400101051 [Cited on page 79.]

[130] R. Przeniosło, I. Sosnowska, M. Loewenhaupt, and A. Taylor, "Crystal field excitations of NdFeO3," *Journal of Magnetism and Magnetic Materials*, vol. 140-144, no. PART 3, pp. 2151–2152, 1995. [Cited on pages 82, 123, and 124.]

[131] G. Kresse and D. Joubert, "From ultrasoft pseudopotentials to the projector augmented-wave method," *Physical Review B*, vol. 59, no. 3, pp. 1758–1775, jan 1999. [Online]. Available: https://link.aps.org/doi/10.1103/PhysRevB.59.1758 [Cited on page 82.]

[132] M. A. Carpenter, "Static and dynamic strain coupling behaviour of ferroic and multiferroic perovskites from resonant ultrasound spectroscopy," *Journal of Physics: Condensed Matter*, vol. 27, no. 26, p. 263201, jul 2015. [Online]. Available: https://iopscience.iop.org/article/10.1088/0953-8984/27/26/263201 [Cited on page 86.]

[133] X. R. Huang, Z. W. Hu, S. S. Jiang, J. H. Jiang, Y. L. Tian, Y. Han, and J. Y. Wang, "Synchrotron radiation topography studies of twinning in NdP5O14 crystals," *Journal of Applied Physics*, vol. 75, no. 12, pp. 7756–7760, jun 1994. [Online]. Available: https://pubs.aip.org/jap/article/75/12/7756/494021/Synchrotron-radiation-topography-studies-of [Cited on pages 86 and 90.]

[134] M. C. Weber, M. Guennou, D. M. Evans, C. Toulouse, A. Simonov, Y. Kholina, X. Ma, W. Ren, S. Cao, M. A. Carpenter, B. Dkhil, M. Fiebig, and J. Kreisel, "Emerging spin–phonon coupling through cross-talk of two magnetic sublattices," *Nature Communications*, vol. 13, no. 1, p. 443, jan 2022. [Online]. Available: https://www.nature.com/articles/s41467-021-27267-8 [Cited on pages xix, 87, 91, 96, 97, and 111.]

[135] Z. W. Hu, P. Q. Huang, S. S. Jiang, J. Y. Wang, J. H. Jiang, and J. Y. Zhao, "Synchrotron x-ray topography study of Er-doped LaP5O14 crystal," *Journal*

of Applied Physics, vol. 74, no. 12, pp. 7124–7128, dec 1993. [Online]. Available: https://pubs.aip.org/jap/article/74/12/7124/496145/Synchrotron-x-ray-topography-study-of-Er-doped [Cited on pages 90 and 94.]

[136] G. Gorodetsky, S. Shaft, and B. M. Wanklyn, "Magnetoelastic properties of TmFe <math display="inline"> <mrow> <msub> <mrow> <mi mathvariant="normal">O</mi> </mrow> <mrow> <mn>3</mn> </mrow> </msub> </mrow> </math> at the spin reorientation region," *Physical Review B*, vol. 14, no. 5, pp. 2051–2056, sep 1976. [Online]. Available: https://link.aps.org/doi/10.1103/PhysRevB.14.2051 [Cited on page 91.]

[137] G. Gorodetsky and S. Shtrikman, "Measurements of acoustic velocity and attenuation shifts at the spin-reorientation phase transition of TmFeO3," *Journal of Applied Physics*, vol. 51, no. 2, pp. 1127–1130, feb 1980. [Online]. Available: https://pubs.aip.org/jap/article/51/2/1127/501666/Measurements-of-acoustic-velocity-and-attenuation [Cited on page 91.]

[138] G. Gorodetsky and B. Lüthi, "Sound-Wave—Soft-Mode Interaction near Displacive Phase Transitions: Spin Reorientation in ErFe <math display="inline"> <mrow> <msub> <mrow> <mi mathvariant="normal">O</mi> </mrow> <mrow> <mn>3</mn> </mrow> </msub> </mrow> </math>," *Physical Review B*, vol. 2, no. 9, pp. 3688–3698, nov 1970. [Online]. Available: https://link.aps.org/doi/10.1103/PhysRevB.2.3688 [Cited on page 91.]

[139] G. Gorodetsky, F. Missell, and C. Garland, "Ultrasonic velocities near the spin-reorientation transitions in ErFeO3 at high pressure," *Journal of Physics and Chemistry of Solids*, vol. 39, no. 7, pp. 723–725, jan 1978. [Online]. Available: https://linkinghub.elsevier.com/retrieve/pii/0022369778900057 [Cited on page 91.]

[140] N. K. Dan'shin, S. V. Zherlitsyn, S. S. Zvada, G. G. Kramarchuk, M. A. Sdvizhkov, and V. D. Fil', "Dynamic properties of YbFeO3 in the vicinity of an orientational phase transition," *Sov. Phys. JETP*, vol. 66, no. April 1987, pp. 1227–1232, 1987. [Cited on page 91.]

[141] M. A. Carpenter and E. K. Salje, "Elastic anomalies in minerals due to structural phase transitions," *European Journal of Mineralogy*, vol. 10, no. 4, pp. 693–812, jul 1998. [Online]. Available: http://www.schweizerbart.de/papers/ejm/detail/10/

83259/Elastic_anomalies_in_minerals_due_to_structural_ph?af=crossref [Cited on pages 91 and 92.]

[142] R. E. A. McKnight, C. J. Howard, and M. A. Carpenter, "Elastic anomalies associated with transformation sequences in perovskites: I. Strontium zirconate, SrZrO 3," *Journal of Physics: Condensed Matter*, vol. 21, no. 1, p. 015901, jan 2009. [Online]. Available: https://iopscience.iop.org/article/10.1088/0953-8984/21/1/015901 [Cited on pages 92, 93, and 97.]

[143] E. K. H. Salje, B. Wruck, and H. Thomas, "Order-parameter saturation and low-temperature extension of Landau theory," *Zeitschrift for Physik B Condensed Matter*, vol. 82, no. 3, pp. 399–404, oct 1991. [Online]. Available: http://link.springer.com/10.1007/BF01357186 [Cited on pages 94 and 95.]

[144] H.-W. Meyer, S. Marion, P. Sondergeld, M. A. Carpenter, K. S. Knight, S. A. Redfern, and M. T. Dove, "Displacive components of the low-temperature phase transitions in lawsonite," *American Mineralogist*, vol. 86, no. 4, pp. 566–577, apr 2001. [Online]. Available: https://www.degruyter.com/document/doi/10.2138/am-2001-0419/html

[145] H.-W. Meyer, M. A. Carpenter, A. Graeme-Barber, P. Sondergeld, and W. Schranz, "Local and macroscopic order parameter variations associated with low temperature phase transitions in lawsonite, CaAl2Si2O7(OH)2·H2O," *European Journal of Mineralogy*, vol. 12, no. 6, p. 1139, 2000. [Cited on pages 94 and 95.]

[146] M. A. Carpenter, A. Buckley, P. A. Taylor, and T. W. Darling, "Elastic relaxations associated with the Pm3m R3c transition in LaAlO 3 : III. Superattenuation of acoustic resonances," *Journal of Physics: Condensed Matter*, vol. 22, no. 3, p. 035405, jan 2010. [Online]. Available: https://iopscience.iop.org/article/10.1088/0953-8984/22/3/035405 [Cited on pages 94 and 170.]

[147] N. J. Perks, Z. Zhang, R. J. Harrison, and M. A. Carpenter, "Strain relaxation mechanisms of elastic softening and twin wall freezing associated with structural phase transitions in (Ca,Sr)TiO 3 perovskites," *Journal of Physics: Condensed Matter*, vol. 26, no. 50, p. 505402, dec 2014. [Online]. Available: https://iopscience.iop.org/article/10.1088/0953-8984/26/50/505402 [Cited on page 97.]

[148] Z. Zhang, J. Koppensteiner, W. Schranz, J. B. Betts, A. Migliori, and M. A. Carpenter, "Microstructure dynamics in orthorhombic perovskites," *Physical*

Review B, vol. 82, no. 1, p. 014113, jul 2010. [Online]. Available: https://link.aps.org/doi/10.1103/PhysRevB.82.014113 [Cited on page 97.]

[149] J. Chrosch and E. K. H. Salje, "Temperature dependence of the domain wall width in LaAlO3," *Journal of Applied Physics*, vol. 85, no. 2, pp. 722–727, jan 1999. [Online]. Available: https://pubs.aip.org/jap/article/85/2/722/289148/Temperature-dependence-of-the-domain-wall-width-in [Cited on page 98.]

[150] K. B. Aring and A. J. Sievers, "Role of the Ytterbium Spins in the Spin Reorientation in YbFeO3," *Journal of Applied Physics*, vol. 41, no. 3, pp. 1197–1198, mar 1970. [Online]. Available: https://pubs.aip.org/jap/article/41/3/1197/790350/Role-of-the-Ytterbium-Spins-in-the-Spin [Cited on pages 111 and 121.]

[151] U. Staub, L. Rettig, E. M. Bothschafter, Y. W. Windsor, M. Ramakrishnan, S. R. V. Avula, J. Dreiser, C. Piamonteze, V. Scagnoli, S. Mukherjee, C. Niedermayer, M. Medarde, and E. Pomjakushina, "Interplay of Fe and Tm moments through the spin-reorientation transition in TmFeO3," *Physical Review B*, vol. 96, no. 17, p. 174408, nov 2017. [Online]. Available: https://link.aps.org/doi/10.1103/PhysRevB.96.174408 [Cited on page 111.]

[152] T. Yamaguchi and K. Tsushima, "Magnetic Symmetry of Rare-Earth Orthochromites and Orthoferrites," *Physical Review B*, vol. 8, no. 11, pp. 5187–5198, dec 1973. [Online]. Available: https://link.aps.org/doi/10.1103/PhysRevB.8.5187 [Cited on page 111.]

[153] J. Jiang, G. Song, D. Wang, Z. Jin, Z. Tian, X. Lin, J. Han, G. Ma, S. Cao, and Z. Cheng, "Magnetic-field dependence of strongly anisotropic spin reorientation transition in NdFeO 3 : a terahertz study," *Journal of Physics: Condensed Matter*, vol. 28, no. 11, p. 116002, mar 2016. [Online]. Available: https://iopscience.iop.org/article/10.1088/0953-8984/28/11/116002 [Cited on pages 111, 112, and 116.]

[154] E. E. Zubov, I. Fita, R. Puzniak, and A. Wisniewski, "Spin-reorientation phase transition and induced spin reversals in <math> <mrow> <mi>NdFe</mi> <msub> <mi mathvariant="normal">O</mi> <mn>3</mn> </msub> </mrow> </math> : Theory and experiment," *Physical Review B*, vol. 110, no. 13, p. 134404, oct 2024. [Online]. Available: https://link.aps.org/doi/10.1103/PhysRevB.110.134404 [Cited on page 111.]

[155] G. Song, J. Jiang, X. Wang, Z. Jin, X. Lin, G. Ma, and S. Cao, “Selective excitation of spin resonance in orthoferrite PrFeO3 with impulsive polarized terahertz radiation,” *Journal of Applied Physics*, vol. 114, no. 24, dec 2013. [Online]. Available: https://pubs.aip.org/jap/article/114/24/243104/371448/Selective-excitation-of-spin-resonance-in [Cited on page 116.]

[156] A. Mukhin, M. Biberacher, A. Pimenov, and A. Loidl, “Antiferromagnetic resonances and magnetization of a canted antiferromagnet,” *Journal of Magnetic Resonance*, vol. 170, no. 1, pp. 8–14, sep 2004. [Online]. Available: https://linkinghub.elsevier.com/retrieve/pii/S1090780704001685 [Cited on pages xx, 118, 119, 120, and 125.]

[157] S. Blundell, *Magnetism in Condensed Matter*. Oxford University PressOxford, oct 2001. [Online]. Available: https://academic.oup.com/book/54773 [Cited on pages 124 and 129.]

[158] S. Mitsudo, K. Hirano, H. Nojiri, M. Motokawa, K. Hirota, A. Nishizawa, N. Kaneko, and Y. Endoh, “Submillimeter wave ESR measurement of LaMnO3,” *Journal of Magnetism and Magnetic Materials*, vol. 177-181, no. PART 2, pp. 877–878, jan 1998. [Online]. Available: https://linkinghub.elsevier.com/retrieve/pii/S0304885397005258 [Cited on page 125.]

[159] G. Cinader, “Effect of Antisymmetric Exchange Interaction on the Magnetization and Resonance in Antiferromagnets,” *Physical Review*, vol. 155, no. 2, pp. 453–457, mar 1967. [Online]. Available: https://link.aps.org/doi/10.1103/PhysRev.155.453 [Cited on pages 125 and 126.]

[160] G. Gorodetsky and D. Treves, “Second-Order Susceptibility Terms in Orthoferrites at Room Temperature,” *Physical Review*, vol. 135, no. 1A, pp. A97–A101, jul 1964. [Online]. Available: https://link.aps.org/doi/10.1103/PhysRev.135.A97 [Cited on pages 126 and 129.]

[161] D. Pinkowicz, M. Rams, W. Nitek, B. Czarnecki, and B. Sieklucka, “Evidence for magnetic anisotropy of [NbIV(CN)8]4− in a pillared-layered Mn2Nb framework showing spin-flop transition,” *Chemical Communications*, vol. 48, no. 67, p. 8323, 2012. [Online]. Available: https://xlink.rsc.org/?DOI=c2cc32234j [Cited on page 129.]

[162] T. C. Damen, S. P. S. Porto, and B. Tell, “Raman Effect in Zinc Oxide,” *Physical Review*, vol. 142, no. 2, pp. 570–574, feb 1966. [Online]. Available: https://link.aps.org/doi/10.1103/PhysRev.142.570 [Cited on page 163.]

[163] S. W. Lovesey, “Orthoferrite with a hidden lanthanide magnetic motif: NdFeO3,” *Physical Review B*, vol. 107, no. 21, p. 214426, jun 2023. [Online]. Available: https://doi.org/10.1103/PhysRevB.107.214426https://link.aps.org/doi/10.1103/PhysRevB.107.214426 [Cited on page 164.]

[164] A. Nowick and B. Berry, *Anelastic relaxation in crystalline solids*. New York, London: Academic Press, 1972. [Cited on page 170.]

A. Appendix

A.1. Conversion from standard to non-standard setting

For orthorhombic perovskites, common to find in the literature the non-standard setting P*bnm* instead of the standard P*nma*. The two settings are related by the cyclic permutation $(x,y,z)_{Pnma} \longrightarrow (y,z,x)_{Pbnm}$.

The configuration of polarized Raman scattering experiments are often represented using Porto's notation [162]. This notation consists in four letters: **A(BC)D**, where [162]:

- **A** represents the direction of propagation vector of incident light, $\mathbf{k}_i$
- **B** represents the direction of polarization vector of incident light, $\mathbf{E}_i$
- **C** represents the direction of polarization vector of scattered light, $\mathbf{E}_s$
- **D** represents the direction of propagation vector of scattered light, $\mathbf{k}_s$

In the Raman backscattering geometry, which is the one used in all the polarized measurements in this thesis, propagation of light is in the same direction for both incident and scattered beams, so $\mathbf{k}_i = \mathbf{k}_s$.

Pnma	A_g	B_{1g}	B_{2g}	B_{3g}
X(YY)X	x	-	-	-
X(YZ)X	-	-	-	x
X(ZZ)X	x	-	-	-
Y(XX)Y	x	-	-	-
Y(XZ)Y	-	-	x	-
Y(ZZ)Y	x	-	-	-
Z(XX)Z	x	-	-	-
Z(XY)Z	-	x	-	-
Z(YY)Z	x	-	-	-

Pbnm	A_g	B_{3g}	B_{1g}	B_{2g}
Y(ZZ)Y	x	-	-	-
Y(ZX)Y	-	-	-	x
Y(XX)Y	x	-	-	-
Z(YY)Z	x	-	-	-
Z(YX)Z	-	-	x	-
Z(XX)Z	x	-	-	-
X(YY)X	x	-	-	-
X(YZ)X	-	x	-	-
X(ZZ)X	x	-	-	-

Pnma	A_g	B_{1g}	B_{2g}	B_{3g}	B_{1u}	B_{2u}	B_{3u}
Pbnm	A_g	B_{3g}	B_{1g}	B_{2g}	B_{3u}	B_{1u}	B_{2u}

FIGURE A.1: Polarization selection rules for Raman modes. First column is the Porto's notation and "x" represents that the mode can be observed in that configuration. Orange table shows the selection rules for the P*nma* setting and blue table for the P*bnm*. Bottom table presents the direct relation of Raman and IR modes between the two settings.

A.2. Classification of magnetic point and space groups

The following table with the classification of magnetic point groups and the relation with different magnetic modes(components) helps to understand the choice of the magnetic space group $P2_1'/n'$ for the magnetic structure in the spin-reorientation region. First step is restricting the magnetic classes that allow ferromagnetism. The second step limits the search to classes with only two ferromagnetic components, F0F (note that the ***F*** vector during the SRT is in the ac-plane). The possible point groups belong to monoclinic symmetry, category No. 4: $2'$, m' and $2'/m'$.

Through a group-subgroup analysis using the k_SUBGROUPSMAG tool from Bilbao Crystallographic Server, the non magnetic P*nma*1' has a group-subgroup relation with several monoclinic subgroups, but the $P2_1'/c'$ space group (belonging to the magnetic point group $2'/m'$) is the one that shows a direct relation with the magnetic space groups above (P*b'n'm* equivalent to P*n'ma'*, Γ_4 irrep) and below (P*bn'm'* equivalent to P*n'm'a*, Γ_2 irrep) the spin-reorientation. Therefore, $P2_1'/c'$ (equivalent to $P2_1'/n'$) magnetic space group is the one that describes the magnetic structure of $NdFeO_3$ across the SRT [86, 87, 163].

	WITH FERROMAGNETISM				WITHOUT FERROMAGNETISM			
Crystal system →	Tri-clinic	Mono-clinic	Mono-clinic	Ortho-rhombic	Ortho-rhombic	Ortho-rhombic	Mono-clinic	Tri-clinic
Cat. no. ⟶	1	4	3	7	6	8	5	2
Magnetic Class ⟶ / Magnetic site-symmetry point group ↓								
1 $\bar{1}$								
		$2'$ m' $2'/m'$						
			2 m $2/m$					
				$2'2'2$ $m'm2'$ $m'm'2$ $m'm'm$				
					222 $mm2$ mmm			
						$2221'$ $mm21'$ $m'mm$ $m'm'm'$ $mmm1'$		
							$2'/m$ $2/m'$ $21'$ $m1'$ $2/m1'$	
								$\bar{1}'$ $11'$ $\bar{1}1'$
$1, \bar{1}$ **(3 components)**	"FFF"	"FAF"	"AFA"	"AFB"	"ABC1"	"ABC2"	"ABA"	"AAA"
$2', m', 2'/m'$ **(2 components)**	—	"F0F"	—	"AF0"	—	"AB0"	"A0A"	—
$2, m, 2/m$ $2'2'2, m'm2'$ $m'm'2, m'm'm$ **(1 component)**	—	—	"0F0"		"0A0"			—
$\bar{1}', 2'/m, 2/m'$ $222, mm2, mmm$ $m'mm, m'm'm'$ **(0 components)**	—	—	—	—	"000"			

FIGURE A.2: Classification of magnetic point and space groups in triclinic, monoclinic and orthorhombic systems related to different magnetic modes. Columns denote magnetic classes and rows the site-symmetry magnetic point groups. Adapted from [87].

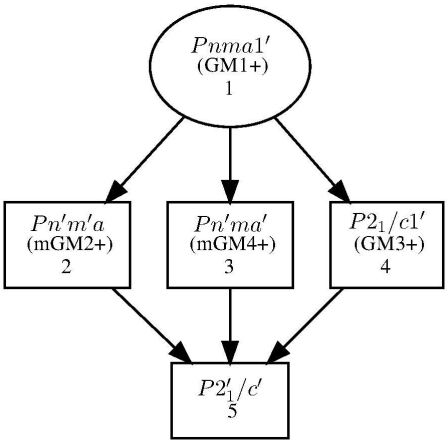


FIGURE A.3: Group-subgroup relation between magnetic space groups. Adapted from k_SUBGROUPSMAG tool from Bilbao Crystallographic Server.

A.3. Structural analysis of $NdNiO_3$ film on cooling

Analogously to the structural analysis presented in Chapter 3 for heating run, the same was done for the Raman spectroscopy data collected in cooling run, as shown in Figure A.4. The spectral region of interest is in the 280 - 340 cm^{-1} range.

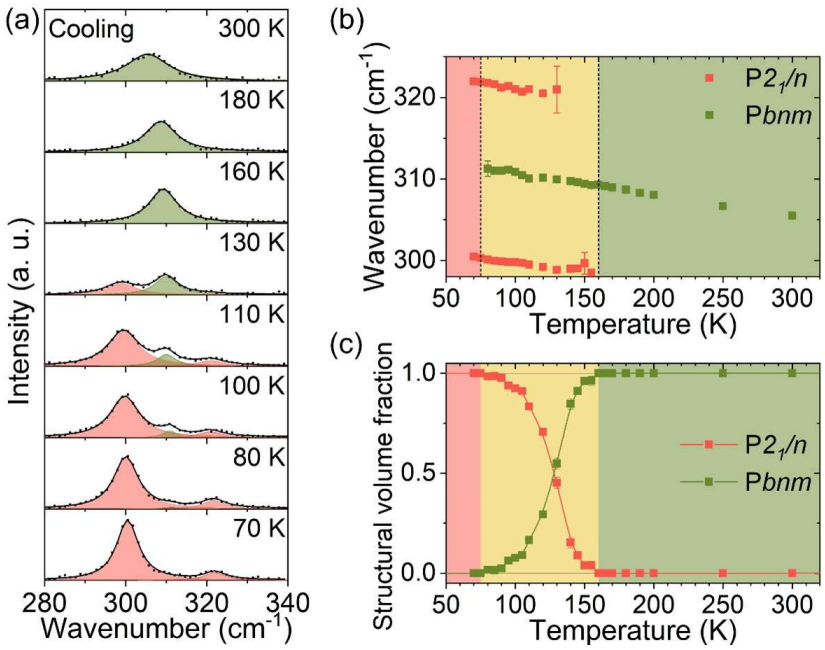


FIGURE A.4: (a) Representative unpolarized Raman spectra of the NNO film, measured in cooling run, along with the result of the spectral deconvolution. Spectral components of $P2_1/n$ phase are represented in pink and of P*bnm* phase in green. Temperature dependence of (b) wavenumber and (c) structural volume fraction, i.e., normalized intensity of the Raman modes observed in the 280 to 340 cm^{-1} range. M-modes: 300 + 321 cm^{-1} (the $P2_1/n$ monoclinic phase) and O-mode: 305 cm^{-1} (P*bnm* orthorhombic phase). Dashed lines represent the structural transition temperatures, above which the Raman bands associated with the monoclinic phase disappear. Shaded regions represent: P*bnm* phase in green, the coexistence the two structural phases in yellow and $P2_1/n$ phase in pink.

A.4. IR reflectivity analysis in $NdFeO_3$

As mentioned in Chapter 4, reflectivity spectra analysis is described by a slightly higher number of excitations than expected from factor-group analysis in Equation 4.1. Some of these excitations are assigned to: crystal-field excitations (CF), leakages from other polarizations due to small misalignments of the samples or multiphonon scattering processes. Table A.1 shows the parameters obtained from the IR reflectivity spectra fitting.

TABLE A.1: Parameters obtained from the IR reflectivity spectra fitting and corresponding symmetry assignment.

Geometry	4 K				300 K				Symmetry assignment
	ω_{TO}	γ_{TO}	ω_{LO}	γ_{LO}	ω_{TO}	γ_{TO}	ω_{LO}	γ_{LO}	
E||a	82.8	7.4	84.2	7.5	88.7	11.6	89.3	12.3	CF
	113.8	4.5	114.9	4.6	110.2	10.1	112.3	11.3	$B_{3u}(1)$
	170.2	8.2	172.9	12.0	142.5	8.3	142.8	9.4	Leakage from $B_{1u}(1)$
	178.3	7.1	194.0	6.1	173.5	8.8	190.6	5.6	$B_{3u}(2)$
	260.8	8.7	270.5	3.4	256.6	12.6	267.4	8.9	$B_{3u}(3)$
	274.1	4.1	307.2	8.9	271.67	8.8	308.4	18.0	$B_{3u}(4)$
	319.2	7.0	321.1	4.9	–	–	–	–	$B_{3u}(5)$
	340.9	10.4	352.4	4.6	341.5	18.3	353.0	8.7	$B_{3u}(6)$
	357.2	13.1	374.1	14.2	–	–	–	–	CF
	376.5	14.2	400.3	10.7	358.4	18.6	395.5	13.4	$B_{3u}(7)$
	400.6	10.6	425.8	11.9	395.7	14.7	413.8	19.1	Leakage from $B_{2u}(7)$
	426.0	11.6	438.5	15.2	413.8	20.5	439.1	16.3	Multiphonon scattering
	438.7	14.5	451.5	13.7	–	–	–	–	Multiphonon scattering
	452.4	13.8	489.7	22.2	439.2	16.8	493.3	18.4	$B_{3u}(8)$
	493.3	25.2	518.0	14.6	495.7	15.8	512.0	16.8	Leakage from $B_{1u}(6)$
	550.6	17.4	642.1	8.7	549.3	32.5	637.3	8.6	$B_{3u}(9)$
E||b	82.4	7.3	83.3	7.2	–	–	–	–	CF
	95.3	11.5	95.9	12.0	90.1	11.5	90.4	12.2	Multiphonon scattering
	112.3	6.8	113.7	8.0	109.6	9.3	111.3	9.4	$B_{2u}(1)$
	171.1	6.8	172.9	9.6	147.0	9.9	147.6	10.7	Leakage from $B_{1u}(1)$
	179.8	5.8	193.7	5.2	174.1	8.1	190.3	5.8	$B_{2u}(2)$
	259.6	8.7	271.7	4.4	255.4	12.0	266.8	12.1	$B_{2u}(3)$
	275.3	2.9	307.2	10.3	272.3	10.3	307.8	21.9	$B_{2u}(4)$
	315.6	6.4	318.6	8.3	–	–	–	–	$B_{2u}(5)$
	340.3	9.6	352.4	8.3	342.7	20.8	353.0	8.9	$B_{2u}(6)$
	360.2	14.1	372.3	19.8	357.8	19.6	395.9	12.6	CF
	376.5	23.3	400.0	12.8	–	–	–	–	Leakage from $B_{3u}(7)$
	401.8	13.0	419.2	20.5	397.0	14.1	413.8	18.8	$B_{2u}(7)$
	419.8	22.3	451.8	15.5	413.8	20.4	439.1	16.3	Multiphonon scattering
	452.4	15.7	486.1	19.9	439.2	16.8	484.9	21.1	Leakage from $B_{3u}(8)$
	497.7	24.3	518.0	14.3	490.9	23.2	512.0	17.1	$B_{2u}(8)$
	548.1	17.2	639.7	7.5	543.3	32.2	636.1	7.3	$B_{2u}(9)$
E||c	84.5	12.6	85.8	14.1	91.4	11.2	92.2	11.9	CF
	162.3	3.3	166.6	4.7	119.3	13.9	120.6	15.0	Leakage from $B_{3u}(2)$
	167.5	4.3	174.4	8.3	165.0	7.0	170.8	8.8	$B_{1u}(1)$
	183.1	9.0	197.0	3.2	172.6	10.4	191.8	7.0	$B_{1u}(2)$
	276.5	6.0	298.2	3.8	271.1	9.3	297.0	14.6	$B_{1u}(3)$
	303.6	10.3	304.8	8.9	–	–	–	–	$B_{1u}(4)$
	329.5	11.8	350.0	14.4	330.7	20.9	354.8	19.7	$B_{1u}(5)$
	350.6	17.0	371.0	20.8	355.4	22.9	384.3	26.1	Leakage from $B_{3u}(4)$
	372.9	21.3	445.7	15.2	384.6	28.2	438.7	16.1	Leakage from $B_{3u}(5)$
	445.8	13.9	487.9	15.8	439.1	15.3	484.3	19.5	Leakage from $B_{3u}(6)$
	505.4	18.9	510.8	22.6	506.6	11.6	507.8	11.1	$B_{1u}(6)$
	549.3	23.1	648.1	7.4	540.9	35.0	644.5	9.4	$B_{1u}(7)$

A.5. RUS data on cooling for $NdFeO_3$

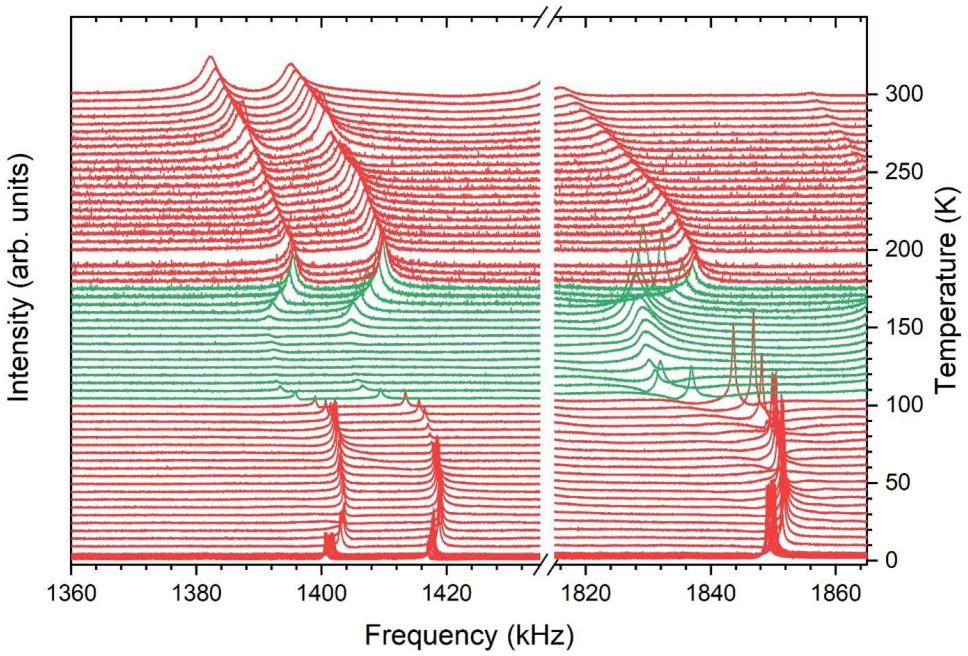


FIGURE A.5: Stack of RUS spectra scanned over 1360 to 1870 kHz, recorded in cooling run, from 2 to 300 K. Spectra have been offset up the left axis in proportion to the temperature at which they were collected, and this temperature scale is shown on the right axis.

A.6. Landau-type theory for SRT in $NdFeO_3$

A starting point for treating strain/order parameter coupling in $NdFeO_3$ is the Landau-type description for SRT given by free energy, *G*, due to the transition expressed as an expansion in $sin(\theta)$ as [90]:

$$G = G_0 + K_1 sin^2(\theta) + K_2 sin^4(\theta) \tag{A.1}$$

where G_0 is the isotropic energy, K_1 and K_2 are the anisotropic constants. Considering a second order transition, to minimize the free energy with respect to the order parameter requires

$$\begin{aligned} \tfrac{\partial G}{\partial \theta} &= K_1 sin(2\theta) + 4K_2 sin^3(\theta) cos(\theta) = 0 \\ \tfrac{\partial^2 G}{\partial \theta^2} &= 2K_1 cos(2\theta) + 4K_2 \left[3sin^2(\theta)cos^2(\theta) - sin^4(\theta)\right] > 0 \end{aligned} \tag{A.2}$$

Assuming K_2 is a positive constant and K_1 is temperature dependent:

$$K_1 = 2K_2 \frac{T - T_1}{T_1 - T_2} \tag{A.3}$$

where T_1 and T_2 are the temperatures limits of SRT. The solutions of Equation A.2 are [90]:

$$\begin{aligned} \theta = 0^\circ, T > T_1 \\ sin^2(\theta) = -\frac{K_1}{2K_2}, T_2 \leq T \leq T_1 \\ \theta = 90^\circ, T < T_2 \end{aligned} \tag{A.4}$$

For $NdFeO_3$, values of θ were determined by: neutron powder diffraction (Slawinski *et al.* [70]) using the relation $\theta = \arctan\left(\frac{M_{[100]}}{M_{[001]}}\right)$, where $M_{[100]}$ and $M_{[001]}$ are components of the net magnetic moment parallel to $[100]$ and $[001]$ respectively; and directly from THz spectroscopic measurements (Song *et al.*[77]).

A.7. Phenomenological description of elastic relaxation process in SRT

To better understand the relaxation processes detected within the spin reorientation interval, a phenomenological analysis was carried out where the formal relationship between elastic moduli and acoustic loss for an anelastic process is given by [146, 164]:

$$tan\delta = \Delta\frac{\omega\tau}{1+\omega^2\tau^2} \approx \frac{Q^{-1}}{\sqrt{3}} \tag{A.5}$$

where ω is the angular frequency and τ is the relaxation time for the loss mechanism. In the case of a standard linear solid the parameter $\Delta = \frac{C_U - C_R}{C_R}$ for $(C_U - C_R) << C_R$, where C_U is the relevant elastic constant for the unrelaxed state and C_R the elastic constant of the relaxed state. A ferroelastic domain wall moving in response to an appropriately oriented shear stress experiences a viscosity, V, and is subject to a restoring force, k. The relaxation time, τ, of the defect is given by the ratio of the viscosity to the restoring force [146, 164]:

$$\tau = \frac{V}{k} \tag{A.6}$$

There is no direct evidence that the defects with a ferroelastic strain component in the monoclinic structure are anything other than fully mobile, corresponding to the condition $\omega\tau < 1$. It is reasonable to assume that V will be effectively constant over a narrow temperature interval but the restoring force will vary with the magnitude of the strain contrast, $2e_5$, across the domain walls. Displacement in one direction and in exactly the opposite direction will produce the same restoring force and so cannot depend on the sign of e_5. In the lowest approximation, k might scale with e_5^2. C_U and C_R refer to the difference between unrelaxed, C_{55}^0, and relaxed, C_{55}, elastic constants due to bilinear coupling $\lambda_5 e_5 sin(2\theta)$. As noted above, however, the predicted pattern of softening is not seen overtly in the variations of f^2 for any resonances. A higher order term is also allowed by symmetry, $\lambda_5' e_5^2 sin^2(2\theta)$, which contributes to softening or stiffening according to:

$$C_{55} - C_{55}^0 = 2\lambda' sin^2(2\theta) \tag{A.7}$$

Assuming that e_5 scales with $sin(2\theta)$, from the bilinear coupling term and the angular frequency ω is approximately constant over the temperature range between T_1 and T_2, Equation A.5 can be written as:

$$Q^{-1} \propto Ae_5^2 \frac{\frac{A'}{e_5^2}}{1+\frac{A'^2}{e_5^2}} \propto e_5^4 \propto sin^4(2\theta) \tag{A.8}$$

where A and A' are constants, and $A'2 >> e_5^4$. Equation A.8 provides a picture of how the existence of mobile ferroelastic domain walls with only a very small contrast in shear strain across them in the SRT interval might be detected.

A.8. $NdFeO_3$ magnon and phonon spectra under magnetic field

This section presents the complete set of measurements of magnon spectra under magnetic field. The analysis discussed in Chapter 7 was based on these results. The extinction coefficient spectra of $NdFeO_3$, $\kappa(\omega)$, was calculated directly from the THz absorption spectra, using PKGraph software. Figure A.6 and Figure A.7 show the $\kappa(\omega)$ with an external magnetic field applied along a- and c-axis, respectively, for several fixed temperatures.

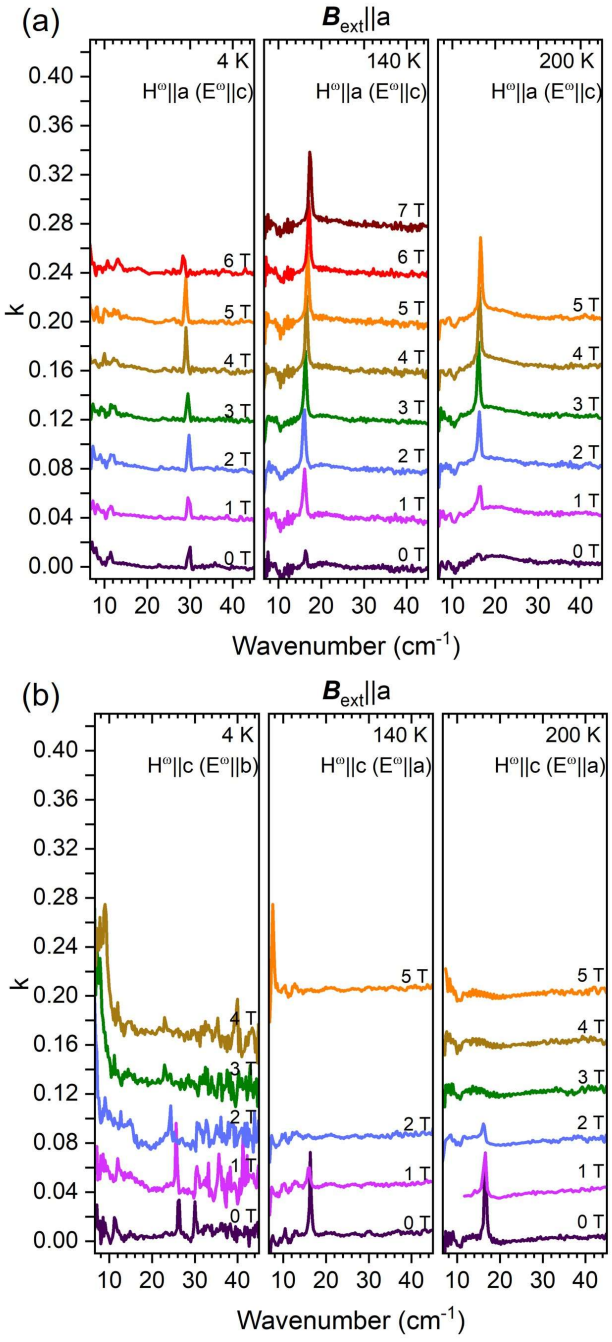


FIGURE A.6: Representative extinction spectra recorded at 4, 140 and 200 K for the THz polarization (a) $H^{\omega}||a$ and (b) $H^{\omega}||c$, at different fixed magnetic field strengths (0-7T) applied along the a-axis.

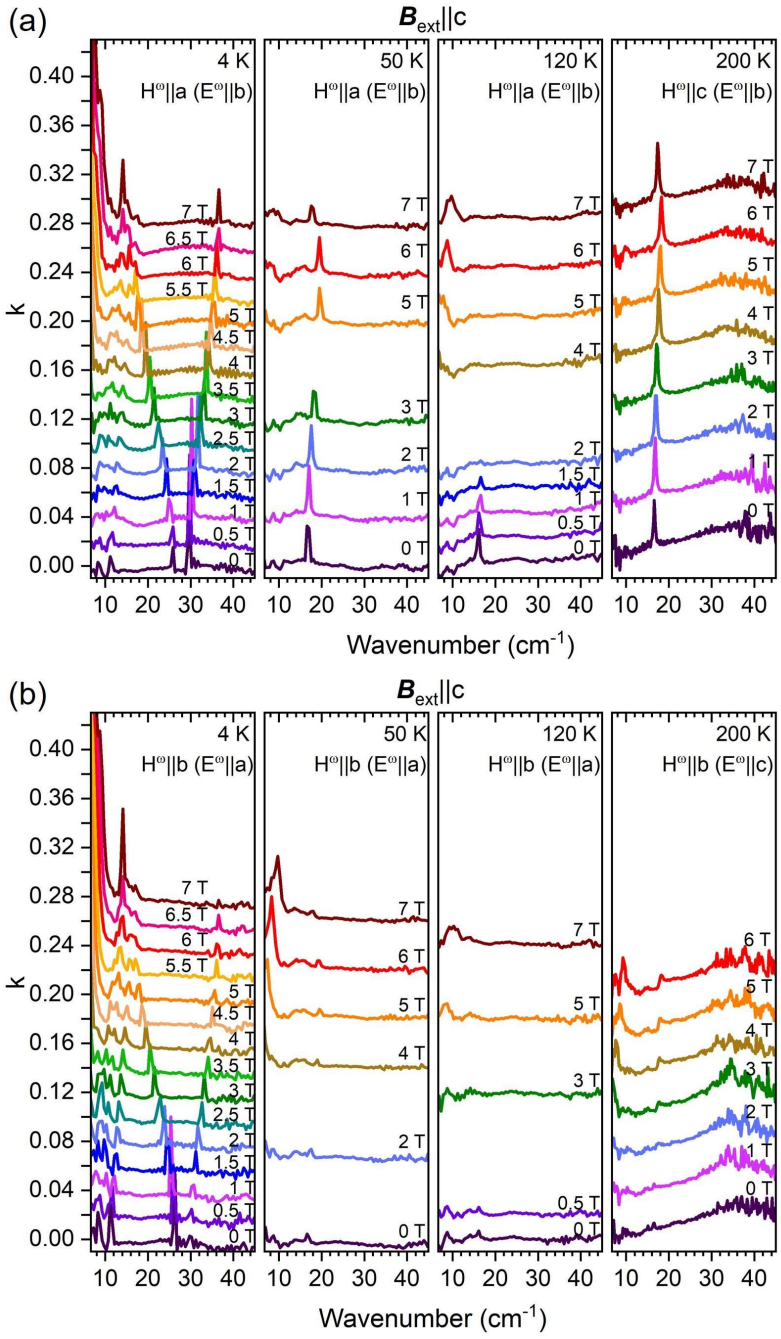


FIGURE A.7: Representative extinction spectra recorded at 4, 50, 120 and 200 K for the THz polarization (a) H^{ω}||a,c and (b) H^{ω}||b, at different fixed magnetic field strengths (0-7T) applied along the c-axis.

Figure A.8 show the unpolarized Raman spectra evolution with magnetic field applied along a- and c-axis, at fixed temperatures. The figures focus on the magnon spectral range.

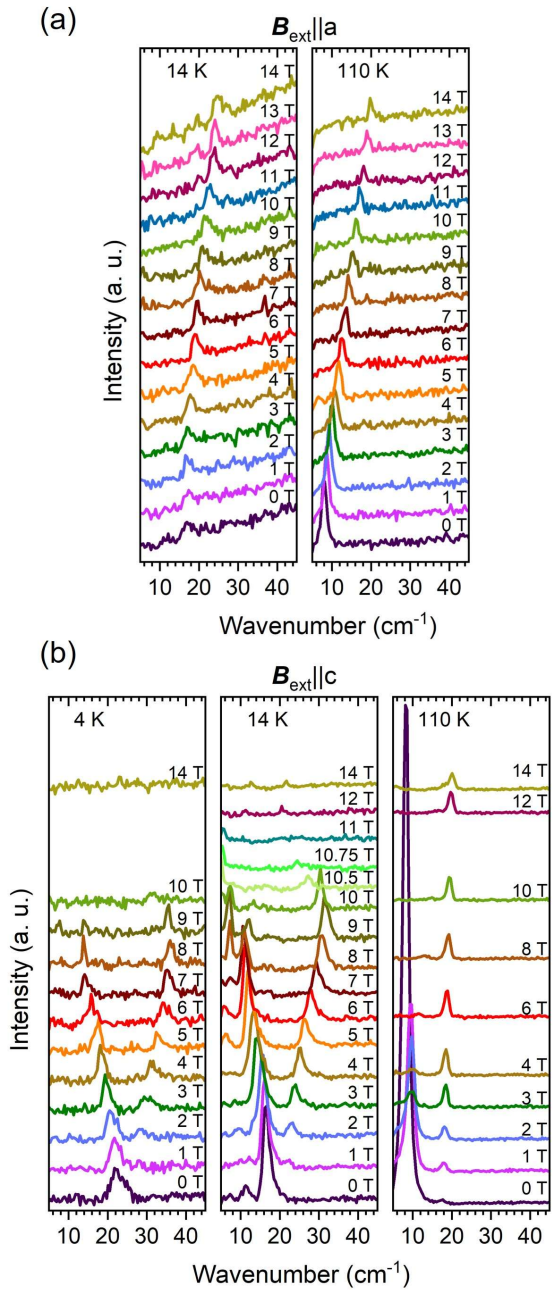


FIGURE A.8: Representative extinction spectra recorded at 4, 50, 120 and 200 K for the THz polarization (a) H^{ω}||a,c and (b) H^{ω}||b, at different fixed magnetic field strengths (0-7T) applied along the c-axis.

This section presents the complete set of measurements of phonon spectra under magnetic field, probed by unpolarized Raman spectroscopy. The spectral range is focused on Nd-oscillations modes (also called Nd-shifts) was probed at 110, 14 and 4 K, by (see Figure A.9).

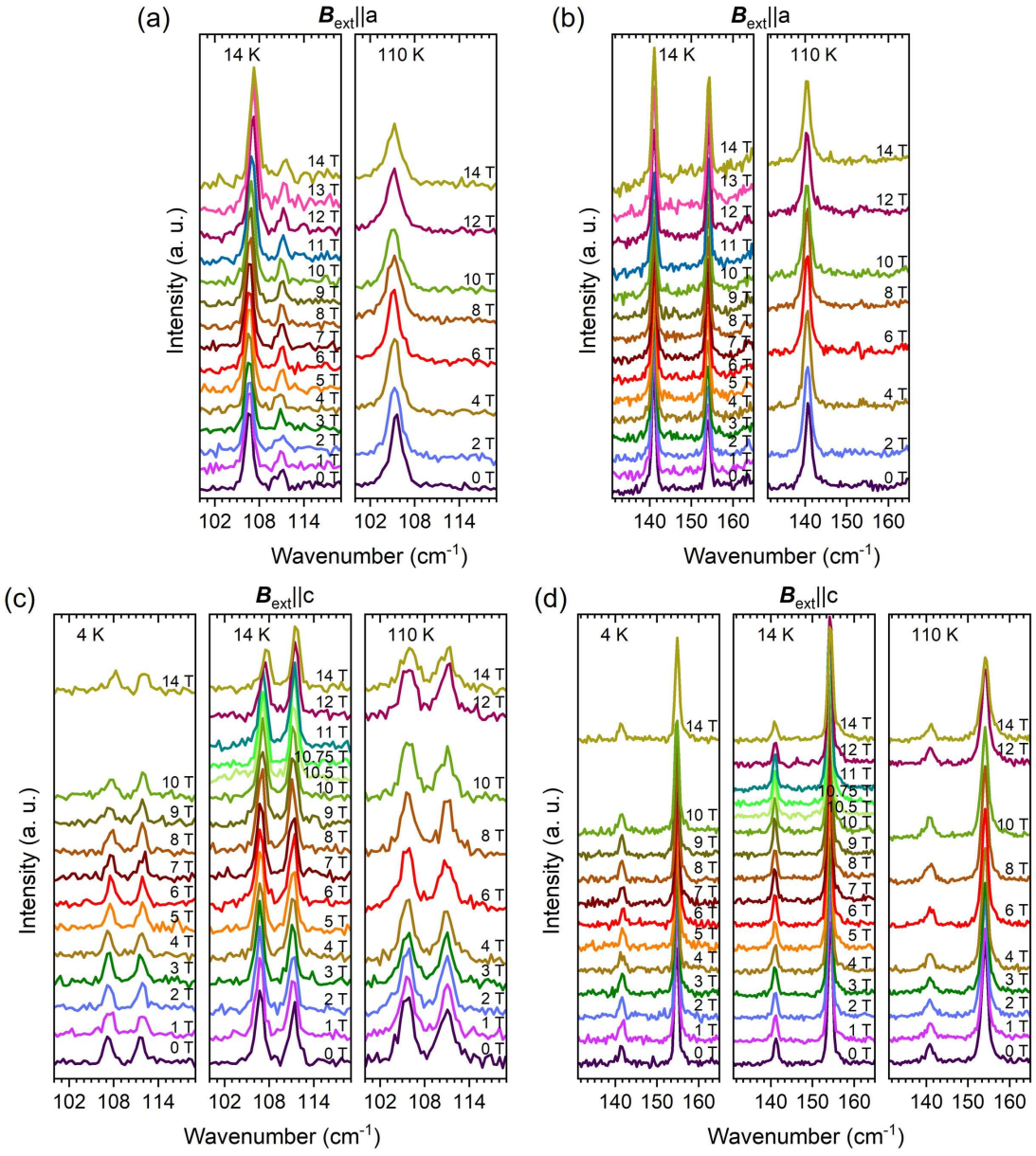


FIGURE A.9: Unpolarized Raman spectra recorded at 4, 14 and 110 K for (a)-(b)$\boldsymbol{B}_{ext}$||a and (c)-(d)$\boldsymbol{B}_{ext}$||c, where the spectral ranges show the Nd-shifts phonons.